In silico tumor growth validation based on human brain cancer models

Επαλήθευση της υπολογιστικής προσομοίωσης ανάπτυξης του όγκου βασισμένη σε μοντέλα για καρκίνο εγκεφάλου ανθρώπου

PhD Thesis

Mariam-Eleni Oraiopoulou
University of Crete, School of Medicine

Antonios F. VAKIS	Supervisor
Evangelos SAKKALIS	Advisor
Dimitrios MAVROUDIS	Advisor
Joseph PAPAMATHEAKIS	Examiner
Ioannis ZACHARAKIS	Examiner
Ioannis CHARALAMPOPOULOS	Examiner
Triantafyllos STYLIANOPOULOS	Examiner

Heraklion 2018

Abstract

Glioblastoma is the most malignant brain cancer and is not considered a curable disease so far. From the moment of the first diagnosis and in order to fight against such a greed type of cancer, the real battle is against time. Not only clinical therapeutic progress and empirical confront, but also experimental data and simulated predictions must be evaluated and reclaimed. In this PhD thesis, a multidisciplinary framework that integrates basic and translational research is presented targeting both the validation of computer-based predictions of Glioblastoma growth progress, while attempting a better understanding of Glioblastoma pathophysiology/pathobiology. In this attempt, a carefully planned combination of *in vitro, in vivo* and *in silico* experimental approaches were mobilized.

Patient-specific cell cultures were used in experimental assays to assess Glioblastoma pathophysiologic factors and parametrize/initialize/validate the computational predictive algorithms, accordingly. This thesis can be divided in three areas of focus: i) primary cell cultures establishment, ii) the biological experiments and iii) the use of the computational tools.

i)   Tissue from naïve-from-treatment patients with (high grade) brain cancer was excised during the biopsy and/or the partial /gross resection, as routinely done in the clinical practice. Apart from the immunohistopathological biopsy examination to confirm the Glioblastoma case, if needed, part of this tissue was used for the transplantation of immunodeficient mice that served as "living incubators". Additionally, cryopreservation of the collected biological sample assured the reduced risk of the genetic drift in the subsequent procedures. After a short period of direct cell culturing or serial passaging between lab animals, the primary cell cultures were established for each Glioblastoma case.

ii)   Followingly, the primary cell cultures were phenotypically characterized and used in 2D and 3D experimental assays. The thesis primarily focuses on proliferation and invasion, two of the most dominant Glioblastoma characteristics. Available protocols were selected according to the Glioblastoma hallmark under study. Imaging modalities of optical and advanced fluorescent microscopy were used to monitor the growth of small-sized avascular Glioblastoma spheroids using imaging protocols optimized per scanning procedure. All the critical features from the biological experiments were translated so that Glioblastoma-specific biomarkers could be identified. In addition, 2D and 3D assays were also used to evaluate the efficacy of specific drugs on primary Glioblastoma cells.

iii)   All data collected from the *in vitro* experiments were used for initialization, parametrization and validation of Glioblastoma growth predictive computational algorithms. We used hybrid modeling comprised of two compartments; the discrete, where tumor cells are treated as individual entities, able to proliferate, die, move or respond to various stimuli set during the simulation process and the continuous compartment, which describes extracellular components of the tumor

microenvironment using reaction-diffusion equations. The computational model was used both as an experimental tool that reproduces our *in vitro* findings and supports our hypotheses regarding Glioblastoma pathophysiology, and also as a guide to future experiments when new hypotheses are generated.

Either *in vivo* or *in vitro*, Glioblastoma expansion is majorly attributed to proliferation and local spreading. Most of all, Glioblastoma's heterogenic nature dictates the use of realistic patient-specific environments. Taken the Glioblastoma critical growth characteristics, we focused on the study of proliferation and invasion by using the established primary cell lines cultured in 3D conditions. The well-described U87MG and T98G Glioblastoma cell lines served as control in our experiments.

Focusing on proliferation, the combined *in vitro-in silico* approach supported that the variance in tumor staging can be attributed to the differential proliferative capacity of the different Glioblastoma cell types. More specifically, the intra-tumoral heterogeneity together with the overall proliferation reflected in both the proliferation rate and the mechanical cell contact inhibition, but not the cell size, can predict the *in vitro* evolution of different Glioblastoma cell lines growing under the same 3D conditions.

On the subject of Glioblastoma invasion, we presented that the primary Glioblastoma spheroids adopt a novel, cohesive pattern mimicking perivascular invasion in the brain, while the U87MG and the T98G adopt a typical, starburst, invasive pattern under the same 3D *in vitro* experimental setup. Confocal imaging indicated alternative proliferative and adhesive characteristics of the invading cells. Mathematically, we focused on the role of the intrinsic heterogeneity with respect to cell-to-cell adhesion. Our proposed mathematical approach suggested that allowing phenotypic heterogeneity within the tumor population is sufficient for variable invasive morphologies to emerge, which remain originally undetectable by conventional imaging.

Glioblastoma prognosis remains poor mainly because of the high inter- and intra-tumoral heterogeneity and the post-surgery relapse. Glioblastoma adjuvant chemotherapy includes Temozolomide; yet, not all Glioblastoma patients are responsive. The latest trends in Glioblastoma clinical trials usually refer to Doxorubicin; yet, it is unable to adequately overpass the blood brain barrier. A range of Temozolomide and Doxorubicin concentrations were used to treat the primary Glioblastoma spheroids based on the IC_{50} values previously estimated in 2D. Using optical microscopy to monitor the growth pattern, sensitivity to both drugs was observed. Doxorubicin in general was found to be effective in less concentrated doses. In particular, the effective concentrations of Doxorubicin and Temozolomide exhibit four orders of magnitude difference. In order to further discriminate growth inhibition in disabling cell division from cell death, we used Light Sheet Fluorescence imaging to visualize the drug penetration and necrosis. According to the fluorescent images, Doxorubicin was able to accumulatively cause necrosis. On the other hand, in Temozolomide-treated spheroids slight growth-inhibiting effects were observed in a non-consistent dose-response relationship. Our results are in line with variable drug responsiveness of

individual Glioblastomas. We have indications regarding the option of a Temozolomide-Doxorubicin therapeutic scheme to disable proliferation and increase cytotoxicity against Glioblastoma. An *in vitro* drug screening tool was proposed that is able to efficiently integrate the compounds' testing in 2D and 3D and to further fluorescent-image the drug-induced cell death. We followingly suggest to extend these observations to the hybrid discrete-continuous model and further predict the combination or the sequential therapeutic scheme of the two drugs.

Overall, in this PhD thesis, we claim that future research should be based on primary cells directly collected from patients and that common cell lines should only serve as landmarks to unite studies of different groups. For every primary established cell line, not only molecular, but also physiological parameters should be estimated to enable a more precise future clustering of different Glioblastoma cases. Estimations starting with the typical doubling time and evolving to more delicate features such as unique invasive capabilities, death patterns or drug responsiveness and others, are highly important. To this front, computational models may serve as predictor tools not only for estimating cancer progress, but also for designing targeted biological experiments and allow a better understanding of the involved biological phenomena. Simulations of cancer progress should not anymore be based on theoretical values, especially if clinical translation is of interest.

Preparing our future experiments, we additionally set up the technical methods for *ex vivo* experimentation and *in vivo* heterotopic and orthotopic xenografts that are more closely to the precision medicine and theranostics. Undoubtedly, taking into account the molecular aspects of each of the physiologic features discussed, as well as additional imaging techniques capable of providing spatial information of tumor cells physiology and microenvironment will enhance our understanding regarding Glioblastoma nature, verify and further improve our predictability.

In NeuroOncology, the application of accurate cancer predictive algorithms validated with experimental data is a field concerning both basic and translational researchers, as well as the clinicians. In any case, by advancing our mathematical approaches and taking advantage of *in vitro* and *in vivo* experimental methodologies, which enable tight control of experimental parameters and high reproducibility, it may be possible to eventually verify the precise set of their computational counterparts needed towards a systematic *in silico* mapping of Glioblastoma ontogenesis. If we target the holistic description of tumor evolution, we should follow a stepwise approach, where computational tools can definitely help in identifying the most important parameters affecting the final outcome.

Περίληψη

Το Γλοιοβλάστωμα συνιστά τον πιο κακοήθη και επιθετικό καρκίνο του εγκεφάλου και μέχρι σήμερα, δε θεωρείται ιάσιμη ασθένεια. Από την πρώτη στιγμή της διάγνωσης και με στόχο την καταπολέμηση μίας τόσο άπληστης μορφής καρκίνου, η πραγματική μάχη είναι με το χρόνο. Εκτός από την πρόοδο στην κλινική θεραπεία και την εμπειρική αντιμετώπιση, πειραματικά δεδομένα και προβλεπτικές προσομοιώσεις πρέπει να αξιολογούνται και να αναμορφώνονται. Σε αυτή τη Διδακτορική Διατριβή, ένα διεπιστημονικό πλαίσιο που ολοκληρώνει τόσο τη Βασική όσο και τη Μεταφραστική έρευνα παρουσιάζεται στοχεύοντας τόσο στην επαλήθευση υπολογιστικών προβλέψεων για την ανάπτυξη του Γλοιοβλαστώματος όσο και επιχειρείται μία καλύτερη κατανόηση της παθοφυσιολογίας/παθοβιολογίας του. Σε αυτό το εγχείρημα, ένας προσεκτικός συνδυασμός των *in vitro, in vivo* και *in silico* πειραματικών προσεγγίσεων σχεδιάστηκε.

Στην εν λόγω εργασία, συνδυάστηκαν η χρήση κυτταροκαλλιεργειών εξατομικευμένων ανά ασθενή σε πειραματικές διεργασίες σε σχέση με παθοφυσιολογικούς παράγοντες του Γλοιοβλαστώματος και ακολούθως, προβλεπτικοί αλγόριθμοι παραμετροποιήθηκαν, αρχικοποιήθηκαν και επαληθεύθηκαν, ανάλογα. Η εργασία δομείται σε τρία κύρια σημεία: i) την εγκαθίδρυση των πρωτογενών κυτταροσειρών, ii) τα βιολογικά πειράματα και iii) τη χρήση υπολογιστικών εργαλείων και την αξιολόγηση αυτών.

i) Σε πρώτο στάδιο γινόταν η παραλαβή ιστού από ασθενείς με (υψηλού βαθμού) καρκίνο του εγκεφάλου που δεν είχαν δεχθεί θεραπεία κατά τη διάρκεια της βιοψίας ή/και της μερικής/ολικής εγχείρησης, όπως γίνεται στην κανονική κλινική διαδικασία. Πέρα από τις ανοσοϊστοπαθολογικές εξετάσεις βιοψίας ώστε να επιβεβαιωθεί ή όχι το περιστατικό Γλοιοβλαστώματος, εφόσον κρινόταν απαραίτητο, τμήμα του ιστού χρησιμοποιούνταν για την εμφύτευση σε ανοσοκατεσταλμένα ζώα που εξυπηρετούσαν ως «ζωντανοί επωαστήρες». Επιπρόσθετα, μέρος του βιολογικού δείγματος αποθηκευόταν σε βαθιά κατάψυξη ώστε να εξασφαλιστεί ο μειωμένος κίνδυνος γενετικής παρέκκλισης κατά τη διάρκεια των μεταγενέστερων διαδικασιών. Έπειτα από μία σύντομη περίοδο άμεσης εργαστηριακής καλλιέργειας ή διαδοχικών επανεμφυτεύσεων σε πειραματόζωα, η πρωτογενής κυτταροσειρά παραγόταν για κάθε ασθενή.

ii) Στη συνέχεια, οι πρωτογενείς κυτταροκαλλιέργειες χαρακτηρίζονται φαινοτυπικά και χρησιμοποιούνται σε 2Δ και 3Δ πειραματικά πρωτόκολλα. Η εν λόγω εργασία επικεντρώνεται κυρίως στον πολλαπλασιασμό και τη διήθηση, δύο από τα κυρίαρχα χαρακτηριστικά του Γλοιοβλαστώματος. Τα πρωτόκολλα αυτά επιλέγονταν ανάλογα με το υπό μελέτη χαρακτηριστικό του Γλοιοβλαστώματος. Απεικονιστικές τεχνικές οπτικής και προηγμένης μικροσκοπίας φθορισμού

χρησιμοποιήθηκαν για την παρακολούθηση της ανάπτυξης μικρών ανάγγειων σφαιριδίων Γλοιοβλαστώματος με απεικονιστικά πρωτόκολλα που βελτιστοποιούνταν ανάλογα με την πειραματική διαδικασία. Όλα τα κύρια χαρακτηριστικά που αναγνωρίστηκαν στα βιολογικά πειράματα μεταφράστηκαν με στόχο την ταυτοποίηση βιοδεικτών ειδικών για το Γλοιοβλάστωμα. Επιπρόσθετα, τόσο 2Δ όσο και 3Δ πρωτόκολλα χρησιμοποιήθηκαν ώστε να αξιολογηθεί η αποτελεσματικότητα συγκεκριμένων φαρμάκων στα πρωτογενή κύτταρα Γλοιοβλαστώματος.

iii) Το σύνολο των δεδομένων που συλλέχθησαν από τα εργαστηριακά πειράματα χρησιμοποιήθηκαν στην αρχικοποίηση, παραμετροποίηση και επαλήθευση υπολογιστικών προβλεπτικών αλγόριθμων για την ανάπτυξη του Γλοιοβλαστώματος. Χρησιμοποιήσαμε τεχνικές υβριδικής μοντελοποίησης αποτελούμενη από δύο τμήματα: το διακριτό, όπου τα κύτταρα λογίζονται ως διακριτές οντότητες ικανές να πολλαπλασιάζονται, να πεθαίνουν, να κινούνται ή να απαντάνε σε ποικίλα ερεθίσματα που διαμορφώνονται κατά τη διάρκεια της υπολογιστικής διαδικασίας και το συνεχές, όπου τα εξωκυττάρια συστατικά του συστήματος μοντελοποιούνται με χρήση εξισώσεων αντίδρασης-διάχυσης. Το υπολογιστικό μοντέλο χρησιμοποιήθηκε τόσο ως πειραματικό εργαλείο που αναπαριστά τα εργαστηριακά ευρήματα και ενισχύει τις υποθέσεις μας αναφορικά με την παθοφυσιολογία του Γλοιοβλαστώματος, όσο και με στόχο να καθοδηγήσει τα μελλοντικά μας πειράματα στις περιπτώσεις που εναλλακτικές υποθέσεις προέκυψαν.

Είτε σε *in vivo* ή *in vitro* επίπεδο, η εξέλιξη του Γλοιοβλαστώματος αποδίδεται κυρίως στον πολλαπλασιασμό και την τοπική διήθηση. Περισσότερο από όλα, η ετερογενής φύση του Γλοιοβλαστώματος επιτάσσει τη χρήση ρεαλιστικών εξατομικευμένων συστημάτων. Με δεδομένα τα καίρια αναπτυξιακά χαρακτηριστικά του Γλοιοβλαστώματος, επικεντρωθήκαμε στη μελέτη του πολλαπλασιασμού και της διήθησης με χρήση εγκαθιδρυμένων πρωτογενών κυτταροσειρών που καλλιεργήθηκαν σε 3Δ συνθήκες. Οι πολύ καλά μελετημένες κυτταροσειρές Γλοιοβλαστώματος, U87MG και T98G, χρησιμοποιήθηκαν ως δεδομένα αναφοράς στα πειράματά μας.

Επικεντρωνόμενοι αρχικά στον κυτταρικό πολλαπλασιασμό, η συνδυαστική *in vitro-in silico* προσέγγιση υποστήριξε ότι η ποικιλομορφία μεταξύ της σταδιοποίησης του όγκου δύναται να αποδοθεί στη διαφορική αυξητική ικανότητα των διάφορων κυτταρικών τύπων Γλοιοβλαστώματος. Πιο συγκεκριμένα, η ετερογένεια εντός του όγκου μαζί με το συνολικό πολλαπλασιασμό που αντανακλώνται τόσο στο ρυθμό πολλαπλασιασμού όσο και στη μηχανική κυτταρική αναστολή λόγω επαφής, αλλά όχι στο κυτταρικό μέγεθος, δύνανται να προβλέψουν την εργαστηριακή εξέλιξη των διάφορων κυτταροσειρών Γλοιοβλαστώματος που μεγαλώνουν υπό τις ίδιες 3Δ συνθήκες.

Στο θέμα της διήθησης του Γλοιοβλαστώματος, παρουσιάσαμε ότι τα πρωτογενή σφαιρίδια υιοθέτησαν ένα νέο, συνεκτικό μοτίβο που φαίνεται να μιμείται την περιαγγειακή διήθηση στον εγκέφαλο, ενώ τα U87MG και τα T98G σφαιρίδια υιοθετούν το τυπικό, ακτινωτό, διηθητικό μοτίβο υπό την ίδια 3Δ πειραματική διάταξη. Με χρήση συνεστιακής μικροσκοπίας, βρέθηκαν ενδείξεις για διαφοροποιημένα αυξητικά και συνεκτικά χαρακτηριστικά μεταξύ των διαφορετικών διηθητικών κυττάρων. Μαθηματικώς, επικεντρωθήκαμε στο ρόλο της εγγενούς ετερογένειας σε σχέση με την κύτταρο-προς-κύτταρο συνεκτικότητα. Η προτεινόμενη μαθηματική μας προσέγγιση δεικνύει ότι επιτρέποντας φαινοτυπική ετερογένεια στον καρκινικό πληθυσμό είναι ικανό ώστε να αναδειχτούν διάφορες διηθητικές μορφολογίες οι οποίες παραμένουν μη ανιχνεύσιμες στην πραγματικότητα με τις γνωστές απεικονιστικές τεχνικές.

Η πρόγνωση για το Γλοιοβλάστωμα παραμένει φτωχή κυρίως εξαιτίας της υψηλής ετερογένειας μεταξύ ασθενών και στον όγκο του ίδιου ασθενή, αλλά και εξαιτίας της μετεγχειρητικής υποτροπής. Η επικουρική χημειοθεραπεία κατά του Γλοιοβλαστώματος περιλαμβάνει την Τεμοζολαμίδη- ωστόσο, δεν είναι όλοι οι ασθενείς ευαίσθητοι σε αυτή. Οι πιο πρόσφατες τάσεις στις κλινικές μελέτες του Γλοιοβλαστώματος συχνά αναφέρονται στη Δοξορουμπικίνη- ωστόσο, είναι αδύνατο να περάσει επαρκώς τον αιματεγκεφαλικό φραγμό. Ένα εύρος συγκεντρώσεων Τεμοζολαμίδης και Δοξορουμπικίνης χρησιμοποιήθηκαν σε πρωτογενή σφαιρίδια βασισμένο στις IC_{50} τιμές που εκτιμήθηκαν σε 2Δ πειράματα. Με χρήση οπτικής μικροσκοπίας για την παρακολούθηση του αυξητικού μοτίβου, παρατηρήθηκε ευαισθησία και στα δύο φάρμακα. Σε γενικές γραμμές, η Δοξορουμπικίνη ήταν πιο αποτελεσματική σε λιγότερο συμπυκνωμένες δόσεις. Συγκεκριμένα, οι αποτελεσματικές συγκεντρώσεις της Δοξορουμπικίνης και της Τεμοζολαμίδης διαφοροποιήθηκαν κατά τέσσερις τάξεις μεγέθους. Με στόχο να διακρίνουμε περεταίρω την αναστολή της αύξησης σε άρση της κυτταρικής διαίρεσης ή κυτταρικό θάνατο, χρησιμοποιήσαμε Απεικόνιση Λεπτής Δέσμης Φθορισμού ώστε να οπτικοποιήσουμε τη διείσδυση του φαρμάκου και τη νέκρωση. Σύμφωνα με της φθορίζουσες εικόνες, η Δοξορουμπικίνη ήταν ικανή να προκαλέσει νέκρωση με σωρευτικό τρόπο. Από την άλλη μεριά, τα σφαιρίδια στα οποία έγινε αγωγή με Τεμοζολαμίδη, μη σημαντικά ανασταλτικά αυξητικά φαινόμενα παρατηρήθηκαν σε μη συστηματικό δοσοεξαρτώμενο τρόπο. Τα αποτελέσματά μας είναι σύμφωνα με τη διαφορική απόκριση των υποτύπων του Γλοιοβλαστώματος. Έχουμε ενδείξεις σε σχέση με ένα θεραπευτικό σχήμα που συνδυάζει Τεμοζολαμίδη-Δοξορουμπικίνη με στόχο να αδρανοποιήσει τον πολλαπλασιασμό και να αυξήσει την κυτταροτοξικότητα κατά του Γλοιοβλαστώματος. Ένα εργαστηριακό εργαλείο διαλογής φαρμάκων προτάθηκε το οποίο είναι ικανό να ελέγχει επαρκώς τα δραστικά συστατικά σε 2Δ και 3Δ επίπεδο και επιπλέον, να απεικονίζει με φθορισμό τον επαγόμενο από το φάρμακο κυτταρικό θάνατο. Προτείνουμε επίσης σε επόμενο στάδιο να επεκτείνουμε αυτές τις παρατηρήσεις στο υβριδικό διακριτό-συνεχές

υπολογιστικό μοντέλο και να προχωρήσουμε στην πρόβλεψη ενός θεραπευτικού σχήματος τους συνδυασμού των δύο φαρμάκων σε επίπεδο δόσεων και χρονισμού.

Συνολικά, σε αυτή τη Διδακτορική Διατριβή, ισχυριζόμαστε πως η μελλοντική έρευνα οφείλει να βασίζεται σε πρωτογενή κύτταρα που συλλέγονται απευθείας από τους ασθενείς και οι κοινές κυτταροσειρές θα πρέπει να εξυπηρετούν μόνο ως σημεία αναφοράς μεταξύ ερευνητικών έργων από διαφορετικές ομάδες. Για κάθε εγκαθιδρυμένη πρωτογενή κυτταροσειρά, όχι μόνο μοριακές, αλλά και φυσιολογικές παράμετροι θα πρέπει να εκτιμώνται ώστε να επιτραπεί μία πιο ακριβής μελλοντική κατηγοριοποίηση των διάφορων περιστατικών Γλοιοβλαστώματος. Εκτιμήσεις που εκκινούν από τον κοινότυπο χρόνο κυτταρικού διπλασιασμού και εξελίσσονται σε πιο λεπτεπίλεπτα χαρακτηριστικά, όπως ειδικοί μηχανισμοί διηθητικών μοτίβων, κυτταρικού θανάτου ή απόκρισης σε φάρμακα και άλλα, είναι υψηλής σημασίας. Με γνώμονα αυτό, τα υπολογιστικά μοντέλα μπορούν να εξυπηρετήσουν ως προβλεπτικά εργαλεία όχι μόνο της καρκινικής εξέλιξης, αλλά και του σχεδιασμού στοχευμένων βιολογικών πειραμάτων και να επιτρέψουν την καλύτερη κατανόηση των εμπλεκόμενων βιολογικών φαινομένων. Οι προσομοιώσεις της καρκινικής εξέλιξης δεν πρέπει πλέον να εξαρτώνται από θεωρητικές τιμές, ιδίως όταν το ενδιαφέρον επικεντρώνεται στην κλινική μεταφραστικότητα.

Επιπλέον, προετοιμάσαμε την τεχνική βάση για τα άμεσα μελλοντικά μας πειράματα που στοχεύουν τόσο σε *ex vivo* πειράματα όσο και σε ορθοτοπικά ξενομοσχεύματα, τα οποία είναι πιο κοντά στον άνθρωπο και στη χρήση στοχευμένων και εξατομικευμένων διαγνωστικών τεστ. Αναμφισβήτητα, λαμβάνοντας υπόψη τις μοριακές πτυχές καθενός από τα φυσιολογικά χαρακτηριστικά που συζητήθηκαν, καθώς και πρόσθετες τεχνικές απεικόνισης ικανές να παρέχουν χωρική πληροφόρηση για τη φυσιολογία και το μικροπεριβάλλον των όγκων, η κατανόησή μας σχετικά με τη φύση του Γλοιοβλαστώματος θα ενισχυθεί σημαντικά, ενώ θα επαληθεύσουμε και θα βελτιώσουμε περαιτέρω την ικανότητα και ακρίβεια των προβλέψεών μας.

Στη Νευρο-Ογκολογία, η εφαρμογή ορθών αλγορίθμων πρόγνωσης του καρκίνου επικυρωμένων με πειραματικά δεδομένα είναι ένα πεδίο που αφορά τόσο τους βασικούς όσο και τους μεταφραστικούς ερευνητές, καθώς και τους κλινικούς γιατρούς. Σε κάθε περίπτωση, βελτιώνοντας τις μαθηματικές προσεγγίσεις μας και εκμεταλλευόμενοι *in vitro* και *in vivo* πειραματικές μεθοδολογίες, οι οποίες επιτρέπουν τον αυστηρό έλεγχο των πειραματικών παραμέτρων και υψηλή επαναληψιμότητα, μπορεί τελικά να επιτύχουμε να ολοκληρώσουμε όσο το δυνατόν το σύνολο των υπολογιστικών παραμέτρων, μεταβλητών και μηχανισμών που απαιτούνται προς μια συστηματική *in silico* χαρτογράφηση της ανάπτυξης και εξέλιξης του Γλοιοβλαστώματος. Αν στοχεύσουμε στην ολιστική περιγραφή της εξέλιξης του όγκου, θα πρέπει να ακολουθήσουμε μια σταδιακή, κλιμακωτή προσέγγιση,

όπου τα υπολογιστικά εργαλεία μπορούν σίγουρα να βοηθήσουν στην αναγνώριση των πιο σημαντικών παραμέτρων που επηρεάζουν το τελικό αποτέλεσμα.

Table of contents

Keywords

Glioblastoma (GB), primary cell cultures, animal models, cancer predictive algorithms, imaging cancer pathophysiology, *in vitro*, *in vivo*, *in silico*, xenografts, inter-tumoral heterogeneity, intra-tumoral heterogeneity, infiltrative edema, translational biomarkers, doubling time, proliferation, translational biology, invasion, invasive rim, migration mechanisms, hybrid discrete-continuous modeling, mathematical modeling, T98G, U87MG, Glioblastoma cell lines, multicellular spheroids, Temozolomide, Doxorubicin, Light Sheet Fluorescence Microscopy (LSFM), Optical Microscopy, Fluorescence Molecular Tomography (FMT), Fluorescence Stereomicroscope (FSM), Magnetic Resonance Imaging (MRI), simulations, cellular automata (CA), fluorophores, probes, image analysis, continuous modeling, on-lattice models, cell-to-cell adhesion, cell-to-matrix adhesion, preclinical drug screening, theranostics, necrosis, spontaneous cell death, World Health Organization (WHO), Extracellular Matrix (ECM), secondary cell lines, Confocal Microscopy

Glossary

The following glossary introduces a short way to understand the main terms used in this manuscript. All definitions are Glioblastoma-related.

General Information

World Health Organization (WHO) = specialized international agency concerned with the health

Glioblastoma (GB) = primary parenchymal WHO grade IV brain cancer

Extracellular Matrix (ECM) = structural and biochemical cell microenvironment

Translational biomarkers = the impact of a certain compound upon the physiology of the related tissue or organ

Translational biology = the translation of basic biologic findings

In vitro = (*"within the glass"*, Latin) experiment performed outside a living organism

In vivo = (*"within the living"*, Latin) experimentation on a living organism

In silico = experimentation performed via computer simulation

Cancer Hallmarks

Necrosis = progressive and most-often irreversible form of cellular death

Invasion = migration of the cancer cells towards neighboring tissue through the ECM

Infiltrative edema = imaging biomarker of Glioblastoma composed by cancer cells and retention fluids surrounding the tumor lesion bulk

Invasive rim = the marginal cancer cells of the infiltrative zone

Migration mechanisms = the morphologic, biomechanical and molecular functions involved in cell motility

Inter-tumoral heterogeneity = Glioblastoma subtypes differ between patients

Intra-tumoral heterogeneity = a given Glioblastoma tumor is composed by several sub-clones

Proliferation = cancer expansion as a result of cellular growth and division

Doubling time = a constant rate between cell divisions

In vitro

Primary cell cultures = cell cultures established directly from collected biological samples in a patient-specific way

Secondary cell lines = a primary cell cultures' sub-culture of a given stability

Glioblastoma cell lines = cell cultures of Glioblastoma either primary or secondary

Multicellular spheroids = *in vitro* spherical aggregates of cells, a 3D culture technique

In vivo

Animal models = the induced cancer development in lab animals

Xenografts = a graft of cancer sample implanted to an animal recipient

In silico

Mathematical modeling = the abstract mathematical translation of a biological process

Cancer predictive algorithms = computational modeling of the complex cancer growth progress

Simulations = the outcome of a mathematical model that represents a biological process or set of processes

Cellular automata (CA) = discrete cell-based models of tumor growth

Continuous modeling = simulation of the sub-cellular components diffusion using continuous variables

Hybrid discrete-continuous modeling = the simulated integration of both gradients and individual cells by the use of continuous and discrete variables, respectively

Imaging

Light Sheet Fluorescence Microscopy (LSFM) = fluorescence optical technique using light-sheet to illuminate, a.k.a. Selective Plane Illumination Microscopy (SPIM)

Optical Microscopy = the use of visible light to allow a magnified view of objects

Confocal Microscopy = fluorescence optical technique using a focused laser beam to create a scanning point of light to illuminate

Fluorescence Molecular Tomography (FMT) = volumetric imaging technique that accounts for the diffusive propagation of photons in tissue

Fluorescence Stereomicroscope (FSM) = fluorescent dissecting microscope

Magnetic Resonance Imaging (MRI) = biomedical imaging technique of both anatomical and physiological markers

Fluorophores = chemical compounds that re-emit photons most usually of longer wavelength upon excitation

Probes = fluorescent physiologic markers

Image analysis = refers to several digital image processing techniques

Imaging cancer pathophysiology = *in situ* characterization of cancer-related processes

Drug screening

Preclinical drug screening = non-clinical or experimental testing of therapeutic compounds toxicity

Theranostics = the use of specific-targeted diagnostic tests for patient-centered care

Thesis preface

The work included in this PhD study was part of a larger multidisciplinary project aiming at a better understanding, characterization, and translation of Glioblastoma, the most malignant cancer of the central nervous system. In the introductory chapter the state of the art *in vitro-in vivo-in silico* Glioblastoma phenocopying methods are described. Within the next section, the heterogenic nature of the Glioblastoma is shown and the primary or secondary Glioblastoma cell lines used are described in means of the parental, the engrafted, and the established Glioblastoma cells. In the following chapter, the Glioblastoma growth progress is examined both *in vitro* and *in silico*. The mathematical model used in this study is parametrized and initialized accordingly. Regarding the investigation over the invasive Glioblastoma nature, a cohesive Glioblastoma invasive pattern is presented in the fourth chapter, not observed before, when comparing primary and secondary Glioblastoma spheroids cultured in an ECM-like substrate. In the fifth chapter, the drug sensitivity of Glioblastoma cells in Doxorubicin and Temozolomide is observed and further correlated to necrosis-induced mechanisms and/or cell cycle arrest. Given the above, an unconventional therapeutic scheme is discussed combining Temozolomide and Doxorubicin for small Glioblastoma tumors and a possible way of computationally modeling this hypothesis is presented. In the overall conclusions section the main findings of this thesis are summarized and future perspectives are given. A report of the research accomplishments during the PhD is also provided, along with the relevant published studies. Finally, in the **APPENDIX** section, preliminary results on the subject of Glioblastoma necrosis are shown.

Overall, throughout this PhD work,

➔ A total of 22 patients were sampled; 13 of them were male and 9 of them were female. 20 out of 22 were histopathologically diagnosed with Glioblastoma.

➔ A total of 47 xenografts were generated; 6 of them were intracranially engrafted and 41 animals were subcutaneously injected either as a part of serial passaging or not.

➔ A total of 4 primary cell cultures were established; 3 of them were physiologically characterized.

Thesis Impact

Overall, the PhD contribution can be summarized as:

1. We introduced a new protocol regarding the **primary Glioblastoma cell cultures**. There have been many protocols described in the literature regarding the lab treatment of the primary Glioblastoma cells, but none of them is yet universally accepted.
2. We generated **3D hanging drop cell cultures** for both primary and secondary Glioblastoma cell cultures in various growth media for monitoring tumor evolution, as well as for drug screening.
3. We established the technical expertise to prepare **orthotopic xenografts** in the facilities of the Institute.
4. We optimized the **LSFM-confocal imaging protocols**. Such a step is proven crucial in order to better monitor spatio-temporarily the Glioblastoma progress.
5. We experimented with the FMT, a promising preclinical imaging modality in order to monitor Glioblastoma growth evolution *in vivo*. We observed that the **FMT tomographic algorithm** that produces the 3D tumor reconstruction was inadequate for observing the GB pathophysiology.
6. Glioblastoma pathophysiology/pathobiology was assessed *in vitro* regarding **growth**, **invasion** and **response to treatment.** New experimental findings were observed in all three Glioblastoma hallmarks tested. Specifically: i) through an *in vitro/in silico* study focusing on proliferation, we demonstrated that the intra-tumoral heterogeneity together with the overall proliferation reflected in both the proliferation rate and the mechanical cell contact inhibition, can sufficiently predict the *in vitro* evolution of different Glioblastoma cell lines, ii) the primary Glioblastoma spheroids adopt a novel, cohesive invasive pattern mimicking perivascular invasion in the brain, not reported before *in vitro* for Glioblastoma, and iii) in pre-clinical drug screening, we tested *in vitro* (2D and 3D) two widely known drugs, Temozolomide and Doxorubicin. We used LSFM imaging to visualize the drug penetration and the cell death and we found extensive necrosis on Doxorubicin-treated spheroids relative to Temozolomide-treated spheroids.
7. We constructed a hybrid, **discrete-continuous computational model** based on the biological question and the potential biological mechanisms involved so as to account for the critical Glioblastoma hallmarks needed per application. We then properly initialized, parametrized and validated the computational model according to the data derived from our biological experiments. The ability of both validating the model's outcome, as well as guiding the biological experiments as indicated by the computational results was also supported.
8. An *in vitro* **drug-screening method** was proposed that is able to efficiently integrate the compounds' testing in 2D and 3D and to further LSFM-image the drug-induced cell death. This way, not only the effect of the compounds under study in the cells is observed, but also the physiology-related mechanism of action is also considered.

9. From the beginning, we hypothesized that the Glioblastoma heterogenic nature can be better described by the additional use of **primary cell lines in parallel to secondary cell lines.** The results of the experiments conducted are in favor of this hypothesis showing considerably different proliferative, invasive and death patterns, as well as drug responsiveness.

1. Background

> This chapter summarizes all the basic *in vitro, in vivo* and *in silico* models used in GB research and argues in favor of a fused avatar model that combines them all. A brief overview of the key objectives related to the Thesis is given.

In 1926, the term 'spongioblastoma multiforme' was firstly introduced by P. Bailey and H. Cushing [1] and also, a couple of years later, by L. Davis [2] in a seminal effort to classify brain neoplasms. Etymologically, the term 'spongioblastoma' was inspired from the morphology of the cells identified within the samples and the considerable developmental origin of growth. The term 'multiforme' referred to their polymorphous appearance. More specifically however, the most malignant and aggressive form of all was 'glioblastoma (GB) multiforme', most frequently observed among all their cases.

Nowadays, the term 'multiforme' is considered redundant, and GB is attributed to half of the primary intra-axial tumors. According to the revised World Health Organization (WHO) classification [3, 4], GB is a Grade IV astrocytoma, a glioma arising most usually from (astro-) glial cells and their precursors [5], representing the ˜20% of all primary intracranial tumors. Penetration into brain parenchyma differentiates GB from malignant meningioma, whilst necrosis is the main macroscopic difference of GB from WHO grade III anaplastic astrocytoma. GB is considered to be an end-stage disease [6].

Most GB symptoms are considered non-specific. The impairments and deficits that a brain tumor is responsible for may be ascribed to the location of its first appearance. They later consolidate and deteriorate as the tumor develops. GB lesions are generally reported to the hemispheric white matter tracts and symptoms are determined according to the structures and tissues affected varying between silent progress to severe functional fluctuations.

Prognosis and Treatment

The estimated prognosis for the GB is grim due to the high propensity, almost inevitable, for tumor recurrence and the duration of survival without treatment is estimated to be 4-7 months whereas a median survival of 12 to 15 months is expected following resection and/or adjuvant treatments, whilst a 5 or 10 year survival estimated for the 3 and 1% of patients diagnosed with GB, respectively [7, 8]. Disease first therapeutic management is maximal safe resection followed by routine chemotherapy, most commonly with temozolomide [9], and usually anti-angiogenic treatment as maintenance therapy [10-12]. Second-line approaches are radiotherapy and immunotherapy [13], whilst there is no monotherapy applied. Additively to treatment resistance is the inevitable suboptimal tumor debulking in such a sensitive organ as the brain, further eliminating the chance for good prognosis.

Hallmarks

The clinically observable **GB** hallmarks are invasiveness dominating against surrounding normal brain tissue, excessive and convulsive proliferation [14] and intricate vascularization underpinned from both pre-existing brain vessels recruitment and newly-generated angiogenic ones [14-16]. Those features mostly recapitulate its pathophysiology [17]. The final diagnostic criteria of GB, given by WHO description, are microvascular hyperplasia, cellular proliferation, nuclear atypia, architectural disruption (microcysts), (pseudopalisading) necrosis and peritumoral edema [6, 7, 18] identified using differential diagnosis of both histopathological examination of biopsy material and image-guided verification. It has to be noted that the proper tissue sampling during biopsy is of high importance [19, 20], since the phenomenon of co-existing grade markers and intra-tumoral spatial heterogeneity in the same region is highly probable and able to mislead treatment strategy.

Facts & Theories

The pathophysiology of **GB** together with its limited therapeutic potential clarifies the reasons why the probability of tumor relapsing after (gross) removal is very high. There is no efficient way to completely remove the tumor because of the tentacle-like infiltration of the surrounding parenchyma, mostly known as the peritumoral infiltrative edema [21, 22]. In other words, GB cells migrate away from the main tumor bulk following normal brain neural tracts and vessels [23], even forming daughter masses the so called secondary structures of Scherer [24]. The invasion to the brain stroma is most usually occurred in response to paracrine chemotactic gradients and haptotactic interaction with extracellular matrix (**ECM**) which, along with the heterogenic nature, lead to inability of overall healing. Common drug delivery agents, irrespective of their efficiency, fail to access the tumor regional targets because of the blood brain barrier (**BBB**) existence in normal maternal vessels [12], while the peritumoral edema and the dysfunctional vessel network within the tumor insufficiently supply the tumor with nutrients, oxygen and drugs increasing aggressiveness and resistance. The lack of common consensus in imaging criteria (e.g. Response Assessment in Neuro-Oncology – RANO [25], Response Evaluation Criteria In Solid Tumors – RECIST [26], etc.) and the general difficulties for evaluating and closely monitoring (pseudo-) progression also comprise a major problem in overall progression [27].

Secondary GB extracranial metastases, though rare, usually situate in visceral organs [28]. As a matter of fact, the theory of cancer circulating cells (**CTCs**) is supported also for GB cases [27, 29, 30]. However, although GB migrating cells locally invade brain parenchyma *en masse* or as single cells [31], and whether or not invading vasculature, they rarely establish successful micrometastases [29].

Existing theories converge on the idea that intratumoral heterogeneity is established and maintained in early stages of the disease [20].Either referring to extracranial colonization or multifocal and recurrent GB, the current most conventional and dominant hypothesis is in favor of cancer stem cells (**CSCs**). CSCs enable self-renewal, are immortalized and maintain proliferative capacity exhibiting plasticity [32, 33]. Worth noted, therapy resistance is attributed both to inability to

overpass the BBB and failure to effectively target the CSCs [34]. CSCs are also characterized by tumor-initiating abilities that can also be seen in those cells that exhibit spheroidal structure generation in 3D cultures *in vitro* or tumor mass formation when engrafted *in vivo* under lab conditions [35]; also heterogeneous due to epigenetic transformations after seeding. Alternative theories on the origin, establishment and expansion of GB pathogenesis refer to neuroectodermal derivation [36], neural stem cell migration and differentiation failures during brain neurogenesis [37-40] and other (micro-)environmental causes [41].

All these facts and theories conclude that it is of great importance to faithfully represent in controlled conditions the patient's disease individually in order to promote precise therapeutic potential. Moreover, there are many peculiarities of GB physiology regarding proliferation and cell death patterns, invasion, genotypic and phenotypic heterogeneity, neovascularization, as well as microenvironment complexity when compared to other malignancies requiring improved preclinical models capable of recapitulating this complexity. Thus, it is evident why GB research remains an open challenge demanding systemic and multidisciplinary efforts. Current experimental approaches in the direction of predictive preclinical modeling together with their advantages, limitations and their potential applications are discussed below serving as a summarized overview of the current state of GB understanding and modeling approaches.

1.1 Phenocopying GB: approaches, advantages, limitations

Phenocopying GB, or generally any type of human cancer, provides meaningful feedback of its pathobiology/pathophysiology when carefully organizing experimental procedures by means of both basic/preclinical and translational research are conducted. GB involves processes at multiple scales from sub-cellular to cellular and further to tissue level that interact with each other spatiotemporarily to produce the complexity we observe. No matter the nature of the GB model under study, the essential features needed to be met are to adequately reflect GB spatiotemporal pathophysiology, to ensure heterogeneity and emerging capabilities, as well as to enable reproducibility and stability adding prognostic value. Currently, three possible and complementary approximations (Table 1) have emerged on the subject of phenocopying GB trends, each having advantages and limitations:

i)   *in vitro* **cell culturing** either by using cell lines or by establishing one in the laboratory using patient-derived human cells

ii) *in vivo* **generated animal models** to further recapitulate GB conditions

iii) *in silico* **designed predictive algorithms** which enable GB progression predictions at micro-, meso- and/or macro- scopical level, while systematically integrating experimental and/or clinical data to aid in hypothesis testing and scientific understanding.

Table 1 summarizes the different *in vitro*, *in vivo* and *in silico* models depicting the currently most representative approaches and their respective level of physiology. It has to be clarified that the

macro-, meso- and micro-scopic scales are defined according to tissue/organ, cellular and subcellular/molecular interactions, respectively. In the following sections each approach is analyzed.

Tables 2-4 summarize the key points of the different types of models, as well as their origins. Relevant examples are also given per model. The preclinical value of each model is also discussed regarding both user-centered parameters and the level of compliance with the actual GB pathophysiology. More specifically, the models are compared based on their experimental convenience, reproducibility, controllability and feasibility, as well as their cost-effectiveness trade-off, their level of physiology and their potency to differentiate. In addition, their potential to be used for biomarker identification, their predictive power regarding the actual GB pathophysiology and their translational power are also discussed and depicted in Tables 2-4.

The challenge for better prognosis and efficient personalized treatment is to properly integrate all the available information so as to identify molecular alterations present in GB samples, reveal the intense GB heterogeneity, reconstruct, as accurately as possible, the complex network of interactions of cells that influence their dynamic behavior and functional role and account for the complex interactions of GB cells with their microenvironment. These multi-scale processes do not operate independently but communicate with each other. In order to cope with the massive amount of data that need to be analyzed and synthesized at genetic, epigenetic, metabolic and phenotypic level, mathematical and computational methods are inevitably required. Thus, GB research appears to additionally get the interest of computational fields of research such as bioinformatics and systems biology. On top of that, multi-scale, mathematical models that take into account feedbacks between the intracellular dynamics, cellular processes and interactions with the local microenvironment are also highly important.

Table 1. Categorizing GB types of phenocopying models.

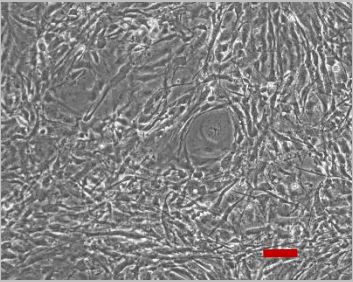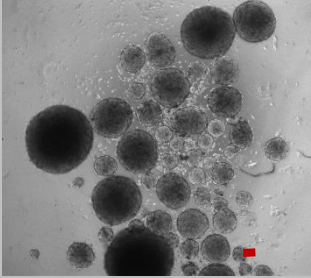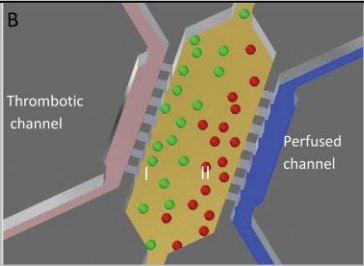| Type of study	Type of model	Scaling
in vitro	2D or 3D lab on a chip	micro- meso-
in vivo	carcinogen-induced transgenic allografts / xenografts	meso- macro-
in silico	cellular automata/continuous/hybrid PBPKs	micro- meso- macro-

It can be considered that phenocopying GB in the microscopic level is not directly reflected to the GB physiologic parameters and the biological tumor ontology. However, none ideal GB model can be designed if critical signaling pathways and microenvironmental constituents involved are not investigated [42, 43]. Especially regarding the (sub-) cellular/molecular metabolic features, to recent

venerable relevant studies [44-46] would rather be referred that further emphasize on research techniques and mechanisms of action. The genetic and proteomic microarrays of GB cells appear to additionally get the interest of computational fields of research such as bioinformatics.

1.1.1 Cell cultures

Especially for the biological experiments, the minimum requested parameters to phenocopy GB are genetic, epigenetic and phenotypic characteristics that facilitate the growth and death rate monitoring, the invasive capacity tracking and the regulation of the nutrients-waste equilibrium; correlated to either trophic gradients or vasculature [5, 47]. All *in vitro* studies enable the high potential of reproducibility between experiments because of the controllable customized lab conditions, as well as the emphasis on a single or few desired features [48]. This way, they provide valuable information about several aspects of GB pathophysiology and pathobiology. However, desired homology to the complex GB clinical nature is not possible since cell culturing offers information in only the micro- and meso-scopic level (Figure 1) and fails to replicate the anatomical, functional and microenvironmental brain and brain tumor conditions [49-51].

Table 2. Summary of *in vitro* GB models. An example of 2D and 3D cell culture is given (brightfield images). Scalebars are set to 100µm. The last image was adopted from [52] referring to a LOC model of sub-cellular resolution in GB invasion microfluidics. The arguments of the evaluation of each model vary between "–", referring to a zero contribution, and "+", "++" and "+++" to discriminate the level of compliance.

Model	Example	Origin	Arguments			
				2D	3D	LOC
2D cell culture		• primary or secondary • human or rodent	experimental convenience	+++	+++	+
			reproducibility	+++	++	+++
			cost-effectiveness	+++	++	+++
			controllability	+++	+++	+++
			microscopy	+++	++	+++
3D cell culture			mesoscopy	+	+++	+++
			macroscopy	-	-	+++
			differentiation	++	++	+
			predictability	+	++	++
			feasibility	+	++	+++
			translational efficacy	++	+++	+++
lab on a chip (LOC)			biomarker identification	+++	+++	+++

Currently, cancer research and pharmaceutical industry focus on the development of more advanced cell culture models capable of better describing the interactions between cancer cells and the complex microenvironment. By cell culturing, either in 2D or in 3D, the vast majority of GB hallmarks may be artificially produced. For example, as described in [53], a physiologic feature such

as vascular mimicry; one of the most characteristic GB mechanisms of neo-vascularization followed by GB cells and not endothelial ones, is resembled using an assay which enables tube formation. However, even when multicellular spheroid-formed [54], cultures do not replicate in detail tumor's characteristic structure and complex physiology [55]. On the other hand, lab-on-a-chip (LOC) as depicted in Table 1 refers to a rather alternative 3D *in vitro* integrated micro-physiological trial which enables wet lab-scale experimentation carried out in reduced-size automated circuit [56]. LOC innovative technology is common to cancer research, and especially GB [52], since the resemblance to *in vivo* physiology is remarkable, the conditions tested are controllable and the biomimetic screening is efficient and selective [57] leading cell culturing deeper than aggregation [58]. In the following, description of the most widely used *in vitro* GB models is given. Table 2 summarizes the main features of the *in vitro* models and presents their main advantages and disadvantages.

1.1.1a Sphere cultures VS monolayers

Conventional 2D monolayer cell cultures growing in substrates and incubation conditions that closely resemble cells' natural environment have shown considerable liabilities for drug evaluation of the *in vivo* response, although they have played an important role in drug discovery, development and understanding in the past. Despite the simplicity and cost-effectiveness of culturing cells as monolayers, there is no nutrient or waste, signal or drug gradient formed in their microenvironment and cells grow flat-embedded which has nothing to do with the multidimensional tissue structures reflecting the abnormal physiology of a solid tumor [47]. On the contrary, the tissue-inspired 3D cell cultures are more beneficial regarding a variety of characteristics and are supposed to be a bridge over *in vitro* and *in vivo* research [47, 59]. It has to be noted though that not all cell cultures maintain the ability to aggregate; a factor strongly depending by the growth medium whether chemically defined and/or serum free or supplemented [5, 60-62]. In general, all 3D techniques share the common principles of overcoming the cell's intrinsic characteristic of attaching to a surface and enhancing cell-to-cell adhesion. More specifically, 3D tumors develop as avascular tumor masses that allow non-uniform exposure to nutrients and oxygen, generating subregional heterogeneity and alternative cell-to-cell and cell-to-matrix interactions. 3D cell cultures also display gradient distribution in exposure to drug molecules when treated, which makes the drug response more realistic. Additionally, gene expression typically varies among the cells depended on their localization in the tumor mass, which facilitates the maintenance and study of the various molecularly and phenotypically different clones that co-exist in tumor cell lines.

Arguably regarding drug screening, 3D cultures shall serve as preliminary animal testing in the same way that preclinical studies precede phase trials to humans. In an attempt to explain differential drug response in 3D drug screening, as it is known, cellular genetic content dictates its phenotype, however, cells growing in 3D recapitulate ECM and stromal interactions leading to phenotypically distinct behaviors. Thus, introducing instability in the 3D experimentation makes reproducibility and consistency questionable and along with the anatomical and diffusive constrains different results appear regarding drug penetration and efficacy [63].

A more optimal and neurocentric cell cultural condition that preserves the sub-anatomical brain structure is the organotypic *ex vivo* implantation of GB cells in the form of cell aggregates within brain slices [49, 64]. Though closer to brain physiology than artificial microenvironments, more adaptive and much easier to handle, yet the need for exogenous trophic factors supply to maintain stability for a short period of time positions this technique in between the *in vitro* and the *in vivo* experimentation [65].

1.1.1b Cell lines vs (short-term) primary cell cultures
There are plenty of established GB cell lines reported in bibliography, assigned to the vast majority of GB molecular subtypes [4, 66, 67]. Depending on the type of the experiment in progress the researcher has to decide the most suitable one. For example, the U87MG cells comprise an established GB cell line derived from a patient diagnosed with glioma WHO grade IV (aka GB) [68]. This cell line is one of the most known and well-characterized since it is in lab use for many years. Moreover, their full-genome analysis exists. U87MG is used both to be further analyzed and as a control line. However, thorough genetical and phenotypical description of this particular cell line; or any other cell line under consideration, no matter its human origin, declares the high potency of alterations through years and between the different research groups [69]. In other words, these cells, even if deeply frozen in low passages, are over 45 years old, a fact that determines a controversy whether they are still the same cells maintaining all the heterogeneities and dormancies or have been transformed to a partially homogeneous population, especially when taking into account their intrinsic aberrant genome profile [70]. Interestingly, genetic drifts and cultural shifts even in a single lab scale make evident the need for regular cell line authentication that is now widely recognized and required by a number of journals [69]. On the other hand, no matter the level of modification, because of their widespread use among researchers U87MG along with the U251 and the T98G stand for control cell lines in order to maintain relevance between GB studies [5].

The demand for better translational models that more precisely recapitulate the genetic and phenotypic heterogeneity of the original tumor and could better approximate the therapeutic efficacy has led researchers to the use of patient-derived GB cells. As stated in [71], engrafted cell lines originated by malignant gliomas fail to have clinical relevance in therapeutic outcome prediction, as in the case of *in vitro* drug screening. This is the reason why the idea of using patient-derived GB cells in order to assess GB in an individualized way is getting more and more interest nowadays [72]. Biological material is sampled directly from brain tissue lesions during biopsy or maximal safe partial/gross resection. Retrospectively, it has been shown that the more gross the resection the better the prognosis since the isolated infiltrative GB cells that are not removed will eventually cause tumor relapse [73]. The vast majority of the research protocols regarding patient involvement criteria refer to candidates with GB symptomatology usually naive from treatment since most of the therapeutic schemes have a strong impact on cancer cell biology [14, 74]. The tissue particles sampled, with regional or not criteria [20], are processed in lab conditions for the establishment of patient-specific short-term GB cell cultures. Less than 5% of the total initial tumor mass [30, 35] preserves the intrinsic ability of multi-potent proliferating and subsequent aggregation into ellipsoid structures

when cultured in non-adherent substrate. The CSCs are a subset of those cells capable to initiate a tumor mass [38], thus they are also able to develop into xenografts when engrafted either in the same or in a different organ/tissue of origin, overpassing host's incongruous conditions [30]. The initial *in vivo* location of CSCs' niche is speculated to be related to hypoxia, the bulk of the tumor mass. The constant secretion of factors evoked by low-oxygen concentration enables the undifferentiation of CSCs within hypoxic regions along with their tendency towards blood vessels chemotaxis [35, 75]. It has to be also noted that there are controversies regarding the relationship between CSCs and the cell of origin of GB [40]. With lineage tracing within the cancer cells subpopulations of different GB specimens examined, it has been revealed that not all precursor cells where present prior to malignancy, suggesting that the cell of origin is deceptive regarding either the dominant clone or the CSCs [39]. In the case of GB, these cells are called GB stem cells or GSCs [76].

It has to be noted that there have been many protocols described in the literature regarding the lab treatment of the primary GB cells [61, 77, 78], but none of them is yet universally accepted. In general, the primary cancer cells need to survive, aggregate and proliferate under the currently most accepted chemically-defined serum-free and EGF/FGF supplemented medium [5, 60, 62, 79-81]. Serum-free or serum-containing and/or chemically-defined media are expected to promote different phenotypical behaviors within a certain population of cancer cells and further encourage clonal selectivity. In other words, when facing with a new, completely undescribed and of unknown composition biopsy sample of human GB cells it is rather demanding to check the cells' behavior under different, but yet standardized, trophic conditions. It has to be noted here that right after their violent excision of the maternal tissue, GB cells, no matter their level of adaptation, need trophic factors and mitogens to sustain environmental shock [55]. However, this is the one side of the coin since the sensitivity to external stimuli is eventually lost after prolonged subsequent passages of monolayer cultures [47]. According to relevant protocols [61, 77, 78], there is an argument regarding the period of time that, under a fixed setup of conditions and media, primary cells preserve the same characteristics with those excised from the patient and/or the ability to grow as neurospheres [60]. Additionally, spontaneous senescence, independently to cultural conditions, has been interpreted as a major drawback of primary GB cell line stabilization over time [82].

Epithelial-to-mesenchymal and mesenchymal-to-epithelial (EMT-MET) transition has been shown to be induced also by the differential presence and potency of growth factors [30]. To be more specific, the circulatory cancer cells (CTCs) that are associated with the EMT-MET transition *in vivo*, change between the two phenotypical status as a matter of the imbalance of epithelial features and the in-activation of certain biochemical pathways of metabolism, growth and movement [27]. Hallmarks of GB cancer related to this transition include (a) the proliferation rate fluctuations, (b) migration and invasion phenomena and (c) cell-to-cell and/or cell-to-matrix adhesion and polarity phenomenal shifts.

In the meanwhile, in each step of the procedure of culturing the primary GB cells, histopathological and immunohistochemical examinations must be evaluated to validate the phenotypic profile of the

collected cells and the patient's biopsy. Also, each sample must be deeply frozen to allow reusability and further studies. It has been shown [79] that properly cryopreserved specimens are satisfyingly able to maintain viability levels, genetic and phenotypic mosaicism, as well as other evoked modifications when compared to fresh primary cell cultures. Conditional stability can be also maintained through passaging of the primary cells when consecutively engrafted in hosts' environment. In other words, when either orthotopically or ectopically engrafted, GB cells can be assumed to be exposed to a stable microenvironment within the host's stroma, but also between different hosts of the same strain [83]. In this case, the cells preservation might be achieved through *in vivo* serial passaging in 'living incubators'; a process described later.
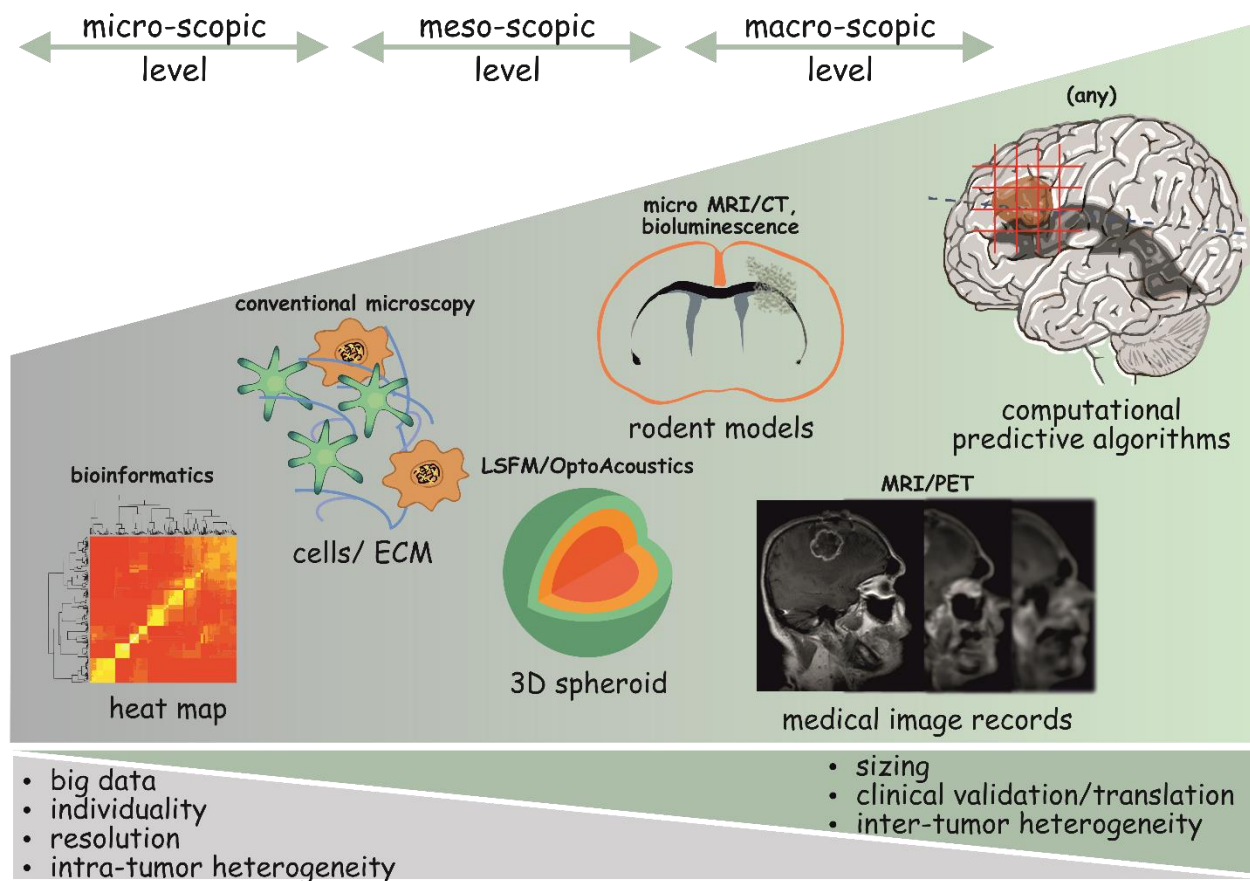

Figure 1. Current trends regarding phenocopying GB. All levels of scaling (left-right arrows), either experimental or clinical, along with the most indicative imaging techniques (above images) are presented. The microscopic level is mainly dedicated to (sub-) cellular and microenvironmental features. The mesoscopic level is referred to the 3D cell cultures and *ex/in vivo* implants, while the macroscopic level is only referred to *in vivo* models either of human or rodent origin. The computational models have no limitations regarding the level of scaling. Inclined arrows beneath indicate tendency towards particular characteristics.

1.1.2 Animal models

Obviously, *in vitro* cancer models are by far more controllable than animal ones and serve as a substandard model [47] to state GB's pathophysiology. However, stable experimental conditions are of high importance since variability enhances instability of the cancer cell population under study. In other words, animal GB models serve as both "living incubators" for environmental stability and as *in vivo* tumor models to recapitulate GB. When growing within the host, the conditions for the tumor are supposedly stable under the assumption that animals of the same strain, gender, age and weight maintain the same environment for the implanted cells when engrafted in the same region following a standard experimental protocol. As symbolized before, cancer cells within lab animals might be considered as growing in living incubators [47] and the effects of the applied experiment are observed overall [71]. Many *in vivo* GB models in animals, most often rodent (especially murine) [42, 84], have been established, as also depicted in Table 3.These include:

(1) chemically-induced (CI) models via carcinogens; mostly studying environmental causes of mutagenesis in a realistic brain microenvironment, whilst relative not corresponding to GB phenotypically and declaring a rather incidental reproducibility [5, 71],

(2) genetically-engineered models based on driver, glioma-related, genetic modifications (GEM) [33]. They examine the role of specific isolated pathways, avoiding the interference of irrelevant (or not) alterations [85]. They also allow an immune response and the BBB constrained drug disposition [5]. Nevertheless, they are limited regarding GB heterogeneity and predicting drug response [86] and they fail to be controlled or reliably reproduced [5, 71, 87], and

(3) transplants, which may be:

a. allografts, or syngeneic models (SM), where the donor and the recipient are of the same inbred immunocompetent lineage so as the transplant not to be rejected and progress to a native environment suitable for immunotherapy assessment, but the tissue is of murine glioma cell lines [5] or not of human origin [88], or

b. patient-derived xenografts (PDX or xenolines [89]), either orthotopic (PDOX) or ectopic, referring to immunodeficient (or not, [87, 90]) animals engrafted with human material of primary or secondary cell lines to mimic the parental tumor in means of both macroscopic and microscopic characteristics and mechanisms [71, 91]. Nevertheless, the tumor stroma is murine; alternatively, even though the transplant is of human origin, it spreads in a non-donor's cellular scaffold with non-human factors being present [86, 92].

Animal models serve mostly as macroscopic translational platforms to test therapy efficacy and GB progression. They necessitate advanced imaging techniques of high resolution capable of monitoring physiological and molecular GB processes. Another important aspect of animal usage in experimentation relates to bioethical issues arising by a general scientific disposition of eventually eliminating the number of lab animals. However, in order to focus on critical GB hallmarks of any

physiological level, it is inevitable to use animals. Interestingly, not only the animal model, but also the region of the lesion are of major importance. Followingly, one of the most unlimited and prevalent, yet of multiple variability, animal modeling technique is discussed; transplants.

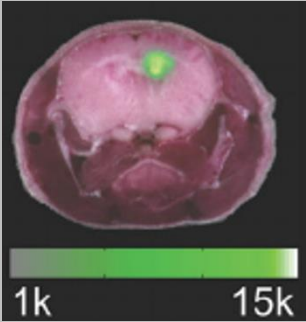*1.1.2a Ortho- vs hetero- topic transplantation*

A diagnosed **GB** clinical case can be image-reported, usually accidently, in full conformation, which means that any attempt of description is arbitrary and limited to the present and future time points. Additionally, the chance to find an untreated case of **GB** post-operationally prior to recurrence is limited. Also, most of the techniques available to scan and evaluate the progress of the neoplasm are imaging modalities mostly applied to a macroscopic level of description. Either *in vitro* or *in vivo*, human cancer surrogate "avatars" substitute the parental **GB** tumor and experimentally monitor the pathophysiology of the disease from the very first moment, displaying as many real **GB** characteristics as possible with no additional hassle for the patient. Local stability regarding conditions is attained when xenografting animals with the fresh or pre-cultured human tumor tissue sample. Also, the steady and constant supply of nutrients, growth factors and oxygen is established. However, the region of engraftment determines the final set of surrounding environmental parameters, which are of great importance for the development and progress of the implant.

The engrafted **GB** cells within the host have three potentials:

1. inability to form a tumor,
2. form a tumor mass delineated within the host's tissue, and
3. form a focal tumor which infiltrates the surrounding environment and penetrates towards periphery [14].

Tissue biopsies from aggressive **GB** clinical cases exhibit a more invasive xenograft phenotype, which is sufficiently correlated with worse survival likelihood [14]. **Surrounding microenvironment has indeed a very essential contribution to the tumor establishment within the host.** Either of primary or of secondary origin the seeded cells, there have been reported differences regarding the occurrence of the disease in mouse models when ortho- or trans- injected [14, 61, 92].

Table 3. Summary of *in vivo* GB models. Examples are given per method. The upper image is a fluorescent image of GFP-expressing subcutaneously engrafted primary GB cells overlaid to the host's color image. The image below was adapted from [93] referring to a comparative fluorescence cryosection image on the host's brain color image of iRFP-expressing GB cells. The arguments of the evaluation of each model vary between "–", referring to a zero contribution, and "+", "++" and "+++" to discriminate the level of compliance.

Model	Origin	Example	Arguments	CI	GEM	SM / PD(O)X
carcinogen-induced (CI)	• heterotopic or orthotopic • human or rodent • primary or secondary		experimental convenience	+	++	+++
			reproducibility	+	+++	++
			cost-effectiveness	+	+++	+
			controllability	+	+++	++
			microscopy	+	+	+
transgenic (GEM)			mesoscopy	++	++	++
			macroscopy	+++	+++	+++
			differentiation	++	+	++
allografts / xenografts (SM / PD(O)X)			predictability	++	+++	++
			feasibility	++	+++	++
			translational efficacy	+	+++	++
			biomarker identification	+	++	+++

In general, a complex neoplasm-host cellular interplay is established when an implant is stereotactically and orthotopically engrafted into a mouse. Some of the host's components that support this front, as reported in [71], are:

1. the anatomical barriers; an organ has cytoarchitecture
2. the ECM molecules
3. the cytokines and growth factors
4. the cellular determinants, such as endothelial cells
5. the tissue-specific progenitor cells, and
6. the immune cells; (not directly) within brain.

To be more specific, unlike subcutaneous engraftment, when **GB** cells are orthotopically implanted in the brain (as illustrated in the mouse brain section in Figure 1), the mouse molecular neuronal background regarding growth factors, cytokines etc. is altered. Within the brain, perineuronal satellitosis in means of glioma cells allocating juxtacellularly to neuronal bodies is achieved [39]. Obviously, transferring cells to the organ of origin is more natural than heterotopic engraftment [87]. Another crucial GB hallmark, infiltrativeness within the host brain parenchyma is lost in heterotopic engraftment [14]. However, mouse brain lacks homology to the human brain [47] and this is the main reason why xenografts can well-approximate, but are also discrete from the clinical cases. More importantly, the severe combined immunodeficiency of the host in order to accept the implant is most often unavoidable [87] [61, 71]. Clearly, independently of the region of the engraftment the immune response detected is remarkably eliminated on the contrary to the tumor of origin. Especially when referring to preclinical drug screening studies, the absensce of the **BBB** in subcutaneously engrafted tumors further rebates the reliability of the animal brain tumor model [87]. With regard to animal GB models other than rodents, Drosophila models though more descriptive when tracking early oncogenic and metastatic events, they lack both immune and neo-angiogenic responses [94].

The time from the primary cells injection to the onset of neurological deficits following stereotactic brain engraftment in PDOXs varies between two to eleven months between different studies [61, 95], usually approaching the life span of the lab animal. It has to be noted that time-efficiency can be promoted through flank-injection of secondary GB cell lines [96]. However, these models are less close to the successful generation of a **GB** PDOX [88]. On the other hand, many researchers recommend the procedural heterotopic transplantation passaging through "living incubators" to promote cell stability to primary cell cultures prior to forming a PDOX [5, 91]. However, since clone selection pressure processes propagate evolutionary dissimilarities between patient **GB** and the serial PDXs, the direct formation of PDOXs can be considered harder to succeed yet closer to the primary tumor of origin [91].

1.1.3 Mathematical modeling

It becomes evident that biological experiments in all levels of complexity are highly important aiding our understanding of GB pathology and potential therapy efficacy. Yet, they are highly demanding and time-consuming in a way that becomes impossible to test the effect of every single potential variable on GB evolution. On top of that, because of the multifaceted processes involved and the variable methods used, they produce a vast amount of data that need a systematic organization and interpretation that can be given by the formal language of mathematics. As the involved biological processes are complex and interrelated, the great research challenge is to appropriately incorporate them into a complete, mathematical description, utilizing the available knowledge and data to better understand and predict how tumors evolve, directing conditions and verifying hypotheses which cannot be easily tested in the laboratory.

In general, mathematical and computational (a.k.a. *in silico*) modeling unfold into two broad and complementary directions: (i) statistical models, aiming towards the identification of disease-associated and disease-driving alterations where molecular signatures, regulatory pathways and mechanisms related to targeted disease phenotypes are searched through analyzing a vast amount of data including imaging data from diverse imaging modalities, OMICS and existing information and knowledge; and (ii) mechanistic, first-principle-based models, aiming at describing and understanding the principles underlying tumor evolution by taking into account the hallmarks of cancer, the tumor microenvironment and their complex interactions.

First-principle-based mathematical and computational models are widely used to describe the complex evolution of tumors as they can manage the multiscale nature of the biological processes involved, integrate the information from multiple biological experiments [97, 98] and/or clinical examinations [99-102]. Furthermore, the models predict behaviors of the system that can guide new targeted experiments [89, 103]. Numerous mathematical models have been also proposed to describe glioma progression [98, 104-107] including critical aspects of tumor evolution such as inter- and intra-tumor heterogeneity [108-110], molecular signaling and metabolism [44, 111], cell-to-cell and cell-to-matrix adhesion [105, 107, 112-115], remodeling of the extracellular space [116, 117], irregular angiogenesis [105, 118-120] and evolutionary dynamics [80, 121], as well as treatment outcomes [101, 122, 123] and others. As it is denoted in Figure 2, *in silico* brain tumor predictive algorithms enable GB simulation with an adjustable scaling of the available data of reference where experiments are carried out computationally. **It becomes evident that given the complex complementary biological interactions, the mathematical approaches are necessary to faithfully integrate them in a competent time period.** By definition, *in silico* models lack any experimental error, are cheap, accurate, non-interversional and, generally, timesaving as they can provide a rapid means to systematically test the influence of individual and multiple cellular components under a spectrum of environmental conditions. In other words, critical GB physiological hallmarks are thought to be translated into their computational counterparts enabling tumor progress prediction.

Yet, though patient-oriented, most *in silico* models proposed are either theoretical or generic, lacking proper, patient-specific parametrization as they require data which are impossible to collect at the required spatial and temporal scale. These models are most often parameterized integrating pre-existing data reported in the literature derived from different research groups not following the same procedures that may not reflect any real tumor type. Thus, they usually fail to be close to reality due to arbitrary parametrization and lack of ground truth validation [19, 98, 99, 121, 124]. The identification of a plausible mechanistic model and its proper parameterization able to quantitatively explain a large set of data that were not used to calibrate the model and predict the clinical/experimental outcome remains a demanding challenge although recent efforts drive research focus towards this direction [100].
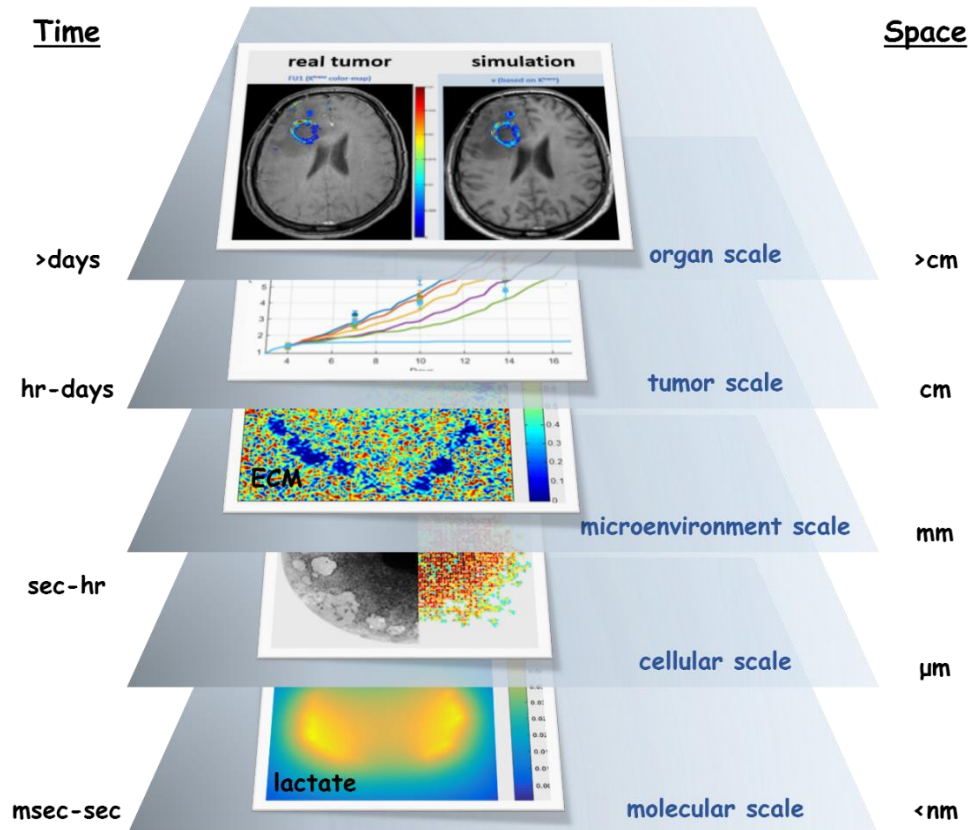
Figure 2. Discrimination of multiscale computational models. Simulated examples are given per scale, while the relevant spatiotemporal ranges are denoted. Metabolic and structural components are less than few nanometers big, the average human cell size is approximately twenty microns in diameter, whilst no submillimeter tumor is detectable by conventional imaging. Equilibration of metabolite concentrations ranges between milliseconds to tens of seconds. Time scale of genetic regulation takes minutes and time constants associated with cell growth range between hours to days.

Such models enable the exploration of multiple hypotheses that allow a better understanding of tumor evolution and its complex components, which cannot be easily tested in the laboratory. There is a debate whether mathematical modeling introduces subjective causality and whether the observed results are emergent phenomena. Nevertheless, an intrinsic implementation characteristic of such models is doubtably correlated to their proposed applications in representing an experiment while optimizing the relevant parameters and/or predicting the progress of a data-driven initialization.

Computational models may be of any scale. Multiscaled computational models deal with many scales. As depicted in Table 4, several mathematical approaches have been proposed to describe the complex, multiscale spatiotemporal tumor evolution. Among them, continuous or analytical mathematical models are commonly used to describe tumors at tissue level focusing more on the collective, averaged behavior of tumor cells. Continuous modeling is usually mathematically simpler using time-dependent growth laws (exponential or logistic) and more clinically relevant [125]. The

continuum methods approximate tumor cells and their microenvironment as continuous variables described by reaction-diffusion type of equations or continuous mechanical models. It has been recognized that both biochemical and biomechanical forces affect brain tumor dynamics, therapy delivery and response and thus, they should be taken into account combined to increase predictive power and clinical impact. Reaction-diffusion models are mathematically described as a system of nonlinear partial differential equations (PDEs) able to be numerically solved, and often used to spatiotemporally describe cell reactions in means of proliferation and changing transition states and cell diffusion in means of migration. Computational models can simulate in 2D or 3D and are able to be applied in any dataset and there are recent references reviewing all types of modeling GB progress and relevant applications [107, 125, 126]. However, on the case of GB therapy computational modeling there are contradictory opinions regarding their possible feasibility [127] or not prior to clinical implementation [126].

On the other hand, individual-cell-based models using discrete and hybrid discrete-continuous mathematics can describe the behavior of each cancer cell individually bridging the scaling gap with its behavior within the tumor microenvironment [128]. Individual-cell-based models can incorporate various phenotypes, describe the behavior of each cancer cell individually as it interacts with its microenvironment and account for stochasticity in the cellular events. These models are in general more suitable to describe *in vitro* experiments and small-sized tumors.
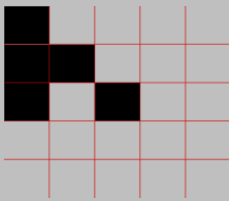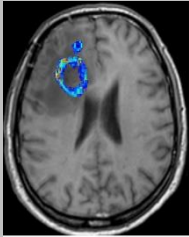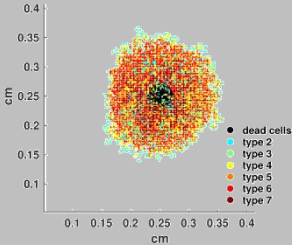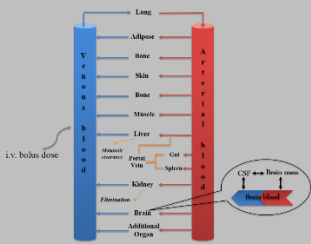
A common example of discrete modeling is the cellular automaton (CA) which is a dynamic rule-based model where time, space and cell states are discredited. CAs can describe macroscopy, yet based on predominantly microscopic parameters. In CA models, each tumour cell operates individually (i.e. grows, divides, moves and dies) and interacts locally with other neighboring cells following a set of biologically-inspired rules. As mentioned before, CA models have been also extended to hybrid HDC models in an attempt to additionally designate the interactions between cells and the microenvironment. These models integrate data from both experimental and/or clinical sources and have been widely used to describe critical aspects of tumour evolution and invasion including genotype to phenotype relations [129], inter- and intra-tumoral heterogeneity [104, 113], the effect of autocrine/paracrine signaling on cell proliferation and motility [129, 130], cell-to-cell and cell-to-matrix adhesion [104, 112, 114, 131, 132], phenotypic plasticity [133-135], the formation of invasive branches [108], evolutionary dynamics [136, 137], the interplay with the brain anatomic features [100, 138] and the microenvironmental factors [139], as well as treatment outcomes [101, 140].

Although always existing, the popularity of big data and machine leaning approaches in healthcare and cancer domain has been recently regained because of the high-throughput platforms, multiple and diverse imaging modalities, as well as fast computation and hardware development. The ability of (advanced) machine learning algorithms to incorporate big data independently of origin or meaning and extract key quantitative and qualitative features, while dictating important variables, make them an important tool in mathematical oncology [141]. This way, novel across data features,

even potential parameters, can be shown to have a direct impact on the disease progression and can be further integrated in first-principle-based computational modeling. Furthermore, apart from feature selection, machine learning can be helpful in the generalizability of the mechanistic computational models in means of increasing data fitting accuracy and amplifying the predictability of the model [142]. Instead of isolating key factors, by using machine learning, computational GB models can be performed in large-scale datasets and evaluate more than one variables at a time or combinations of them. However, as no standardized imaging or experimental protocols exist per clinical GB case so far, the extracted features are usually of not-known clinical or biological relevance.

Another mathematical approach widely used in the drug discovery and development is the physiologically-based pharmacokinetic models (PBPKs) where both preclinical and clinical results are extrapolated into whole-body physiology of drug activity. These models assume each organ or compartment as a complex sub-system and determine the detailed concentrations of drugs incorporate mechanistic understanding of the pharmacokinetic and pharmacodynamic behavior of a drug and its metabolites. Though PBPKs more roughly estimate the tumor's sufficient and necessary conditions, yet the available results consider critical aspects of the organism such as the BBB and /or renal excretion [143]. However, **irrespectively of the mathematical approach, the biological data are necessary for all the computational models parameterization and validation in order to faithfully represent the biological processes.**

Table 4. Summary of *in silico* GB models. Examples are given per method. First, a discrete model represented by a lattice of (non-)occupied cells of a cancerous region. Second, the image depicts the reaction-diffusion model's prediction regarding the vasculature of a simulated whole-tumor overlaid to the respective DCE-MRI image. Followingly, a small tumor spreads as predicted by a hybrid model. The last image refers to a PBPK whole-body model description where the tumor is represented by an additional organ following GB physiology rules. The arguments of the evaluation of each model vary between "–", referring to a zero contribution, and "+", "++" and "+++" to discriminate the level of compliance. The data-driven computational models can be compared with respect to the biological phenomenon, either clinical or experimental, under study.

Model	Origin	Example	Arguments			
				CA	CM	HDC	PBPKs
cellular automata (CA)			experimental convenience	+	+	++	++
			reproducibility	+	+++	++	+++
continuous (CM)	• basic or preclinical research • imaging or translational input data • temporal/spatial/spatiotemporal • deterministic or stochastic • bottom-up or top-down GB description • cell- or tissue-level • mechanistic or phenomenological		cost-effectiveness	+++	+++	+++	+++
			controllability	+++	++	++	+++
			microscopy	+++	+	+++	++
hybrid (HDC)			mesoscopy	++	+++	+++	+++
physiology-based pharmacokinetic (PBPKs)			macroscopy	+	+++	+++	+++
			differentiation	+	+	+	+
			predictability	+	+	++	++
			feasibility	++	++	+++	+++
			translational efficacy	+++	+++	+++	+++
			biomarker identification	+++	+++	+++	+++

Given the complex interactions and heterogeneity involved in GB progression, morphology and drug resistance, predicting the outcomes of preclinical and clinical studies *a priori* is difficult. It has to be clarified that the complex brain and the brain tumor ontogeny can be difficult presented in a deterministic mathematical framework. However, parameter and model decision stochasticity could more adequately describe phenomenologically different growth pattern dynamics to mechanistically same simulated tumors, in favor of inter-tumoral individuality and genetic and/or phenotypic heterogeneity. Clearly, better understanding of GB pathophysiology could lead to better future treatment for patients. In case that the computational model is theoretical and the value of the parameters incorporated is arbitrary or averaged and not the best fit of experimental and/or clinical data, then, although it can provide valuable insights, it lacks validation. It can be postulated that a continuously optimized data-driven mathematical model that incorporates the underlying mechanisms and the involved interactions can explain the potential outcomes and provide guidelines for optimal therapy planning, better understanding of GB pathophysiology and dictate future testable experiments. In other words, **computational simulations enable the identification of discrete factors that are involved in both tumor growth and therapy response, as well as their spatiotemporal evolution in differentiating conditions; something that is not an option in wet experimentation.** This way, hypotheses are tested and experiments are guided in the most cost-effective and time-efficient way. Ideally, a pan-cancer model would have translated all the critical biological parameters and integrated them into their computational counterparts; considering individualized GB cases, but on the other hand enabling unsupervised broaden predictions in absence of validation data.

1.2 Different perspectives in approaching GB pathophysiology

Mechanistically, all cancer procedures can be considered to hijack normal cells' mechanisms, but also to mismanage them from the organism's beneficial/survival scope. In other words, cancer pathophysiology is an altered version of its common components. However, mutations determine cancer cell fate and depending on the triggered/driver alterations, they can be extrapolated to cancer pathophysiology. Identifying and targeting therapeutically all the disease-associated mutations in every heterogeneous GB sample would be one path of the road. The other way is to focus on their phenotypic footprint, that is the way all these alterations are coordinated to produce GB pathophysiology in various conditions. This is the reason why we believe that the use of primary human cells in lab experiments will allow a better understanding of GB underlying mechanisms such as heterogeneity, invasion and neo-vascularization. On top of that, therapy efficacy strongly depends on all those mechanisms. The development of preclinical models where all *in vitro*, *in vivo* and *in silico* information is combined could more faithfully represent the individual patient's tumor and microenvironment towards the development of precision medicine.

Undoubtedly, the importance of advanced quantitative imaging methods and the identification of critical translational biomarkers are evident [144]. Spatial labeling data providing information with regards to cell proliferation, cell death, cell motility, cell distribution, metabolite distribution, microvessel distribution and components of the ECM are more than important considering the need for reliable understanding of the biological phenomena to be included within a mathematical

description constrain. In other words, the imaging techniques ranging from conventional and confocal microscopy, Light Sheet Fluorescence Microscopy and OptoAcoustics, as well as micro MRI/CT, bioluminescence and MRI/PET imaging (indicatively mentioned in Figure 1) are able to provide dynamic spatial information of different scaling in real time [145] for the different GB hallmarks under study.

1.2.1 Imaging techniques

Biological imaging refers to any technique used to monitor a biological experiment. For centuries, the most useful tool of a researcher used to be the optical microscope where we traditionally used light to magnify and investigate objects or features too small to be detected by the naked human eye. However, since the need for not only superficial structures and phenomena observations became evident, the different imaging techniques evolved to a wide spectrum of resolution, penetration depth, photonics and scaling of interest. This way, imaging techniques can be discriminated into the micro-, meso- and macroscopic level according to the size of the sample and/or the tissue depth to be scanned. The modality used to visualize the phenomena under study can vary between light, fluorescence, radioactivity or even sound! Interestingly, apart from the anatomical information depicted in the captured digital images, another more important aspect is the physiologic status under which the biological phenomena take place. Hence, the use of laboratory animals in any biological application is closely correlated to the imaging experimental technique to be utilized. Notably, **in favor of the 3R ethical endeavors (reduction, refinement, replacement), imaging can substantially reduce the number of animals included in a research study.**

Image Processing

The substandard visual qualitative image analysis has to be replaced by robust image processing and analysis since high-throughput experiment produce delicate quantitative imaging data. It is obvious that robust image processing is accompanied by computer power and developing computational algorithms allowing for the refined analysis of large numbers of images in a (semi-)automated way, rather than having a user sit at a bench and look at a screen while not excluding subjective biases. This multidisciplinary task involves both programming specialists and empirically-driven biologists in order to sequentially acquire the proper image, remove the background noise, segment the image in order to identify the regions of interest, filter the image to model the signal intensity, register if needed to another image and extract, or even classify, features [146]. Off course, there is no golden rule for the image process to be followed per experimental protocol and/or biological application and the certain imaging technique used to capture the digital image has to be taken into account *a priori*.

Imaging Modalities

There are several imaging techniques used for the observation of the biological applications using laboratory animals. One common classification between the imaging techniques is according to their application into clinical practice and/or their use only for experimental purposes.

Main Imaging Techniques in the Clinical Practice

Clinical imaging techniques are applied to both laboratory animals and human since they are invasive up to an acceptable extent. It is evident though that their micro-versions have been customized for laboratory animal scanning slightly modified from those applied to human. Followingly, three well-known clinical imaging techniques are briefly described regarding real time live whole-body imaging of lab animals [147].

➔ Computed Tomography (CT)

CT is the 2D or 3D reconstruction of the tomographic data produced by the differential tissue absorption of x-rays. CT is considered an invasive imaging technique because of the demands of ionizing radiation. Though it can provide less detailed anatomical information, it is widely commercially available because of its cost- and time-effectiveness and it is usually combined to functional imaging techniques [148].

➔ Magnetic Resonance Imaging (MRI)

MR imaging technique is based on the differential distribution of paramagnetic gadolinium (Gd) based tracers or water protons within the body and their detection trough radiofrequency pulses within an applied magnetic field. MRI involves different sequences dedicated to different physiologic aspects; even quantification of chemical species within tissue. This way, MRI is not just a non-invasive anatomical imaging technique of high volumetric resolution, but also it can provide physiological and functional information [147, 148].

➔ Positron Emission Tomography (PET)

PET is a method of nuclear medicine regarding radionuclide imaging which combines both functional and molecular imaging. In other words, PET employs positron emitters physiologic tracers depending on the application, even radiolabeled drugs. PET machinery is expensive, it provides poor spatiotemporal resolution and the need for radioactive compounds, β and γ radiation, is unavoidable. These are the main reasons why most often PET is combined to hybrid imaging with other techniques providing anatomical information [147].

Main Preclinical Imaging Techniques

Preclinical imaging techniques are developed in order either to renew older modalities or to establish new ones. They are common among lab animal experiments and most usually customized.

➔ Fluorescence Molecular Tomography (FMT)

FMT is a form of optical imaging where fluorescent probes serve as optical reporter systems that when externally excited at a certain wavelength they emit photons in a shifted wavelength that can be detected through charged-coupled detector (CCD) cameras. It is considered a molecular imaging

technique since the probes used are administrated or expressed to the lab animal according to the target physiological biomarker [146]. The idea is to enhance the image contrast, yet light transport through the scattering tissue is non-linear, thus penetration depth and resolution are suboptimal but can be further improved by using theoretical models regarding tissue light transport and probe's kinetic estimates [145].

➔ Opto- or Photo- Acoustics (PA)

PA is a combination of optical imaging and ultrasound, where acoustic signals produced by photothermal expansion are generated by non-ionizing pulsed laser light absorbance and detected through an acoustic detector. In other words, PA has the accuracy of the spectroscopy and the depth resolution of the ultrasound ranging between micro- and meso-scopic scaling and being capable of both molecular and functional imaging with the minimum invasiveness [147].

➔ Light Sheet Fluorescence Microscopy (LSFM)

Optical imaging of tumor spheroids is technically challenging, since these are large and highly scattering specimens. LSFM or Single plane illumination microscopy (SPIM) is a novel optical microscopy technique firstly introduced to life sciences in 2004 [149] and is based on fluorescence imaging enabling laser light-sheets to illuminate the sample to be scanned in a way of avoiding photodamage. It provides excellent optical sectioning and high contrast images as opposed to confocal microscopy with deep penetration of light into the specimen and high image acquisition speed. It combines optical sectioning, the main characteristic of confocal and two photon microscopes, with multi-angle and multispectral imaging which are performed in optical and fluorescence tomography. The biggest advantage of LSFM imaging is that it can be applied on whole-body live small animal molecular scanning with minimum harm when combined to optical projection tomography [147]. LSFM has the potential to overcome several of the challenges that prevent high resolution imaging of live tumor spheroids.

Translational Imaging

As denoted above, an imaging discipline serves more than just monitoring the anatomical extension of a certain target within the body. The identification and parametrization of detectable biological features into imaging biomarkers are called translational imaging. This way, along with the anatomical, the physiological, functional and molecular type of information is translated within the digital images to provide prognostic, monitoring and predictive value. Several emerging potentials arise by translational imaging and therefore, the techniques are just the tool to assess the hidden info.

It is obvious that from the moment of the experimental indications of a certain feature that can potentially be identified as a biomarker, there are many translational gaps and assumptions to be evaluated before it can be routinely used into clinic practice. **Imaging laboratory animals is for the moment the most reliable way to test the hypothesis under study before extrapolating to the human**

[150]. In other words, translational imaging provides to the experimenter the way to bridge the Basic Research with the Medicine and theranostic applications.

1.2.2 *In vitro, in vivo, in silico*

Either adherent culturing or organotypic-like spheroid formation, cell cultures, even when human-derived, are supposed to be more suitable for rough drug screening and pre-clinically testing of experimental active drug substances. On the other hand, phenocopying GB using animal models enables the closest-to-maternal mimicry of the mechanisms of tumor initiation and progression. Though this approximation comes out with treatment options, most often, evaluation in clinic fails. The reason for this discrepancy is because tumor models do not reflect the biological properties of the patient's tumor as a whole. Also, pharmacokinetics, as well as cellular heterogeneity and physiology in animals differs from that of humans [71]. In addition, *in vitro* experiments and animal models are highly demanding and time-consuming, while they produce an amount of data that needs systematic interpretation and understanding to be clinically meaningful. It becomes evident that a complementary path is needed to overcome those hurdles and better succeed in the fight against GB.

As recommended by lab animal welfare societies, the most recent research trends argue against animal experimentation, with an exception regarding Drosophila *melanogaster* and lower invertebrates, and recommend their eventual replacement by cell cultures and computational simulations. Nevertheless, regarding cancer evolution predictability, the computational models need to be supplied with the less arbitrary data possible. In other words, if the input data meticulously reflect the cancer pathophysiology, the computational predictive power is amplified. If this is the case, the most reasonable approach is by experimental procedure and by the use of translational biomarkers to describe the cancer genetic or phenotypical features, unique for each patient.

Imaging modalities, together with other experimental techniques, provide post-process descriptive information regarding the GB physiology under research, indicative of the micro-, meso- and/or the macro-scopic level, depending on the method. It has to be noted that the final clinical occurrence involved is a result of an interplay between all levels within the tumor mass. For example, if only focusing on the cancer cells characteristics without taking into consideration the surrounding ECM, the principle is confined to generalization. The unrecorded experience of the clinicians, even if not experimentally proven, also supports this front and further provides data for the models. In other words, the more descriptive the models' input needs to be, the more laboratory and clinical specialties are required to collaborate in order to successfully parametrize and initialize GB predictive computational models. Nevertheless, *in silico* modeling cannot yet serve as an experimental, preclinical or clinical substitute.

So, after all, which is the right model to phenocopy GB? The question to be tackled is what each model is able to offer while minimizing cost and time. Taken individually none of the approximations described above efficiently enables the overall description of GB. The differences

among the techniques are mainly attributed to their level of clinical relevance and the insight they provide regarding the **GB** complexity; properties which are both important and complementary. Alternatively, the proper choice to approximate the disease depends on what is more close to the patient's specific case. Going deeper to this claim, the ideal **GB** model to study **GB** pathophysiology is not necessarily the same with the one needed to assess a patient-specific approximation and vice versa. Yet, no model is self-standing by means of feasibility and it has to be clarified that there is not, at least not yet, a golden rule for the most convenient and representative **GB** model. All types of models described earlier have been used to serve certain purposes or combined to serve others. Also, a **GB** avatar model can be assumed to combine advantages from all model types; by xenografting the biopsy tissue samples of the patient in the form of collected tissue fragments or cultured cells or even spheroids in order to create his mouse models and by reforming the data to simulate the case for predictive purposes of the disease progress or the therapeutic outcome and the survival [61]. Alternatively, we speculate that a future **GB** avatar can be a fusion of advanced *in vitro-in vivo-in silico* modeling in a way that all forces are called against **GB** and in favor of precise theranostics where all the required experimental steps are repeated until a valid prediction outcome for the patient. As described in Figure 3, *in vitro-in vivo-in silico* modeling is an iterative procedure of parameters-variables-methods that is fed from data derived from each patient. Repeated refinement, guidance of new experiments and constant re-establishment of the major components needed (filtering) are organized and conducted for valid predictions. To go back to the patient, an extrapolation/translation step is also needed in order to make patient-specific predictions. This step also needs refinement, repetition and coordination together with the previous step for the best possible outcome with clinical relevance.
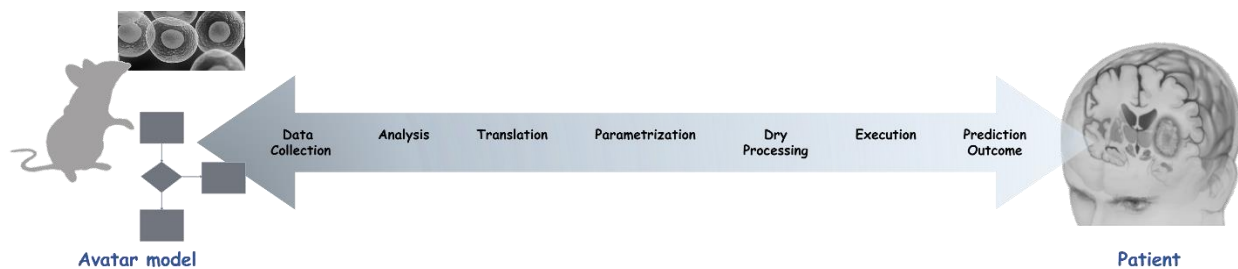

Figure 3. Systems Biology example in phenocopying GB. The step-by-step procedure from the *in vitro-in vivo-in silico* fused avatar model towards the personalized medical scheme. A path of constant feedback should be followed from the initial data collection and translated input towards the model parametrization and predictive output to be validated and vice versa.

For the moment, the use of lab animals is inevitable because of i) the complex nature of GB regarding multiple subtypes and intrapatient clonal heterogeneity [20, 85, 151] which further discriminate patient cohorts, ii) together with the practical difficulties of maintaining tissue sample abilities post-operatively, and iii) the misleading current primary cell handling protocols. After dissociation and short-term culture of collected GB cells, their subsequent implantation to hosts enables the stability of the environmental conditions in order to establish the patient's personal cell line. Meanwhile, assumed the homology to human, the more realistic representation of the actual GB clinical image refers to the relevant orthotopically transplanted mouse model. Good research practice elucidates lab animals' welfare by eliminating time of overall tumor progress monitoring after the appearance of neurological or other symptoms. Nevertheless, in order to prevent the use of lab animals, the policy of forming the primary cell cultures and the animal models must be followed as a first step [61], whilst subsequently, a database of all the cases will be formed so that the idea of *in silico* clinical trials[1] could be open. Taken this for granted, no other animal experiments would be of interest since the patient case would be matched to the relevant recorded one. Various markers and lab examinations would correlate the patient case of interest to the relevant primary cell culture already established, accordingly. To this future front, a consolidated protocol for both clinicians and researchers should be prepared and followed by multiple centers and institutes under generally accepted bioethics. Furthermore, this proband concept is not only important for reducing animal experiments, but also essential for fast growing and highly invasive tumors such as GB where time is critical. This way, biological input data would be at the disposal of all bioengineering researchers able to be combined, evaluated and complemented, so that arbitrary and theoretical parameters would be eventually replaced in a data-driven way. After all, *"a chain is as strong as its weakest link"* and the adaptivity of either holistic or reductionist models discussed in conditional, replicable, stochastic, emerging and individualized terms, is about to guarantee fidelity in phenocopying GB process.

---

[1] See also the Avicenna project .

2. Primary GB cells isolation and characterization

This chapter aims at describing the basic initial steps repeated for every GB patient included in this project. These steps include the patient eligibility criteria, the tissue sample collection, the xenotransplantation and the establishment of the primary cell culture. The characteristics of the GB cell lines used are presented accordingly.

One of the most characteristic features of GB that limits therapeutic potential is heterogeneity [152]; both different molecular GB subtypes [6, 153] and subclonal cell populations coexist within the same tumor [20, 33, 154]. Hence, the importance of individualized GB treatment and understanding of patient-specific GB pathophysiology is evident and research plans towards this aim are of great interest.

As explained in the introductory section, the use of the widely scientifically-studied common GB cell lines passaged in lab conditions for decades [70] is nowadays questionable with respect to their clinical relevance in therapeutic outcome prediction and to their ability of representing the extensive heterogeneity observed among patients [69]. To this front, a common GB trend is the use of patient-derived GB cells to enable preclinical physiologic estimations and personalize therapeutic strategy. Basic researchers cooperate with clinicians in order to isolate GB cells and promote the establishment of short-term primary GB cell cultures [14, 61, 78, 79], which provide additional results back to the patient. Established methods for biological research and early drug discovery utilize cell lines grown on plastic culture flasks. Over the years, the ability of these *in vitro* systems to provide biologically-relevant answers and describe drug effects is limited due to the fact that they are too simplistic and do not include key players of the phenomenon. Hence, researchers seem to mobilize more realistic experimental approaches such as 3-dimensional (3D) cell cultures [47, 54, 155-157] and/or *ex/in vivo* implantations [61, 88, 92, 158] to better imitate cancer in a mechanistic and conditional way. Biological 3D models comprise an important step to describe the early phases of tumor progression before going to the complexity of *in vivo* systems.

The initial step of this work is to utilize primary tumor cells collected from GB patients and subsequently cultivated *in vitro* in an attempt to describe the establishment procedure of the primary cell lines and their key physiologic characteristics.

2.1 Sampling procedure

Brain tissue sample is collected from the lesions during biopsy or maximal safe (gross or partial) resection of patients with indications of GB based on symptoms and MR images, while still naïve from treatment and later histologically proved to be GB cases. Small samples of different, non-necrotic, tumor regions were obtained and immediately transferred to cool sterile normal saline solution. All samples and data are anonymously provided with the informed patients' consents by

the Neurosurgical Clinic of the General University Hospital of Heraklion, Crete, Greece. In order to identify each GB case, the acronym GBP (GB patient) along with the serial number of the patient was given at each sample and maintained throughout the whole procedure. The protocol has been approved by the Hospital's Ethical Committee (Protocol number: 442120205-2018).

2.2 Establishment of the primary cell cultures and mouse engraftment

Following sampling in the surgical room, GB cells are directly transported to the lab, where the tissue is mechanically dissociated. After gradually removing all cell debris and dead tissue parts, cancer GB cells are cultured as monolayers in standard lab conditions. As regards the media used in cultivation, in line with the literature [62], we most commonly used the Dulbecco's modified Eagle medium (DMEM) as base medium, alone or mixed, and/or Neurobasal medium. DMEM was either serum-free plus cytokines (FGF2-EGF, Peprotech, UK) and B27 (ThermoFisher Scientific, UK) or plus 10% of fetal bovine serum (FBS) supplemented with 50μg/ml gentamycin (PANREAC Applichem, Germany), briefly mentioned as DMEM++. This is the zero passage or P0 cell culture of the relevant GB case. As explained before, there is much heterogeneity between GB cases and the selective protocol of tissue handling is slightly modified per case.

Early *in vitro* growing GBs were also *in vivo* passaged once in order to further preserve conditional stability and assist the GB cells survive, aggregate and proliferate. Specifically, a concentrated amount of single cell suspension solution, complemented with 30% Matrigel (Corning®, USA) to enhance connectivity, was either orthotopically or ectopically injected to male NOD/SCID/IL2Rγ null (NSG strain) most commonly 2-months-old mice.

Orthotopic implantation

When stereotactically engrafted into the brain, the injection site was -2.0 A/P (anterior-posterior axis), -2.3 D/V (dorsal-ventral axis) and -2.0 M/L (medial-lateral axis) from the bregma targeting the striatum of the right hemisphere; so that moving disorder can be easily detectable after tumor formation. The injected material was drained using a Hamilton syringe (30G, ThermoFisher Scientific, UK) following a small burr hole using a drill. The rate of the injection was 0.1ul/1.5min plus 3 minutes for the needle removal to avoid tissue damage. Anesthesia was a common mix of Ketamine/Xylazine solution[2] of one or two intraperitoneal repetitions and all the procedures were in sterility. Antibiotics (Neomycin, ThermoFisher Scientific, UK) was used during the recovery

---

[2] Common mouse cocktail dose 0.1mL/20g mouse weight which contains 87.5 mg/kg Ketamine and 12.5 mg/kg Xylazine for 20-30 minutes of induced anesthesia.

period after stitching and the animals were monitored for any neurological symptoms. None animal was detected positive for tumor formation in the brain or elsewhere after necropsy following cervical dislocation. Orthotopic implantations were limited to the first three GB cases and the secondary cell lines since we believe that prior to the primary GB cell culture establishment there is low success rate.

Ectopic implantation

The subcutaneous injections were conducted to the right flank. Using this approach, GB cells are exposed to a stable microenvironment within the murine host's stroma [83], in immunosuppressed human-like 'living incubators'. Most usually within one month, a small-sized tumor was formed within the host, subsequently removed and re-cultured. For each GB case, after the first passage within the animal, one part of the isolated GB cells was deeply frozen; another part was histologically examined to check whether the homology is preserved from the patient to the lab animal, and the rest was frequently checked regarding physiological behavior stability until the primary GB cell line was successfully established. After the first implantation, the cells were collected and re-cultured until the cell culture was successfully established. In order to discriminate the serial subcutaneous passages, they were numbered accordingly (P1, P2, etc.). All possible steps were taken to avoid animal suffering at each stage of the experiments. All animal experimental protocols were conducted in accordance with and under the approval of the Foundation for Research and Technology Ethics Committee and the General Directorate of Veterinary Services, Region Crete (permit numbers: EL 91BIObr 01 and EL 91 BIOexp 02).

2.3 Characterization of the established primary GB cells

It is worth mentioning that acquiring this kind of longitudinal data is an arduous task, particularly due to limited availability of GB cases and subsequently, constrained cell culturing success. For these reasons, we report our results from the analysis of a preliminary longitudinal data set of six GB cases.

GBP01

The first case included in this project was a 26-years-old male patient hospitalized with personality disorder and diagnosed with GB in the basal ganglia after the first biopsy. Patient GBP01 was sampled for GB cells isolation both from the main brain lesion during biopsy and the following gross removal, as well as post-surgery vein blood was collected. Unfortunately, the patient deceased a year after.

Though the histopathological examination of the sampled tissue was a typical GB case, the isolated cells were unable to survive in cultivation. It has to be noted that both animal orthotopic transplantations failed due to anesthesia.

Patient GBP01 is a case report regarding the extracranial GB tumor growth. The high intracranial pressure because of the edema resulted in the skull absence after surgery and the gradual meningeal,

subcutaneous and finally, skin invasion. Interestingly, unlike the **GB** cells directly sampled from the primary tumor, there were circulating **GB** cells extracted from the blood sample that better responded to lab culture conditions. The **GB CTCs** detected were too adhesive, immediately attached to the flask's surface. As it can be seen in Figure 4, even after a month in cultivation the **GB** cells are importantly many. This is why we subcutaneously engrafted an unknown but dense concentration of these cells following the described procedure, but no tumor was detected up to the aged animal's death (15-months-old, natural causes).
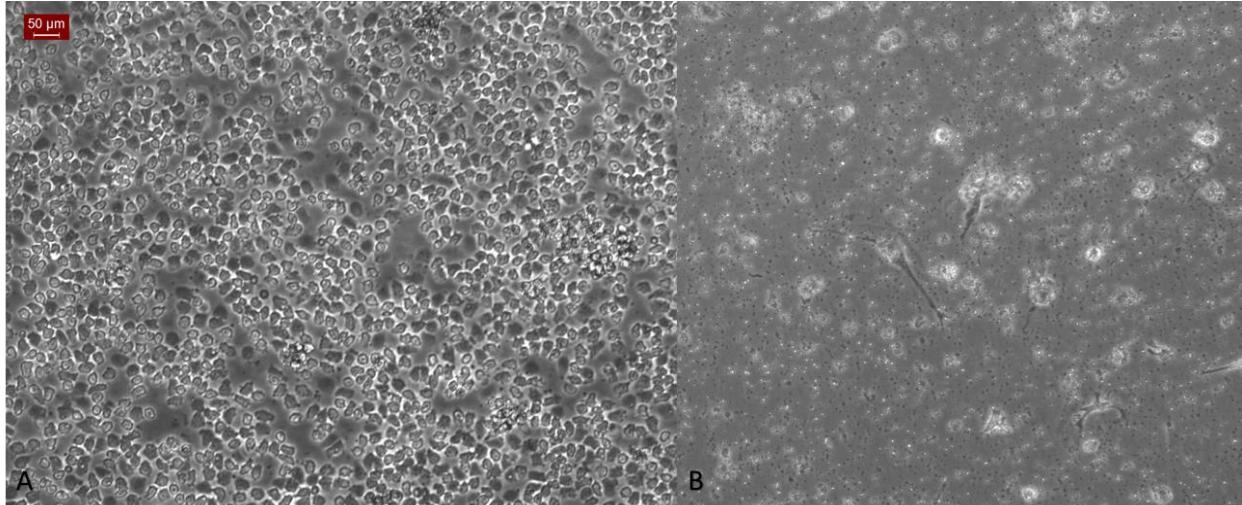
Figure 4. Circulating GB cells from patient GBP01 in cultivation after a day (A) and after a month in cultivation with supplemented DMEM. Scalebar is set to 50 microns.

GBP03

The second case is a 76-years-old male patient with *de novo* **GB** close to the left brain motor area; also called GBP03. The post-biopsy **MRI** scans of the relevant patient are shown in Figure 5.
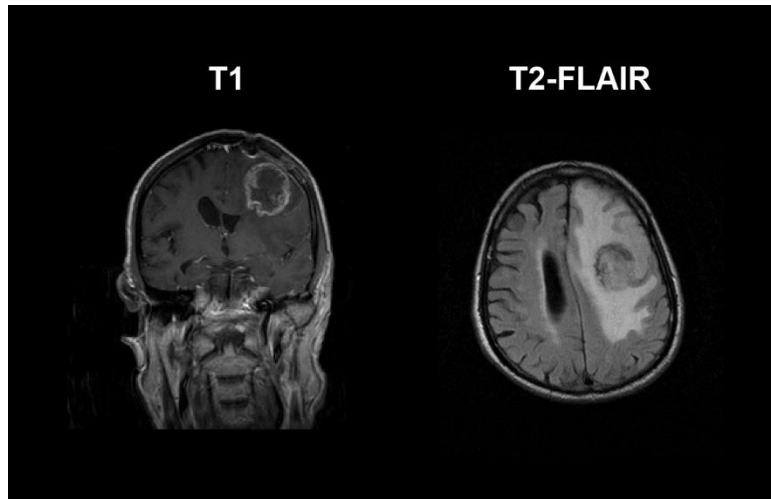
Figure 5. Post-biopsy Magnetic Resonance (MR) images from patient GBP03. On the left, a coronal T1-MR image where the highly necrotic ring-shaped lesion can be seen frontotemporally in the left hemisphere, near motor area. Notice the mark of biopsy cavity formed by the trepanation of the skull. On the right, an axial T2-FLAIR MR image is shown, where the bright peritumoral infiltrative edema is remarkably extended causing space-occupation of the left hemisphere and internal pressing of the lateral ventricle.

There is no GBP03-P0 cells left frozen or in cultivation since all were immediately engrafted ectopically after sampling. GBP03 cells were serially passaged up to animal GXP7 (GB xenograft passage number 7). Followingly, the immunohistopathological recordings of the original patient tumor along with indicatively the first two passages are presented including both morphological description and routine brain tumor histological markers. As it can be seen in Figure 6, the morphological features are similar between the original tumor and the implants, however the surrounding host stroma is irrelevant to the brain parenchyma. Proliferation marker Ki67and p53 oncoprotein expression profile are increased through passaging, while the neuronal markers are decreased as expected. The immunohistopathological profile of the xenografts is not changeable through passages.
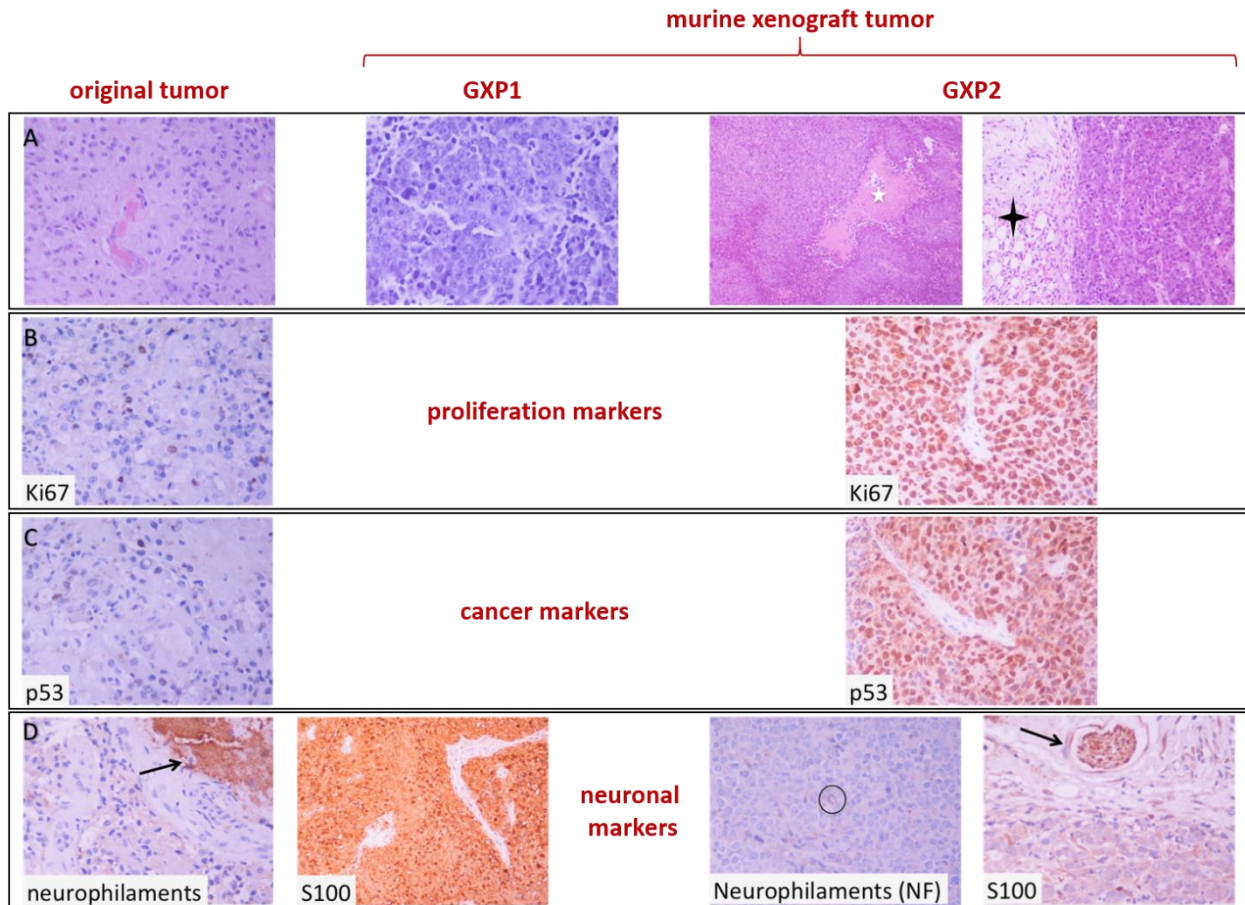
Figure 6. Immunohistopathological images of the GBP03 original and engrafted tumor biopsies. (A) Eosin and hematoxylin (H&E) staining to show morphological characteristics. White asterisk indicates necrosis in the engrafted tumor but not the original one, while black cross marks the murine subcutaneous fat. (B) The proliferation marker Ki67 is altered from 10-12% in the original tumor up to 90-100% to the second murine passage. (C) p53 varies from negative up to a mutated suggestive gene expression pattern. (D) For the original tumor, the neuronal markers expression pattern is S100[3]+ and neurophilaments[4]-, while in the murine host it is focally positive (black circle) for the neurophilaments and S100+ in the indicative peripheral nerve (black arrow). DAB is used as chromogen and H&E as counterstain. Original magnifications at 400x (GXP2 H&E images are at 40x and 200x).

---

[3] Marker of the neural crest.

[4] Neurofilaments (NF) are intermediate filaments found in the cytoplasm of neurons.

An empirical observation from our findings in the case GBP03 (and others) is that the more the primary cells were passaged the faster the tumor detection after engraftment, but not necessarily the growth rate. This observation was not further investigated regarding the cell transformations occurred between passages, yet it is in line with relevant studies [61]. The anticipated results are that after passage four (more or less) the cells can be considered as stabilized regarding growth characteristics [61]. A subcutaneous growing tumor is observed in Figure 7 as it is shown in the animal in naked eyes and after fluorescence excitation. In Figure 8, the tumor growth progress of the engrafted animals by using GFP-transfected[5] GBP03 cells was monitored in the *in vivo* live FMT imaging. As it has been investigated, FMT is suitable for tumor detection and qualitative characterization of tumor progress, but not correlated to anatomical information or tumor cell density since signal enhancement cannot be linearly translated. Notice that in Figure 8C, unlike what is known from the literature about the tumor's necrotic core formation being enhanced over time [159], the bigger the tumor the higher the cellularity in the center region.
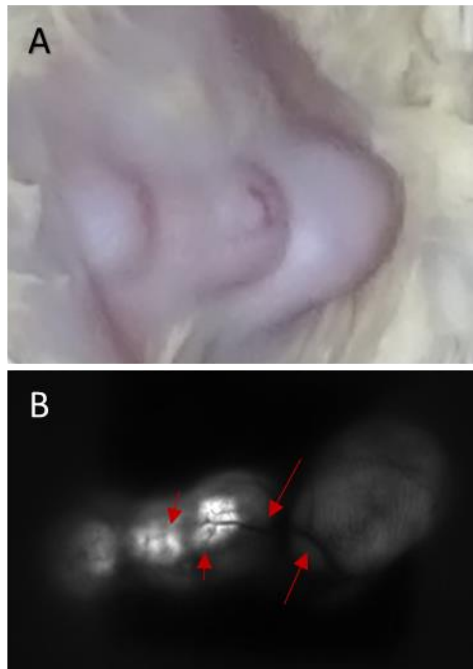

Figure 7. Animal GBP03-GXP3. The multi-nodular subcutaneous growing tumor as it can be observed (A) in photograph and (B) after fluorescence excitation. Arrows indicate the tumor blood vessels that are depicted like shadows since they do not express any fluorophore.

---

[5] GBP03 GB cells were lentivirusly-transfected so as to permanently express the green fluorescence protein (GFP).
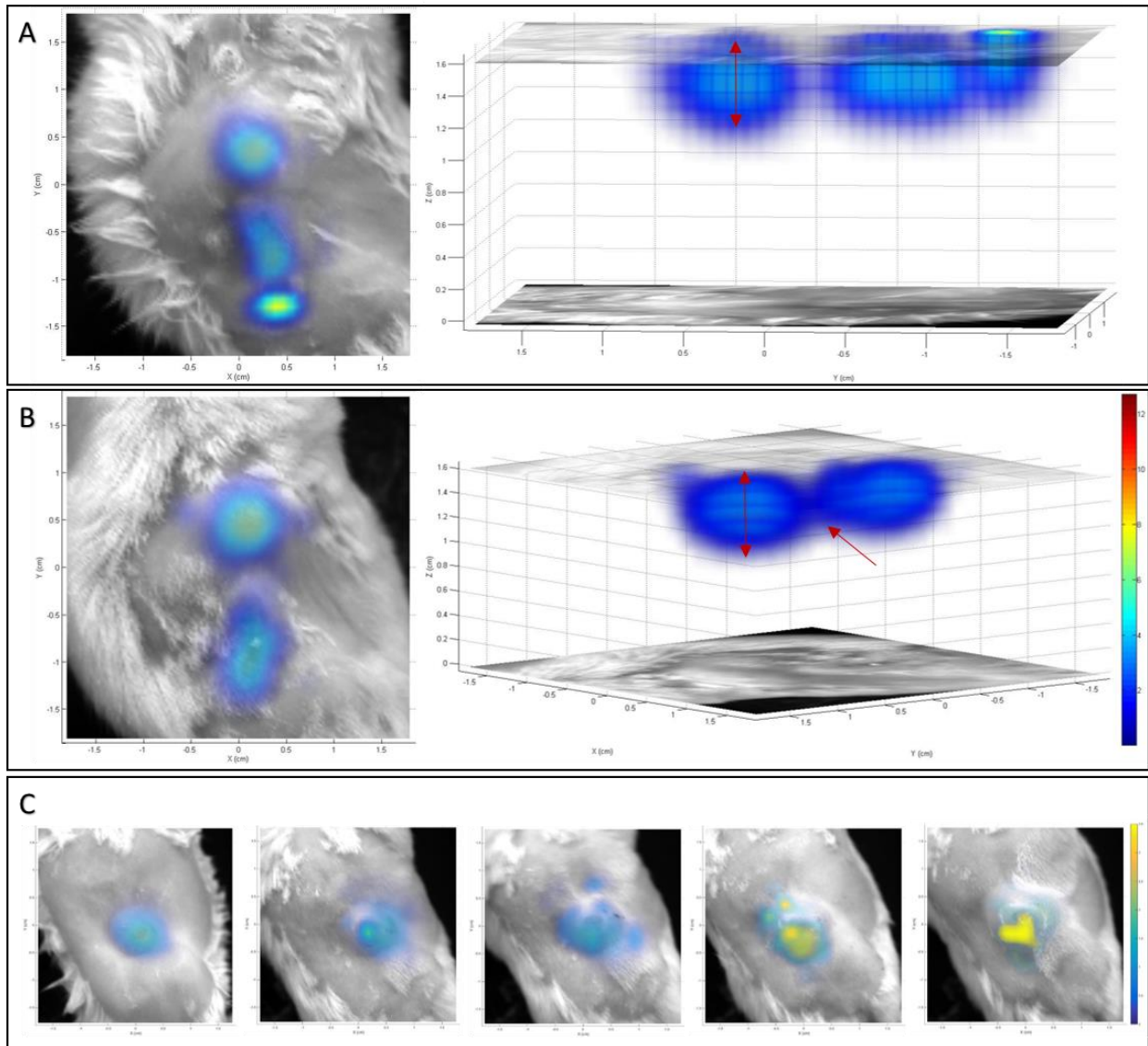
Figure 8. The FMT-scanned subcutaneous tumor of the animal GBP03-GXP3 is shown in XY and XZ projections 25 (A) and 27 (B) days after engraftment. In (C), the XY projections of the injected GBP03-GXP4 animal are shown, scanned every 2 days after tumor detection. Pseudocolor band indicates cell density.

GBP06

The third case, called GBP06 cell line, was collected during the gross resection of a 47-years-old female patient with a tumor in the medulla proven to be a secondary GB, which was gradually evolved to grade IV from lower grades within a time period of approximately 20 years.

Figure 9 depicts the morphology of the histopathological examination of the original tumor. Interestingly, lower grades coexist within the biopsy sample along with the grade IV GB characteristics. The engrafted tumor yet resembles the morphologic features of the high grade component. Notice that already in passage 2 the proliferation index Ki67 has turned from 5% in the original tumor to almost 100% in the xenograft.
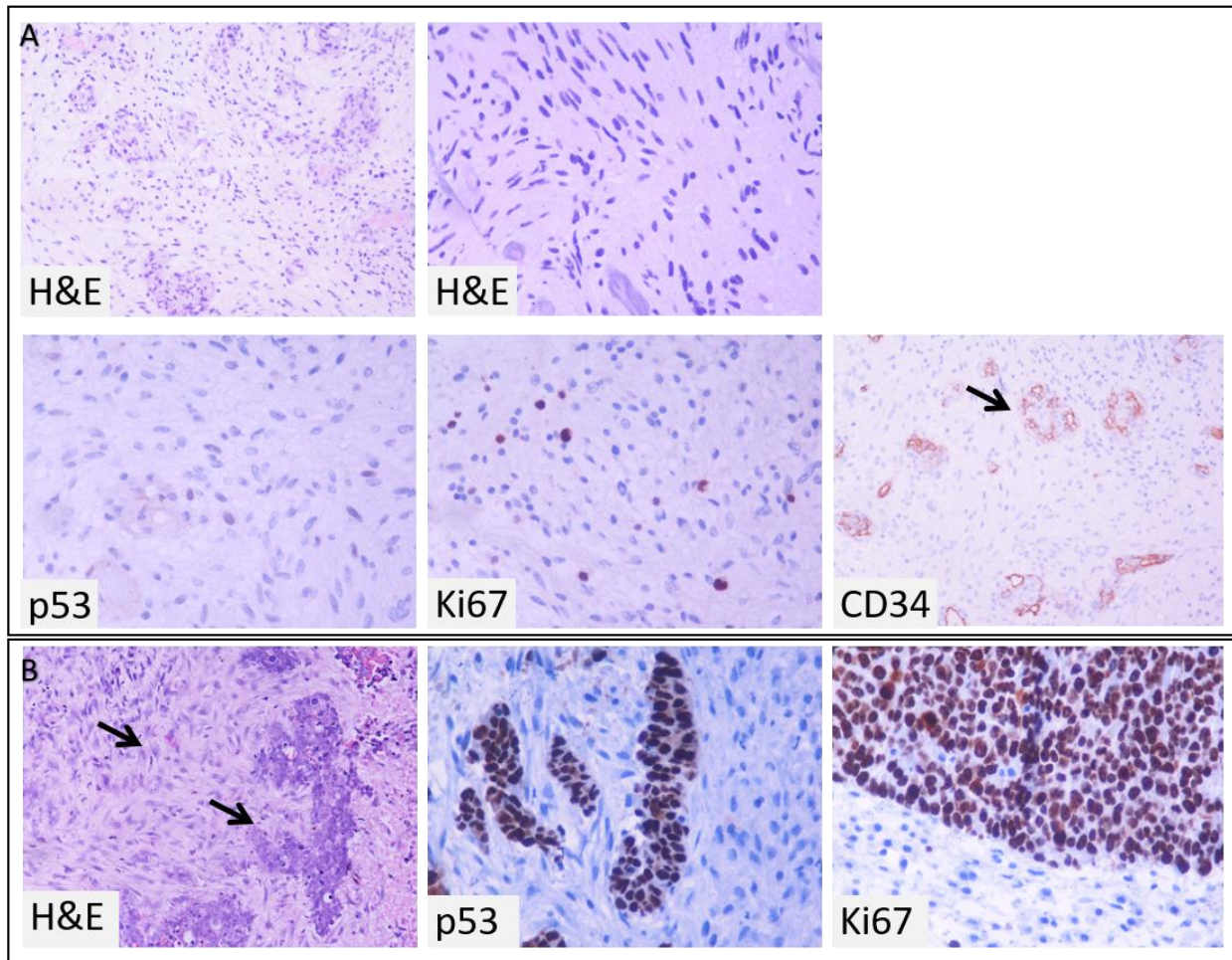

Figure 9. (A) Original GBP06 tumor histology. Upper image are H&E images of the high (200x magnification, left) and the low grade component (400x magnification, right). The immunophenotype is suggestive for wild type *p53* gene expression and proliferation index Ki67 ˜ 5%. Black arrow indicates glomeruloid capillary formations. (B) Xenograft tumor of GBP06-GXP2. Black arrows in the H&E image (100x magnification) indicate the host stroma (upper) and the engrafted tumor (lower). The p53 protein expression pattern is suggestive of mutated *p53* gene, while Ki67 proliferation index is almost 100%. DAB is used as chromogen and H&E as counterstain.

GBP06 cells were serially passaged up to animal GXP4. Interestingly, though none obvious mistake during engraftment method was noticed, passage 1 and few other passages next appeared to form tumor masses intraperitoneally, apart from the subcutaneous. GBP06 cells were treated so as to

express three different colors (GFP, mCherry and Venus). As denoted in Figure 10, intraperitoneal masses observed post-mortem with a fluorescence stereomicroscope (FSM, Leica, Germany) appeared to have a non-uniform color distribution. These masses were separately cultivated and re-injected to animals, but though there were formed xenografts, neither the high growth rate nor the color discrimination were maintained.
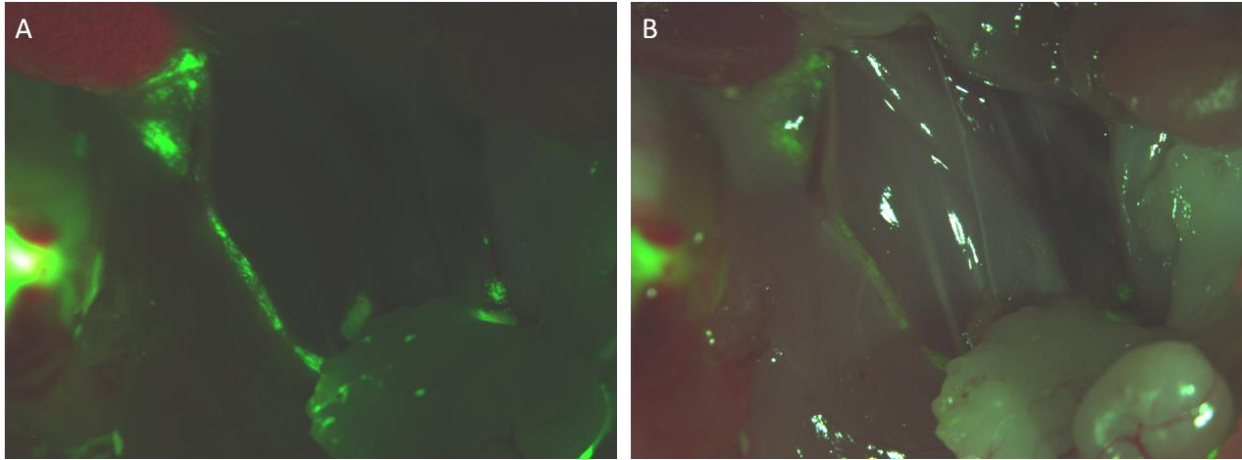

Figure 10. Intraperitoneal FSM images of the animal GBP06-GXP1 captured post-mortem. (A) Excitation with the three wavelengths. (B) Brightfield image overlaid to image A. GB cells express three colors and though all are excited, only GFP is dominant among the masses formed intraperitoneally.

GBP08

The forth sample, called GBP08, was provided during biopsy by a 53-years-old male patient with primary GB in the temporal-occipital left hemisphere.

As it is shown in Figure 11, there are similarities and differences between the original and the xenograft tumors (GXP1 and GXP2). All tumors are composed of highly atypical glial cells. The neoplastic cells in the xenograft tumors are more round, while in the original tumor many cells are elongated. The immunophenotype of the neoplastic cells is similar in the original and the xenograft tumors. The neoplastic cells are GFAP[6]+, vimentin[7]+, synaptophysin[8]-, neurophilaments- and EMA[9]-.

---

[6] Glial Fibrillary Protein (GFAP); a glial marker.

[7] Vimentin is a protein of the human cells cytoskeleton.

[8] Synaptophysin is a marker protein of neuroendocrine cells.

[9] Epithelial Membrane Antigen (EMA)

In the original tumor, cells rarely express p53, while in the xenograft tumors almost all cells express high levels of p53 protein. The proliferation index in the original tumor is around 25%, while in the xenograft tumors is almost 100%.
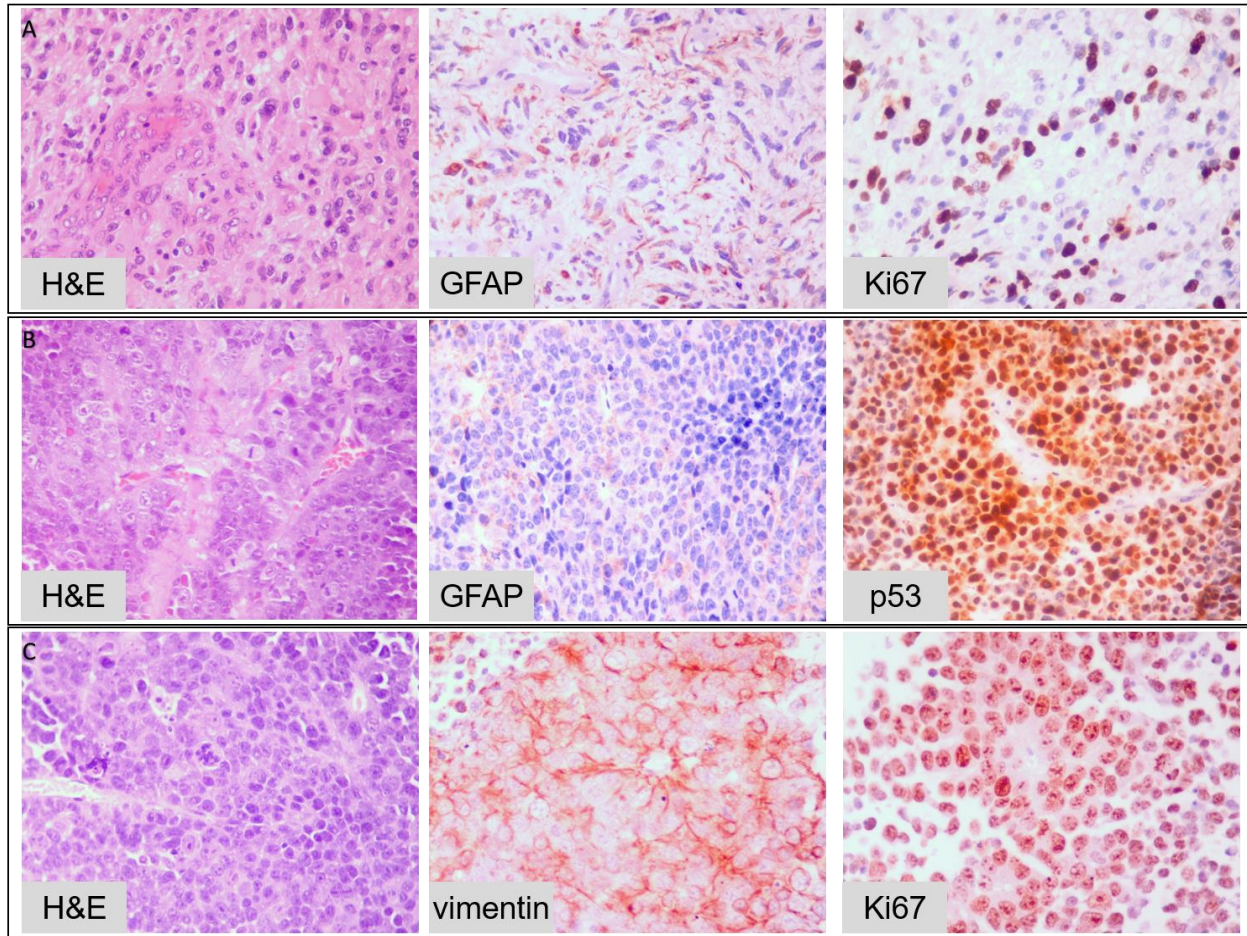

Figure 11. Immunohistopathological examination of the GBP08 original tumor (A), GXP1 (B) and GXP2 (C). DAB is used as chromogen and H&E as counterstain. Original magnifications at 400x.

GBP13

The fifth case described in this section is referred to a 61-years-old female GB patient sampled during total resection. The nodular lesion is located in the left hemisphere fronto-temporally. Unfortunately, the patient deceased from heart breakdown during the recovery period.

As it is depicted in Figure 12, the GBP13 mouse line appeared to most faithfully represent the typical histopathologic features of GB. More specifically, xenograft GXP1 recapitulated most of the characteristics of the primary GB tumor: palisaded necrosis, capillary proliferation, heterogeneous GFAP positivity of GB cells, absence of neurotic differentiation, proliferation index around 25%,

and p53 expression pattern suggestive of wt *p53* gene. As regards the GXP2, it resembles **GB** with a lot of giant cells (giant cell variant). Neoplastic cells are also **GFAP** positive and **NF** negative. Proliferation index is around 20%, and p53 expression pattern is suggestive of wt *p53* gene.

Nevertheless, unlike the other **GB** primary cell lines established, the **GBP13** cells, because of their discrepancy of very slow proliferative rate *in vivo* and inability to survive *in vitro* independently to the tissue culture medium used, were not able to be used as a cell line. No further experiments were conducted using this **GB** case.
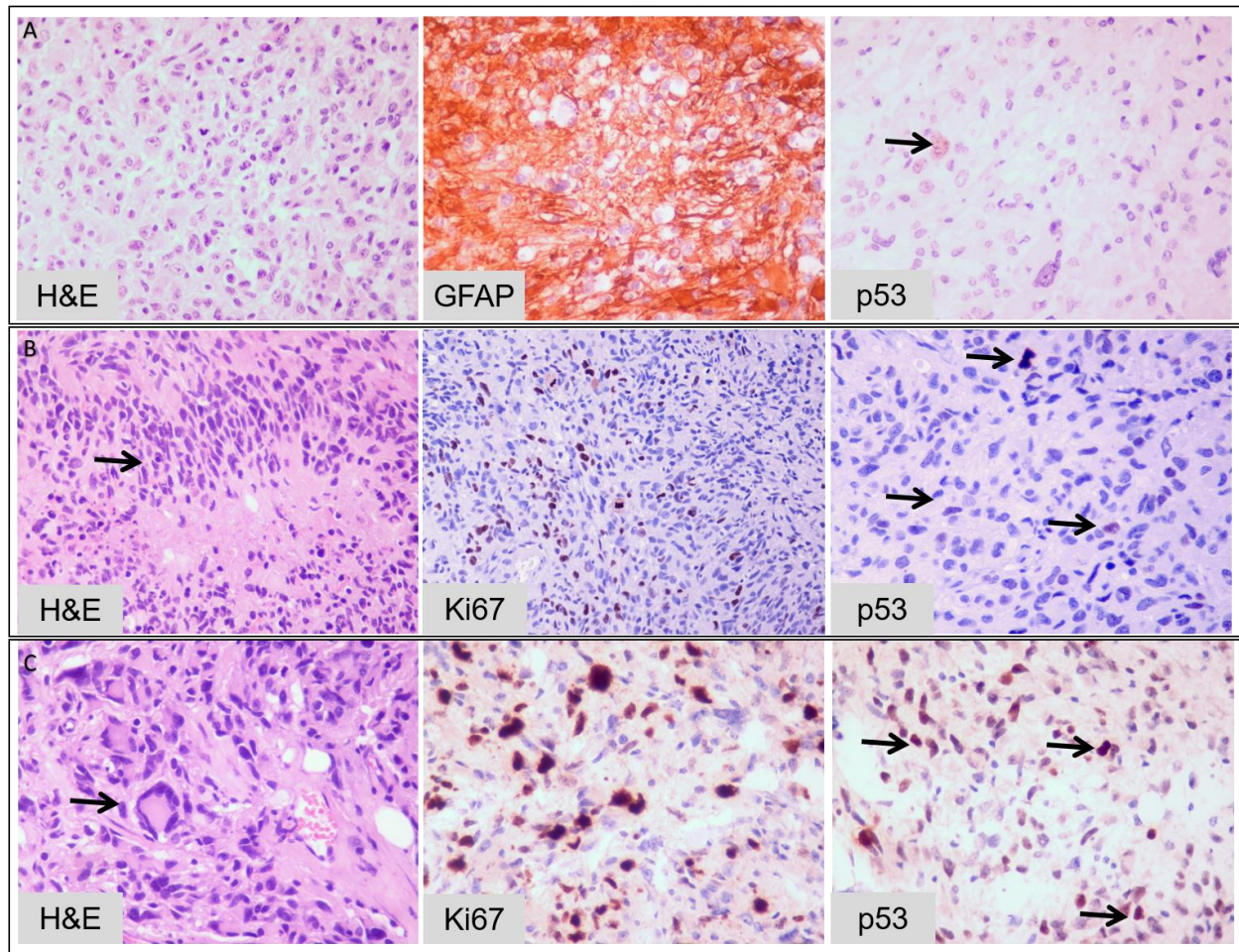

Figure 12. Immunohistopathological examination of the GBP13 tumors. (A) Original tumor: Black arrow indicates a p53-positive cell. (B) GXP1: Black arrows indicate the pseudopalisading necrosis and the p53-positive cells. (C) GXP2: Black arrows indicate a giant cell and p53-positive cells. H&E stain, DAB as a chromogen. Original magnifications at 200x and 400x.

2.4 Characterization of the secondary GB cell lines

Both the U87MG and the T98G GB cell lines were used as control, since they are considered as GB representative [70, 160], as explained in the previous chapter. As expected, the proliferative capacity of both cell lines is high (≈100%).

U87MG

The U87MG or U-87 MG (ATCC® HTB-14™, USA) were sampled from a male patient in 1966 and they are most likely GB of CNS origin [69]. U87MG present a mesenchymal phenotype, though few are known regarding the clinical status of the patient they were collected from. It has to be noted that on the subject of the wide use of the U87MG cell line in GB research and not only, counting more than 1700 references, there are recent works that misidentify this particular cell line when compared to the initial frozen stock [69, 70].

T98G

The T98G or T98-G (ATCC® CRL-1690™, USA) were sampled from a 61-years-old male GB Caucasian patient in 1970's. T98G is a well-known secondary GB cell line of fibroblast-like morphology, usually used in drug screening and molecular GB experimental models [36, 160]. In his pioneering work back in 1979, Stein [161] estimated for the first time the stability of this particular cell line regarding growth properties. Unlike other GB cell lines, as for example the U87MG [69, 162], the T98G cell line is supposed to be representative of GB proliferative and invasive phenotype in *ex vivo*, *in vitro* and *in vivo* studies.

2.5 Discussion

Both primary and secondary GB cell lines were used for the purposes of this study.

In order to describe the primary GB cells as closely as possible to the tumor of origin, cells from the lowest possible passages were used for the physiologic characterization. This way the primary GB cell lines used for the biological experiments were the GBP01-P0, GBP03-P1, GBP06-P0, GBP08-P0 and GBP13-P0, unless otherwise stated.

The U87MG and the T98G cell lines served as a reference, as well as the control between experiments since our own-established GB cell lines are not standardized regarding their pathophysiology/pathobiology.

Whenever needed, the GB cells were lentivirusly transfected in order to permanently express a certain fluorophore; denoted as an acronym after the cell culture name or as empty whether no transfection occurred.

3. Tumor growth over time

Tumor growth expansion is considered one of the critical GB hallmarks. Here, the 3D GB proliferative constants are evaluated for both primary and secondary GB cell cultures *in vitro* and *in silico.*

Excessive proliferation is the most crucial cancer hallmark independently to the cancer type [159]. GB tumors have a remarkable rapid growth that has a critical role regarding the space-occupation and the development of intracranial pressure, usually the main reason of the GB symptomatology [163]. As it is well-understood, both cell division and local spreading are responsible for cancer expansion [164, 165] comprising the most important aspects for cancer progress [159, 166]. *Doubling time* is defined as the average duration of cell growth and division as reflected by the cell cycle 'clock' [167].

3.1 *In vitro* experiments

Here, as an initial step towards understanding the GB heterogeneity among patients, we focus on proliferation. Doubling times, the average cell sizes, the spontaneous cell death rates, as well as the 3D growth rate over time of the in-house-established primary GB cell lines, as well as the U87MG and the T98G secondary GB cell lines are estimated.

Doubling time assay

We used the GBP03-P1, GBP06-P0 and GBP08-P0 primary GB cell lines, as well as the U87MG (*ATCC®* HTB-14™, USA) and the T98G (ATCC® CRL-1690™, USA) cells as control lines. In order to measure the doubling time intervals of the different cell types used we applied a simple protocol in adherent cultures. In a 24-well plate, 20000cells/ml of supplemented DMEM were seeded per cell type at day zero. The plate was incubated in standard lab conditions for approximately a week. Whenever needed, cell culture medium was carefully renewed avoiding the adherent (active) cell population to be disturbed.

Every 24 hours after seeding, the culture medium of one well per cell type was removed and trypsin-EDTA (Sigma-Aldrich, Germany) 1X solution was added for 1-2 minutes. After another 1 minute of trituration in order to produce a single cell solution, all the context was removed from the well and was transferred to a 2ml eppendorf tube. As a final step, 4% formaldehyde was added to permanently fix the cells within the tube which was stored to the refrigerator for further use. The procedure was repeated up to the point that 100% cell confluence was achieved. The cell concentration for each cell type was measured with a 24-hours interval by using a Neubauer hemocytometer.

Cell size estimation

A divided petri dish was plated with a single cell solution of ~2000cells/ml and was incubated in standard lab conditions overnight to let the cells adhere in the surface of the dish. Accordingly, brightfield images of attached single cells were captured in 40x magnification and known acquisition parameters to a Leica DFC310 FX inverse wide-field microscope (Leica, Germany). To check size and shape homogeneity between each cell population so that to assure that the estimated average cell size would be representative, we captured a photograph of a single cell solution within the fixed grid dimensions of the Neubauer hemocytometer.

3D spheroid generation

We used the hanging-drop technique in order to produce spheroids from each cell type, as recommended in [47, 155, 168]. A single cell solution of 625cells/50ul of supplemented double-filtered DMEM was initially seeded per well in a 96-well hanging drop plate (3D Biomatrix, USA). Two rows of wells per cell type were plated so that approximately 24 spheroids were produced. Agarose solution of 1% w/v was added to plate's reservoirs to prevent evaporation of the droplets. After 2-4 days of cells aggregating at the bottom of each droplet, we could consider that the spheroids were finally formed. The growth progress of the spheroids was monitored over time via photographs taken under set acquisition parameters to a Leica DFC310 FX inverse wide-field microscope (Leica, Germany) for pre-decided critical time points (2-days interval).

Data analysis

The average doubling time of each cell line was estimated using exponential linear regression on the doubling time data. The average cell size of each cell line was estimated by segmenting the area of approximately 10 randomly selected cells in brightfield images to ImageJ [169] and averaging. The tumor expansion of the 3D spheroids was again estimated based on the area shown in their brightfield images. The growth curve was estimated by the mean area value ± standard deviation over time. All the above measurements were evaluated per cell type and many experiments were performed for each cell type.

3.1.1 Results

3.1.1a Estimated cell sizes for each cell line

A usual answer of what a common human (cancer) cell diameter could be is about 10 to 100 microns [170, 171], and actually, most computational approaches assume cell size within 10-30 microns [112]. In 2D cultures of low confluence, the cell size and shape are in resting state and not crucially influenced by neighboring cells. As depicted in

Figure 13, there is much homogeneity in the U87MG cell culture with the cells conforming a rather prolonged typically observed shape, with a soma cell size varying between 19 to 24 microns in diameter (see also Table 5). As regards the T98G cells, the typical average cell size observed was 20

microns in diameter and their shape was distinctively flat and polarized. On the contrast, all primary cells used in this study were smaller and typically round with not many cellular protrusions compared to U87MG cells, yet cells of the same cell line appear to differ within the same population. In case of both the U87MG and the T98G cells, it is expected that after all these years in lab conditions there is not much morphological diversity within the cell population and that the cell soma size adequately represents the cell line. On the other hand, regarding primary cells, the cell size is only an average of all possible phenotypes within each cell line. More specifically as denoted in Table 5, GBP03 cells have an average cell diameter of 19 microns, whilst GBP06 are approximately 16 microns and GBP08 are close to 15 microns in diameter. Also, U87MG cells, when growing in adherent cultures, intrinsically form aggregates when much confluent. On the contrary, the primary cells studied here seem to continue as monolayers no matter the level of confluence. Obviously, the average cell size of a certain cell population, no matter how well represented in 2D, it is not maintained when growing in 3D culturing since other physiological parameters that will be discussed next also affect the cell surface-to-volume ratio altering both size and shape.
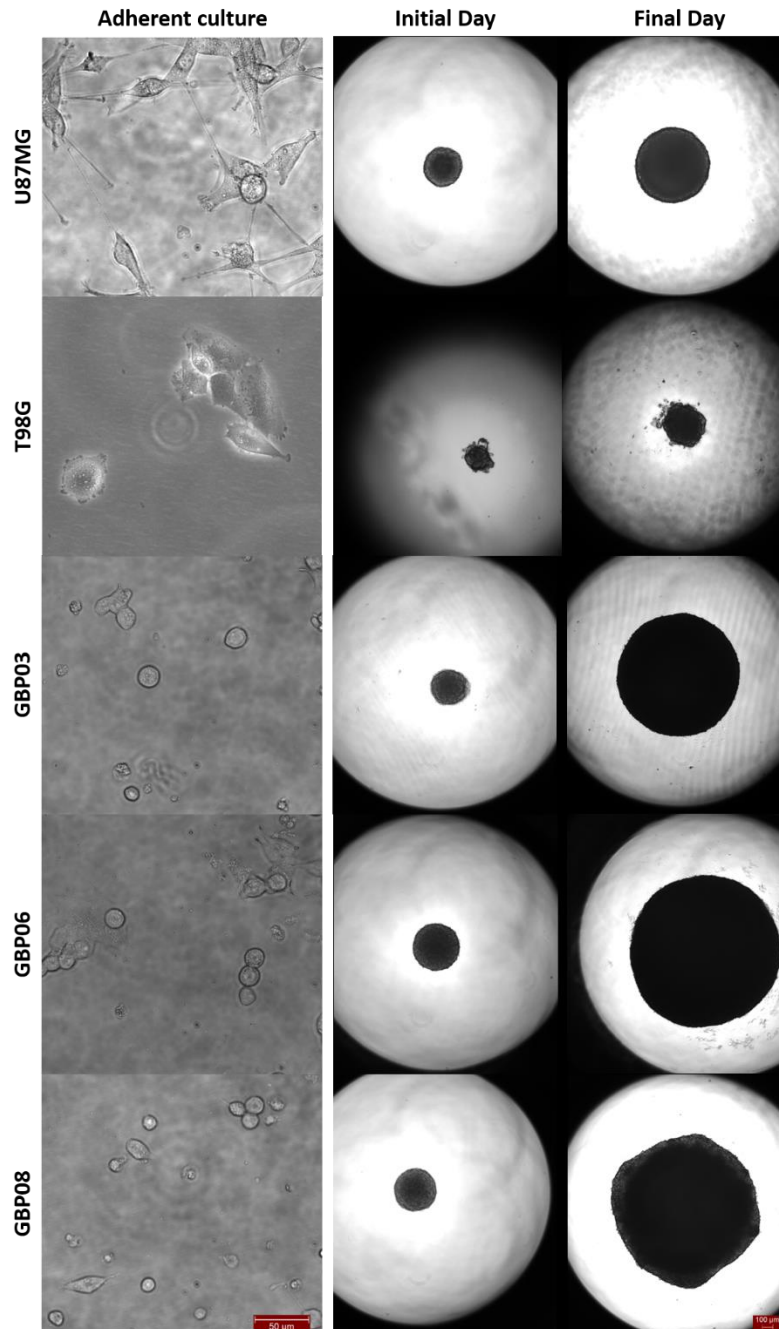
Figure 13. U87MG and T98G cells along with primary GB cells growing as monolayers (left column, 40x magnification) and as hanging-drop spheroids (Initial Day in middle column and Final Day in right column, 4x magnification). Scale bars are 50 and 100 microns, respectively. The initial day is set to be the first day of cell aggregation in spheroidal shape after seeding, meaning Day 2-4. Accordingly, the final day is the time point where spheroids start to deform and decompose, usually approaching well's borders. This day is Day 14 for most primary spheroids.

Table 5. Mean cell sizes and doubling times (± standard deviation) as estimated from the *in vitro* experiments for the respective cell lines.

Cell Type	Cell Diameter (µm)	Doubling time (h)
U87MG	21.5	30.8 ±2.5
T98G	20	28.2 ±1.7
GBP03	19	25.4 ±0.5
GBP06	16	23.5 ±0.7
GBP08	15	23.0 ±1.5

3.1.1b Doubling Time Estimation

Based on the literature, glioma cells usual doubling time ranges from 24 h to a couple of days [172], but more often established primary GB cell lines are recorded to vary few days [60, 79, 173]. Especially for the U87MG cells, they are supposed to have a population doubling time approximating 34 hours, according to their product sheet (ATCC® HTB-14™, USA). Accordingly for the T98G cell line, the ATCC proposed doubling time estimate is 28 h. Our measurements presented in Table 5 are in line with the bibliographic records. Specifically, U87MG cells have a mean doubling time of 30.8 ±2.5 h, which is the slowest division between the cell types we use, followed by the T98G which divide approximately every 28.2 ±1.7, as expected. Among the primary cell lines, GBP03 cells divide approximately every 25.4 ±0.5 h, while GBP06 and GBP08 have similar doubling times estimated at 23.5 ±0.7 h and 23.0 ±1.5 h, respectively.

3.1.1c GB spheroid growth over time

The hanging-drop technique used here to generate the 3D spheroids is a method conditionally approaching the real avascular tumoral state *in vivo* [47]. The spheroid size was determined with optical microscopy and monitored over time. It should be noted that, the imaging approach used here cannot give any quantitative estimate of the compactness of the cells or any other spatial information including the number of the cells, the cell size, shape and polarity, which are definitely different between 2D and 3D structures.

In general, we observe that both primary and secondary GB cells need approximately 4 days from single cell solutions to aggregate into spheroidal structures; while during this starting period, they seem to suppress proliferation capacity. However, most often, primary and T98G cells aggregate sooner than U87MG ones after seeding.

Figure 13, illustrates the growth area of the *in vitro* spheroidal domains as imaged in 2D brightfield images at the initial and final day. The growth curves of each cell line are shown in Figure 14. An

apparent difference between patients, but also between primary and conventional cell lines can be observed. To be more specific, all primary spheroids grow larger than the U87MG and the T98G cells. GBP06 and GBP08 primary spheroids follow an initial fast growing, exponential phase that slows down after approximately 6 days. U87MG and T98G spheroids have an almost linear growth pattern. It has to be noted that the T98G spheroids appear to deform at some level after approximately Day 5 (see Figure 13). This is the reason why we additionally tested the generation of the hanging drop T98G spheroids with supplemented DMEM with 5% BME. As often proposed in such assays [155], it was proven that the presence of some ECM-like substrate also enables better cell adhesion. The morphology of the control T98G spheroids is smoother in the presence of a small BME quantity regarding the surface boundaries observed in the optical microscope. However, independently to the presence of the BME component, the growth pattern of the control spheroids is slightly different. Since the growth pattern over time does not alter, we preferred to use the no-BME control spheroids for comparison. Nevertheless, as it would be described later on chapter 4, BME is also used to evoke the invasion condition and this is why we preferred not to alter the 3D spheroid generation protocol only for the T98G. Taken together with the observations regarding invasion, we suggest that in order to better approximate tumorigenic models by using the T98G GB cell line it is recommended to use adhesive materials.

It has to be clarified that the spheroids reach the well's borders before the plateau and decay phases are observed. The patients GBP06 and GBP08 adopt a high growth pattern, whilst the patient GBP03 follows an intermediate growth rate closer to the U87MG cell line. As already mentioned, especially for the primary cell lines, the initial distribution of the subclones, when plating the cells (Day zero), is random. This eventually leads to a multi-factorial subclonal spheroid growth integrated to average estimations.
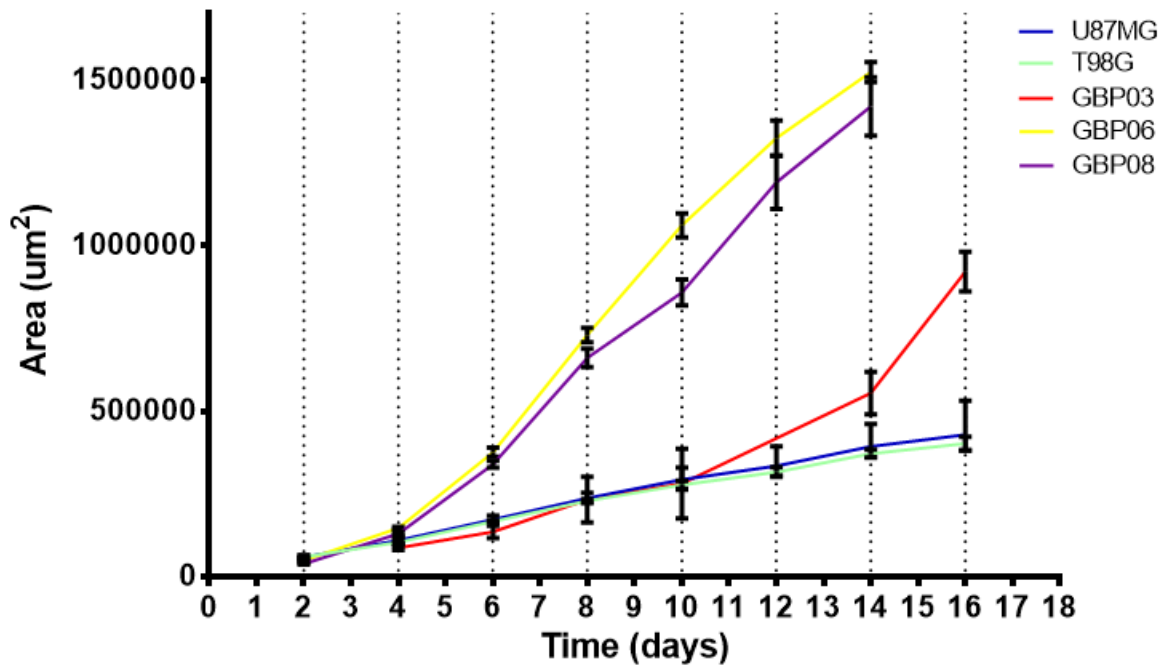
Figure 14. Growth of the tumor spheroid area over time for the *in vitro* experiments of each cell line.

3.2 *In silico* experiments

In previous computational studies, the significance of the proliferative rate has been shown. More specifically, in [174], the proliferation rates of different breast cancer patients are estimated from subsequent **MR** images in conjunction with a simple logistic tumor growth model and show that the proliferation rate estimates could discriminate patient's survival and response to therapy. In another study [175], the role of experimental and simulated diffusion gradients in 3D tumors affecting nutrient, oxygen and drug availability within the tumor and subsequently controlling cell proliferative rate is examined. A mathematical model parameterized from monolayer experiments is used to quantify the diffusion barrier in 3D experiments. In a recent study [164], acquisition of physiologic parameters from multicellular tumor spheroids including proliferation and death spatial profiles are used to constrain and parametrize a mathematical agent-based model that addresses several cell growth mechanisms necessary to explain the experimental observations and reductively translates them to tumor progress over time.

The aim of this work was first to mathematically study the important components affecting the growth dynamics of tumor spheroids when motility is inhibited, mainly including the inter- and intra-tumoral heterogeneity with respect to cell proliferation, and second, to parametrize the mathematical model based on experimentally-estimated parameter values of primary **GB** cell lines in order to increase clinical relevance. Three primary **GB** cell cultures were used in the experiments, as well as the well-known **U87MG GB** cell line as control. All the biological experiments included were performed

simultaneously under the same initial and growth conditions. A hybrid, individual, cell-based mathematical model was used to predict the growth curves of the tumor spheroids and parametrized based on the experimental data. Variations in several mathematical model parameters were explored in order to quantify their effect on tumor growth expansion. The simulated results were compared to the experimental data from the relevant 3D cell cultures and showed that in combination with the proliferation rate, additional factors like the mechanical cell contact inhibition are necessary to predict the *in vitro* evolution of the different GB cell lines under study.

3.2.1 Computational model implementation of tumor spheroids

As explained previously, in general, mathematical models attempt to translate tumor physiology hallmarks [67] into computational parameters and the predicted output is subsequently validated using as ground truth either the experimental [89, 129] or the clinical results [101, 176].

A simplistic on-lattice HDC mathematical model was used to describe the observed tumor growth of the 3D *in vitro* experiments. In the context of the HDC model, each individual cell is described by a discrete cellular automaton, while the local microenvironment is approximated by PDEs. Cell processes are asynchronously and randomly updated. This ensures that in each iteration every cell arbitrarily receives a different priority in the update queue. Cell movement and cell life cycle (including proliferation and death) are sequentially executed every $t_r = 0.8\ h$. In the following, a concise description of the HDC model is provided, while more thorough description can be found in [177] or in [112], where the model was initially proposed.

Computational domain

To simulate a central slice of the 3D *in vitro* tumor spheroids, we set up a 2D regular lattice of size L = 5 mm. The 2D computational domain represents a planar slice through a 3D spheroid. Each $h \times h$ square lattice site can accommodate only a single cell, thus the lattice site defines the cell size. The same lattice is used by both the discrete and the continuous compartments.

Continuous compartment

We assume that oxygen is the only limiting molecule required by the cells in order to proliferate. The whole grid is constantly supplied with oxygen. It has to be clarified though that this assumption oversimplifies the real tumor physiology regarding nutrient supply and waste drainage.

The spatiotemporal evolution of oxygen is described by the PDE shown in (1). Oxygen diffuses with diffusion constant D_o from the boundaries of the computational domain, naturally decays at rate α_o and is consumed by the tumor cells at rate γ_o.

$$\frac{\partial o(x,y,t)}{\partial t} = D_o \nabla^2 o(x,y,t) - \gamma_o o(x,y,t) c_{i,j} - \alpha_o o(x,y,t) \qquad (1)$$

The term $c_{i,j} \in \{0,1\}$ indicates the presence or not of a tumor cell at the lattice point i,j. In order to mimic the laboratory conditions of the medium, oxygen concentration was set to its maximal value at the edge of the computational domain through the application of Dirichlet boundary conditions. Tumor cells die if the local oxygen concentration drops below a random threshold. Specifically, the threshold is assumed to be $o_{deadly} \cdot (1+r)$, where r , a random number from the uniform interval, is [−0.5,0.5] and o_{deadly} is $0.2(ND)$[10]. This is done to desynchronize cell death. Tumor cells die if the local oxygen concentration drops bellow o_{deadly}.

Discrete compartment

Each tumor cell is an individual entity with its own traits. Sets of these traits are assumed to represent a cellular phenotype. A more detailed description of the cell life cycle can be found in [177, 178].

In this work, two mechanisms of tumor cells are mainly considered; proliferation and death. Cellular movement has been neglected considering that the protocol of the *in vitro* experiments do not conditionally allow cell motility. When a cell dies, its location is immediately treated as empty space. On the other hand, the live cells incrementally prepare for proliferation at every time step, until the cell age reaches their doubling time. At that moment, the cell searches for a nearby empty space at the 1-Moore neighborhood. If no empty space is available, the search is expanded to the 2-Moore neighborhood (see Figure 15) and the process is repeated up to r-Moore neighborhood, where r is defined as the proliferation depth and determines the maximum neighborhood size. Examples of Moore neighborhood can be seen in Figure 15. If more than one empty space is found in the same neighborhood, one of them is randomly chosen.

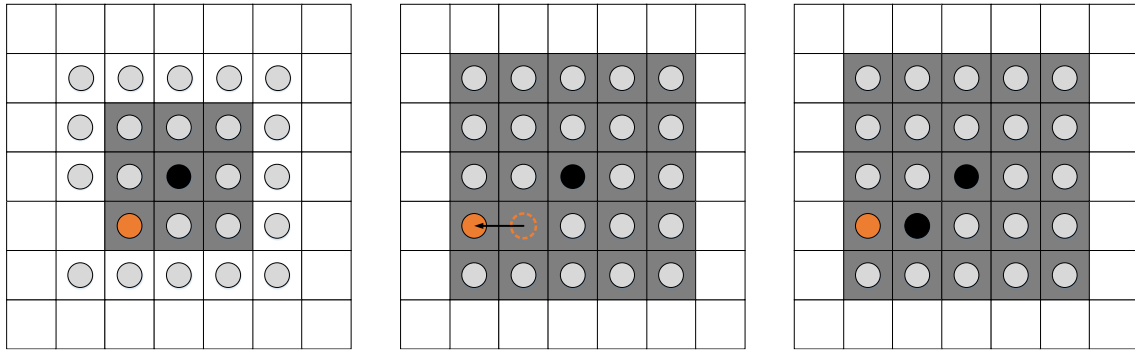[10] A random non-dimensionalized value for the oxygen threshold.

Figure 15. Example of a cell (shown in black) attempting to proliferate. Firstly, the cell searches the 1-Moore neighborhood highlighted by the gray squares in the left image. Being unable to find an empty space, it searches the 2-Moore neighborhood indicated by the gray squares in the center and right images. As an empty space is found, the orange cell is pushed towards the empty space as shown in the central figure. The latter movement frees the empty space on the 1-Moore neighborhood and allows the proliferating cell to place an identical cell (also shown in black) to the adjacent empty space (right image).

As shown in Figure 15, when an empty space is found on a neighborhood other than the 1-Moore, cells are pushed away from the location of the proliferating cell towards the empty space in order to create an empty space to the 1-Moore neighborhood. Then the cell resets its cell age and places a copy of itself at the adjacent empty space. If no empty space has been found, the cell enters a quiescent state at which it constantly searches for empty space, without further increasing its age. The extended proliferating rim describes the maximum distance over which a cell is capable of pushing other cells away in order to create space for its proliferation and reflects the mechanical growth inhibition processes observed in growing cell populations [164].

3.2.2 Results

In this work, the *in vitro*-estimated doubling times and cell sizes of three in-house-established primary GB cell lines, as long as of the U87MG cells, were used to initialize the individual-cell-based mathematical model in an attempt to predict their different growth patterns. A sensitivity study was performed where the effect of important factors affecting tumor spheroid expansion such as the doubling time, the cell size, the depth of the proliferative rim, as well as the co-existence of multiple clones with different proliferative capacities within the tumor were computationally explored. We argue that, as expected, proliferation is one of the most defining characteristics regarding tumor expansion and that tumor predictive computational models should prioritize these remarkable variances between individuals and not just based on theoretically defined values.

Computational Parameter Study

Prior to parametrizing and predicting the growth pattern of the multicellular spheroids, a simple parameter study was performed to determine the extent at which the doubling time and cell size affect the 3D growth simulation, as well as to explore the effect of additional parameters that could

play a significant role in tumor expansion including the depth of the proliferative rim and intra-tumoral heterogeneity.

The discrete and the continuous part of the computational model were parametrized accordingly to meet the experimental setup as shown in Table 6. The length L of the computational domain equals to 5mm to resemble approximately the size of the hanging drop plate. Both the oxygen decay rate and the cell's oxygen consumption rate were adopted from [112]. To numerically solve the PDE (1), its parameters have been non-dimensionalized (ND) by using o_{max}, τ and L, which correspond to the maximum oxygen concentration, the computational iteration time and the domain length, respectively. Dirichlet boundary conditions were used to lock the boundaries to the maximum oxygen concentration to simulate the so-assumed adequate and stable nutrients' availability, since the culture medium during the experiment is periodically refreshed. Also, the alternating directions implicit method was used to numerically solve the PDE [179, 180].

At first, we explored the effect of the doubling time on tumor expansion keeping the rest modeling parameters constant. Specifically, we assumed a tumor cell of size equal to 18μm and considered a depth of proliferative rim equal to 2 cells, while varying the doubling time from 15.5h to 35.5h. Figure 16 (left graph) shows the growth curves of the tumors with different doubling times. As expected, increased proliferative capacity results in increased tumor expansion. If a reference time point is picked at 10 days, we can calculate the absolute increase of area yielded by the decrease of the doubling time. When the doubling time is reduced from 35.5h to 30.5h, the area increases by approximately 24.46%; while comparing the respective areas between the doubling times 20.5h and 15.5h, the area is increased by 54.87%. We can thus conclude that the expansion area is affected more, when the doubling times are lower. As expected, the effect is accumulative, thus if a later/earlier time point was picked the differences would increase/decrease, respectively.

Table 6. The computational parameters used to initialize the HDC model. Non-dimensionalized (ND).

Parameter	Value
Domain length, L	5mm (Methods-Computational Domain)
Cell (& lattice) size, h	14-20μm (Methods-Computational Domain)
Iteration time, τ	8h ((Methods-Computational Domain, [177])
Oxygen consumption, γ_0	1.25 10^{-16} M cell^{-1}s^{-1} (Methods-Computational Domain, [112])
Maximum Oxygen, o_{max}	6.7 10^{-6} M O$_2$ cm^{-3} (Methods-Continuous Compartment, [112])
Oxygen decay rate, α_0	0.0125 (ND) (Methods-Continuous Compartment, [103, 112, 166])

We also explore the effect of cell size on the observable tumor expansion. It should be noted that if counting of the tumor cell population was possible on the *in vitro* experiments, then this parameter would make no difference. We vary the cell size from 14 to 20μm, while keeping the doubling time constant and equal to 25.5h and the proliferation depth equal to 2 cells. Figure 16 (middle), shows that by increasing the cell size, the tumor expansion increases as well, as expected. Indicatively, by comparing the values at simulation time 10 days, the area relatively increases by 21.5%, 29.8% and 31.1% as the cell size increases from 14μm, 16μm and 18μm to 16μm, 18μm and 20μm, respectively.
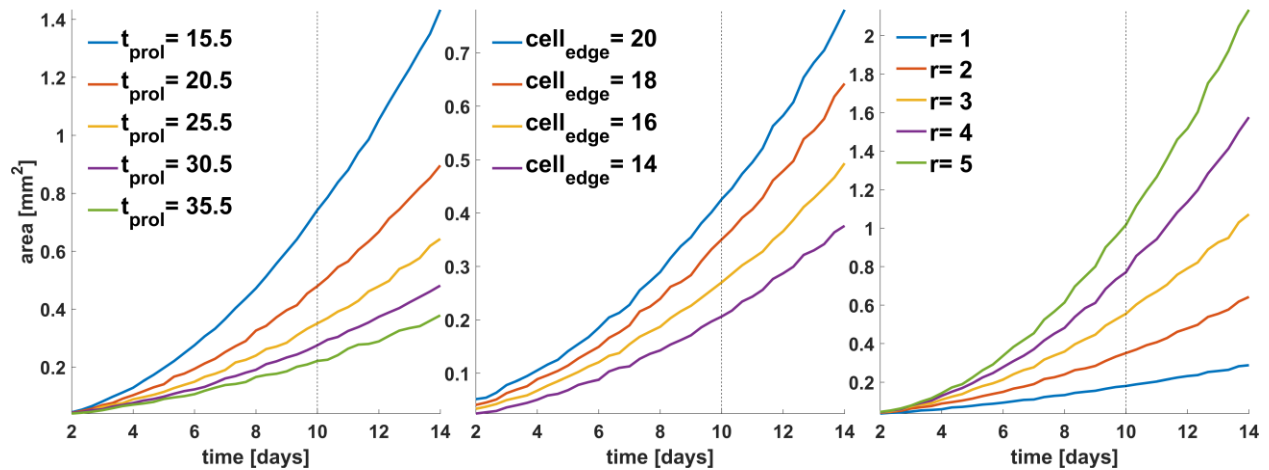
Figure 16. Growth of the tumor spheroid area over time as predicted from the computational model related to altering doubling time from 15.5h to 35.5h (left), the cell size from 14 to 20 microns (middle) and the proliferation depth from 1 to 5 (right).

The depth of the proliferative rim significantly affects the tumor expansion as it increases the number of proliferative cells. Figure 16 (right) illustrates the effect that different proliferation depths have on the tumor area over time. The proliferation time was set to 25.5h and the cell size to 18μm. At the reference point of 10 days, as the proliferation depth increases from 1 to 5 cells with a step of 1 cell, the area increases relatively to its previous value by 94.7%, 58.4%, 38.9% and 31.3%. In other words, a considerable higher expansion of the tumor area (94.7%) is observed when the proliferation depth is increased from 1 to 2, as compared to a change from depth 4 to 5. As the proliferation depth increases, less cells enter the quiescent state, and proliferate instead; this is why the growth area is increased.

To further investigate the role of heterogeneity between our cases, we proceed by performing simulations which contain multiple phenotypes identical in all traits except for their respective doubling time. All phenotypes have their cell size set to 18μm and proliferation depth (r) equal to 2 cells. The proliferation time is randomly selected for each phenotype at the beginning of the simulation from a uniform distribution in the interval (15.5, 35.5) hours. As shown in Figure 17, to illustrate the impact of the phenotypic multitude, two scenarios are considered inspired by [112];

one at which the number of phenotypes is 100 (shown in green line), and another where 10 phenotypes are randomly selected (shown in purple line). Additionally, given the randomness of the phenotypic initialization, each experimental scenario is repeated 50 times. Figure 17 also shows the area expansion over time for three monoclonal examples with doubling times 15.5h (red dashed line), 25.5h (blue dashed line) and 35.5h (yellow dashed line). Figure 18 illustrates the doubling time of the populations that survive over time. As it can be seen, the mean minimum and the mean maximum values of the doubling time are constant for a long period of time indicating the presence of both the fastest and the slowest populations within the tumor, yet the frequency of these populations becomes progressively unequal with the fastest population to actually overpopulate within the tumor. Thus, a decline to minimum values of the mean doubling time is observed.
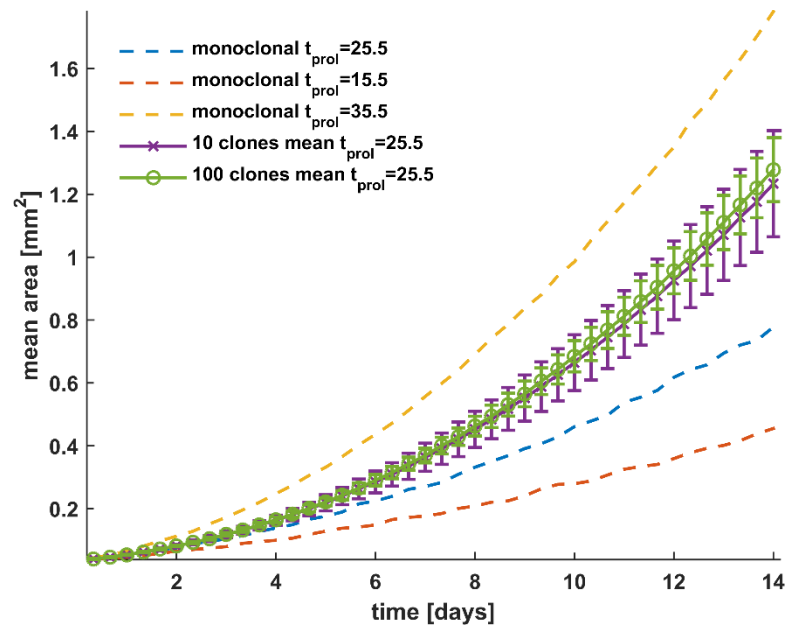

Figure 17. Monoclonal and polyclonal tumor area expansion. For the polyclonal case two scenarios are considered; one at which the number of phenotypes are 100 (green line) and another where 10 phenotypes are randomly selected (purple line). Each experiment is repeated 50 times and the corresponding standard deviation is also shown. The mean area of three monoclonal examples with doubling times 15.5h (red dashed line), 25.5h (blue dashed line) and 35.5h (yellow dashed line) is also illustrated.
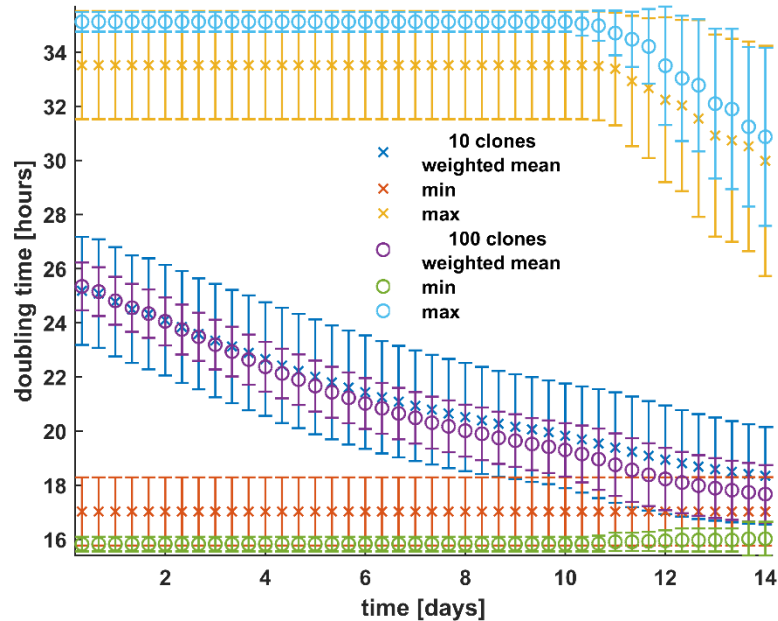
Figure 18. Doubling time of the populations that survive over time in a polyclonal tumor. Two scenarios are considered; one at which the number of phenotypes are 100 and another where 10 phenotypes are randomly selected. Each experiment is repeated 50 times. The minimum, maximum and average doubling times for both scenarios are shown, as well as their corresponding standard deviations.

Comparison between Biological and Computational Results

In the following, we assumed monoclonal populations and parametrized the mathematical model based on the estimated experimental values for the doubling time and cell size for the different GB cell lines. We also parameterized the model without taking into account the *in vitro* estimates of cell sizes and kept the cell size and all the other parameters constant in all the experiments. Parameters within the range of the experimental biological observations were chosen to achieve the best-fitting growth curves. It has to be noted that both the simulated and the biological experiments had an initial seeding population of approximately 625 cells per spheroid per cell type. The simulations show that the *in vitro* estimates of cell sizes do not improve the model predictability and that accounting only for differences in doubling time among GB lines results in very similar growth curves.

The values used by the *in silico* model regarding the doubling time were 33h for the U87MG cells, 25h, 23h and 22h for the GBP03, the GBP06 and the GBP08, respectively; all inspired by their biological counterparts. Figure 19 shows the *in vitro* growth curves and the *in silico* predicted ones for all the GB cell lines. Based on the selected doubling time values and keeping the proliferation depth equal to 2, the growth curves of U87MG and GBP03 cell lines are closely approximated by the *in silico* model. However, the GBP06 and GBP08 cell lines diverge significantly from the *in vitro* results indicating that proliferation alone is necessary, but not sufficient to explain the tumor expansion of different GB cell lines growing under the same initial conditions. Hence, additional

phenomena should be taken into account. For example, increasing the proliferative depth and/or consider the possibility that multiple phenotypes with various proliferative capacities coexist within such tumors, then the *in vitro* and *in silico* growth curves would come in line as our parameter study analysis previously revealed. Alternatively one could advocate that GBP06 and GBP08 contain phenotypes with higher proliferation depth than U87MG (and GBP03) which are expected to thrive in compact environments such as a solid spheroid. It should be noted that the proliferative depth could also be affected by the development of ECM substrate in 3D cultures, even in the conditional absence of a relevant substrate [47], as in our biological experiments. This, along with antagonistic and synergetic relationships of subclones within the growing spheroid could alter the mechanical responses of dividing cells, reflected in terms of proliferation depth to our mathematical model. However, our biological approach did not take into account a priori this parameter, but it was the computational approach that indicates such possible behavior suggesting that ECM production and distribution might also be different in the different cell lines.

Figure 19 also shows the simulated growth curves for the GBP06 and GBP08 after changing their proliferation depth values from 2 to 4 and 3, respectively. The *in vitro* data better correlate the relevant *in silico* data. Also notice that setting the proliferation depth of GBP06 higher than the GBP08 is important to achieve their corresponding growth patterns, where GBP06 grows faster than GBP08, given that the doubling time of the former is higher than the latter and that small differences in their cell sizes are not adequate to reverse their growth patterns. Another point that should be marked is that the subsequent decline observed after Day 8 in the *in vitro* growth curves of these two cell types cannot be predicted by the computational model. This is because the computational model we use does not account for inhibitory stimuli that are probably developed in real growing tumors, since this was beyond the scope of this study.
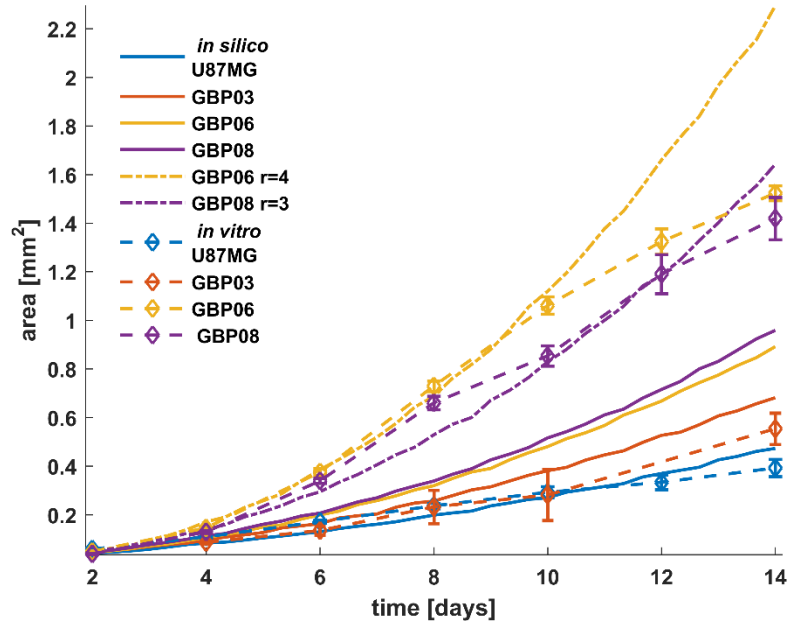
Figure 19. *In vitro* spheroidal growth as opposed to *in silico* for all four cell types with the final chosen sets of doubling times (33h for the U87MG cells, 25h, 23h and 22h for the GBP03, the GBP06 and the GBP08, respectively) and fixed proliferation depth equal to 2. Two additional simulated growth curves are depicted with different proliferation depth values for the GBP06 (r=4, yellow dashed line) and the GBP08 (r=3, purple dashed line) spheroids.

3.3 Discussion

This work utilizes primary tumor cells collected from GB patients and subsequently cultivated *in vitro* as 3D tumor spheroids and computational approaches to study, experimentally parametrize and predict the growth dynamics of tumor spheroids focusing on proliferation. At first, a parameter study was performed in order to evaluate the extent to which important factors such as the doubling time, the cell size, the depth of the proliferative rim, as well as the co-existence of multiple clones with different proliferative capacities within the tumor, affect tumor spheroid expansion when motility is inhibited. The experimentally estimated doubling times and cell sizes of three in-house-established primary GB cell lines, as long as of the U87MG cells, were then used to parametrize the computational individual-cell-based model.

Overall the parameter study verifies the significant effect of proliferation (depicted in both the cellular doubling time and the depth of the proliferative rim) on tumor expansion [164] and underlines additional factors that could play an important role on tumor growth curves including the intra-tumoral heterogeneity that has been widely observed in GB. We also observe that a multiclonal population with the same mean proliferation exhibits a greater tumor expansion than the corresponding monoclonal population because fitter clones survive over time driving tumor expansion at higher rates. Furthermore, the clonal heterogeneity within the tumor mass allows different clones to be selected every time an experiment is performed. Thus, a variation is observed

in the growth curves. The variance is cumulative, increases over time and can reach a difference of 100μm in radius after 14 days of growth (Figure 17). Furthermore, the simulations also show that although the mean growth curves are quite similar, the variance highly depends on the initial number of different clones coexisting within the tumor mass such that fewer initial clones in the population produce higher variability (Figure 18).

Comparing the *in vitro* experiments with the *in silico* predictions, we observe that although the proliferation rate is necessary, yet it is not sufficient, to describe the growth curves we observe experimentally. The simulations show that additional factors including the intra-tumoral heterogeneity together with the overall proliferative capacity reflected in both the proliferation rate and the mechanical cell contact inhibition can predict the evolution of different GB cell lines. Nevertheless, further investigation of the underlying mechanisms is critical.

In general, the compactness of the spheroids can be assigned to two factors in mesoscopic terms: a. the cellularity, in means of cells' size and shape given the space, and b. the levels of stress tolerance, reflecting their response against internal forces within the spheroid which vary between division and entering quiescence state, also known as 'contact inhibition'. As smaller in size and quicker regarding divisions, GBP06 and GBP08 cells appear to grow larger in 3D over time than the other two cell types mainly because of their promoted proliferative capacity reflected by the higher proliferation depth in the respective simulated growth curves (see Figure 19). However, this is only an assumption for our *in silico* trials since there is no indication of the spheroids cell density and proliferation depth to our experimental protocol and this is a limitation of our method needed to be taken into account in future work.

The migratory capability of our cells is conditionally blocked to our experiments so that it can be assumed to play a minor role in the proliferative characteristics studied here. However, when the different cell populations grow in 3D, both ECM can be produced, and the cell shape and polarity could also be affected, such that cell-to-cell and cell-to-matrix adhesion properties could be further explain the divergence observed over time in growth patterns between the *in vitro* and *in silico* experiments (see also chapter 4).

We suggest that, instead of using bibliographic values usually referenced by common GB cell lines, cell doubling time was found to critically enhance the *in silico* predictability, but is insufficient to holistically describe differences in tumor growth over time among the different GB cell lines. The mechanical cell responses to internal forces obtained during the growth of a compact tumor should be further investigated experimentally, as well as the important role of intra-tumoral heterogeneity. The importance of quantitative methods to provide spatial information of proliferative, quiescent and necrotic cells, as well as additional features including the remodeling of ECM and phenotypic distribution regarding intra-tumoral heterogeneity affecting tumor expansion becomes evident.

4. Invasive patterns adopted *in vitro* and *in silico*

The clinical imaging biomarker of the infiltrative edema is translated to the invasive capacity of the GB cells when they are conditionally able to migrate. The invasive morphology of the GB cell cultures is physiologically characterized *in vitro* and *in silico*.

GB cells, are migratory and invade the neighboring brain parenchyma, *en masse* or as single cells [31], and expand, characterizing GB as a diffusive rather than a focal disease [75]. Furthermore, regardless of whether GB cells invade the vasculature, their capability of establishing successful micrometastases is limited [29]. Nevertheless, during this process, another typical GB hallmark develops, the infiltrative peritumoral region edema [11, 21, 35, 181], which, apart from the invasive cancer cells, also includes cells of the immune system, neuronal cells and fibroblasts, as well as other cell components of the tumor microenvironment [154, 159, 182]. During surgical resection, there is a procedural empirical difference between GB and other tumor types that does not allow the GB tumor mass to be excised as a monoblock, because GB is supposed to be a resilient tumor type. Taking into consideration these two facts, surrounding edema and incomplete/subtotal surgical removal (in combination with safe access), it becomes evident that it is virtually impossible from a technical point of view to totally exempt the patient from the malignancy. As a result, tumor relapse may occur [29] in the original or nearby brain regions, which further devastates overall survival [8].

It should be noted that tumor growth and expansion are generally attributed to both proliferation and local spreading [164, 165]. Invasion is a complex, multiscale phenomenon involving processes at different spatial and temporal scales. Migrating tumor cells can mechanistically move by different modes, ranging from single cell to collective locomotion, or even to whole-tissue expansion [183]. The molecular pathways during movement are complex and involve both energy utilization and response to stimuli, either chemical or mechanical or both. The invasive process necessitates both locomotion and proteolysis and involves both cell-to-matrix and cell-to-cell adhesion mechanisms. More specifically, it is believed that in multi-cellular invasion, transmembrane integrins are highly expressed at the "leading edge" tumor cell protrusions (pseudopodia), where they form focal contacts with the actin cytoskeleton. In addition, mechanical feedback through cell-to-cell junctions [184] and/or cell adhesion proteins such as N- and E-cadherin (though the latter is believed to have limited expression in the brain) contribute to the collective migration of glioma cells by promoting direction sensing. Interestingly, differential expression of cadherins has been observed in GB samples as well as disorganization and instability in cell-to-cell interactions [113, 185-191] supporting the presence of intratumoral heterogeneity with respect to cell-to-cell adhesion leaving open questions about its role in invasion.

Collective invasion is driven by gradients of growth factors, cytokines, etc., as well as by different matrix degrading enzymes. Growth factors, such as Transforming Growth Factor-β (*TGF-β*), alter cellular connectivity and interaction [192]. Degrading enzymes called Matrix MetalloProteinases (**MMPs**) are expressed and secreted by the tumor cells and further enable cellular dispersion [192]. Migration towards or away from a diffusible chemical stimulus is defined as "chemotaxis" and the diffusible molecules serve as either chemoattractants or chemorepellents, respectively. "Haptotaxis" on the other hand, refers to cell motility towards **ECM** bound molecules gradients, which are triggered by anabolic and catabolic rearrangements. Interestingly, apart from the biochemically-driven haptotaxis, it has been shown that **ECM** mechanical characteristics, such as stiffness and composition, are sufficient (but not necessary) to promote haptotactic invasion and that cells stratify an adaptive plasticity against relevant ECM-coordinated movement [31].

A number of quantitative *in vitro* models have been developed over the past decades to study glioma invasion, most of which are based on the original trans-well or Boyden chamber assay systems [193-195], where single cells invade from an upper chamber through an ECM-like membrane or an ECM-coated filter to a lower chamber in response to chemoattractants. The latest trends in phenocopying **GB** in general and regarding invasion, mainly involve patient-derived cells -to individualize tumor properties [33, 61] and 3D *in vitro* experiments- to better mimic the parental tumor pathophysiology [47, 157]. Tumor spheroids as a model system can be well characterized and have been shown to reproduce the spatial organization and micro-environmental factors of *in vivo* micro tumors, such as relevant gradients, establishment of cell-to-ECM adhesion and cell-to-cell interactions and deposition of ECM. Recent studies have shown that when glioma cells grow *in vitro* as multi-cellular spheroids, they are able to recapitulate invasive strategies observed *in vivo* including the collective behavior [49, 196].

A comprehensive overview of the mathematical models developed for **GB** progression and therapy response from the clinical perspective and personalized medicine are summarized in [125]. In addition, a thorough review summarizing major studies related to **GB** invasion can be found in Alfonso et al. [107]. Among these studies, the particular importance of the microenvironment and the central role of cell-to-cell and cell-to-ECM interactions on the evolution of invasion are extensively explored, as well as the mechanisms of phenotypic plasticity and adaptation. Nevertheless, most models focus on single-cell migration phenomena. Furthermore, the role of intra- and inter-tumoral heterogeneity and particularly with respect to cell-to-cell adhesion properties is less studied. Anderson [112] accommodates in his model phenotypes with different adhesion properties, however these properties are subject to mutations and thus, vary through time. In that approach, additional properties of cancer cells including their proliferation and migration rates that can supplant the role of heterogeneous cell-to-cell adhesion interactions are also involved. Domschke et al. [197] studied the role of cell adhesion variability on the invasive pattern formation. In their model, variability is taken into account again in a time-dependent manner where cancer cells sequentially mutate into more aggressive phenotypes with respect to cell-to-cell and cell-to-matrix adhesion properties. Furthermore, the local interplay of neighboring cells is not considered. Reher et al. [113]

systematically explored the effect of both intrinsic and extrinsic cues of adhesion heterogeneity yet, specifically on tumor cell dissemination. Overall, none of these studies focuses on the intrinsic heterogeneity with respect to the interplay of co-existing phenotypes with different cell-to-cell adhesion properties and its impact on alternative invasion patterns.

In this work, we study the invasive potential of GB cells under a set of basic experimental parameters, by means of forcing the U87MG and the T98G cells and the three in-house-established primary GB cell lines to form 3D cell cultures at an ECM-like substrate. Our biological experimental results consistently show that the two types of tumor spheroids display different invasive patterns suggesting that different mechanisms of cell motility are adopted. The individual-cell-based computational model was applied accounting also for heterogeneity in cell-to-cell adhesion properties of the cells to predict the variety of the invasive morphologies and kinetics observed. Inspired by the model-driven parameters, we further on confocal-scanned the T98G spheroids and we show preliminary results of the cell-to-cell adhesion and proliferation statuses adopted during invasion. Improving our understanding of the underlying mechanisms, which drive and/or regulate the different invasion patterns observed among the GB subtypes will offer opportunities for alternative and GB type-specific drug targets to prevent post-operative tumor relapse. Furthermore, predicting the various invasive morphologies will potentially help to better assess the extension of invasion, which remains undetectable by conventional imaging modalities.

4.1 Methods

4.1.1 *In vitro* experiments
<u>Invasion assay</u>

We used the GBP03-P1, GBP06-P0 and GBP08-P0 primary GB cell lines, as well as the U87MG (*ATCC*® HTB-14™, USA) and the T98G (ATCC® CRL-1690™, USA) cells. GB spheroids were generated using the hanging-drop technique as explained previously. The 3D spheroids were formed in a Perfecta3D 96-well hanging drop plate (3D Biomatrix, USA) by seeding a single cell suspension solution of approximately 600 cells/50 μl of supplemented DMEM per well for each cell type used. An agarose solution of 1% w/v was added to the plate's reservoirs to prevent evaporation of the droplets.

After 4 days of spheroid formation, twenty spheroids per each cell type were transferred to a 96-well U-bottom plate, initially cooled on ice for 15-20 minutes. The invasion solution was made by diluting ice-cold BME Pathclear (Basement Membrane Extracts, Amsbio, Cultrex®, UK) in supplemented DMEM in a 1:1 ratio. In the U-bottom plate, 100μl of the invasion solution was added per well containing either a primary or a U87MG spheroid. Subsequently, the U-bottom plate was centrifuged for 5 minutes at 300rpm, at 4° C in order to place the spheroids in the center of each well, homogeneously distribute the invasion matrix and eliminate bubbles within it. Incubation for 1 hour at 37° C was followed to allow solidification of the matrix. As a final step, 100μl of warm supplemented DMEM was added per well and the plate was placed at a 37° C humidified cell culture

incubator to promote invasion to the semi-solid gel-like ECM matrix. The same procedure was followed to prepare the confocal samples in the glass-bottom dishes (Greiner, USA); yet more than one spheroid was transferred per chamber.

Negative control

As a negative control experiment, spheroids of each cell line were examined by means of growing in the absence of the ECM-like substrate (i.e. in supplemented DMEM-F12[11] alone). It should be noted that none of the cell lines used exhibit invasion in the absence of ECM and no exogenous ECM is required for the spheroid formation via the hanging drop technique.

Confocal imaging

Imaging of the invasive T98G spheroids was done in cells decorated by three different fluorescent probes. Initially, the T98G cells were treated using the PKH26 (Sigma-Aldrich, Germany) protocol by following the manufacturer's instructions, as well as transfected with GFP or GFP linked to E-cadherin plasmids. Cells were loaded before plating with the lipophilic PKH26 red fluorescent (working solution of 4μl/ml buffer) which was used to monitor their proliferative history. Transfected cells were cytoplasmically expressing either GFP or GFP/E-cadherin. After the invasion assay, the spheroids were permanently fixed with 4% PFA and washed to remove the medium's phenol red. The fixed cells were treated with the nuclear dye Draq7 (Biostatus, UK) overnight at 1:200 dilution to label the nuclei. Invasive T98G spheroids were imaged using a LSM 710, AxioObserver (Carl Zeiss, Germany) confocal microscope in 10x and 40x magnification scanned at 543nm, 488nm and 640nm.

Image segmentation and analysis

Spheroids were monitored using a Leica DFC310 FX inverse wide-field fluorescence microscope (Leica, Germany) over a total period of up to 12 days and photographed every 24h, using a 4x objective lens and fixed acquisition parameters. The brightfield images were semi-automatically segmented in Matlab 6.1 (The MathWorks Inc., Natick, MA, USA).

Tumor expansion kinetics were evaluated based on: i) the time evolution of the tumor spheroid core, and ii) time evolution of the overall invasive rim [198]. The whole invasive area was measured by estimating the maximum radius taken from the core center that encloses all the invasive cells. To

---

[11] DMEM/F12 Medium is a 1:1 synthetic mixture of DMEM and Ham's F-12 Medium; rich and complex, containing all 21 amino acids, 10 vitamins, glucose, zinc, and iron among other components. Together, it combines the high amount of glucose, amino acids and vitamins of DMEM, and the diversified components of F-12.

estimate the invasive rim, the radius of the core maternal spheroid was subtracted from the whole invasive radius. The invasive kinetic profile was quantitatively generated by statistically analysing all results over time with regression analysis of mean values±standard deviation.

4.1.2 Mathematical approach

In this work, we build on the HDC model originally proposed by Anderson [112], but modify several aspects. Specifically, in order to focus on cell-to-cell adhesion, we consider the ECM to be a homogeneous passive scaffold where cells are allowed to migrate, but matrix degradation and remodeling are not considered. In our HDC approach, the phenotypic properties of the tumor cells include proliferation, motility, cell-to-cell adhesion, oxygen consumption and death.

We assume that cell properties are intrinsic properties that are not regulated by the microenvironment. We account for heterogeneous cell populations, which differ only with respect to cell-to-cell adhesion properties. The rest phenotypic properties of the cells are kept the same for all cells, unless otherwise stated. The cell adhesive property is applied during cell movement and generalizes the attractive rule used in Aubert et al. [114]. Specifically, this property describes a cell's preference to bind with a variable number of other cells in its new position. Thus, cells select their preferred neighborhood as they move. Cells with low cell-to-cell adhesive properties prefer empty neighborhoods, whereas cells with high adhesive properties are attracted towards highly populated areas. Cell movement approximates a random walk in a 2D regular lattice, but it is biased towards the adhesion preference of the cell. If explicitly stated, inspired by its mutative biological counterpart, we additionally introduced an intrinsic state transition probability where cells are allowed to stochastically switch phenotype regarding cell-to-cell adhesion only during proliferation and with probability p_{mut}. Otherwise it is assumed that the adhesive property is inherited by the daughter cells during proliferation and it is fixed throughout tumour evolution. We assumed oxygen to be the only limiting source needed by the tumor cells to grow.

The mathematical model used is the same as in chapter 3 and in [80, 199], yet a more detailed description of the methodological approach follows.

Computational domain

We assume that each $h \times h$ lattice site fits a single cell, as previously described, yet of fixed cell size equal to h=20μm.

Cell death

Lack of oxygen triggers cell death. The spatiotemporal evolution of oxygen (*o*) is described in the PDE (1). Tumor cells die if the local oxygen concentration drops bellow o_{deadly}. Dead cells are essentially treated as empty space.

Cell proliferation

The proliferation age of the tumor cells was approximated by the relevant doubling time in the biological experiments (see chapter 3). To proliferate, cells must find empty space for their daughter cells. Otherwise, the cell enters a quiescent state while it keeps searching for empty space. If a quiescent cell finds an empty space, it immediately proliferates. The neighborhood chosen for the proliferation was the Moore neighborhood of size r equal to 2 (for more details also see [80]).

Cell movement

In general, tumor cell motility involves highly complex mechanisms, yet for simplicity and in an attempt to focus on cell adhesion, we only assumed random, diffusive movement and accounted for cell-to-cell adhesion forces. Cells are allowed to move towards empty neighboring locations in the Moore neighborhood. The diffusion equation (2) is discretized to movement probabilities for each individual cell as has been described in [177]. In

$$\frac{\partial c}{\partial t} = D_c \nabla^2 c \ (2)$$

c and D_c denote the cancer cells concentration and their diffusion coefficient, respectively.

The mechanism of adhesion preference is formulated as follows: a cell will only move to empty adjacent locations with neighbors equal to its adhesion preference, which can vary between 0 (non-populated area) and 7 (highly populated area). Schematically, cell movement under the inclusion of cell adhesion preference is shown in Figure 20.
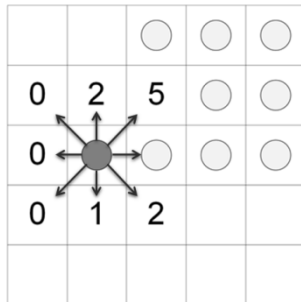
Figure 20. Cell movement depending on adhesion preference. Circles represent cancer cells. The dark grey circle depicts the cancer cell, under investigation. The numbers depict the occupation of each neighborhood, excluding the cell under study. The numbers can thus take values between 0 (non-populated area) and 7 (highly populated area). Cells move to empty sites depending on their adhesion preference. Thus, if for example the cancer cell under study has adhesion preference equal to 0, then it will move left randomly selecting one of the three possible positions.

Description of phenotypes

Phenotypes with different adhesion preferences were allowed to coexist and interact within the tumor. The different phenotypes are referred based on their preference adhesion value. A phenotype with low adhesion value corresponds to a cell with loose cell-to-cell adhesive interactions that prefers to be alone, while a phenotype with high adhesive value implies that a cell forms strong adhesive interactions, attracted by high populated neighborhoods. We categorize our phenotypes as follows:

we call phenotypes with adhesion preference 0 and 1, low adhesive; phenotypes with preference 6 and 7, highly adhesive; and those with adhesion preference in [2, 5], middle adhesive phenotypes.

4.2 Results

The invasion of the well-described **U87MG** and **T98G**, as well as of three primary **GB** cell lines was studied in this work. In the 3D invasion assay, cell migration was fully **ECM**-dependent since no invasion was observed in its absence. Spheroids were monitored over a total period of 12 days and the invasive patterns formed were consistently observed in all the experiments per cell type.

4.2.1 Invasive pattern of U87MG cells over time

Figure 21 presents consecutive brightfield images of a representative **U87MG** spheroid undergoing invasion within a 24-hour time interval (excluding the last two images, t216 and t288). As shown in Figure 21, **U87MG** cells exhibited an immediate invasive phenotype within the first 24h after seeding. They extended symmetrically from the core maternal spheroid towards the periphery within the **ECM**-like substrate following a non-cohesive migration pattern. In accordance with relevant studies [157, 195, 200], random prolonged cellular protrusions were also observed; yet no noticeable cell path track in the **ECM** was detected in the brightfield images. This type of outgrowth behaviour continues until approximately 72h with slight variation. After 96h, the most distant cells had reached the boundaries of the well. In line with previous reports [200], at this time, satellite cell clusters were also starting to form, and invasion adopted a more complex dynamic behavior. Interestingly, after 288h of allowed invasive condition with no nutritional exhaustion, the surrounding aggregates seemed to deform, whilst the maternal spheroid, that had remarkably grown, had no more defined borders, while all peripheral cells were prolonged.
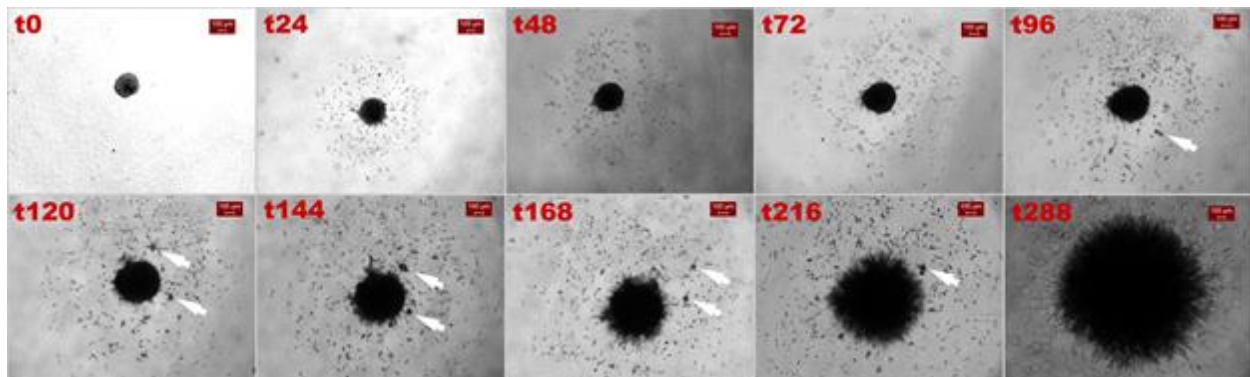

Figure 21. Invasion of the U87MG spheroids over time. Brightfield images at a 4x magnification and scalebar is set at 100μm. White arrows indicate cell aggregates.

Figure 22 shows the temporal evolution of the average values of the core and invasive radii from all the experiments for the **U87MG** spheroids based on the segmented brightfield images. The time evolution of the negative control experiments is also depicted. Considering that after 96h, the most

distant invasive cells of the U87MG spheroids reach the boundaries of the well, we focus on this time period.

The invasive radius of the U87MG spheroids showed a rapid expansion the first 24h that slowed down at later times. The opposite behaviour is observed for the core radius which evolves slower than the invasive radius. After the first 24h, the mean expansion speed equals to 9µm/h for the U87MG cells. The expansion speed the first 24h is estimated equal to 32.7µm/h for the U87MG cells.
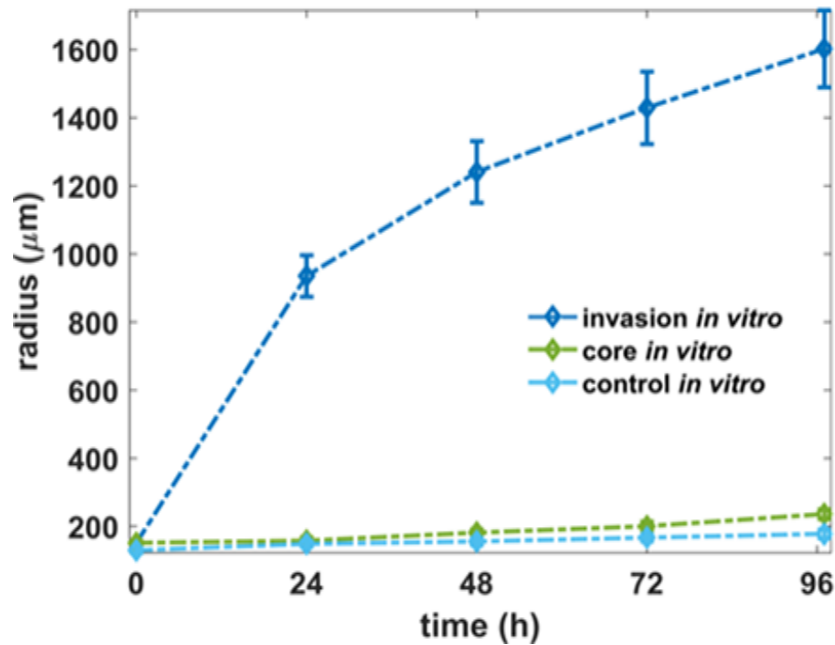

Figure 22. Time evolution of tumour core and invasive radii for the U87MG spheroids with and without the invasive condition. The radii from twenty spheroids per timepoint were analysed with regression analysis. The error bars denote the standard deviation.

4.2.2 Invasive pattern of T98G cells over time

In Figure 23, T98G spheroidal growth expansion from two indicative spheroids is presented over time with and without the invasive condition. The respective spatiotemporal evolution curves are depicted in Figure 24. After day 8, the invasive T98G spheroids reach a plateau, which can be attributed to the fact that the invasive cells extend up to the borders of the well. A radial, non-symmetric invasion is observed. Under the invasion-blocked condition, the T98G spheroids evolve similarly to the core of the invasive spheroids over time. This might be indicative of a proliferation-associated invasion.
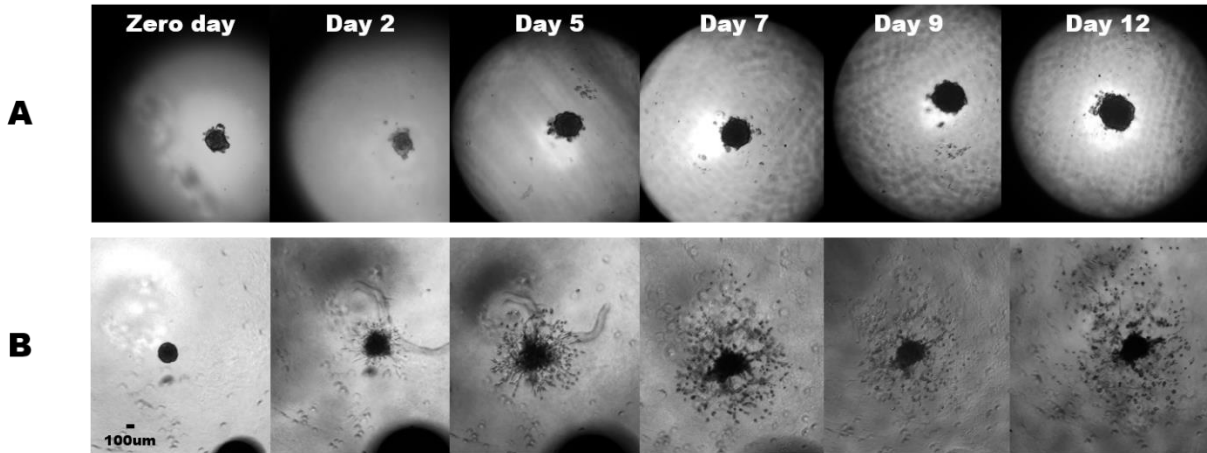
Figure 23. T98G spheroids over time without (A) and with (B) the ECM-like substrate. Brightfield images at 4x magnification. Scalebar is set at 100um.
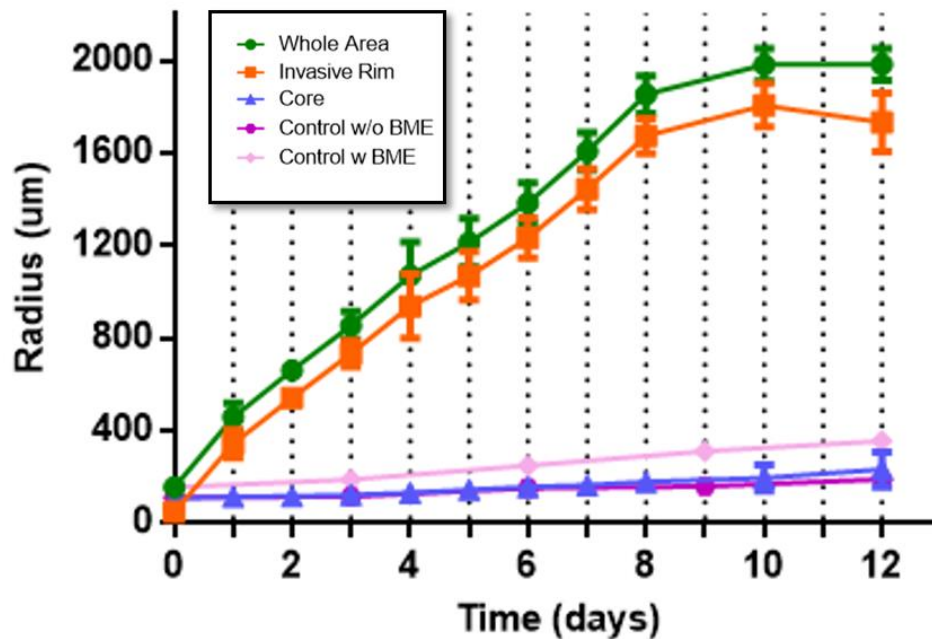
Figure 24. The spatiotemporal evolution of the invasive (whole area, invasive rim and core) and the control T98G spheroids.

4.2.3 Invasive pattern of primary cells over time

<u>GBP03</u>

Primary GBP03-P1 spheroids adopted an apparently alternative, cohesive invasive morphology with boundary instabilities, not reported before in relevant studies [49, 158, 183, 196, 201]. Figure 25 illustrates the evolution of the invasion pattern of a representative primary spheroid. The same invasive pattern was consistently observed in all primary GB spheroids of the same patient that we tested. Initially, few invasive cells seem to asymmetrically exit away from the maternal core spheroid towards the periphery. At intermediate time points, the invading cells appear to collectively form a cohesive, sheet-like structure (as described in [183]). Finally, in the following time points until 288h, the invasive pattern appears unaltered, but still enhanced.
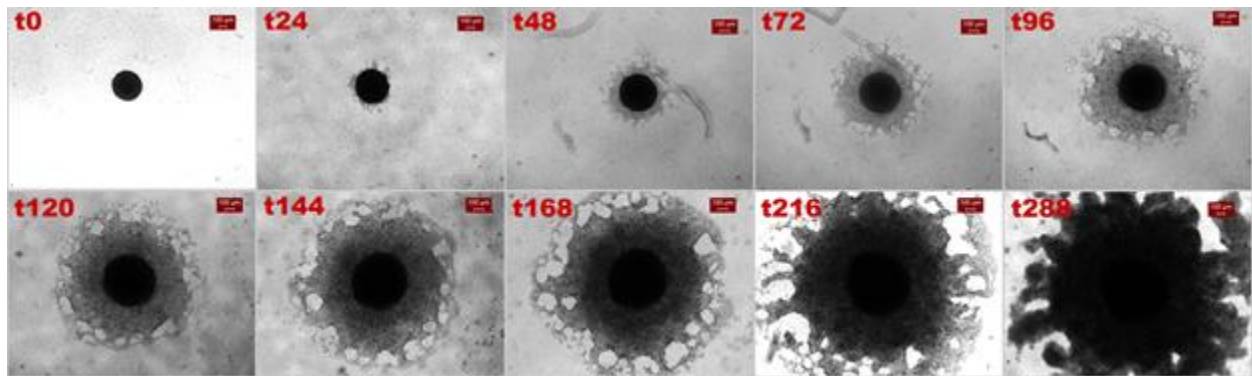
Figure 25. Invasion of the primary GB spheroids over time. Brightfield images at a 4x magnification and scalebar is set at 100µm.

The temporal evolution of the average values of the core and invasive radii, as well as of the negative control, from all the experiments for the primary GBP03 spheroids based on the segmented brightfield images is depicted in Figure 26. We focus on the first 96h for comparative reasons with the U87MG cells.

The invasive radius of the primary spheroids displayed a slow expansion during the first 24h that was followed by a faster linear expansion. Various mechanisms can affect the motility of the GB cells *in vitro* including stress as the cells are transferred to an invasion matrix [157] and ECM production by the tumor cells [47], which dynamically alter their kinetics. Although interesting, the exact underlying molecular mechanisms involved in motility regulation are beyond the scope of the present study. In both the U87MG and the primary spheroids, the core radius evolves slower than the invasive radius. After the first 24h, the GBP03 mean expansion speed equals to 7.1µm/h. Nevertheless, in the first 24h the expansion speed is considerably different between the GBP03 and the U87MG and estimated equal to 1.7 and 32.7 µm/h, respectively.
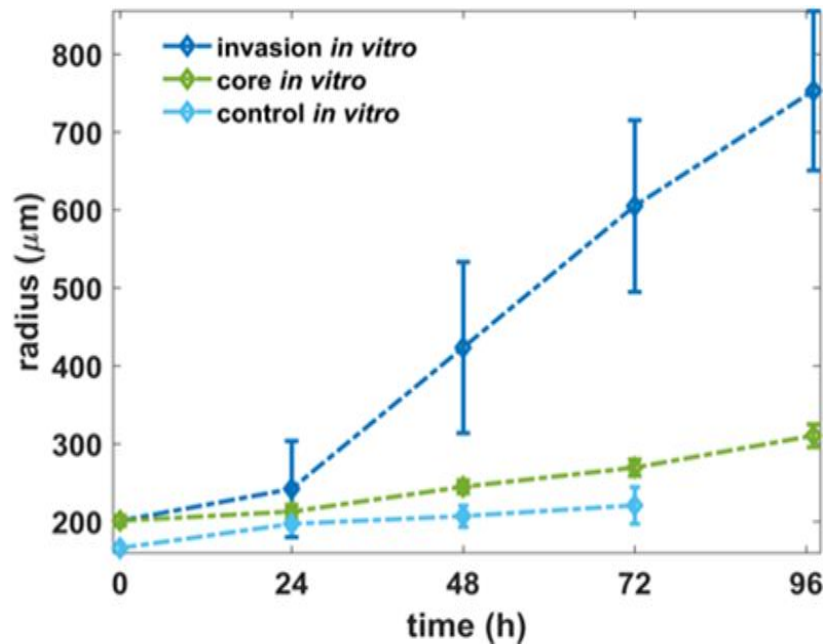
Figure 26. Time evolution of tumour core and invasive radii for GBP03-P1 spheroids with and without the invasive condition. The radii from twenty spheroids per timepoint were analysed with regression analysis. The error bars denote the standard deviation.

GBP06

The invasive phenotype that was observed in the GBP06-P0 cells following the same invasion assay was similar to that of the GBP03-P1, but of different dynamics. In general, as it can be seen in Figure 27, the GBP06 spheroids were less expansive over time.
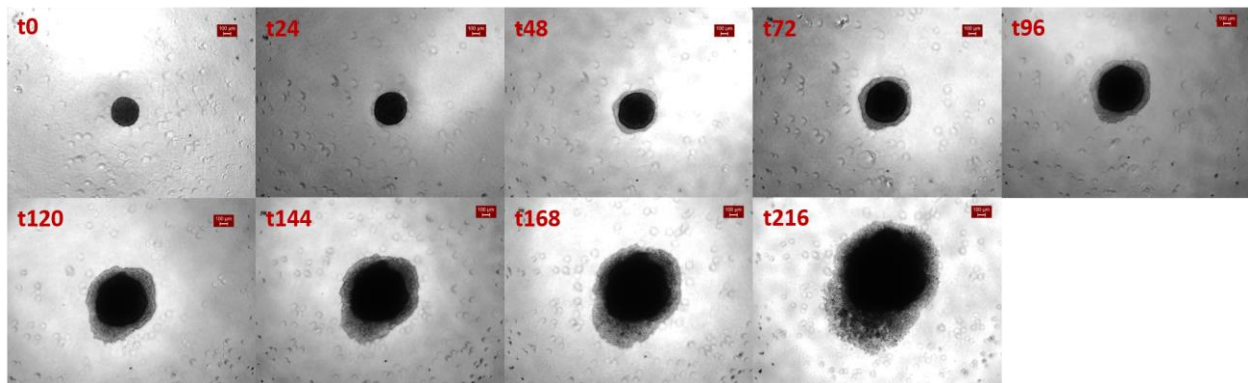
Figure 27. The invasive morphology adopted by the GBP06-P0 spheroids under the same experimental setup. Photomicrographs are brightfield images at a 4x magnification and scalebar is set at 100 microns.

GBP08

As with the GBP03 and the GBP06, also the GBP08-P0 cells appear to collectively and cohesively invade the surrounding ECM-like substrate under the same experimental setup (see Figure 28). Interestingly, as it can also be shown in Figure 29, the initial delay was replaced by a highly expansive phenotype over time after 72h of free invasion.
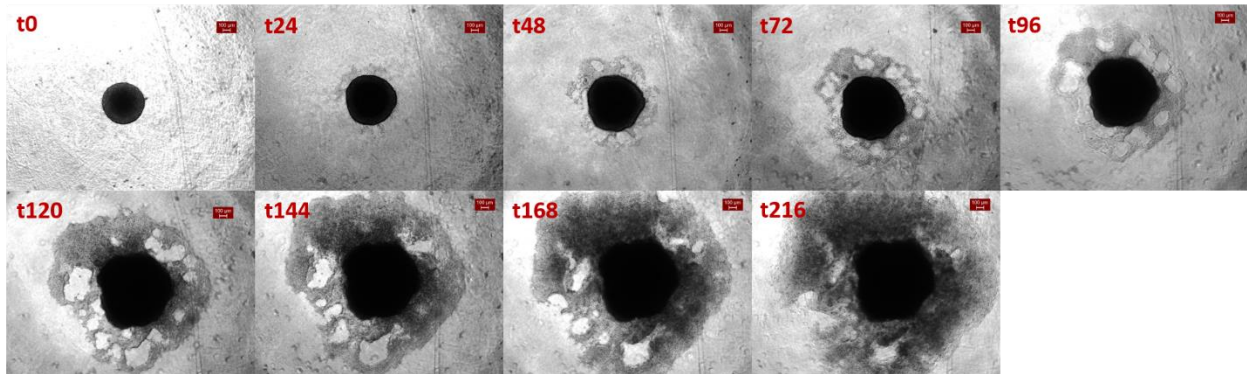

Figure 28. The invasive morphology adopted by the GBP08-P0 spheroids under the same experimental setup. Photomicrographs are brightfield images at a 4x magnification and scalebar is set at 100 microns.
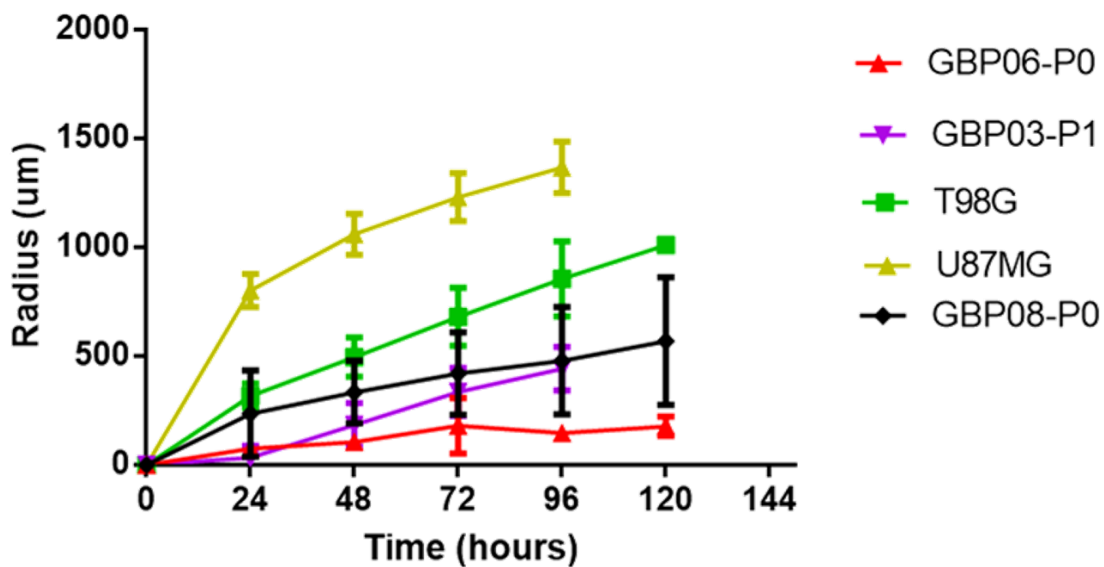

Figure 29. The invasive growth dynamics of all the GB cell lines tested. The radius of the invasive rim is plotted over time.

4.2.4 *In silico* experiments

We further on investigated the invasive profiles of the U87MG and the GBP03 spheroids with the HDC model.

The *in silico* tumor was initialized to a size close to the initial tumor size of the biological experiment and grew for 9 days unless a cell reached the edge of the computational domain within a proximity of 5 cells. Thus, a disc of size approximately 140μm in radius for the U87MG and of 200μm for the primary cells located in the center of the computational domain was initially assumed completely filled with cancer cells. The simulations were repeated 50 times for each cell line. Variation in the computational results derived from the randomness in the cellular movement and the arbitrary initialization of cellular phenotypes and cell age. To describe the different invasion patterns observed, we assumed that tumors are composed of phenotypes with different adhesive properties. Specifically, we focus on the temporal evolution of the core and the invasive radii, as well as the local compactness and local sparseness of the tumor.

4.2.4a Different mixture of phenotypes produces different morphologies

A spectrum of different morphologies arises when phenotypes of various cell-to-cell adhesion properties are combined. These morphologies vary from highly compact, where invasion is hardly observed, to cohesive patterns and even to non-cohesive migration patterns, under the same microenvironmental conditions. As expected, highly adhesive phenotypes strongly attract and are attracted by many other cells, thus forming dense and symmetric patterns with limited motility and reduced invasive radius. On the other hand, phenotypes with loose cell-to-cell interactions adopt non-cohesive migration strategies and travel unbiased further away from the maternal spheroid showing decreased compactness and increased invasive expansion and sparseness. Interestingly, the interplay of these phenotypes can produce a variety of different dynamics for the expansion of the core and invasion radii, as well as a variety of morphologies with different overall compactness and sparseness. In this set, all the experiments were performed with fixed proliferation and diffusion rates equal to 31h and $5 \cdot 10^{-9} cm^2/s$, respectively.

4.2.4b Phenotypes of low and high adhesiveness resemble the invasive pattern of the U87MG spheroids

We observed that in order to describe the U87MG cell line, low adhesive phenotypes and highly adhesive phenotypes should be considered. The latter are necessary to describe the maternal immotile core, while the former represent the highly migrating invasive cells. Figure 30a shows the simulated results of the U87MG invasive spheroids at 96h. Few phenotypes of low adhesiveness can also be observed trapped within the core due to spatial competition. The proliferation time was set equal to 31h and the diffusion coefficient was set equal to $D_c = 5 \cdot 10^{-9} cm^2/s$.
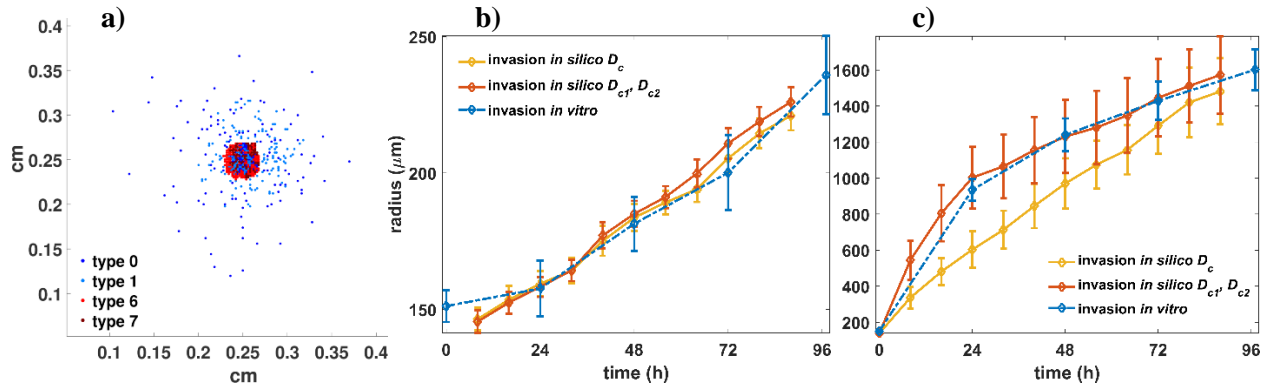
Figure 30. *In silico* predictions of the U87MG cell type: a) snapshot of the simulated U87MG spheroid at 96h (left), b) the temporal evolution of the core radius and c) the invasive radius for both the *in vitro* and *in silico* experiments over time.

4.2.4c Phenotypes of middle and high adhesiveness resemble the invasive pattern of the primary spheroids

To recapitulate the cohesive primary cell line morphology, phenotypes with middle to strong cell-to-cell adhesive interactions were assumed. Low adhesive phenotypes were excluded from this experiment. We should note that alternative combinations of phenotypes may possibly produce similar results, as for example using only the middle adhesive phenotypes. However, in that case the tumor compactness initially decreases and only after a period of time increases forming a compact core. On the contrary, including phenotypes with high adhesion, an almost immediate increase in tumor compactness was observed better resembling the core expansion of the *in vitro* experiments. The diffusion coefficient was set to $D_c = 2 \cdot 10^{-8} cm^2/s$ and the proliferation time was set to $25h$, in accordance to the doubling time estimate. A snapshot at 152h of the tumor evolution is illustrated in Figure 31a. As can be seen in Figure 31b, apart from the trapped cells in the core, we can observe that relatively low adhesive phenotypes (types 2, 3, 4) tend to appear in the tips of the tumor sprouts, while phenotypes with relatively stronger cell-to-cell adhesive interactions (types 5, 6 and 7) are more likely to be found closer to the tumor core. Interestingly, all phenotypes coexist within the tumor, increasing their populations as tumor evolves, with the phenotypes of types 4 and 5 to be systematically present at higher. Moving towards the center, the tumor becomes denser and after approximately 150h necrotic cells start to appear. It is noteworthy that as time passes new gaps are formed, while the gaps already formed between the sprouts gradually close without trapping any of the highly adhesive phenotypes.
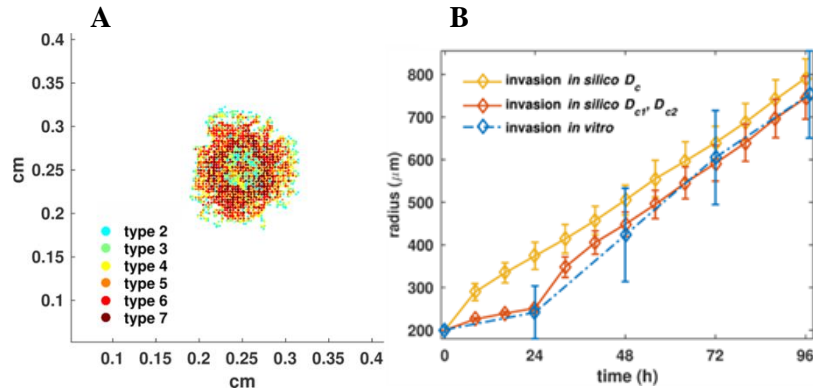
Figure 31. *In silico* predictions of the primary cell type. A snapshot of the simulated primary spheroid at 96h (A) and the temporal evolution of the invasive radius of both the *in vitro* and *in silico* experiments (B) are shown.

4.2.4d Temporal evolution predictions of spheroid expansion

Note that, *in silico,* for the primary GBP03 cell type, we cannot distinguish the core from the invasive area based on the distribution of phenotypes, as we can do for the U87MG spheroids due to their mixed spatial distribution. Thus, for the primary spheroids, we focus only on the temporal evolution of the invasive radius. Furthermore, in order to better approximate the different kinetics observed before and after the first 24h, we assumed two distinct phases in tumor expansion governed by different motility rates in addition to the single motility rates. Specifically for the U87MG spheroids, we set the diffusion coefficient in the time period [0, 24]h equal to $D_{c1} = 1.5 \cdot 10^{-8} \ cm^2/s$ and for the rest period equal to $D_{c2} = 3 \cdot 10^{-9} \ cm^2/s.$ On the other hand, for the primary GB cell line we assumed $D_{c1} = 4 \cdot 10^{-10} cm^2/s$ and $D_{c2} = 4 \cdot 10^{-8} cm^2/s$. The temporal evolution of the expansion for both the U87MG and the primary spheroids is shown in Figure 30 and Figure 31, respectively. The relative *in vitro* observations are also shown for direct comparison. By allowing different motility rates at the different growth phases the *in vitro* and the *in silico* curves converge for both cell types.

4.2.4e The role of proliferation and motility rates

Variation in proliferation time and diffusion coefficient affects overall tumor growth and morphology. Specifically, for the U87MG simulations, increased proliferation rate substantially affects the cell population, increases the expansion rate of the core and also affects the expansion rate of the invasive radius. On the other hand, increased motility rate considerably increases the invasive radius, but only slightly affects the expansion of the core and the cell population. Note that counterintuitively, increasing the proliferation of the U87MG cell type results in decrease of the overall compactness and increase of the sparseness after a time period. Due to the significantly less space competition, the outgrowth of the invasive cells is favored relative to the growth of the core cells.

Notably, for the primary spheroids, proliferation strongly affects the expansion of the invasive radius, as well as the cell population. Increased proliferation also results in more smooth and round tumors

increasing tumor compactness and reducing sparseness. Similarly, increasing the motility rate of the primary cells results in increase of both the invasive radius and the cell population as it allows more free space for cell growth and motility. Increase in motility rate considerably decreases the compactness of the spheroid and increases sparseness.

Interestingly, variations in proliferation and motility rates also alter the relative frequency of phenotypes. Overall, for the primary GB spheroids, we observed that by either increasing the motility of the cells or decreasing their proliferation, less compact tumors are formed allowing more free space for the middle adhesive phenotypes to relatively increase their population. We should note however, that by selectively inhibiting the proliferation of the middle adhesive phenotypes, the highly adhesive phenotypes dominate in the population forming fully compact tumors.

4.2.4f Phenotypic switch

An intrinsic state transition probability of tumor cells was introduced to allow them to stochastically change phenotype during mitosis with probability equal to 0.5. For the simulations regarding the U87MG cells, we assume four possible phenotypes with adhesive values 0, 1, 6 and 7 (low and highly adhesive). All transitions among these phenotypes are possible and are equally likely. For the simulations of the primary cells, we assume six possible phenotypes (middle and highly adhesive) with adhesive values 2, 3, 4, 5, 6 and 7. Again, each phenotype has an equal probability of being selected. The new phenotype was randomly chosen and applied to both daughter cells.

The result of this phenotypic switch was that now the self-organization of cells reflected in the diverse frequency of each phenotype as tumor evolves is not evident and all phenotypes involved have equal representation in the population. Regarding the U87MG cell type in particular, although slight changes were observed in the tumor expansion, interestingly, cell aggregates peripherally to the maternal spheroid similar to those appearing at the later stages of U87MG spheroids invasion (Figure 21) were also observed. Regarding the primary GB spheroids, we observed that an equal contribution of all phenotypes in the tumor composition introduces an eventual decrease of the overall cell population and tumor expansion and prompts the formation of a denser tumor similar to the morphology observed after 120h in the respective biological experiment (Figure 25). Thus, allowing random phenotype transition in both cases could possibly predict the morphologies observed at later time points, although alternative mechanisms triggered by the evolving tumor microenvironment and not necessary requiring mitosis could account for these morphologies, too. Even more, a microenvironmental regulated phenotypic switch could also be a potential mechanism explaining the evolution of the invasion pattern.

4.2.5 Imaging the physiology of invasion

Both the computational modeling results and the experimental observations of the T98G (not only) invasive spheroids indicated the importance of at least two major factors during invasion; proliferation and cell-to-cell adhesion. To qualitatively validate our above hypothesis, as well as earlier studies [202, 203] proposing a connection between proliferation and invasion, we assessed the distribution and topology of physiologic fluorescent markers. More specifically, Figure 32 depicts

the maximum intensity projection of a T98G spheroid after 24h of free invasion. The PKH26 signal intensity (red) that is inversely correlated to proliferation, indicates that highly proliferative cells populate the outer invasive rim. Additionally, sporadic mitotic cells (blue) are observed (arrows) within the invasive rim. Interestingly, the dividing cells can be also found perpendicularly to the plane of focus. Overall, these are in support of concurrent proliferation and invasion processes. When focusing at the invasive regions, the cytoplasmic GFP expression (green) is indicative of the cellular protrusions and/or cytoskeleton rearrangements formed during invasion. The E-cadherin expressing cells are localized in the regions of cell contact during invasion. These invasive phenotypic features including strands of numerous cells, cell-to-cell discontinuous cohesiveness and sporadic proliferation, resemble the collective cell invasive pattern [183].
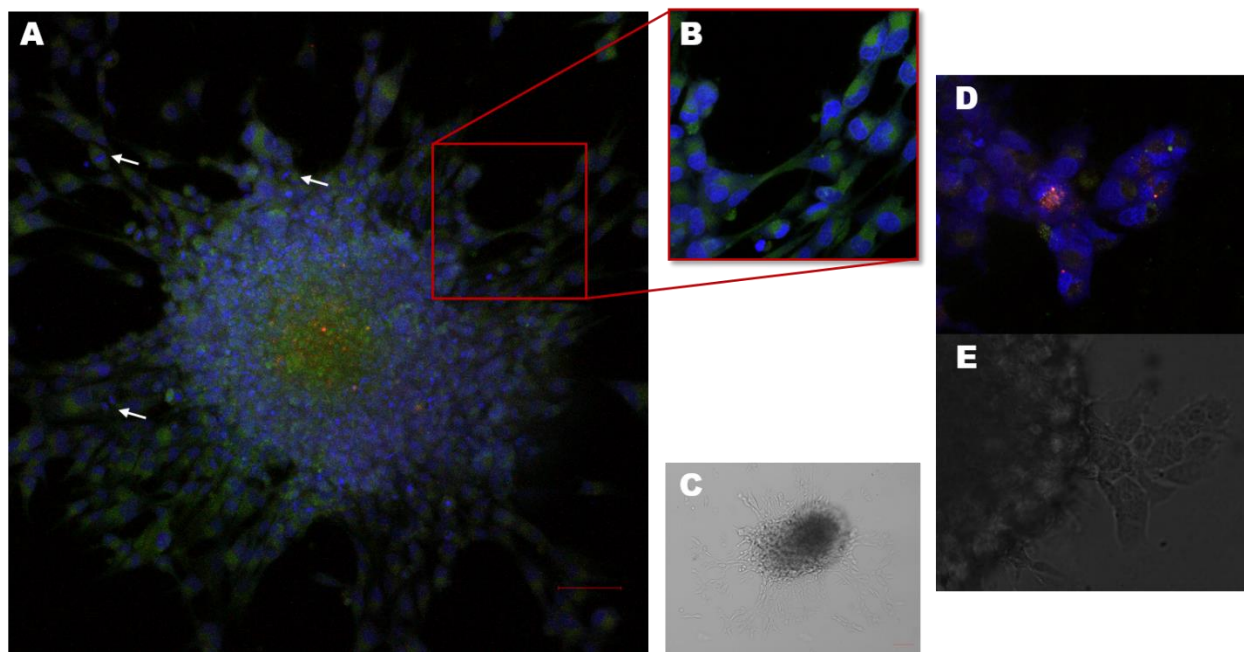

Figure 32. Confocal image of a T98G invasive spheroid after 24h. B. Magnified illustrated invasive region. C. The brightfield image of the invasive spheroid of image A. D.-E. An invasive region in both fluorescent and brightfield images. Cells that are in contact appear to have E-cadherin expression at the adhesive spots. High PKH26 (red) signal intensity indicates low proliferative activity. Nuclei are shown in blue. GFP is shown in green. White arrows depict dividing cells. Scalebar is set at 100μm.

4.3 Discussion

In this work, we explored the invasive potential of GB cells using a rather simple, but yet realistic, set of experimental parameters. We utilized patient-derived cancer cells along with the established and commonly used U87MG and T98G cell lines. GB cells are cultured in 3D in an ECM-like substrate. Our biological experiments show that the two types of tumor spheroids, the primary and the secondary, display considerably distinct invasive patterns suggesting different mechanisms of cell

migration. Surprisingly, none of the primary cell lines developed a similar invasive pattern as of the one expected from the bibliography or observed in both the secondary cell lines. In an attempt to explore possible mechanisms involved, an individual cell-based mathematical approach was adopted to indicate the potential role of the intrinsic heterogeneity with respect to cell-to-cell adhesion on tumor morphology and growth dynamics.

It has to be clarified that the invasive capacity is not necessarily correlated to the aggressiveness of the cell line. Furthermore, not all GB cell cultures expressing the same invasive phenotype evoke the same underlying mechanisms and/or are necessarily genotypically related. Comparative studies between both phenotypic and molecular descriptions should be carried out in cell lines, since several GB molecular subtypes have been classified [20, 76]. For this application, the GBP03 and the U87MG cell lines were chosen.

We implemented the 3D tumor spheroid invasion assay [157, 204] in order to investigate the initial steps of invasion from spheroids formed using single cell suspensions. The main advantage of this assay as compared to standard trans-well assays is that it can recapitulate the basic 3D structure of tumours and replicate features of collective cell invasion observed *in vivo*. In addition, this is a simple, quick and standardized assay that enables analysis of invasion with high reproducibility in a 96-well plate format. However, we should note that monitoring of invasion in the existing 3D spheroid invasion assays relies on brightfield imaging of the spheroid from the bottom of 96-well U-plates, which confines microscopic analysis of 3D spheroids to a 2D plane leading to exclusion of cell clusters invading in the depth dimension.

Based on the *in vitro* invasive protocol followed here, the two GB cell lines used, exhibited a markedly different invasive pattern. In consistence with other studies [157, 195, 201, 204-207], U87MG cells appeared to colonize the ECM via a process indicating non-cohesive, starburst migration. On the other hand, the GB primary spheroids kept expanding to massively conquer the surrounding regions rather than individually migrating potentially governed by homotypic attraction [208]. A unique, collective invasive pattern with morphological instabilities of cohesive protrusions near the boundary resembling perivascular invasion in the brain [49] was observed. It is well recognized that exploring the physiological and molecular patterns of these cells might enable the design of novel therapeutics targeting the recurrence process. The ability to early detect the phenotypic composition of an evolving tumor is undoubtedly of significant prognostic value.

In order to further investigate potential intrinsic mechanisms involved in the invasion patterns observed, an individual-cell-based computational model accounting for intra-tumoral heterogeneity was developed. More specifically, different cell-to-cell adhesive properties adopted by the GB cells were assumed, although additional or even alternative mechanisms could also play a role in the observed tumor behaviour. Reher et al. [113] have extensively studied mathematically the role of cell adhesion heterogeneity specifically on cell dissemination opening the question of whether this heterogeneity is present in gliomas and how it affects the migration mechanisms and tumor morphology. In support to our work, recent studies [113, 185-191] have shown differential

expression of cadherins, as well as observable disorganization and instability in cell-to-cell interactions within various GB cell lines. Primary cells most usually overexpress cell adhesion molecules such as integrins or cadherins, whilst common/established cell lines do not [45, 55, 113, 209]. Furthermore, complementing cell-to-cell, cell-to-ECM interactions were also shown computationally to play an important role in tumor invasion with cell-to-cell interactions affecting predominantly the invasion pattern and cell-to-ECM influencing the invasion speed [112, 210]. A variety of mathematical models have been developed to describe the emergence of invasion in cancer cells and GB specifically as summarized in Alfonso et al. [107] yet, to the best of our knowledge, none of these studies focuses on the formation of invasive patterns, by taking into account the interplay of co-existing phenotypes with different cell-to-cell adhesion properties on tumor evolution and morphology. In this work, tumor expansion and morphology were explored and compared with the *in vitro* experimental data. Tumor expansion was quantitatively evaluated based on the temporal growth of the tumor spheroid core and the invasive radii. In general, tumor expansion is attributed to both the proliferative and migratory capacity of tumour cells. Thus, their role on tumor morphology and evolution was also investigated under the proposed framework.

Interestingly, we showed that by selecting (during model initialization) phenotypes with different cell-to-cell adhesion preference to coexist within the tumor is sufficient to resemble the distinct invasion patterns and the expansion rates we observed *in vitro* between the primary and the U87MG cells. We also observed that variation in proliferation time and diffusion coefficient affects overall the tumor compactness, sparseness as well as the tumor expansion rates and changes the relative frequency of phenotypes according to cell type indicating potential mechanisms that could alter tumor evolution and inhibit invasion. Forcing a strong dependence between adhesiveness and proliferation to mimic a potential "go-or-grow" mechanism, we observed that although for the U87MG cells such hypothesis could possibly apply, proliferation plays a more complex and important role for the primary cells under the specific modelling assumptions. Interestingly, we also observed that by allowing cells to randomly switch phenotypes throughout tumor evolution, the self-organization of cells reflected in the diverse frequency of each phenotype was lost and all phenotypes involved have equal representation in the population with an impact on the evolution of the primary cell type. More specifically, in the primary tumors, we observed that by disabling the phenotypic switch, both the total tumor population and expansion increased indicating that random phenotypic switch with respect to cell-to-cell adhesion does not favor tumor evolution.

It has to be noted that though the main aim of this work was to describe the different invasive morphologies experimentally observed, hypotheses of environmentally-triggered motility such as the "go-or-grow" [211] and/or hypoxia-driven migration [212, 213] regarding the proliferation to migration and/or adaptation to cell death switch would be interesting to be included in our future work in order to explore their role in tumor morphology and dynamics. Additionally, it would be also interesting to extend our proposed mathematical model in 3D and explore whether and to what extend the observed morphologies are affected, although the work of Anderson [214] has shown very similar invasive patterns between the 2D and 3D implementation of his model. On top of that,

the effect of a more realistic description of the motility in a lattice-free framework that does not limit the possible directions of cell movement [132] would be also of interest.

GB cells have been shown to exhibit a different invasive phenotype among different ECM components [64, 215], mainly regarding collagen type [216, 217] and rigidity/stiffness [31, 218, 219]. In addition, GB spheroids are also able to self-produce ECM [164] (see also APPENDIX Figure 44), while ECM deposition dynamically changes over time, a fact that should also be taken into account in our future investigations. Use of time-lapse cell migration monitoring will be of importance to verify the direction and velocity of cell movement, as well as the sprouting development. In future studies, more advanced imaging modalities should also be employed, such as light-sheet fluorescence microscopy (LSFM) or multispectral optoacoustic imaging (MSOT), which offer superior resolution at the sub-cellular level [145]. The preliminary results of the physiologic markers we show regarding both proliferation and cell-to-cell adhesion using confocal-imaged T98G invasive spheroids are in this direction. The confocal imaging invasion assay was proved easier to be applied in the T98G spheroids. Yet, a comparative study between all GB invasive spheroids should be formed and extrapolated to further molecular markers. In combination with optical reporters of cell physiology, i.e. apoptosis, cell junctions, cell division, neural markers, etc., it will be of great benefit to further dissect the GB invasion properties and even better approximate the cellularity within a given tumor volume. Another technique that could be beneficial as a measure of compactness of the spheroids could be the immunohistopathological examination of permanently fixed spheroids, where specific markers of cellularity are available. On top of that, more advanced hybrid spheroid 3D invasion assays such as co-cultures with organotypic brain slices [220] (see also APPENDIX Figure 45) and microfluidic platforms [221, 222] are still under development and could be used to better recapitulate *in vivo* conditions accounting for interactions among different cells, shear forces and vasculature.

5. Pre-clinical *in vitro* and *in silico* drug screening

> The Temozolomide-Doxorubicin therapeutic paradox is targeted. An *in vitro* drug screening protocol is proposed combining 2D and 3D experiments with LSFM imaging to monitor the drug-induced impact on the primary GB cells. A potential computational approach is assumed.

Adjuvant Temozolomide (TMZ) chemotherapy is considered the front line GB treatment along with maximal safe surgical resection and radiotherapy. Prognosis remains poor mainly because of the high inter- and intra-tumoral heterogeneity and post-surgery relapse. GB recent trends in preclinical [223-226] and clinical [227-229] trials usually refer to Doxorubicin (DOX); a well-known (breast) cancer chemotherapeutic which is also approved from the FDA (Food and Drug Administration). For example, as depicted in Figure 33, there are currently at least four clinical trials worldwide recruiting GB eligible patients to test DOX-derivatives and DOX-excipients either as a monotherapy or adjuvantly.

Status	Study Title	Conditions	Interventions	Locations
Recruiting	Prolonged Exposure to **Doxorubicin** in Patients With **Glioblastoma** Multiforme and Diffuse Intrinsic Pontine Glioma	• **Glioblastoma** (GBM) • DIPG • Brainstem Glioma, Pediatric • (and 5 more...)	• Drug: **Doxorubicin**	• Meyer Children's Hospital Florence, Italy
Not yet recruiting	**Doxorubicin**-loaded Anti-EGFR-immunoliposomes (C225-ILs-dox) in High-grade Gliomas	• **Glioblastoma**	• Drug: C225-ILs-dox	
Recruiting	A Study to Evaluate the Safety, Tolerability and Immunogenicity of EGFR(V)-EDV-Dox in Subjects With Recurrent **Glioblastoma** Multiforme (GBM)	• **Glioblastoma** • Astrocytoma, Grade IV	• Drug: EGFR(V)-EDV-Dox	• John Hopkins Hospital Baltimore, Maryland, United States • Lenox Hill Hospital, Northwell Health New York, New York, United States
Recruiting	Using MRI-Guided Laser Heat Ablation to Induce Disruption of the Peritumoral Blood Brain Barrier to Enhance Delivery and Efficacy of Treatment of Pediatric Brain Tumors	• Glioma • Pilocytic Astrocytoma • Anaplastic Astrocytoma • (and 6 more...)	• Device: MRI-guided laser ablation • Drug: **Doxorubicin** • Drug: Etoposide • (and 2 more...)	• Washington University School of Medicine Saint Louis, Missouri, United States

Figure 33. List of current GB clinical trials involving DOX worldwide. Provided by the clinicaltrials.gov.

Taken for granted the sonorous impact of the two drugs in chemotherapy and GB's symptoms restraint necessity, the research regarding possible alternatives in the therapeutic schemes proposed is evident. Apart from the novel idea to administrate an old chemotherapeutic of wide applicability, the few relevant studies that exist aim at either the explanation of the DOX mechanism of action and toxicity to the GB cells [223, 226], the combined TMZ-DOX treatment option [223, 229] or the DOX drug delivery potentials within the brain [225, 226, 230] and the GB cells [231]. It has to be clarified that there is also recent literature concerning the *in vivo* combination of the two drugs,

yet in cancer types other than GB [232-234]. As regards the *in silico* approximation of a TMZ-DOX combination there is none to our knowledge. Nevertheless, there are computational works for the population dynamics and treatment responses based on biological data dedicated to the simulation of other drug combinations applied in GB progress, such as the use of co-treatment TRAIL (tumor necrosis factor TNF-related apoptosis-inducing ligand)-TMZ therapy in order to predict induced cell death [235] or to other cancer types as well, such as drug response prediction in breast cancer depending on dosage [175] or the combination of an inhibitor of proliferative endothelial cells and a cytotoxic drug for the proliferative tumor cells [103]. There is a variety of TMZ simulations concerning the drug efficacy prediction in GB patients based on (follow up) imaging data [236, 237]. On the other hand, there are many DOX-related bioengineering references related to the DOX-induced senescence in the cancer cell population and the effective dosage in treatment planning [175, 178]. In order to better-understand the explanations proposed, it is crucial to describe the key features of each drug.

TMZ

TMZ is a lipophilic imidazotetrazine derivative of a DNA-alkylating agent (dacarbazine) which was firstly introduced in cancer therapy in the 1970's to target melanoma cancer. Lately, TMZ was advanced to GB and astrocytoma patients [238] and has the trade names Temodar®, Temodal®, Temcad® and others [239]. TMZ is well-distributed in the brain being able to overpass the restrictive BBB with a bioavailability of 98% when orally administrated [240]. It has to be noted that the brain tumor-to-plasma TMZ-disposition is most usually higher than the brain-to-plasma one since the BBB permeability of the diseased brain tissue is higher and therefore, the lipophilic TMZ is supposed to be better-delivered through the compromised BBB towards the tumor lesion [241]. TMZ is a small prodrug (see Figure 34) that is rapidly hydrolyzed to its short-lived active metabolite (MTIC[12]) at physiologic pH, with no need for an enzymatic reaction [238]. MTIC is further on metabolized to react with the DNA. The well-described molecular mechanism of TMZ can be summarized as blocking the cell division process by disrupting the DNA replication and subsequent G2/M cell cycle arrest accompanied or not by cell death. Half of the TMZ-treated GB patients do not positively respond in treatment [239], yet to date, no other chemotherapeutic against GB has been reported to be more effectual. In TMZ-sensitive GB cells, the MTIC's active compound most usually adds a methyl group in the purine DNA bases; N^7 (70%) or O^6 (9%) positions of the guanine residues resulting in the incorporation of a thymine residue opposite to the methylguanine or N^3 (6%) position

---

[12] TMZ is hydrolyzed in physiologic pH within the cell and gives its active compound, MTIC or 3-methyl-(triazen-1-yl) imidazole-4-carboxamide. Followingly, MTIC prevents cell division by disrupting normal DNA replication. MTIC rapidly degrades to 5-aminoimidazole-4-carboxamide (AIC) and methyldiazonium ion which is an active alkylating species. This species produces methyl adducts at the accessible nucleophilic atoms in DNA.

of the adenine residue followed by the eventual activation of the mismatch repair mechanism up to apoptosis depending on the DNA damage extent [238, 239]. TMZ response may also vary between senescence (G0 phase option) which is the most likely to occur, autophagy preceding apoptosis and required to induce senescence or apoptosis, but not necrosis (less than 5% of cell death), all triggered by the single-base lesion methylguanine O^6 residue in a temporal manner [242]. TMZ-resistant cells most usually overexpress the O^6 methyltransferase (MGMT) and other relevant components and/or have limited DNA repair mechanisms so that the tolerance of the treated cells is increased [239]. Especially for the MGMT, it is not only the MGMT protein expression levels that have been correlated to the TMZ response, but also the MGMT promoter which, if hypermethylated, is associated with enhanced TMZ responsiveness both *in vitro* and in clinic [238]. When comparing TMZ-resistant GB cell lines to the parental cell line of which they derived from, both migration and proliferation appear to increase [243]. It has to be noted that the U87MG cell line is bibliographically categorized as TMZ-sensitive, whilst the T98G is supposed to be TMZ-resistant [239]. As regards the bibliographic IC_{50} values, the recommended dosage for the cells varies between 10-1000uM or even more depending on the cell line, the cell culture (2D or 3D) and the cytotoxicity assay used [239], for the animals is 120 mg/kg/day [239] and for the patients is 150-200 mg/m^2 once per day for 5 days every 28 consecutive days [238, 244].

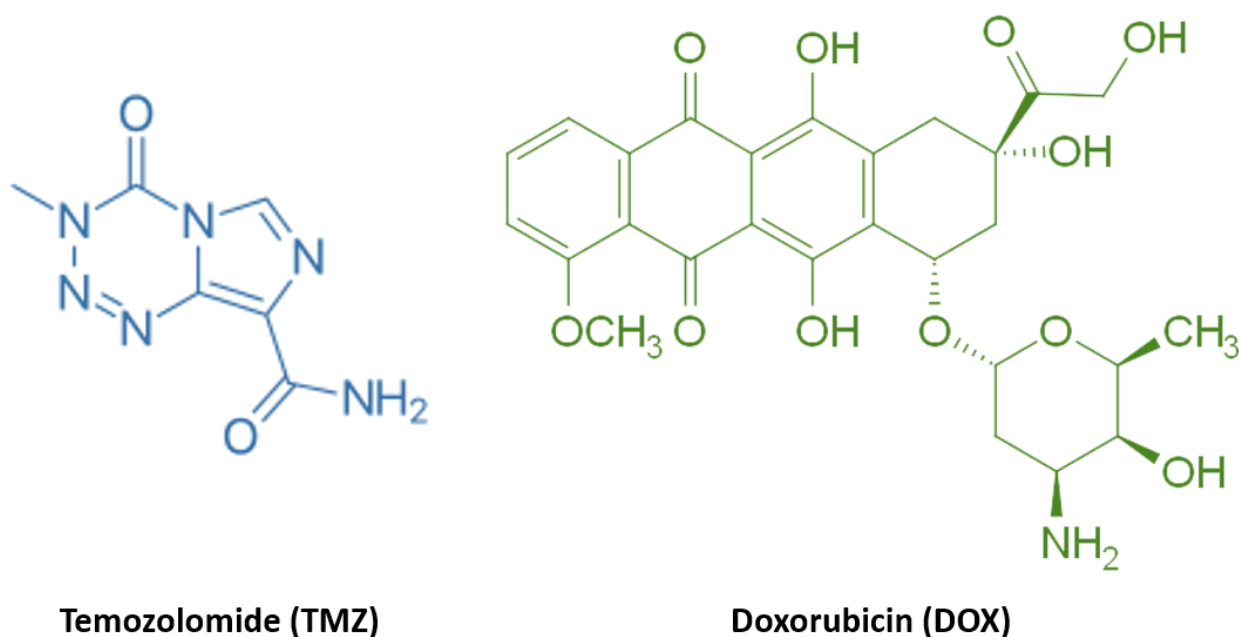**Temozolomide (TMZ)**   **Doxorubicin (DOX)**

Figure 34. Structural formula of TMZ (left) and DOX (right), both FDA-approved chemotherapeutics. TMZ is a small molecule of ~194 Da, whilst DOX in its most common wild type form is a natural product of ~543 Da.

DOX

DOX is one of the oldest chemotherapeutics being reported from the 1970's, routinely used for various cancer types. It is the generic name of the drugs Adriamycin®, Rubex® and others. DOX is cytotoxic, a non-selective class I anthracycline and antitumor antibiotic, extracted from *Streptomyces peucetius var. caesius* [245]. DOX has the major side-effect of cardiotoxicity [226] in means of heart pumping capability and this is why it has to be administrated in lower doses if intravenously injected and there is a lifetime maximum dose depending on the patient. Especially regarding the brain interstitium, DOX is unable to overpass the BBB because of i) high molecular weight, ii) low lipophilicity and iii) the efflux from the CSF (cerebrospinal fluid) due to the p-glycoprotein [226]. The main reason why DOX is not widely used in GB treatment is that in order to achieve adequately effective concentration within the brain via systematic administration, the adverse reaction to avoid congestive heart failure is possible. The maximum recommended cumulative dose for patients is 450-550 mg/m^2 [246]. Interestingly, there is no pill for DOX. On the other hand though, it has been shown that the effective concentration against GB cells is extremely low ~ 10–50 ng/ml [226] or ~ 0.05uM in 2D and 0.17uM in 3D *in vitro* studies [247]. There has been reported pH-related chemoresistance regarding DOX; DOX influx is not facilitated in the common cancerous acidic extracellular pH and DOX efficacy increases in alkaline intracellular pH [248]. DOX is considered a cell cycle-specific chemotherapeutic because it affects only dividing tumor cells. The mechanism of action of DOX is not fully understood. More specifically, it disrupts the DNA repair mediated by the topoisomerase II resulting in a large number of DNA fragments, it itself intercalates genomic and mitochondrial DNA molecules inhibiting transcription and it increases quinone type iron-mediated free radical production which damage the cell structure up to cell death [245]. DOX most usually promotes necrosis of the previously proliferating cells 24h after treatment [249] and even prolonged late effect [250]. As an anthracycline, DOX within the body is characterized by a rapid distribution phase and a slow elimination phase, but the drug's distribution is slow within the tumor since it shows high affinity for the biomolecules. However, there is no need for excessive doses to assess the inner tumor regions since DOX is stored within the cell and re-released after cell death [251] to accumulatively affect neighboring cells. A unique characteristic of DOX is that, unlike other chemodrugs, it has autofluorescence often used to identify interaction with the cancer cells [252].

In this work, the own-established primary GBP08-P0 cell culture was used, together with the well-studied U87MG cell line which served as control. The primary GB cell line is used in order to result in unbiased treatment outcome and better recapitulate the GB heterogenic nature, while the secondary one to standardized the initial drug concentrations and efficacy. 3D spheroids were generated and treated with a range of TMZ and DOX concentrations, based on the IC_{50} values previously estimated in 2D. Optical microscopy was used to monitor the growth pattern for up to approximately 12 days after treatment. Sensitivity to both drugs was observed; DOX in general was found to be effective in less concentrated doses. In order to further discriminate growth inhibition in disabling cell division from eventually leading to cell death, we used LSFM imaging to visualize

the drug penetration and cell death. According to the fluorescent images, DOX was able to accumulatively cause necrosis. On the other hand, in TMZ-treated spheroids, growth-inhibiting effects were observed in a non-consistent dose-response relationship. Our results are in line with variable drug responsiveness of individual GBs. The option of a TMZ-DOX therapeutic scheme to disable proliferation and increase cytotoxicity against GB is indicated. The results can be further used to parametrize and validate our GB predictive computational algorithm to support this hypothesis and simulate possible therapeutic schemes including a metronomic combination of the two drugs. Such a feasibility is presented in the last section.

5.1 Methods

5.1.1 Adherent cultures and drug treatment

Our own-established GBP08-P0 primary GB cell culture was used. The U87MG cell line was used as a control for the 2D experiments to standardize the drug concentrations with bibliographic ones. Cells were cultured in 48-well plates in DMEM++ in standard lab conditions. Twenty four hours after seeding (50000 cells/ml/well) cells were drug-treated and incubated for 72hrs.

5.1.2 Cell viability assay

The MTT (3-[4, 5- dimethylthiazol-2-yl]-2, 5-diphenyl tetrazolium bromide) *in vitro* toxicology assay was carried out as per manufacturer's recommendations (Sigma Aldrich, USA). Absorbance was spectrophotometrically measured at 590nm and the background absorbance was measured at 660nm.

5.1.3 Spheroid generation and drug treatment

An initial single cell suspension solution of approximately 625 GBP08-P0 cells was used to generate the spheroids via the hanging drop technique. The spheroids were grown for up to 23 days and treated with a range of concentrations of the anticancer agents DOX and TMZ from day 4 to day 7 (as in [178])[13], based on the IC_{50} values previously estimated in 2D. From this point onward, half of the medium was replaced with fresh every two days. Every three days, photographs of the growing spheroids were captured in a Leica DFC310 FX inverse wide-field fluorescence microscope (Leica, Germany) using a 4x magnification and standard acquisition parameters in order to monitor the spheroid growth.

5.1.4 LSFM imaging

We employed LSFM imaging to investigate the response of the GB primary spheroids to the front line chemotherapeutic agents, DOX and TMZ, respectively.

---

[13] 10ul of medium were removed of each well and replaced by the appropriate drug solution so that the final dilution (1:5) was conducted within the well. Control spheroids were treated with 1:1000 dimethylsulfoxide (DMSO) solvent, in which all the drugs stock solutions were diluted.

Apparatus description

As illustrated in Figure 35, the custom built **LSFM** is composed of two separate light paths, one for illumination and one for detection that are established on orthogonal axes. For the specimen illumination, a set of continuous wave diode lasers are used. Each laser beam is introduced with the use of a flip mirror in the illumination path, resulting to three separate co-incident and co-aligned beams. The selected laser line is expanded and then directed to a cylindrical lens and between them, an iris diaphragm defining the beam diameter and a vertical slit enhancing the performance of the cylindrical doublet are placed. The laser beam is shaped by the cylindrical lens into a thin plane of light (light sheet) and focused on the corner mirror. After the mirror the formed light sheet is imaged through a 2x telescope to the back focal plane of the illumination objective (Mitutoyo, Plan Apo, 5x/0.14, WD=34.0mm). The detection path is composed of a second microscope objective (Mitutoyo, Plan Apo, 10x/0.28, WD=33.5mm) that is used in order to collect the emitted light and project it through an apochromatic doublet tube lens (ITL200,Thorlabs) on a thermoelectrically cooled, electron multiplying CCD camera (1004x1002 pixels sensor, pixelsize: 8μm) (Ixon DV885, ANDOR Technology). Right after the detection objective, an iris diaphragm is placed in order to alter the numerical aperture (NA) of the detection and thus, control the depth of field. Between the iris and the tube lens a filter wheel is placed with various bandpass emission filters (479/40nm, 512/17nm, 605/70 and 700/40nm) in order to record the desired part of the emitted spectrum as appropriate for each biomarker.
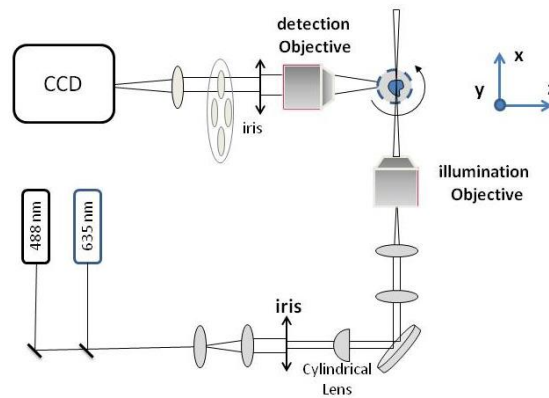

Figure 35. LSFM apparatus

For appropriate imaging results only a very thin region around the focal plane of the specimens has to be illuminated. Moreover, the light sheet has to be established orthogonally to the detection axis with its thinnest part placed in the middle of the field of view. The resolution of the LSFM is defined by the properties of the detection (lateral resolution) and the illumination (axial resolution) axis, respectively. As a result, the resolution is anisotropic. The combination of multiple views of the specimen along different direction can result in almost isotropic resolution similar to the lateral one.

Sample preparation

The sample is placed and stabilized inside fluorinated ethylene propylene (FEP) tubes that contain an index matching aqueous solution of Cygel (Biostatus, UK). FEP tubes were chosen due to their refractive index that is similar to that of water. The tubes are then inserted inside a tank made by antireflection optical glass (Hellma Analytics), filled with warmed water in order to maintain Cygel solidification and stabilization of the spheroid. The specimen is mounted to a sample holder with 4 degrees of freedom. Four motorized software controlled stages (8MT175, 8MR180, Standa) allow the micrometric translation along x, y, and z-axes and rotation around the vertical y-axis.

DOX penetration into the spheroids was determined by direct imaging of its inherent fluorescence. In order to assess the cell viability and death, spheroids were additionally counterstained with the far-red nuclear dye Draq7 (Biostatus, UK) 16-20hrs before loading them to the LSFM microscope.

Imaging Procedure

The spheroids were imaged in our custom LSFM setup using the excitation wavelength at 635nm, while detection was performed with two bandpass emission filters (605/70 and 700/40nm) for DOX and Draq7, respectively. Each spheroid was imaged sequentially at 4 different projections (0°, 90°, 180°, and 270°) of 45-65 optical sections each.

5.1.5 Data analysis

Drug response was evaluated measuring spheroids area reductance as opposed to control untreated spheroids in regular intervals, from day 4 (before the drug treatment) and for up to 14 days at least. Spheroid area was segmented using the ImageJ. The growth curves were analyzed using Prism 5 software (GraphPad Software, Inc., USA) with regression analysis. The dose-response curves were also generated using the formula **%growth inhibition= ((positive control-test value)*100)/ positive control** of the 2D spectroscopic measurements evaluated on day 3 after treatment, where the positive control corresponds to the viable cell population estimate of the untreated cells.

The same formula was used for the surface values of the 3D spheroids for the day 10 after treatment as opposed to the log[c] of the relevant drug concentrations. Positive control corresponds to the surface of the untreated spheroid and test value corresponds to the surface of the treated spheroid under study. The IC_{50} was defined as the drug concentration where half of the cell population and the surface area was inhibited, respectively for the 2D and the 3D assays.

For the LSFM scans, stacks were created for each projection and maximum intensity projections/3D projections were produced using ImageJ. Diametrical projections (0° with 180°, and 90° with 270°) were registered and fused together for all the emission data and finally, the two resulting pairs were combined together in order to achieve the isotropic resolution in all directions.

5.2 Results

The responsiveness in TMZ and DOX of a primary GB cell line was studied in this work using 2D and 3D *in vitro* assays. LSFM-scans of the control and the drug-treated spheroids were used to discriminate the cell death from the growth inhibition effect.

5.2.1 *In vitro* drug responsiveness

Figure 36 depicts the dose-response curves for the 2D and the 3D assays for the case of TMZ (left) and DOX (right). Unlike the DOX-treated cells which appear to have the same dose-related responsiveness in both assays, the TMZ-treated cells revealed a different pattern between the two assays tested. More specifically, a non-consistent dose-response pattern was observed in the 3D experiments.
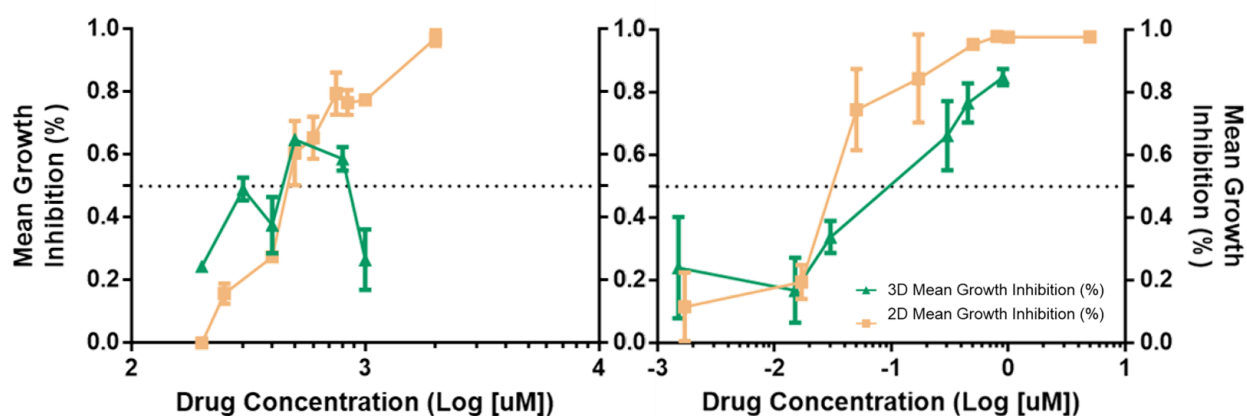
Figure 36. Dose-response curves for the 2D and the 3D experiments regarding TMZ (left) and DOX (right).

Comparing the effective dose regime of the two drugs in the primary GB spheroids, we observed that DOX appeared to be very effective even in three orders of magnitude less than TMZ. In Figure 37, the brightfield images of the respective untreated (control) and treated spheroids with TMZ of 500uM and DOX of 0.9uM are shown. Notice that unlike the TMZ-treated spheroids which have no apparent difference to the control ones, the DOX-treated spheroids have reduced in size and a surrounding pool of dead cells after day 7 indicating a "dying" spheroid. The relevant growth-inhibition curves over time are depicted in Figure 38. Notice the fictitious threshold of DOX concentration at around 0.3uM. Above this concentration threshold we observed that spheroid recovery is not allowed. Additionally, unlike in the 2D experiments, in the 3D experiments three days after DOX treatment there is no obvious response independently to the dosage.
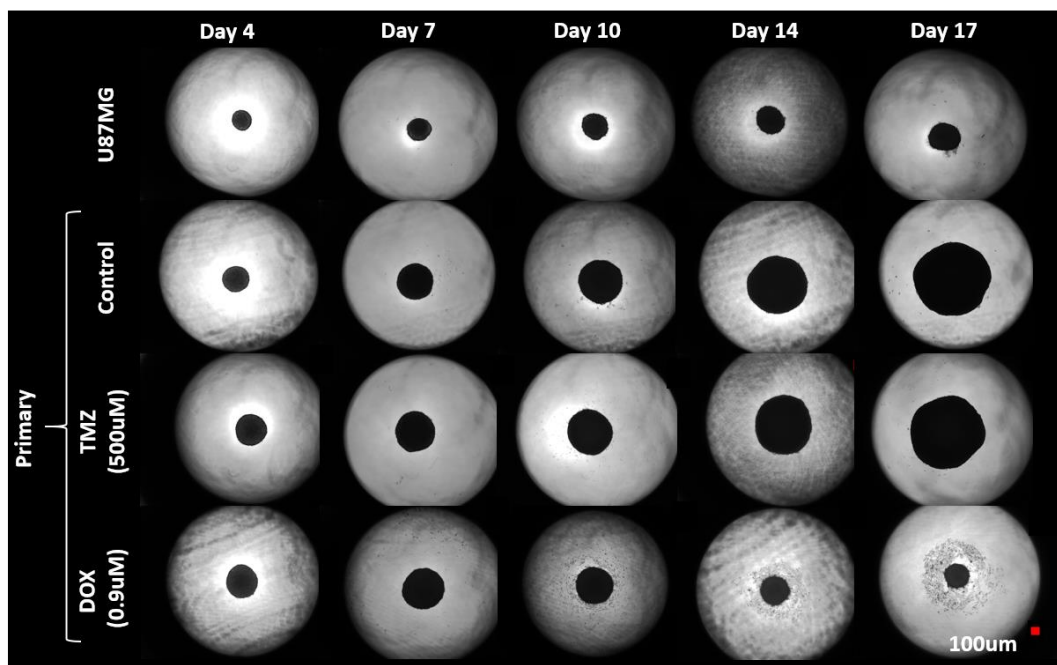
Figure 37. Brightfield images of the control and the drug-treated spheroids over time. The U87MG spheroids are used as a reference cell line. One representative concentration is presented from each drug. Scale bar is set at 100 microns.
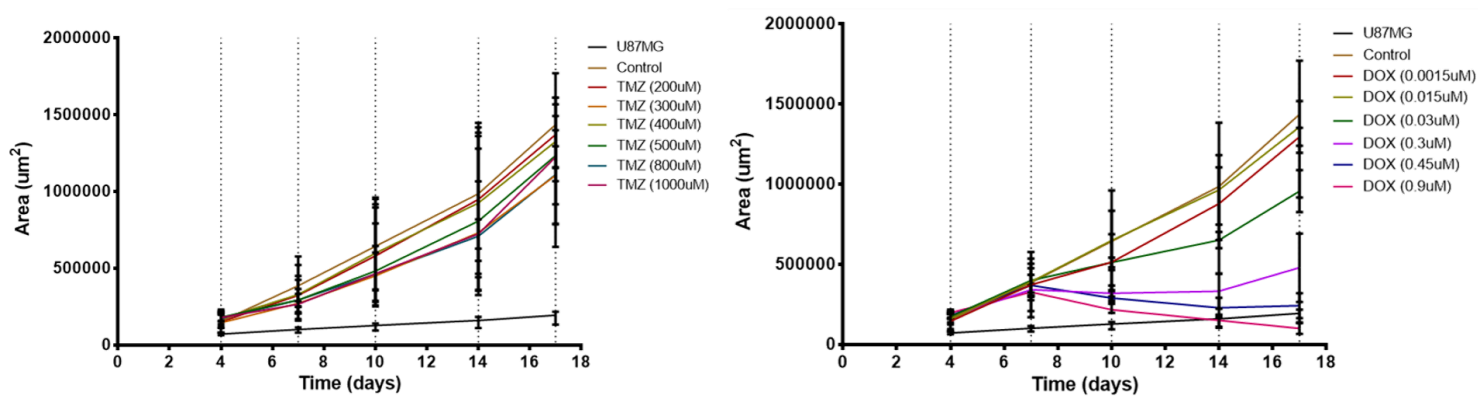

Figure 38. Growth-inhibition curves for TMZ (left) and DOX (right). Error bars denote the standard deviation.

5.2.2 Cell viability monitoring using LSFM imaging

The patient-derived GB spheroids treated with the commonly used anti-cancer agents TMZ and DOX were scanned using LSFM imaging at day 7 and day 11 to estimate spheroid cell viability using the cell death nuclear stain Draq7. LSFM further enabled discrimination between cell death and growth inhibition after treatment. As it can be seen in Figure 39, both the control untreated GB spheroid and the TMZ-treated one appear to grow similarly exhibiting a same death pattern in both time points. The control and the TMZ-treated spheroid are of the same size. It has to be noted that the center of the specimen has a reduced resolution analysis since the size of the spheroid in both cases reached the penetration depth limit of the LSFM modality. On the contrary, the DOX-treated spheroid appears to have a spotted death pattern, especially after day 7, which is in line with the temporal growth-inhibition curves. Furthermore, we can observe that the dead cells are not colocalized with the drug molecules that can be also imaged due to the autofluorescent DOX properties; thus, a DOX-affected cell is not necessarily a dying cell at least within the time window of our observations. As expected [253], DOX penetration and accumulation was more pronounced in the cells of the spheroid periphery. In day 11, the indication of the brightfield images (Figure 37) that all DOX-treated spheroids more or less die after day 7 is evidenced. It has to be clarified that the physiology of the spheroids regarding the distribution of the drug and the necrotic cells becomes apparent with the LSFM imaging technique, whereas the most typically used optical microscopy is limited to the growth patterns.
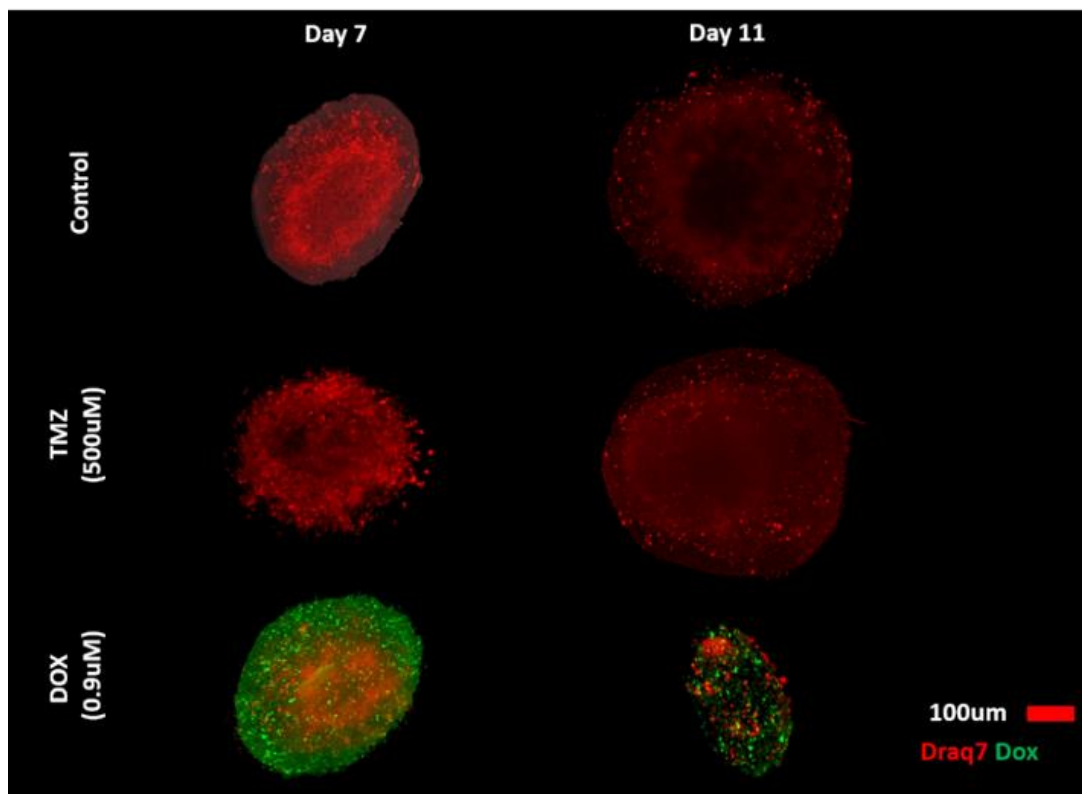
Figure 39. Cell death of the live LSFM-scanned primary GB spheroids. The intrinsic cytotoxicity of a representative untreated spheroid is depicted (upper row). A representative TMZ-treated spheroid cell death pattern is also shown (middle row), as well as a DOX-treated one (lower row). DOX is also marked with green. The max intensity z stacks are depicted for two time points. In day 11, the control and the TMZ-treated spheroids are so large that the center of the specimen could not be properly scanned reaching the penetration scanning depth limit of the modality. Scale bar is set at 100 microns.

5.3 Discussion

An *in vitro* drug screening protocol was proposed combining 2D and 3D experiments on primary GB cells. TMZ and DOX were the two drugs evaluated in this work. Given the growth inhibiting effects observed *in vitro* for the two drugs, as well as the reported mechanisms of action, we investigated whether this result can be further discriminated in either cell proliferation arrest and/or cell death using LSFM imaging.

Interestingly, we observed that unlike DOX which shows a similar dose-response pattern in both 2D and 3D experiments, TMZ has a noisy unidentified response pattern in 3D (see Figure 36). In general, the core difference between the 2D and 3D experiments that makes the latter possessing features of real solid avascular tumors lies in several aspects including diffusion gradients of the drug, oxygen and nutrients, as well as interaction and competition among cells for nutrients and space. Considering both the TMZ molecular mechanism of action [238, 239] and the experimental

evidence, there is a possibility that the chemoresistance in TMZ in the 3D experiments may be partially attributed in hypoxia. More specifically, the main difference between the 2D and the 3D drug screening assays used is that when in 3D, the diffusion of the drug is not immediate towards all the tumor regions as in 2D and additionally, there is a gradient of the oxygen (and other nutrients) from the periphery towards the core of the spheroid. As it can be seen in Figure 39, though TMZ molecules cannot be seen due to lack of fluorescence, there is no differential pattern of the induced-cell death compared to the control spheroids. Thus, it can be assumed that:

i)   the TMZ is adequately distributed to all spheroid regions at the time point observed; the assumption is valid if the theoretical high TMZ disposition [241] is considered
ii)   or TMZ does not cause death
iii)   and/or TMZ needs a longer time period to affect the cells.

However, it has been shown that the TMZ efficacy is essentially reduced under hypoxic conditions when tested for the U251N GB cell line [254]. Additionally, as previously mentioned, down-regulation of both the MGMT protein and the MGMT promoter expression levels have been correlated to higher TMZ responsiveness [238]. Also, in a recent research [255], the inner hypoxia-preserved GB cells of the tumor mass were more TMZ chemoresistant and this was MGMT-related since hypoxia-induced factors, such as HIF1-α, may alter the MGMT phenotype. Hence, in future experiments, chemically-induced hypoxia in the 2D assay, as well as the expression MGMT levels have to be tested to further explain the TMZ response pattern in 3D.

Another interesting feature depicted in Figure 38 Figure 39is the delayed DOX-related response from day 7 to day 10. In the LSFM images of in both day 7 and day 11 the drug molecules are evenly distributed in the spheroid regions and additionally, the cell death pattern of day 7 is not morphologically different from the respective untreated spheroid. Though the exact DOX mechanism of action is not known, the internalization of the DOX molecules within the cells is considered to take more than 24h [242, 256]. More specifically, there is evidence that the drug molecules are consumed from the exposed cells, they bound to nuclear elements and react with them causing the proliferative cells to die and deform. The uptake rate can be obviously related to the delay period of each of the cascade events such as the cell type, the administration method (here 2D or 3D), the cell cycle state, the chromatin composition, the mismatch repair mechanisms, etc. Following the nuclear and cellular membranes damage, the active drug molecules are re-distributed to the ECM and are able to be re-consumed by the neighboring cells and so on [251]. This way, no matter whether the exposure to the drug is ended, the drug affects the cells accumulatively and for a prolonged time period.

In this study we also aimed at presenting the use of our custom built LSFM setup for the study of tumor spheroids, the optimization of imaging protocols and the effect of chemotherapy. LSFM is particularly well suited for fluorescence imaging of large, sensitive living specimens, such as tumor spheroids, as it provides true optical sectioning capabilities, good spatial resolution and minimal phototoxicity. To better illustrate the utility of LSFM for drug screening, LSFM is capable of

providing physiology related information, as compared to the traditionally used brightfield images that are mostly limited to monitoring growth. Our results demonstrate the potential of this technology to quantitatively assess the distribution, drug penetration and cytotoxic potency of anti-neoplastic agents in living 3D cell cultures and to serve as a useful tool in preclinical drug screening towards individualized therapy. Such a high sensitivity imaging technique is expected to serve the ambitious goal of approaching personalized cancer simulations based on patient-specific data in order to optimize therapy decisions after successful translation in the clinical setting.

5.3.1 Proposed computational approach

We could further use the LSFM images to validate and parametrize a preclinically-driven custom computational predictive model. Taken the image-guided indications and the theoretically-supported hypothesis about the differential drug-induced mechanisms triggered in the primary GB cells, we can parametrize accordingly our HDC model so that it can reproduce the conducted biological experiments and extrapolate them to a combined drug therapeutic scheme. To our knowledge, this is the first time a computational predictive algorithm is proposed to be used to predict the TMZ-DOX effect in GB enabling a drug screening tool that is difficult to be experimentally tested and challenging to be clinically applied.

A formalized interpretation of the biological findings of this work could serve in two ways: i) validation of the experimental data under the hypothesis that the proliferative GB cells enter the quiescence state after TMZ treatment and die after DOX treatment, as well as ii) predict the TMZ-DOX combination effect in relation to both the dosage and the timing.

In brief:

The oxygen (representing all nutrients) and the drug concentrations are modeled as continuous elements, while the GB cells are assumed as discrete entities capable of proliferating, entering the quiescence state or die. As the invasion is conditionally blocked in the *in vitro* experiments, the HDC model does not account for cellular movement. As a first step, all tumor cells are considered phenotypically identical, unless otherwise stated.

Especially for the two drugs, driven by the experimental assays used and the relevant biological findings, the 2D experiments are simulated first and followingly, extrapolated in 3D. In the 2D simulations the growth-inhibition curves are translated so as to represent the cytostatic state probability for the TMZ-treated cells and the cytotoxic state probability for the DOX-treated ones (see also [178]). Both TMZ and DOX are considered to affect the proliferative tumor cells in a proportional way to the administrated concentration and the DOX-effect is considered irreversible. The drug is provided once and in the 2D experiments is followingly discontinued, while in the 3D experiments, the drug concentration is subdivided every 48h. The drugs are assumed to be homogeneously distributed when administered. Additionally, DOX is considered to have a prolonged effect over time independently to the concentration subtraction. As with the previous

applications also here, the 3D computational approach represents the planar central slice of the simulated spheroids.

Computational domain

We assumed an $h \times h$ lattice site which fits a single cell of fixed size equal to h=15μm, as *in vitro* estimated (for more details see [80] or chapter 3).

Cell proliferation

At each iteration period, cells are able to divide in case their proliferation age approaches their doubling time which equals to xx=20h, as *in vitro* estimated (for more details see [80] or chapter 3). A cell proliferates in case of nearby empty space.

Cell cycle arrest

The cell enters the quiescent G0 state in case it keeps searching for empty space to proliferate. We also assume quiescence in case of TMZ-treated cells.

Cell death

We consider either spontaneous or drug-induced cell death. The spontaneous cell death is nutrient-dependent triggered by the lack of oxygen and equals to the 10% of the total population, as *in vitro* estimated (for more details see [80] or chapter 3). Cells are also able to undergo necrosis in case of: i) terminal proliferation arrest (or long-lasting quiescent period) in response to TMZ treatment and/or ii) response to DOX treatment. We assumed that dead cells first enter the necrosis procedure followed by the lysis, where dead cells are treated as empty space.

5.3.2 Proposed clinical administration methods for DOX

As it has been explained earlier, there is a strong difficulty in achieving an efficient DOX systemic concentration in the GB lesion within the brain without prompting cardiotoxicity or other adverse reactions [246]. This is the reason why there are several current studies investigating alternative methods of administration that will not deteriorate the drug's active compounds efficacy, but, more crucially, will be harmless for the GB patient. Some of the clinical and/or experimental tested techniques dedicated in brain cancer are the microdialysis [257], drug molecules modifications and nano-carriers [258], reversible opening of the BBB [259], local drug administration [226]. We have clinical findings in favor of drug delivery systems directly inserted within the tumor cavity as implants that can be put during the scheduled operation of the patient and can be externally controlled for dosage and repetitions from the medical doctor. Such an implant in the form of a mechanical pump is under construction from our group.

There is still missing knowledge regarding the observed results in this study. As regards the potential *in silico* application, assuming a positive correlation between the drug concentration and the probability of a cell to die, we can conclude that by allowing cells to also undergo cytostasis, the dose

needed for a cell to die can be reduced compared to the case where cells are only allowed to live or die from a given drug. This hypothesis is in favor of a potential synergy between cytostatic and cytotoxic drugs aiming at overall dose reduction. In any case, investigating the molecular status of the GBP08-P0 primary GB cells that were studied will further argue on the mechanisms of action indicated here for the two drugs. Another limitation of our approach was that we did not investigate the cell death type; we identified only the distribution pattern of the necrosis marker Draq 7. Finally, the best way to assess the combination or the sequential therapeutic scheme is to conduct the biological experiments of the TMZ-DOX combination concentrations and treatment schedule as it will be proposed by the computational predictive algorithm.

TMZ is reported to be efficient in half of the GB patients and also TMZ-resistance usually occurs after the drug is discontinued [260]. The inter- and intra- tumoral heterogeneity of GB indicates both primary and secondary resistance mechanisms. In other words, the clinical experience does not guarantee TMZ-treatment success and the experimental facts verify that even in the case of a responsive GB cells population, not all cells respond and the timing of the treatment is important. On the other hand, DOX is considered a not suitable chemotherapeutic in brain oncology. Alternative therapeutic schemes and time-efficient drug screening tools should be generated in order to enrich our understanding of the GB pathophysiology and the therapeutic planning.

6. Overall conclusions

Brain cancer is not limited to the primary lesion that can be clinically observed through imaging or surgically excised. The massive proliferation is a defining characteristic of the tumor nature, essential for its progress. GB is constantly aggressively growing intra-axially, disturbing brain functionality. When focusing in such a greed form of cancer, proliferation underlying processes become incompatible in cancer progress. In GB, heterogeneity is another typical hallmark, not only among patients with differences between GB molecular subtypes, but more unexpectedly, between different regions of the same tumor with the presence of intra-tumoral subclonal dormancies. We claim that future research should be based on primary cells directly collected from patients and that common cell lines should only serve as landmarks to unite studies of different groups. For every primary established cell line, not only molecular, but also physiological parameters should be estimated to enable a more precise future clustering of different GB cases. Estimations starting with the typical doubling time as shown here and evolving to more delicate features, such as delineation of necrotic and hypoxic regions or invasive capability or others, are highly important.

The invasive cancer cells' properties are also factors that highlight the importance of personalized therapeutic planning to eliminate recurrence and improve the patient's quality of life. Along this line, to study the invasive patterns of our primary and secondary GB cell lines, we cultured them as spheroids that better mimic *in vivo* growth. Surprisingly, unlike earlier published work suggesting migration as single cells, we found that GB spheroids follow a cohesive, tissue-folding-like migration. We used this information to parametrize our HDC tumor growth model to reproduce and further investigate the mechanistic aspect of this observation. Our results indicate that the distinct cell-to-cell adhesive forces within growing spheroids is a major contributor and needs to be further molecularly validated. In-depth understanding of different invasion patterns among GB subtypes and its potential mechanisms that might drive/regulate the observed heterogeneity will offer opportunities for alternative drug targets to prevent GB relapsing post-operatively and improve our understanding of the extension of invasion, which still remains undetectable by conventional imaging modalities.

On the subject of the differential drug responsiveness of GB regarding the TMZ and DOX-treated primary GB spheroids, based on our findings, we hypothesize a potential synergy between cytostatic and cytotoxic drugs aiming at overall dose reduction with maximal tumor elimination. The cytostatic TMZ is currently the front line chemotherapeutic in GB treatment, but not all GB patients are adequately responsive; including the patient's cells we tested. On the other hand, DOX is difficult to be applied in the CNS tumors mainly because the effective tumor dosage is accompanied by severe cytotoxicity in additional targets within the body. A probabilistic, HDC model capable of additionally incorporating drug-induced cytostatic/cytotoxic growth inhibition mechanisms was proposed to describe the evolution and response of the treated spheroids depending on the properties of the drug. Additional experiments that combine the two drugs and study the various

mechanisms of action evoked after treatment in both the molecular and the mesoscopic level would be of great interest.

In this study, we targeted at the **GB** pathophysiology description and we argued in favor of the utility of the computational models as predictor tools. Simulations of cancer progress, either *in vitro* or *in silico*, should not anymore be based on theoretical values, especially if clinical translation is of interest. If we target the holistic description of tumor evolution, we should follow a stepwise approach, where computational tools can definitely help in identifying the most important parameters affecting the final outcome. Overall, we propose that by advancing our mathematical approaches and taking advantage of *in vitro* and *in vivo* experimental approaches, which better mimic the clinical **GB** image, it may be possible to eventually verify the precise set of their computational counterparts needed towards a systematic *in silico* mapping of **GB** progression.

7. Thesis overall achievements

A brief description summarizing the PhD research accomplishments during the last three years follows.

As regards the <u>academic records</u>:

➔ 5 lab rotations, 2 undergraduate theses and 1 postgraduate thesis were guided.

➔ 8 lectures were given in the courses Neurosurgery (A. Vakis, Medical School), Brain Connectivity Analysis Using EEG/MEG (V. Sakkalis, Medical School), Bioinformatics and Simulation of Physiological Systems (Tsiknakis Manolis, Department of Informatics Engineering).

➔ The following courses were successfully examined: Neurosurgery (Grade 10, Medical School), Molecular Oncogenesis (Grade 9, Department of Biology), Programming I (Grade 8, Department of Mathematics), C++ (Grade 5.5, Department of Computer Science)

➔ 5th International Lab Animal Course of the Federation of European Laboratory Animal Science Associations (FELASA) on "Care and Use of Laboratory Animals: mice, rats and zebrafish", June 4-15, University of Crete (Biology Department) and IMBB-FORTH, Heraklion, Greece, 2018 (**FELASA Certificate ID: 051/15_16_2018**)

➔ 1st Technology Summer Conference of the European Society for Molecular Imaging – ESMI, TOPIM TECH on "MULTIPARAMETRIC IMAGING", July 10 – 15, MAICh, Chania, Greece, 2016

➔ Biophotonics and Molecular Imaging (BiMI) Summer School, July 27 - 31, IESL- FORTH and Department of Biology, University of Crete, Heraklion, Greece, 2015

➔ Writing and approval of the scientific protocol by the General Hospital of Heraklion Scientific Committee (**Protocol number: 442120205-2018**) as regards the bioethical procedures and the protocols used.

The following <u>fellowships/awards</u> were given for the PhD support:

08.2018-11.2018: Post Graduate Fellowship funded by FORTH

08.2017-07.2018: **General Secretariat for Research and Technology (GSRT) and Hellenic Foundation for Research and Innovation (HFRI) (Scholarship Number: 130178/I2/31-7-2017)**

01.2017-07.2017: Post Graduate Fellowship funded by FORTH

06.2016: **Winning prize of the best free announcement in the 30th Panhellenic Conference of Neurosurgery**

01.2016-12.2016: Post Graduate Fellowship funded by FORTH

03.2015-12.2015: Trainee / Associated Researcher Fellowship funded by FORTH

The research works publicly announced were:

Publications (2/5 published)

1. **Oraiopoulou M.E.**, Tzamali E, Tzedakis G, Liapis E, Zacharakis G, Vakis A, Papamatheakis J, Sakkalis V , "Integrating *in vitro* experiments with *in silico* approaches for Glioblastoma invasion: the role of cell-to-cell adhesion heterogeneity", Nature Scientific Reports, **2018**, **8**(1): p. 16200
2. **M.-E. Oraiopoulou**, E. Tzamali, G. Tzedakis, A. Vakis, J. Papamatheakis, and V. Sakkalis, "*In Vitro/In Silico* Study on the Role of Doubling Time Heterogeneity among Primary Glioblastoma Cell Lines", BioMed Research International, **2017**, vol. 2017, Article ID 8569328, 12 pages
3. **Oraiopoulou M.E.**, Tampakaki M., Tzamali E., Tamiolakis T., Makatounakis V., Vakis F. A., Zacharakis G., Sakkalis V., Papamatheakis J., "The T98G Glioblastoma cell line phenotypic characterization", Tissue and Cell, Elsevier, **2018**. (under review)
4. **Oraiopoulou M-E**, Tzamali E, Papamatheakis J, Sakkalis V, "Phenocopying Glioblastoma: A Review" (**2018**, under submission to the Journal of Translational Oncology)
5. **M-E Oraiopoulou**, E Tzamali, G Tzedakis, S E Psycharakis, E Parasiraki, A F Vakis, G Zacharakis, J Papamatheakis, V Sakkalis, "The Temozolomide-Doxorubicin paradox in primary Glioblastoma *in vitro-in silico* preclinical drug screening", (**2018**, to be submitted)

Conference Papers (1)

1. S. E. Psycharakis, E. Liapis, A. Zacharopoulos, **M.-E. Oraiopoulou**, J. Papamatheakis, V. Sakkalis, and G. Zacharakis, "High resolution volumetric imaging of primary and secondary tumor spheroids using multi-angle Light Sheet Fluorescence Microscopy (LSFM)", 40th International Conference of the IEEE, Engineering in Medicine and Biology (EMB), Honolulu, Hawaii, United States, **2018**.

Oral Presentations (6)

1. Stylianos Psycharakis, **Mariam-Eleni Oraiopoulou**, Evangelos Liapis, Athanasios Zacharopoulos, Joseph Papamatheakis, Vangelis Sakkalis and Giannis Zacharakis (**2018**) "Imaging cancer development and therapeutic response on patient-derived live cell organoids using multi-projection light sheet fluorescence microscopy" World Molecular Imaging Congress, Seattle, WA, USA
2. **Oraiopoulou M.E.** (**2017**) "Computational prediction of the invasive pattern observed in primary and secondary Glioblastoma spheroids" Conference of Clinical and Translational Oncology, Heraklion, Greece
3. **Ωραιοπούλου Μ.Ε.**, Τζαμαλή Ε., Παπαματθαιάκης Ι., Σακκαλής Ε., Μανωλίτση Κ., Βάκης Α. (**2017**) "ΝΕΟ ΜΟΝΤΕΛΟ ΕΡΜΗΝΕΙΑΣ ΤΗΣ ΔΙΗΘΗΤΙΚΗΣ ΣΥΜΠΕΡΙΦΟΡΑΣ

ΤΟΥ ΓΛΟΙΟΒΛΑΣΤΩΜΑΤΟΣ: *IN VITRO* ΜΕΛΕΤΗ" 31ο Πανελλήνιο Συνέδριο Νευροχειρουργικής, Ιωάννινα, Ελλάδα

4. Tserevelakis G., Avtzi S., Tsagkaraki M., **Oraiopoulou M.E.**, Papamatheakis J., Zacharakis G. (2017) "Hybrid PhotoAcoustic and Confocal Laser Scanning Microscopy" 12th Annual Meeting, European Molecular Imaging Meeting, Cologne, Germany

5. Κουγεντάκης Γ., Μανωλίτση Κ., **Ωραιοπούλου Μ.Ε.**, Παπαματθαιάκης Ι., Βάκης Α. (2016) "ΠΑΡΟΥΣΙΑ ΜΕΤΑΣΤΑΤΙΚΩΝ ΚΥΤΤΑΡΩΝ ΣΤΟ ΑΙΜΑ ΑΣΘΕΝΩΝ ΠΑΣΧΟΝΤΩΝ ΑΠΟ ΓΛΟΙΟΒΛΑΣΤΩΜΑ. ΠΡΟΔΡΟΜΗ (*Πρόδρομη παρουσίαση μικρής σειράς 6 περιστατικών*)." 30ο Πανελλήνιο Συνέδριο Νευροχειρουργικής, Βόλος, Ελλάδα

6. **Ωραιοπούλου Μ.Ε.**, Παπαματθαιάκης Ι., Ζαχαράκης Ι., Σακκαλής Ε., Μανωλίτση Κ., Βάκης Α. (2016) "ΠΑΡΑΣΚΕΥΗ ΖΩΙΚΩΝ ΜΟΝΤΕΛΩΝ ΚΑΙ ΠΡΩΤΟΓΕΝΩΝ ΚΥΤΤΑΡΟΚΑΛΛΙΕΡΓΕΙΩΝ ΑΠΟ ΙΣΤΟΛΟΓΙΚΗ ΔΕΙΓΜΑΤΟΛΗΨΙΑ ΑΣΘΕΝΩΝ ΜΕ ΓΛΟΙΟΒΛΑΣΤΩΜΑ (*Πρόδρομη ανακοίνωση*)" 30ο Πανελλήνιο Συνέδριο Νευροχειρουργικής, Βόλος, Ελλάδα (1st award)

Poster Presentations (7)

1. **M-E Oraiopoulou**, S E Psycharakis, E Parasiraki, E Tzamali, G Tzedakis, A F Vakis, V Sakkalis, J Papamatheakis, G Zacharakis (2018) "Light sheet fluorescence microscopy imaging of primary Glioblastoma 3D cultures treated with Temozolomide and Doxorubicin", 13th European Molecular Imaging Meeting (EMIM), San Sebastian, Spain

2. **M.E. Oraiopoulou**, E. Tzamali, G. Tzedakis, E. Liapis, G. Zacharakis, A. Vakis, V. Sakkalis, J. Papamatheakis (2017) "Unforeseen invasive morphology observed in primary Glioblastoma cell line spheroids" Chemical Biology of Disease Meeting, Heraklion, Greece (*presented by Mariam-Eleni Oraiopoulou both as a poster and a speed talk*)

3. E. Parasiraki, **M.E. Oraiopoulou**, S. Psycharakis, V. Sakkalis, A. Vakis, G. Zacharakis, J. Papamatheakis (2017) "Glioblastoma preclinical drug screening in 2D and 3D primary cultures" Chemical Biology of Disease Meeting, Heraklion, Greece (*presented by Mariam-Eleni Oraiopoulou both as a poster and a speed talk*)

4. **M.E. Oraiopoulou**, S. Psycharakis, E. Tzamali, V. Sakkalis, A. Vakis, J. Papamatheakis, G. Zacharakis (2016) "Imaging pathophysiologic parameters of primary Glioblastoma spheroids with light sheet microscopy towards theranostic heuristics" 11th annual event of the European Technology Platform on Nanomedicine, Heraklion, Greece coorganized by ETPN and FORTH – IESL

5. E. Parasiraki, **M.E. Oraiopoulou**, V. Sakkalis, A. Vakis, G. Zacharakis, J. Papamatheakis (2016) "Drug screening in 2D and 3D primary glioblastoma cell cultures: A preliminary study" 67th National Conference of the Hellenic Society of Biochemistry and Molecular Biology (HSBMB), Ioannina, Greece

6. E. Parasiraki, **M.E. Oraiopoulou**, S. Psycharakis, V. Sakkalis, A. Vakis, G. Zacharakis, J. Papamatheakis **(2016)** "Comparing primary to cell line glioblastoma cells in 2D and 3D cultures A preliminary study" EMBO summer workshop, Spetses, Greece

7. **M.E. Oraiopoulou**, S. Avtzi, S. Psycharakis, E. Tzamali, V. Sakkalis, J. Papamatheakis, A. Vakis, G. Zacharakis **(2016)** "Imaging glioblastoma pathophysiology on animal and 3D cell culture models to improve *in silico* predictability" 1st ESMI Imaging technology summer workshop TOPIM TECH, MAICh-Chania, Greece

Acknowledgments

την Κρήτη που συνάντησα ως τώρα στις σπουδές μου και με οδήγησαν ως το σήμερα.

Ξεχωριστά θέλω να ευχαριστήσω τη φίλη και αφανή και επιφανή συντονίστρια της όλης αυτής εργασίας, τον άνθρωπο πίσω και μπροστά από όλα, την τόσο μα τόσο σπουδαία Μητέρα και Ερευνήτρια Δρ. **Ελευθερία Τζαμαλή**. Χωρίς εσένα δε θα κατάφερνα τίποτα. Μακάρι να μπορέσω να σου επιστρέψω κάποτε έστω τα μισά από όσα μου προσφέρεις εσύ.

Ευχαριστώ ακόμη τους φίλους και συναδέλφους, **Γεώργιο Τζεδάκη**, Δρ. **Βαγγέλη Λιάπη**, και **Στέλιο Ψυχαράκη** οι οποίοι υπήρξαν υπομονετικοί μαζί μου και με κάνανε να χαίρομαι κάθε φορά που προχωράγαμε μαζί σε κάτι παρά τις όποιες δυσκολίες. Οφείλω να αναφέρω την Νευροχειρουργό πλέον **Κατερίνα Μανωλίτση** που με βοήθησε να αφομοιωθώ στην Κλινική, την κα. **Δέσποινα Τσουκάτου** η οποία με βοήθησε με τα ζωάκια μας, καθώς και τον κ. **Τάκη Μακατουνάκη** που διεκπεραιώνει πάντα με κάποιο τρόπο όποιο παράλογο πρωτόκολλο θα ζητήσω. Ευχαριστώ την κάποτε προπτυχιακή πρώτη μου φοιτήτρια, **Ελευθερία Παρασυράκη** και την τωρινή μεταπτυχιακή, **Μάιρα Ταμπακάκη** οι οποίες με άντεξαν στο διάστημα που συνεργαστήκαμε, γίναμε καλές φίλες και για τις οποίες έχω την πεποίθηση πως θα καταφέρουν πολλά κάποια μέρα. Ευχαριστώ και όλα τα παιδιά που είμαστε μαζί στο εργαστήριο και φτιάχνουνε μία όμορφη καθημερινότητα εδώ και τόσα χρόνια.

Δεν μπορώ παρά να χρωστάω ευγνωμοσύνη σε όλους μου τους φίλους εντός και εκτός εργαστηρίου ή σχολής. Θα αναφέρω ονομαστικά κάποιους που τράβηξαν το βαρύ φορτίο των παράπονών μου και συμμερίστηκαν, ακόμη κι όταν δυσκολευόντουσαν, τις ερευνητικές δυσκολίες, αλλά κυριότερα χαίρονταν με τις χαρές μου και υπέμειναν να ασχολιόμαστε δημοκρατικά μόνο με εμένα για παρατεταμένες περιόδους! Ευχαριστώ πολύ **Ιωάννα**, **Κώστα**, **Ροδούλα**,

Άγγελε, Μαρία, Παναγιώτη, Νικόλ. Οι συζητήσεις μας δε συγκρίνονται με τα καλύτερα άρθρα! Από εκεί αντλώ τις όποιες ιδέες! Ευχαριστώ την ψυχοθεραπευτική Θ.Ο.Π.Κ. και τα παιδιά που μαζί εκτεθήκαμε, καθώς και το δάσκαλό μας κ. Γιώργο Αντωνάκη.

Πιο πολύ όμως από όλους, ευχαριστώ μαμά, μπαμπά και Βάιε, τους παππούδες μου, τα ξαδέρφια, τους θείους μου και όλη την οικογένειά μου μαζί με τα σκυλάκια και τα γατάκια μας (αυτά που είναι και αυτά που δεν είναι πια εδώ) που μου δίνουν εδώ και τόσα χρόνια εφόδια να συνεχίζω και να προσπαθώ και τους καμαρώνω όλους ξέροντας πια πως σε αυτούς οφείλω τα πάντα. Άρα και αυτή την εργασία ...

«Θα τον αλλάξουμε τον κόσμο ...

Το θέμα είναι να παραμείνουμε άνθρωποι ...»

Κάθε άλλο παρά τυπικά, σας ευχαριστώ όλους ...

References

1.   Bailey, P. and H. Cushing, *A classification of the tumors of the glioma group on a histogenetic basis with a correlated study of prognosis*1926: JB Lippincott, Philadelphia. 175 p.
2.   Davis, L., *Spongioblastoma Multiforme of the Brain.* Ann Surg, 1928. **87**(1): p. 8-14.
3.   Kleihues, P., et al., *The WHO classification of tumors of the nervous system.* J Neuropathol Exp Neurol, 2002. **61**(3): p. 215-25; discussion 226-9.
4.   Louis, D.N., et al., *The 2016 World Health Organization Classification of Tumors of the Central Nervous System: a summary.* Acta Neuropathol, 2016. **131**(6): p. 803-20.
5.   Lenting, K., et al., *Glioma: experimental models and reality.* Acta Neuropathol, 2017. **133**(2): p. 263-282.
6.   Ali-Osman, F., *Brain tumors.* Contemporary cancer research2005, Totowa, N.J.: Humana Press. xi, 393 p.
7.   Flynn, J.R., et al., *Hypoxia-regulated protein expression, patient characteristics, and preoperative imaging as predictors of survival in adults with glioblastoma multiforme.* Cancer, 2008. **113**(5): p. 1032-42.
8.   Hou, L.C., et al., *Recurrent glioblastoma multiforme: a review of natural history and management options.* Neurosurg Focus, 2006. **20**(4): p. E5.
9.   Hart, M.G., et al., *Temozolomide for high grade glioma.* Cochrane Database Syst Rev, 2013. **4**: p. CD007415.
10.   Emblem, K.E., et al., *Vessel architectural imaging identifies cancer patient responders to anti-angiogenic therapy.* Nat Med, 2013. **19**(9): p. 1178-1183.
11.   Pope, W.B., J.R. Young, and B.M. Ellingson, *Advances in MRI assessment of gliomas and response to anti-VEGF therapy.* Curr Neurol Neurosci Rep, 2011. **11**(3): p. 336-44.
12.   Peschillo, S., et al., *New therapeutic strategies regarding endovascular treatment of glioblastoma, the role of the blood-brain barrier and new ways to bypass it.* J Neurointerv Surg, 2015.
13.   Elens, I., *Clinical Study: Resection and Immunotherapy for Recurrent Grade III Glioma.* ISRN Immunology, 2012. **2012** (2012): p. 1-9.
14.   Joo, K.M., et al., *Patient-specific orthotopic glioblastoma xenograft models recapitulate the histopathology and biology of human glioblastomas in situ.* Cell Rep, 2013. **3**(1): p. 260-73.
15.   Carmeliet, P., *Mechanisms of angiogenesis and arteriogenesis.* Nat Med, 2000. **6**(4): p. 389-95.
16.   Hardee, M.E. and D. Zagzag, *Mechanisms of glioma-associated neovascularization.* Am J Pathol, 2012. **181**(4): p. 1126-41.
17.   Brat, D.J. and E.G. Van Meir, *Vaso-occlusive and prothrombotic mechanisms associated with tumor hypoxia, necrosis, and accelerated growth in glioblastoma.* Lab Invest, 2004. **84**(4): p. 397-405.
18.   Brat, D.J., et al., *Pseudopalisades in glioblastoma are hypoxic, express extracellular matrix proteases, and are formed by an actively migrating cell population.* Cancer Res, 2004. **64**(3): p. 920-7.
19.   Hu, L.S., et al., *Multi-Parametric MRI and Texture Analysis to Visualize Spatial Histologic Heterogeneity and Tumor Extent in Glioblastoma.* PLoS One, 2015. **10**(11): p. e0141506.
20.   Sottoriva, A., et al., *Intratumor heterogeneity in human glioblastoma reflects cancer evolutionary dynamics.* Proc Natl Acad Sci U S A, 2013. **110**(10): p. 4009-14.
21.   Pavlisa, G., et al., *The differences of water diffusion between brain tissue infiltrated by tumor and peritumoral vasogenic edema.* Clin Imaging, 2009. **33**(2): p. 96-101.

22.   Lee, E.J., et al., *Diagnostic value of peritumoral minimum apparent diffusion coefficient for differentiation of glioblastoma multiforme from solitary metastatic lesions.* AJR Am J Roentgenol, 2011. **196**(1): p. 71-6.

23.   Juliano, J., et al., *Comparative dynamics of microglial and glioma cell motility at the infiltrative margin of brain tumours.* J R Soc Interface, 2018. **15**(139).

24.   Holland, E.C., *Glioblastoma multiforme: The terminator.* Proceedings of the National Academy of Sciences, 2000. **97**(12): p. 6242-6244.

25.   Wen, P.Y., et al., *Updated response assessment criteria for high-grade gliomas: response assessment in neuro-oncology working group.* J Clin Oncol, 2010. **28**(11): p. 1963-72.

26.   Eisenhauer, E.A., et al., *New response evaluation criteria in solid tumours: revised RECIST guideline (version 1.1).* Eur J Cancer, 2009. **45**(2): p. 228-47.

27.   Sullivan, J.P., et al., *Brain tumor cells in circulation are enriched for mesenchymal gene expression.* Cancer Discov, 2014. **4**(11): p. 1299-309.

28.   Fonkem, E., M. Lun, and E.T. Wong, *Rare phenomenon of extracranial metastasis of glioblastoma.* J Clin Oncol, 2011. **29**(34): p. 4594-5.

29.   Ramakrishna, R. and R. Rostomily, *Seed, soil, and beyond: The basic biology of brain metastasis.* Surg Neurol Int, 2013. **4**(Suppl 4): p. S256-64.

30.   Lombard, A., N. Goffart, and B. Rogister, *Glioblastoma Circulating Cells: Reality, Trap or Illusion?* Stem Cells Int, 2015. **2015**: p. 182985.

31.   Zaman, M.H., et al., *Migration of tumor cells in 3D matrices is governed by matrix stiffness along with cell-matrix adhesion and proteolysis.* Proc Natl Acad Sci U S A, 2006. **103**(29): p. 10889-94.

32.   Singh, S.K., et al., *Identification of human brain tumour initiating cells.* Nature, 2004. **432**(7015): p. 396-401.

33.   Chen, J., R.M. McKay, and L.F. Parada, *Malignant glioma: lessons from genomics, mouse models, and stem cells.* Cell, 2012. **149**(1): p. 36-47.

34.   Fakhoury, M., *Drug delivery approaches for the treatment of glioblastoma multiforme.* Artificial Cells, Nanomedicine, and Biotechnology, 2016. **44**(6): p. 1365-1373.

35.   Oh, S.Y. and H. Kim, *Molecular culprits generating brain tumor stem cells.* Brain Tumor Res Treat, 2013. **1**(1): p. 9-15.

36.   Kiseleva, L.N., et al., *Characterization of New Human Glioblastoma Cell Lines.* Cell and Tissue Biology, 2018. **12**(1): p. 1-6.

37.   Goffart, N., J. Kroonen, and B. Rogister, *Glioblastoma-initiating cells: relationship with neural stem cells and the micro-environment.* Cancers (Basel), 2013. **5**(3): p. 1049-71.

38.   Dirks, P.B., *Brain tumor stem cells: the cancer stem cell hypothesis writ large.* Mol Oncol, 2010. **4**(5): p. 420-30.

39.   Liu, C., et al., *Mosaic analysis with double markers reveals tumor cell of origin in glioma.* Cell, 2011. **146**(2): p. 209-21.

40.   Schiffer, D., et al., *On the origin and growth of gliomas.* Anticancer Res, 2010. **30**(6): p. 1977-98.

41.   Alcantara Llaguno, S.R. and L.F. Parada, *Cell of origin of glioma: biological and clinical implications.* Br J Cancer, 2016. **115**(12): p. 1445-1450.

42.   Janbazian, L., J. Karamchandani, and S. Das, *Mouse models of glioblastoma: lessons learned and questions to be answered.* J Neurooncol, 2014. **118**(1): p. 1-8.

43.   Aboulkheyr Es, H., et al., *Personalized Cancer Medicine: An Organoid Approach.* Trends Biotechnol, 2018. **36**(4): p. 358-371.

44.   Strickland, M. and E.A. Stoll, *Metabolic Reprogramming in Glioma.* Front Cell Dev Biol, 2017. **5**: p. 43.

45.   Parker, N.R., et al., *Molecular heterogeneity in glioblastoma: potential clinical implications.* Front Oncol, 2015. **5**: p. 55.

46.   Quail, D.F. and J.A. Joyce, *The Microenvironmental Landscape of Brain Tumors.* Cancer Cell, 2017. **31**(3): p. 326-341.

47.   *White paper - 5 Reasons Cancer Researchers Adopt 3D Cell Culture: A Review of Recent Literature.* 3D Biomatrix Inc. , 2013.

48.   Katt, M.E., et al., *In Vitro Tumor Models: Advantages, Disadvantages, Variables, and Selecting the Right Platform.* Front Bioeng Biotechnol, 2016. **4**: p. 12.

49.   Gritsenko, P., W. Leenders, and P. Friedl, *Recapitulating in vivo-like plasticity of glioma cell invasion along blood vessels and in astrocyte-rich stroma.* Histochem Cell Biol, 2017.

50.   Hubert, C.G., et al., *A Three-Dimensional Organoid Culture System Derived from Human Glioblastomas Recapitulates the Hypoxic Gradients and Cancer Stem Cell Heterogeneity of Tumors Found In Vivo.* Cancer Res, 2016. **76**(8): p. 2465-77.

51.   Manini, I., et al., *Role of Microenvironment in Glioma Invasion: What We Learned from In Vitro Models.* Int J Mol Sci, 2018. **19**(1).

52.   Ayuso, J.M., et al., *Glioblastoma on a microfluidic chip: Generating pseudopalisades and enhancing aggressiveness through blood vessel obstruction events.* Neuro-Oncology, 2017. **19**(4): p. 503-513.

53.   Francescone, R.A., 3rd, M. Faibish, and R. Shao, *A Matrigel-based tube formation assay to assess the vasculogenic activity of tumor cells.* J Vis Exp, 2011(55).

54.   Friedrich, J., et al., *Spheroid-based drug screen: considerations and practical approach.* Nat Protoc, 2009. **4**(3): p. 309-24.

55.   Li, A., et al., *Genomic changes and gene expression profiles reveal that established glioma cell lines are poorly representative of primary human gliomas.* Mol Cancer Res, 2008. **6**(1): p. 21-30.

56.   Caballero, D., et al., *Tumour-vessel-on-a-chip models for drug delivery.* Lab Chip, 2017. **17**(22): p. 3760-3771.

57.   Ayuso, J.M., et al., *Development and characterization of a microfluidic model of the tumour microenvironment.* Scientific Reports, 2016. **6**: p. 36086.

58.   Liu, Y., E. Gill, and Y.Y. Shery Huang, *Microfluidic on-chip biomimicry for 3D cell culture: a fit-for-purpose investigation from the end user standpoint.* Future Science OA, 2017. **3**(2): p. FSO173.

59.   Herrmann, D., et al., *Three-dimensional cancer models mimic cell-matrix interactions in the tumour microenvironment.* Carcinogenesis, 2014. **35**(8): p. 1671-9.

60.   Sandén, E., et al., *A standardized and reproducible protocol for serum-free monolayer culturing of primary paediatric brain tumours to be utilized for therapeutic assays.* Scientific Reports, 2015. **5**: p. 12218.

61.   Carlson, B.L., et al., *Establishment, maintenance and in vitro and in vivo applications of primary human glioblastoma multiforme (GBM) xenograft models for translational biology studies and drug discovery.* Curr Protoc Pharmacol, 2011. **Chapter 14**: p. Unit 14 16.

62.   Ledur, P.F., et al., *Culture conditions defining glioblastoma cells behavior: what is the impact for novel discoveries?* Oncotarget, 2017. **8**(40): p. 69185-69197.

63.   Zanoni, M., et al., *3D tumor spheroid models for in vitro therapeutic screening: a systematic approach to enhance the biological relevance of data obtained.* Sci Rep, 2016. **6**: p. 19103.

64.   Fayzullin, A., et al., *Time-lapse phenotyping of invasive glioma cells ex vivo reveals subtype-specific movement patterns guided by tumor core signaling.* Experimental Cell Research, 2016. **349**(2): p. 199-213.

65.   Meijer, T.G., et al., *Ex vivo tumor culture systems for functional drug testing and therapy response prediction.* Future Science OA, 2017. **3**(2): p. FSO190.

66.   Sturm, D., et al., *Hotspot mutations in H3F3A and IDH1 define distinct epigenetic and biological subgroups of glioblastoma.* Cancer Cell, 2012. **22**(4): p. 425-37.

67.   McNamara, M.G., S. Sahebjam, and W.P. Mason, *Emerging biomarkers in glioblastoma.* Cancers (Basel), 2013. **5**(3): p. 1103-19.

68.   Ponten, J. and E.H. Macintyre, *Long term culture of normal and neoplastic human glia.* Acta Pathol Microbiol Scand, 1968. **74**(4): p. 465-86.

69.   Allen, M., et al., *Origin of the U87MG glioma cell line: Good news and bad news.* Sci Transl Med, 2016. **8**(354): p. 354re3.

70.   Clark, M.J., et al., *U87MG decoded: the genomic sequence of a cytogenetically aberrant human cancer cell line.* PLoS Genet, 2010. **6**(1): p. e1000832.

71.   Huszthy, P.C., et al., *In vivo models of primary brain tumors: pitfalls and perspectives.* Neuro Oncol, 2012. **14**(8): p. 979-93.

72.   Stylianos E. Psycharakis, E.L., Athanasios Zacharopoulos, Mariam-Eleni Oraiopoulou, and V.S. Joseph Papamatheakis, and Giannis Zacharakis, *High resolution volumetric imaging of primary and secondary tumor spheroids using multi-angle Light Sheet Fluorescence Microscopy (LSFM).* EMBC, 2018.

73.   Michel Lacroix, et al., *A multivariate analysis of 416 patients with glioblastoma multiforme: prognosis, extent of resection, and survival.* Journal of Neurosurgery, 2001. **95**(2): p. 190-198.

74.   Szeto, M.D., et al., *Quantitative metrics of net proliferation and invasion link biological aggressiveness assessed by MRI with hypoxia assessed by FMISO-PET in newly diagnosed glioblastomas.* Cancer Res, 2009. **69**(10): p. 4502-9.

75.   Claes, A., A.J. Idema, and P. Wesseling, *Diffuse glioma growth: a guerilla war.* Acta Neuropathol, 2007. **114**(5): p. 443-58.

76.   Xie, Y., et al., *The Human Glioblastoma Cell Culture Resource: Validated Cell Models Representing All Molecular Subtypes.* EBioMedicine, 2015. **2**(10): p. 1351-63.

77.   Azari, H., et al., *Isolation and expansion of human glioblastoma multiforme tumor cells using the neurosphere assay.* J Vis Exp, 2011(56): p. e3633.

78.   Pavon, L.F., et al., *In vitro Analysis of Neurospheres Derived from Glioblastoma Primary Culture: A Novel Methodology Paradigm.* Front Neurol, 2014. **4**: p. 214.

79.   Mullins, C.S., et al., *Establishment and characterization of primary glioblastoma cell lines from fresh and frozen material: a detailed comparison.* PLoS One, 2013. **8**(8): p. e71070.

80.   Oraiopoulou, M.-E., et al., *In Vitro/In Silico Study on the Role of Doubling Time Heterogeneity among Primary Glioblastoma Cell Lines.* BioMed Research International, 2017. **2017**: p. 12.

81.   Lee, J., et al., *Tumor stem cells derived from glioblastomas cultured in bFGF and EGF more closely mirror the phenotype and genotype of primary tumors than do serum-cultured cell lines.* Cancer Cell, 2006. **9**(5): p. 391-403.

82.   Stoczynska-Fidelus, E., et al., *The failure in the stabilization of glioblastoma-derived cell lines: spontaneous in vitro senescence as the main culprit.* PLoS One, 2014. **9**(1): p. e87136.

83.   Hua, C., D. Jun, and H. Qiang, *Xenograft Model of Human Brain Tumor*2011: INTECH Open Access Publisher.

84.   Kijima, N. and Y. Kanemura, *Mouse Models of Glioblastoma*, in *Glioblastoma*, S. De Vleeschouwer, Editor 2017: Brisbane (AU).

85.   Inda, M.M., et al., *Tumor heterogeneity is an active process maintained by a mutant EGFR-induced cytokine circuit in glioblastoma.* Genes Dev, 2010. **24**(16): p. 1731-45.

86.   Richmond, A. and Y. Su, *Mouse xenograft models vs GEM models for human cancer therapeutics.* Dis Model Mech, 2008. **1**(2-3): p. 78-82.

87.   Chen Hua, D.J.a.H.Q., *Xenograft Model of Human Brain Tumor*, in *Brain Tumors - Current and Emerging Therapeutic Strategies*, A.L. Abujamra, Editor 2011, InTech.

88.   Voskoglou-Nomikos, T., J.L. Pater, and L. Seymour, *Clinical predictive value of the in vitro cell line, human xenograft, and mouse allograft preclinical cancer models.* Clin Cancer Res, 2003. **9**(11): p. 4227-39.

89.   Anderson, J.C., et al., *Kinomic exploration of temozolomide and radiation resistance in Glioblastoma multiforme xenolines.* Radiother Oncol, 2014. **111**(3): p. 468-74.

90.   Garcia, C., et al., *The orthotopic xenotransplant of human glioblastoma successfully recapitulates glioblastoma-microenvironment interactions in a non-immunosuppressed mouse model.* BMC Cancer, 2014. **14**: p. 923.

91.	Patrizii, M., et al., *Utility of Glioblastoma Patient-Derived Orthotopic Xenografts in Drug Discovery and Personalized Therapy.* Frontiers in Oncology, 2018. **8**(23).

92.	Morgan, R.A., *Human tumor xenografts: the good, the bad, and the ugly.* Mol Ther, 2012. **20**(5): p. 882-4.

93.	Deliolanis, N.C., et al., *Deep-tissue reporter-gene imaging with fluorescence and optoacoustic tomography: a performance overview.* Mol Imaging Biol, 2014. **16**(5): p. 652-60.

94.	Waghmare, I., et al., *Intercellular cooperation and competition in brain cancers: lessons from Drosophila and human studies.* Stem Cells Transl Med, 2014. **3**(11): p. 1262-8.

95.	Gholamin S, F.A.H., Mitra S S, et al. , *Establishment of Stereotactic Orthotopic Brain Tumor Xenografts in Mice.* Cureus, 2013. **5**(12).

96.	Hua, C., D. Jun, and H. Qiang, *Xenograft Model of Human Brain Tumor.* Brain Tumors - Current and Emerging Therapeutic Strategies2011.

97.	Swanson, K.R., et al., *Complementary but distinct roles for MRI and 18F-fluoromisonidazole PET in the assessment of human glioblastomas.* J Nucl Med, 2009. **50**(1): p. 36-44.

98.	Swanson, K.R., et al., *Quantifying the role of angiogenesis in malignant progression of gliomas: in silico modeling integrates imaging and histology.* Cancer Res, 2011. **71**(24): p. 7366-75.

99.	Roniotis, A., Oraiopoulou, M. E., et al., *A Proposed Paradigm Shift in Initializing Cancer Predictive Models with DCE-MRI Based PK Parameters: A Feasibility Study.* Cancer Inform, 2015. **14**(Suppl 4): p. 7-18.

100.	Yankeelov, T.E., *Integrating Imaging Data into Predictive Biomathematical and Biophysical Models of Cancer.* ISRN Biomath, 2012. **2012**.

101.	Yankeelov, T.E., et al., *Clinically relevant modeling of tumor growth and treatment response.* Sci Transl Med, 2013. **5**(187): p. 187ps9.

102.	Sakkalis, V., et al., *Web-based workflow planning platform supporting the design and execution of complex multiscale cancer models.* IEEE J Biomed Health Inform, 2014. **18**(3): p. 824-31.

103.	Hinow, P., et al., *A spatial model of tumor-host interaction: application of chemotherapy.* Math Biosci Eng, 2009. **6**(3): p. 521-46.

104.	Anderson, A.R.A., et al., *Tumor Morphology and Phenotypic Evolution Driven by Selective Pressure from the Microenvironment.* Cell, 2006. **127**(5): p. 905-915.

105.	Frieboes, H.B., et al., *Three-dimensional multispecies nonlinear tumor growth-II: Tumor invasion and angiogenesis.* J Theor Biol, 2010. **264**(4): p. 1254-78.

106.	Wise, S.M., et al., *Three-dimensional multispecies nonlinear tumor growth--I Model and numerical method.* J Theor Biol, 2008. **253**(3): p. 524-43.

107.	Alfonso, J.C.L., et al., *The biology and mathematical modelling of glioma invasion: a review.* J R Soc Interface, 2017. **14**(136).

108.	Jiao, Y. and S. Torquato, *Emergent behaviors from a cellular automaton model for invasive tumor growth in heterogeneous microenvironments.* PLoS Comput Biol, 2011. **7**(12): p. e1002314.

109.	Stamatakos, G.S., et al., *A four-dimensional computer simulation model of the in vivo response to radiotherapy of glioblastoma multiforme: studies on the effect of clonogenic cell density.* Br J Radiol, 2006. **79**(941): p. 389-400.

110.	Tzamali, E., et al., *Exploring the competition between proliferative and invasive cancer phenotypes in a continuous spatial model.* PLoS One, 2014. **9**(8): p. e103191.

111.	Ozcan, E. and T. Cakir, *Reconstructed Metabolic Network Models Predict Flux-Level Metabolic Reprogramming in Glioblastoma.* Front Neurosci, 2016. **10**: p. 156.

112.	Anderson, A.R., *A hybrid mathematical model of solid tumour invasion: the importance of cell adhesion.* Math Med Biol, 2005. **22**(2): p. 163-86.

113.	Reher, D., et al., *Cell adhesion heterogeneity reinforces tumour cell dissemination: novel insights from a mathematical model.* Biol Direct, 2017. **12**(1): p. 18.

114.	Aubert, M., et al., *A cellular automaton model for the migration of glioma cells.* Phys Biol, 2006. **3**(2): p. 93-100.

115. Tracqui, P., *From passive diffusion to active cellular migration in mathematical models of tumour invasion.* Acta Biotheor, 1995. **43**(4): p. 443-64.

116. Anderson, A.R.A., *A Hybrid Multiscale Model of Solid Tumour Growth and Invasion: Evolution and the Microenvironment*, in *Single-Cell-Based Models in Biology and Medicine*, A.R.A. Anderson, M.A.J. Chaplain, and K.A. Rejniak, Editors. 2007, Birkhäuser Basel: Basel. p. 3-28.

117. Sander, L.M., *Modeling contact guidance and invasion by cancer cells.* Cancer Res, 2014. **74**(17): p. 4588-96.

118. Daub, J.T. and R.M. Merks, *A cell-based model of extracellular-matrix-guided endothelial cell migration during angiogenesis.* Bull Math Biol, 2013. **75**(8): p. 1377-99.

119. Hubbard, M.E. and H.M. Byrne, *Multiphase modelling of vascular tumour growth in two spatial dimensions.* J Theor Biol, 2013. **316**: p. 70-89.

120. Spanakis, M., et al., *An in silico estimation of the pharmacokinetic profile and the disposition of GD-DTPA in brain tumor lesions of different vasculature through PBPK models*, in *Neuro-Oncology*2014. p. ii85-ii86.

121. Hormuth, D.A., 2nd, et al., *Predicting in vivo glioma growth with the reaction diffusion equation constrained by quantitative magnetic resonance imaging data.* Phys Biol, 2015. **12**(4): p. 046006.

122. Neal, M.L., et al., *Discriminating survival outcomes in patients with glioblastoma using a simulation-based, patient-specific response metric.* PLoS One, 2013. **8**(1): p. e51951.

123. Azuaje, F., *Computational models for predicting drug responses in cancer research.* Brief Bioinform, 2017. **18**(5): p. 820-829.

124. Jensen, R.L., et al., *Preoperative dynamic contrast-enhanced MRI correlates with molecular markers of hypoxia and vascularity in specific areas of intratumoral microenvironment and is predictive of patient outcome.* Neuro Oncol, 2014. **16**(2): p. 280-91.

125. Protopapa, M., et al., *Clinical implications of in silico mathematical modeling for glioblastoma: a critical review.* Journal of Neuro-Oncology, 2018. **136**(1): p. 1-11.

126. HARALAMPOS HATZIKIROU, A.D., CARLO SCHALLER, MATTHIAS SIMON and KRISTIN SWANSON, *MATHEMATICAL MODELLING OF GLIOBLASTOMA TUMOUR DEVELOPMENT: A REVIEW.* Mathematical Models and Methods in Applied Sciences, 2005. **15**: p. 1779-1794.

127. Michor, F. and K. Beal, *Improving Cancer Treatment via Mathematical Modeling: Surmounting the Challenges Is Worth the Effort.* Cell, 2015. **163**(5): p. 1059-63.

128. Kam, Y., K.A. Rejniak, and A.R. Anderson, *Cellular modeling of cancer invasion: integration of in silico and in vitro approaches.* J Cell Physiol, 2012. **227**(2): p. 431-8.

129. Athale, C., Y. Mansury, and T.S. Deisboeck, *Simulating the impact of a molecular 'decision-process' on cellular phenotype and multicellular patterns in brain tumors.* J Theor Biol, 2005. **233**(4): p. 469-81.

130. Caccavale, J., et al., *A simple and accurate rule-based modeling framework for simulation of autocrine/paracrine stimulation of glioblastoma cell motility and proliferation by L1CAM in 2-D culture.* BMC Syst Biol, 2017. **11**(1): p. 124.

131. Kim, Y., et al., *A mathematical model for pattern formation of glioma cells outside the tumor spheroid core.* J Theor Biol, 2009. **260**(3): p. 359-71.

132. Jeon, J., V. Quaranta, and P.T. Cummings, *An off-lattice hybrid discrete-continuum model of tumor growth and invasion.* Biophys J, 2010. **98**(1): p. 37-47.

133. Gerlee, P. and S. Nelander, *The impact of phenotypic switching on glioblastoma growth and invasion.* PLoS Comput Biol, 2012. **8**(6): p. e1002556.

134. Tektonidis, M., et al., *Identification of intrinsic in vitro cellular mechanisms for glioma invasion.* J Theor Biol, 2011. **287**: p. 131-47.

135. Talkenberger, K., et al., *Amoeboid-mesenchymal migration plasticity promotes invasion only in complex heterogeneous microenvironments.* Sci Rep, 2017. **7**(1): p. 9237.

136. Sottoriva, A., et al., *Cancer stem cell tumor model reveals invasive morphology and increased phenotypical heterogeneity.* Cancer Res, 2010. **70**(1): p. 46-56.

137. Gerlee, P. and A.R. Anderson, *A hybrid cellular automaton model of clonal evolution in cancer: the emergence of the glycolytic phenotype.* J Theor Biol, 2008. **250**(4): p. 705-22.

138. Swan, A., et al., *A Patient-Specific Anisotropic Diffusion Model for Brain Tumour Spread.* Bull Math Biol, 2018. **80**(5): p. 1259-1291.

139. Kim, Y., H. Jeon, and H. Othmer, *The Role of the Tumor Microenvironment in Glioblastoma: A Mathematical Model.* IEEE Trans Biomed Eng, 2017. **64**(3): p. 519-527.

140. Powathil, G.G., et al., *Modelling the effects of cell-cycle heterogeneity on the response of a solid tumour to chemotherapy: biological insights from a hybrid multiscale cellular automaton model.* J Theor Biol, 2012. **308**: p. 1-19.

141. Feng, M., et al., *Machine Learning in Radiation Oncology: Opportunities, Requirements, and Needs.* Frontiers in Oncology, 2018. **8**: p. 110.

142. Piccolo, S.R. and L.J. Frey, *Clinical and molecular models of Glioblastoma multiforme survival.* International journal of data mining and bioinformatics, 2013. **7**(3): p. 245-265.

143. Peer, C.J., C.H. Chau, and W.D. Figg, *Jumping the Barrier: Modeling Drug Penetration across the Blood-Brain Barrier.* Clin Cancer Res, 2017. **23**(24): p. 7437-7439.

144. O'Connor, J.P., et al., *Imaging biomarker roadmap for cancer studies.* Nat Rev Clin Oncol, 2016.

145. Ntziachristos, V., *Going deeper than microscopy: the optical imaging frontier in biology.* Nat Meth, 2010. **7**(8): p. 603-614.

146. Uchida, S., *Image processing and recognition for biological images.* Development, Growth & Differentiation, 2013. **55**(4): p. 523-549.

147. Lauber, D.T., et al., *State of the art in vivo imaging techniques for laboratory animals.* Laboratory Animals, 2017. **51**(5): p. 465-478.

148. Pomper, M.G. and J.S. Lee, *Small animal imaging in drug development.* Curr Pharm Des, 2005. **11**(25): p. 3247-72.

149. Huisken, J., et al., *Optical Sectioning Deep Inside Live Embryos by Selective Plane Illumination Microscopy.* Science, 2004. **305**(5686): p. 1007-1009.

150. O'Connor, J.P., et al., *Imaging biomarker roadmap for cancer studies.* Nat Rev Clin Oncol, 2017. **14**(3): p. 169-186.

151. Jackson, A., et al., *Imaging tumor vascular heterogeneity and angiogenesis using dynamic contrast-enhanced magnetic resonance imaging.* Clin Cancer Res, 2007. **13**(12): p. 3449-59.

152. Inda, M.M., R. Bonavia, and J. Seoane, *Glioblastoma multiforme: a look inside its heterogeneous nature.* Cancers (Basel), 2014. **6**(1): p. 226-39.

153. Goodenberger, M.L. and R.B. Jenkins, *Genetics of adult glioma.* Cancer Genet, 2012. **205**(12): p. 613-21.

154. Atlasi, Y., L. Looijenga, and R. Fodde, *Cancer stem cells, pluripotency, and cellular heterogeneity: a WNTer perspective.* Curr Top Dev Biol, 2014. **107**: p. 373-404.

155. Foty, R., *A simple hanging drop cell culture protocol for generation of 3D spheroids.* J Vis Exp, 2011(51).

156. Zanoni, M., et al., *3D tumor spheroid models for in vitro therapeutic screening: a systematic approach to enhance the biological relevance of data obtained.* Scientific Reports, 2016. **6**: p. 19103.

157. Vinci, M., et al., *Advances in establishment and analysis of three-dimensional tumor spheroid-based functional assays for target validation and drug evaluation.* BMC Biol, 2012. **10**: p. 29.

158. Grotzer, M.A., A. Neve, and M. Baumgartner, *Dissecting brain tumor growth and metastasis in vitro and ex vivo.* Journal of Cancer Metastasis and Treatment, 2016. **2**(5): p. 149-162.

159. Hanahan, D. and R.A. Weinberg, *Hallmarks of cancer: the next generation.* Cell, 2011. **144**(5): p. 646-74.

160. Kiseleva, L.N., et al., *A172 and T98G cell lines characteristics.* Cell and Tissue Biology, 2016. **10**(5): p. 341-348.

161. Stein, G.H., *T98G: an anchorage-independent human tumor cell line that exhibits stationary phase G1 arrest in vitro.* J Cell Physiol, 1979. **99**(1): p. 43-54.

162. Aaberg-Jessen, C., et al., *Invasion of primary glioma- and cell line-derived spheroids implanted into corticostriatal slice cultures.* Int J Clin Exp Pathol, 2013. **6**(4): p. 546-60.

163. Black, P., *Management of malignant glioma: role of surgery in relation to multimodality therapy.* J Neurovirol, 1998. **4**(2): p. 227-36.

164. Jagiella, N., et al., *Inferring Growth Control Mechanisms in Growing Multi-cellular Spheroids of NSCLC Cells from Spatial-Temporal Image Data.* PLoS Comput Biol, 2016. **12**(2): p. e1004412.

165. Hegedus, B., et al., *Locomotion and proliferation of glioblastoma cells in vitro: statistical evaluation of videomicroscopic observations.* J Neurosurg, 2000. **92**(3): p. 428-34.

166. Anderson, A.R.A., et al., *Modelling of Cancer Growth, Evolution and Invasion: Bridging Scales and Models.* Math. Model. Nat. Phenom., 2007. **2**(3): p. 1-29.

167. Bertuzzi, A., et al., *Cell loss and the concept of potential doubling time.* Cytometry, 1997. **29**(1): p. 34-40.

168. Tung, Y.C., et al., *High-throughput 3D spheroid culture and drug testing using a 384 hanging drop array.* Analyst, 2011. **136**(3): p. 473-8.

169. Schneider, C.A., W.S. Rasband, and K.W. Eliceiri, *NIH Image to ImageJ: 25 years of image analysis.* Nat Methods, 2012. **9**(7): p. 671-5.

170. Melicow, M.M., *The three steps to cancer: a new concept of cancerigenesis.* J Theor Biol, 1982. **94**(2): p. 471-511.

171. Guertin, D.A. and D.M. Sabatini, *Cell Size Control*, in *eLS*2001, John Wiley & Sons, Ltd.

172. Stensjoen, A.L., et al., *Growth dynamics of untreated glioblastomas in vivo.* Neuro Oncol, 2015. **17**(10): p. 1402-11.

173. Machado, C.M.L., et al., *Morphological characterization of a human glioma cell l ine.* Cancer Cell International, 2005. **5**: p. 13-13.

174. Atuegwu, N.C., et al., *Parameterizing the Logistic Model of Tumor Growth by DW-MRI and DCE-MRI Data to Predict Treatment Response and Changes in Breast Cancer Cellularity during Neoadjuvant Chemotherapy.* Transl Oncol, 2013. **6**(3): p. 256-64.

175. Frieboes, H.B., et al., *Prediction of drug response in breast cancer using integrative experimental/computational modeling.* Cancer Res, 2009. **69**(10): p. 4484-92.

176. de Jong, M., J. Essers, and W.M. van Weerden, *Imaging preclinical tumour models: improving translational power.* Nat Rev Cancer, 2014. **14**(7): p. 481-93.

177. Tzedakis, G., et al., *The Importance of Neighborhood Scheme Selection in Agent-based Tumor Growth Modeling.* Cancer Inform, 2015. **14**(Suppl 4): p. 67-81.

178. Tzedakis, G., et al. *A hybrid discrete-continuous model of in vitro spheroid tumor growth and drug response*. in *Proceedings of the Annual International Conference of the IEEE Engineering in Medicine and Biology Society, EMBS*. 2016.

179. Douglas, J.J., *Alternating direction methods for three space variables.* Numerische Mathematik, 1962. **4**(1): p. 41-63

180. Wachspress, E.L. and G.J. Habetler, *An Alternating-Direction-Implicit Iteration Technique.* J. Soc. Indust. Appl. Math., 1960. **8**(2): p. 403–423.

181. Barajas, R.F., Jr., et al., *Regional variation in histopathologic features of tumor specimens from treatment-naive glioblastoma correlates with anatomic and physiologic MR Imaging.* Neuro Oncol, 2012. **14**(7): p. 942-54.

182. Charles, N.A., et al., *The brain tumor microenvironment.* Glia, 2011. **59**(8): p. 1169-80.

183. Friedl, P., et al., *Classifying collective cancer cell invasion.* Nat Cell Biol, 2012. **14**(8): p. 777-83.

184. Ilina, O. and P. Friedl, *Mechanisms of collective cell migration at a glance.* J Cell Sci, 2009. **122**(Pt 18): p. 3203-8.

185. Asano, K., et al., *Correlation of N-cadherin expression in high grade gliomas with tissue invasion.* J Neurooncol, 2004. **70**(1): p. 3-15.

186. Iwadate, Y., *Epithelial-mesenchymal transition in glioblastoma progression.* Oncol Lett, 2016. **11**(3): p. 1615-1620.

187. Lewis-Tuffin, L.J., et al., *Misregulated E-cadherin expression associated with an aggressive brain tumor phenotype.* PLoS One, 2010. **5**(10): p. e13665.

188. Noh, M.G., et al., *Prognostic significance of E-cadherin and N-cadherin expression in Gliomas.* BMC Cancer, 2017. **17**(1): p. 583.

189. Peglion, F. and S. Etienne-Manneville, *N-cadherin expression level as a critical indicator of invasion in non-epithelial tumors.* Cell Adh Migr, 2012. **6**(4): p. 327-32.

190. Turner, S.G., M. Ahmad, and S.A. Toms, *Mechanisms of Glioma Cell Invasion*, in *Neurooncology - Newer Developments*, A. Agrawal, Editor 2016, InTech: Rijeka. p. Ch. 05.

191. Euskirchen, P., et al., *Cellular heterogeneity contributes to subtype-specific expression of ZEB1 in human glioblastoma.* PLoS One, 2017. **12**(9): p. e0185376.

192. Alves, T.R., et al., *Glioblastoma cells: A heterogeneous and fatal tumor interacting with the parenchyma.* Life Sciences, 2011. **89**(15–16): p. 532-539.

193. Chen, H.C., *Boyden chamber assay.* Methods Mol Biol, 2005. **294**: p. 15-22.

194. Justus, C.R., et al., *In vitro cell migration and invasion assays.* J Vis Exp, 2014(88).

195. Cisneros Castillo, L.R., et al., *Evaluation of Consistency in Spheroid Invasion Assays.* Sci Rep, 2016. **6**: p. 28375.

196. Grundy, T.J., et al., *Differential response of patient-derived primary glioblastoma cells to environmental stiffness.* Sci Rep, 2016. **6**: p. 23353.

197. Domschke, P., et al., *Mathematical modelling of cancer invasion: implications of cell adhesion variability for tumour infiltrative growth patterns.* J Theor Biol, 2014. **361**: p. 41-60.

198. Moriconi, C., et al., *INSIDIA: A FIJI Macro Delivering High-Throughput and High-Content Spheroid Invasion Analysis.* Biotechnol J, 2017. **12**(10).

199. Oraiopoulou, M.E., et al., *Integrating in vitro experiments with in silico approaches for Glioblastoma invasion: the role of cell-to-cell adhesion heterogeneity.* Scientific Reports, 2018. **8**(1): p. 16200.

200. Deisboeck, T.S., et al., *Pattern of self-organization in tumour systems: complex growth dynamics in a novel brain tumour spheroid model.* Cell Prolif, 2001. **34**(2): p. 115-34.

201. Jensen, S.S., et al., *Establishment and Characterization of a Tumor Stem Cell-Based Glioblastoma Invasion Model.* PLoS One, 2016. **11**(7): p. e0159746.

202. Adamski, V., et al., *Isolation and Characterization of Fast-Migrating Human Glioma Cells in the Progression of Malignant Gliomas.* Oncol Res, 2017. **25**(3): p. 341-353.

203. Perego, C., et al., *Invasive behaviour of glioblastoma cell lines is associated with altered organisation of the cadherin-catenin adhesion system.* J Cell Sci, 2002. **115**(Pt 16): p. 3331-40.

204. Vinci, M., C. Box, and S.A. Eccles, *Three-dimensional (3D) tumor spheroid invasion assay.* J Vis Exp, 2015(99): p. e52686.

205. Mammoto, T., et al., *Role of collagen matrix in tumor angiogenesis and glioblastoma multiforme progression.* Am J Pathol, 2013. **183**(4): p. 1293-305.

206. Breznik, B., et al., *Mesenchymal stem cells differentially affect the invasion of distinct glioblastoma cell lines.* Oncotarget, 2017. **8**(15): p. 25482-25499.

207. Merz, C., et al., *Neutralization of the CD95 ligand by APG101 inhibits invasion of glioma cells in vitro.* Anticancer Drugs, 2015. **26**(7): p. 716-27.

208. Sander, L.M. and T.S. Deisboeck, *Growth patterns of microscopic brain tumors.* Phys Rev E Stat Nonlin Soft Matter Phys, 2002. **66**(5 Pt 1): p. 051901.

209. Malric, L., et al., *Interest of integrins targeting in glioblastoma according to tumor heterogeneity and cancer stem cell paradigm: an update.* Oncotarget, 2017. **8**(49): p. 86947-86968.

210. Chaplain, M.A.J., et al., *Mathematical Modelling of Cancer Invasion: The Importance of Cell-Cell Adhesion and Cell-Matrix Adhesion.* Mathematical Models & Methods in Applied Sciences, 2011. **21**(4): p. 719-743.

211. Hatzikirou, H., et al., *'Go or grow': the key to the emergence of invasion in tumour progression?* Math Med Biol, 2012. **29**(1): p. 49-65.

212. Qiu, Y., P. Li, and C. Ji, *Cell Death Conversion under Hypoxic Condition in Tumor Development and Therapy.* Int J Mol Sci, 2015. **16**(10): p. 25536-51.

213. Mongiardi, M.P., *Angiogenesis and hypoxia in glioblastoma: a focus on cancer stem cells.* CNS Neurol Disord Drug Targets, 2012. **11**(7): p. 878-83.

214. Anderson, A.R.A., M.A.J. Chaplain, and K.A. Rejniak, *Single-cell-based models in biology and medicine.* Mathematics and biosciences in interaction2007, Basel ; Boston: Birkhäuser. ix, 349 p.

215. Dinca, E.B., R.V. Voicu, and A.V. Ciurea, *Bioluminescence imaging of invasive intracranial xenografts: implications for translational research and targeted therapeutics of brain tumors.* Neurosurg Rev, 2010. **33**(4): p. 385-94.

216. Honma, K., T. Miyata, and T. Ochiya, *Type I collagen gene suppresses tumor growth and invasion of malignant human glioma cells.* Cancer Cell Int, 2007. **7**: p. 12.

217. Huijbers, I.J., et al., *A role for fibrillar collagen deposition and the collagen internalization receptor endo180 in glioma invasion.* PLoS One, 2010. **5**(3): p. e9808.

218. Bordeleau, F., L.N. Tang, and C.A. Reinhart-King, *Topographical guidance of 3D tumor cell migration at an interface of collagen densities.* Phys Biol, 2013. **10**(6): p. 065004.

219. Kumar, S., et al., *Viscoelastic retraction of single living stress fibers and its impact on cell shape, cytoskeletal organization, and extracellular matrix mechanics.* Biophys J, 2006. **90**(10): p. 3762-73.

220. Ohnishi, T., et al., *A novel model of glioma cell invasion using organotypic brain slice culture.* Cancer Res, 1998. **58**(14): p. 2935-40.

221. Bender, B.F., A.P. Aijian, and R.L. Garrell, *Digital microfluidics for spheroid-based invasion assays.* Lab Chip, 2016. **16**(8): p. 1505-13.

222. Bertillot, F., et al., *Microfluidic-Based Generation of 3D Collagen Spheres to Investigate Multicellular Spheroid Invasion.* Methods Mol Biol, 2017. **1612**: p. 269-279.

223. Villodre, E.S., et al., *Low Dose of Doxorubicin Potentiates the Effect of Temozolomide in Glioblastoma Cells.* Mol Neurobiol, 2018. **55**(5): p. 4185-4194.

224. Jiang, P., et al., *Novel anti-glioblastoma agents and therapeutic combinations identified from a collection of FDA approved drugs.* J Transl Med, 2014. **12**: p. 13.

225. MacDiarmid, J.A., et al., *Targeted Doxorubicin Delivery to Brain Tumors via Minicells: Proof of Principle Using Dogs with Spontaneously Occurring Tumors as a Model.* PLoS ONE, 2016. **11**(4): p. e0151832.

226. Lesniak, M.S., et al., *Local Delivery of Doxorubicin for the Treatment of Malignant Brain Tumors in Rats.* Anticancer research, 2005. **25**(6B): p. 3825-3831.

227. Ananda, S., et al., *Phase 2 trial of temozolomide and pegylated liposomal doxorubicin in the treatment of patients with glioblastoma multiforme following concurrent radiotherapy and chemotherapy.* Journal of Clinical Neuroscience, 2011. **18**(11): p. 1444-1448.

228. Chua, S.L., et al., *Phase 2 study of temozolomide and Caelyx in patients with recurrent glioblastoma multiforme.* Neuro Oncol, 2004. **6**(1): p. 38-43.

229. Steinbrecher, A., et al., *Adjuvant chemotherapy with temozolomide and liposomal doxorubicin in the first-line therapy of patients with glioblastoma: A phase-II trial.* Journal of Clinical Oncology, 2005. **23**(16_suppl): p. 1539-1539.

230. Gürsoy-Özdemir, Y., S. Bozdağ-Pehlivan, and E. Sekerdag, *Nanotechnology methods for neurological diseases and brain tumors : drug delivery across the blood-brain barrier*. xvi, 361 pages.

231. Verma, J., et al., *Delivery and cytotoxicity of doxorubicin and temozolomide to primary glioblastoma cells using gold nanospheres and gold nanorods*, in *European Journal of Nanomedicine* 2016. p. 49.

232. Treggiari, E., et al., *Temozolomide alone or in combination with doxorubicin as a rescue agent in 37 cases of canine multicentric lymphoma.* Vet Comp Oncol, 2018. **16**(2): p. 194-201.

233. Gagnon, J., N.G. Dervisis, and B.E. Kitchell, *Treatment-related toxicities in tumor-bearing cats treated with temozolomide alone or in combination with doxorubicin: a pilot assessment.* J Feline Med Surg, 2012. **14**(8): p. 560-5.

234. Miyake, K., et al., *The combination of temozolomide-irinotecan regresses a doxorubicin-resistant patient-derived orthotopic xenograft (PDOX) nude-mouse model of recurrent Ewing's sarcoma with a FUS-ERG fusion and CDKN2A deletion: Direction for third-line patient therapy.* Oncotarget, 2017. **8**(61): p. 103129-103136.

235. Weyhenmeyer, B.C., et al., *Predicting the cell death responsiveness and sensitization of glioma cells to TRAIL and temozolomide.* Oncotarget, 2016. **7**(38): p. 61295-61311.

236. Rockne, R.C., et al., *A patient-specific computational model of hypoxia-modulated radiation resistance in glioblastoma using (18)F-FMISO-PET.* Journal of the Royal Society Interface, 2015. **12**(103): p. 20141174.

237. Shukla, G., et al., *Advanced magnetic resonance imaging in glioblastoma: a review.* Chinese Clinical Oncology, 2017. **6**(4).

238. Thomas, R.P., L. Recht, and S. Nagpal, *Advances in the management of glioblastoma: the role of temozolomide and MGMT testing.* Clinical Pharmacology : Advances and Applications, 2013. **5**: p. 1-9.

239. Lee, S.Y., *Temozolomide resistance in glioblastoma multiforme.* Genes & Diseases, 2016. **3**(3): p. 198-210.

240. Newlands, E.S., et al., *Temozolomide: a review of its discovery, chemical properties, pre-clinical development and clinical trials.* Cancer Treatment Reviews, 1997. **23**(1): p. 35-61.

241. Zhou, Q. and J.M. Gallo, *Differential effect of sunitinib on the distribution of temozolomide in an orthotopic glioma model.* Neuro Oncol, 2009. **11**(3): p. 301-10.

242. Knizhnik, A.V., et al., *Survival and death strategies in glioma cells: autophagy, senescence and apoptosis triggered by a single type of temozolomide-induced DNA damage.* PLoS One, 2013. **8**(1): p. e55665.

243. Tiek, D.M., et al., *Alterations in Cell Motility, Proliferation, and Metabolism in Novel Models of Acquired Temozolomide Resistant Glioblastoma.* Scientific Reports, 2018. **8**(1): p. 7222.

244. Bogdanska, M.U., et al., *A mathematical model of low grade gliomas treated with temozolomide and its therapeutical implications.* Math Biosci, 2017. **288**: p. 1-13.

245. Thorn, C.F., et al., *Doxorubicin pathways: pharmacodynamics and adverse effects.* Pharmacogenetics and Genomics, 2011. **21**(7): p. 440-446.

246. Edwardson, D.W., et al., *Role of Drug Metabolism in the Cytotoxicity and Clinical Efficacy of Anthracyclines.* Current Drug Metabolism, 2015. **16**(6): p. 412-426.

247. LLC, N.B., *3D Tumor Spheroid Analysis Method for HTS Drug Discovery using Celigo Imaging Cytometer.*

248. Swietach, P., et al., *Importance of intracellular pH in determining the uptake and efficacy of the weakly basic chemotherapeutic drug, doxorubicin.* PLoS One, 2012. **7**(4): p. e35949.

249. Wei, L., et al., *Dissecting the Mechanisms of Doxorubicin and Oxidative Stress-Induced Cytotoxicity: The Involvement of Actin Cytoskeleton and ROCK1.* PLoS ONE, 2015. **10**(7): p. e0131763.

250. Czeczuga-Semeniuk, E., et al., *The effect of doxorubicin and retinoids on proliferation, necrosis and apoptosis in MCF-7 breast cancer cells.* Folia Histochem Cytobiol, 2004. **42**(4): p. 221-7.

251. Desoize, B. and J. Jardillier, *Multicellular resistance: a paradigm for clinical resistance?* Crit Rev Oncol Hematol, 2000. **36**(2-3): p. 193-207.

252. Motlagh, N.S.H., et al., *Fluorescence properties of several chemotherapy drugs: doxorubicin, paclitaxel and bleomycin.* Biomedical Optics Express, 2016. **7**(6): p. 2400-2406.

253. Pampaloni, F., N. Ansari, and E.H. Stelzer, *High-resolution deep imaging of live cellular spheroids with light-sheet-based fluorescence microscopy.* Cell Tissue Res, 2013. **352**(1): p. 161-77.

254. Amiri, A., et al., *Inhibition of carbonic anhydrase IX in glioblastoma multiforme.* Eur J Pharm Biopharm, 2016. **109**: p. 81-92.

255. Pistollato, F., et al., *Intratumoral hypoxic gradient drives stem cells distribution and MGMT expression in glioblastoma.* Stem Cells, 2010. **28**(5): p. 851-62.

256. Baek, N., et al., *Monitoring the effects of doxorubicin on 3D-spheroid tumor cells in real-time.* Onco Targets Ther, 2016. **9**: p. 7207-7218.

257. Lin, Y.L., M.T. Wu, and F.Y. Yang, *Pharmacokinetics of doxorubicin in glioblastoma multiforme following ultrasound-Induced blood-brain barrier disruption as determined by microdialysis.* J Pharm Biomed Anal, 2018. **149**: p. 482-487.

258. Zhu, Y., et al., *The Biocompatibility of Nanodiamonds and Their Application in Drug Delivery Systems.* Theranostics, 2012. **2**(3): p. 302-312.

259. Park, J., et al., *Evaluation of permeability, doxorubicin delivery, and drug retention in a rat brain tumor model after ultrasound-induced blood-tumor barrier disruption.* J Control Release, 2017. **250**: p. 77-85.

260. Chen, C., et al., *The efficacy of temozolomide for recurrent glioblastoma multiforme.* Eur J Neurol, 2013. **20**(2): p. 223-30.

261. Raza, S.M., et al., *Necrosis and glioblastoma: a friend or a foe? A review and a hypothesis.* Neurosurgery, 2002. **51**(1): p. 2-12; discussion 12-3.

262. Hambsch, P., et al., *Efficient cell death induction in human glioblastoma cells by photodynamic treatment with Tetrahydroporphyrin-Tetratosylat (THPTS) and ionizing irradiation.* Oncotarget, 2017. **8**(42): p. 72411-72423.

263. Varsegi, G.M. and V. Shidham, *Cell block preparation from cytology specimen with predominance of individually scattered cells.* J Vis Exp, 2009(29).

264. Nirmala, C., et al., *Growth characteristics of glioblastoma spheroids.* Int J Oncol, 2001. **19**(6): p. 1109-15.

265. Fulda, S., *Cell death-based treatment of glioblastoma.* Cell Death & Disease, 2018. **9**(2): p. 121.

Original Publications

Research Article

In Vitro/In Silico Study on the Role of Doubling Time Heterogeneity among Primary Glioblastoma Cell Lines

M.-E. Oraiopoulou,[1,2] **E. Tzamali,**[2] **G. Tzedakis,**[2] **A. Vakis,**[1,3]
J. Papamatheakis,[4,5] **and V. Sakkalis**[2]

[1]*Department of Medicine, University of Crete, Heraklion, Greece*
[2]*Computational Bio-Medicine Laboratory, Institute of Computer Science, Foundation for Research and Technology-Hellas, Heraklion, Greece*
[3]*Neurosurgery Clinic, University General Hospital of Heraklion, Heraklion, Greece*
[4]*Gene Expression Laboratory, Institute of Molecular Biology and Biotechnology, Foundation for Research and Technology-Hellas, Heraklion, Greece*
[5]*Department of Biology, University of Crete, Heraklion, Greece*

Correspondence should be addressed to V. Sakkalis; sakkalis@ics.forth.gr

Received 5 May 2017; Accepted 18 September 2017; Published 31 October 2017

Academic Editor: Sara Piccirillo

The application of accurate cancer predictive algorithms validated with experimental data is a field concerning both basic researchers and clinicians, especially regarding a highly aggressive form of cancer, such as Glioblastoma. In an aim to enhance prediction accuracy in realistic patient-specific environments, accounting for both inter- and intratumoral heterogeneity, we use patient-derived Glioblastoma cells from different patients. We focus on cell proliferation using *in vitro* experiments to estimate cell doubling times and sizes for established primary Glioblastoma cell lines. A preclinically driven mathematical model parametrization is accomplished by taking into account the experimental measurements. As a control cell line we use the well-studied U87MG cells. Both *in vitro* and *in silico* results presented support that the variance between tumor staging can be attributed to the differential proliferative capacity of the different Glioblastoma cells. More specifically, the *intratumoral heterogeneity* together with the overall proliferation reflected in both the *proliferation rate* and the *mechanical cell contact inhibition* can predict the *in vitro* evolution of different Glioblastoma cell lines growing under the same conditions. Undoubtedly, additional imaging techniques capable of providing spatial information of tumor cell physiology and microenvironment will enhance our understanding regarding Glioblastoma nature and verify and further improve our predictability.

1. Introduction

Glioblastoma (GB), a grade IV glioma as categorized by the World Health Organization (WHO) [1], is one of the most aggressive brain cancer types [2] with a poor prognosis for the patient [3], despite the rapid advances in technology and novel therapeutics. One of the most characteristic features of GB that limits therapeutic potential is heterogeneity [4]; both different molecular GB subtypes [5, 6] and subclonal cell populations coexist within the same tumor [7–9]. Hence, the importance of individualized GB treatment

and understanding of patient-specific GB pathophysiology is evident and research plans towards this aim are of great interest.

The use of the widely scientifically studied common GB cell lines passaged in lab conditions for decades [10] is nowadays questionable with respect to their clinical relevance in therapeutic outcome prediction and to their ability of representing the extensive heterogeneity observed among patients [11]. To this front, a common GB trend is the use of patient-derived GB cells to enable preclinical physiologic estimations and personalize therapeutic strategy. Basic

researchers cooperate with clinicians in order to isolate GB cells and promote the establishment of short-term primary GB cell cultures [12–15], which provide additional results back to the patient. Established methods for biological research and early drug discovery utilize cell lines grown on plastic culture flasks. Over the years, the ability of these *in vitro* systems to provide biologically relevant answers and describe drug effects is limited due to the fact that they are too simplistic and do not include key players of the phenomenon. Hence, researchers seem to mobilize more realistic experimental approaches such as 3-dimensional (3D) cell cultures [16–20] and/or *ex/in vivo* implantations [14, 21–23] to better imitate cancer in a mechanistic and conditional way. Biological 3D models comprise an important step to describe the early phases of tumor progression before going to the complexity of *in vivo* systems.

Biological experiments are strongly linked with computational and mathematical (*in silico*) models. *In silico* models offer a systematic framework of understanding the underlying biological processes integrating knowledge and information from multiple biological experiments and/or clinical examinations [24]. By predicting the behavior of the system, new targeted experiments can be designed. In that way, the process of mathematical modeling validation is an iterative refinement procedure [25], which terminates when a valid and biologically plausible and concrete description of the system that reproduces the observed cellular behaviors and growth patterns is found. Several mathematical approaches have been proposed to describe the complex, multiscale spatiotemporal tumor evolution. According to their mathematical perspective, these approaches can be classified into continuum and discrete models. Continuous mathematical models are commonly used to describe tumors at tissue level focusing more on the collective, averaged behavior of tumor cells [26–28]. On the other hand, individual-cell-based models using discrete and hybrid discrete-continuous (HDC) mathematics can describe the behavior of each cancer cell individually as it interacts with its microenvironment. Individual-cell-based models are in general more suitable to describe *in vitro* experiments, animal models, and small-sized tumors [29–34].

In general, such mathematical models attempt to translate tumor physiology hallmarks [35] into computational parameters and the predicted output is subsequently validated using as ground truth either the experimental [36, 37] or the clinical results [38, 39]. As it is well-understood, both cell division and local spreading are responsible for cancer expansion [40, 41] comprising the most important aspects for cancer progress [30, 42]. *Doubling time* is defined as the average duration of cell growth and division as reflected by the cell cycle "clock" [43]. GB tumors have a remarkable rapid growth that has a critical role regarding the space-occupation and the development of intracranial pressure, usually the main reason of the GB symptomatology [44]. In previous studies, the significance of the proliferative rate has been shown. More specifically, in [45], the proliferation rates of different breast cancer patients are estimated from subsequent Magnetic Resonance (MR) images in conjunction with a simple logistic tumor growth model and show that the proliferation rate

estimates could discriminate patient's survival and response to therapy. In another study [46], the role of experimental and simulated diffusion gradients in 3D tumors affecting nutrient, oxygen, and drug availability within the tumor and subsequently controlling cell proliferative rate is examined. A mathematical model parameterized from monolayer experiments is used to quantify the diffusion barrier in 3D experiments. In the recent study [40], acquisition of physiologic parameters from multicellular tumor spheroids including proliferation and death spatial profiles is used to constrain and parametrize a mathematical agent-based model that addresses several cell growth mechanisms necessary to explain the experimental observations and reductively translates them to tumor progress over time.

This work utilizes primary tumor cells collected from GB patients and subsequently cultivated *in vitro* as 3D tumor spheroids. As an initial step towards understanding the GB heterogeneity among patients, we focus on proliferation. The aim of this work is first to mathematically study the important components affecting the growth dynamics of tumor spheroids when motility is inhibited, mainly including the inter- and intratumoral heterogeneity with respect to cell proliferation and, second, to parametrize the mathematical model based on experimentally estimated parameter values of primary GB cell lines in order to increase clinical relevance. Doubling times and the average cell sizes of in-house-established primary GB cell lines from three different patients are used. The well-known U87MG GB cell line is also used as control in the experiments. All the biological experiments are performed simultaneously under the same initial and growth conditions. A hybrid, individual, cell-based mathematical model is used to predict the growth curves of the tumor spheroids and parametrized based on the experimental data. Variations in several mathematical model parameters are explored in order to quantify their effect on tumor growth expansion. The simulated results are compared to the experimental data from the relevant 3D cell cultures and show that, in combination with the proliferation rate, additional factors like the mechanical cell contact inhibition are necessary to predict the *in vitro* evolution of the different GB cell lines under study.

2. Methods

2.1. Sampling Procedure. Brain tissue sample is collected from the lesions during biopsy or gross resection of patients with indications of GB based on symptoms and MR images, while still naïve from treatment and later histologically proved to be GB cases. For the purposes of this study, we used the primary cells of three different patients. The first is a 70-year-old male patient with de novo GB close to the left brain motor area, also called GBP03 cells. The second, called GBP06 cell line, was collected from a 47-years-old female patient with a tumor in the medulla proven to be a secondary GB, which was gradually evolved to grade IV from lower grades within a time period of approximately 20 years. The third sample, called GBP08, was provided by a 53-year-old male patient with also primary GB in the temporal-occipital left hemisphere. All samples are anonymously provided with

the informed patients' consent by the Neurosurgical Clinic of the General University Hospital of Heraklion, Crete, Greece, while the protocol has been approved by the Institutional Ethical Committees. Because of the relatively low success rate of the primary cell culture establishment, we are limited to these three GB cases for this work.

2.2. Primary Cell Cultures. Later to tissue sampling in saline solution, the specimens are immediately transferred to the lab where they are mechanically dissociated into smaller parts and supplemented culture medium is added (Dulbecco's modified Eagle medium (DMEM) with 10% fetal bovine serum (FBS) and 1% gentamycin). After gradually removing all cell debris and dead tissue parts, cancer GB cells are cultured as monolayers in standard lab conditions.

As explained before, there is much heterogeneity between GB cases and the protocol of tissue handling is slightly modified per case. An ectopic, subcutaneous implantation to immunodeficient mice is a procedural step that takes place whether the conditional stability cannot be preserved *in vitro* so that it cannot be assured that the isolated GB cells will survive and proliferate in flask. Therefore, lab animals serve as "living incubators" and usually, after the first implantation, the cells are collected and recultured until the cell culture is successfully established. In this work, GBP03 cells are passaged once, while GBP06 and GBP08 cells are directly used. All possible steps are taken to avoid animal suffering at each stage of the experiments.

2.3. Doubling Time Assay. We use the GBP03, GBP06, and GBP08 primary cell lines as well as the U87MG cells (ATCC® HTB-14™, USA) as control line. In order to measure the doubling time intervals of the different cell types used we apply a simple protocol in adherent cultures. In a 24-well plate, 20000 cells/ml of supplemented DMEM are seeded per cell type at day zero. The plate is incubated in standard lab conditions for approximately a week. Whenever needed, cell culture medium is carefully renewed avoiding the adherent (active) cell population to be disturbed.

Every 24 hours after seeding, the culture medium of one well per cell type is removed and trypsin-EDTA (Sigma-Aldrich, Germany) 1x solution is added for 1-2 minutes. After another 1 minute of trituration in order to produce a single cell solution, all the context is removed from the well and is transferred to a 2 ml Eppendorf tube. As a final step, 4% formaldehyde is added to permanently fix the cells within the tube which is stored to the refrigerator for further use. The procedure is repeated up to the point that 100% cell confluence is achieved. The cell concentration for each cell type is measured with a 24-hour interval by using a hemocytometer.

2.4. Cell Size Estimation. A divided Petri dish is plated with a single cell solution of ~2000 cells/ml and is incubated in standard lab conditions overnight to let the cells adhere in the surface of the dish. Accordingly, brightfield images of attached single cells are captured in 40x magnification and known acquisition parameters to an inverted light microscope (Leica, Germany). To check size and shape

homogeneity between each cell population so that to assure that the estimated average cell size will be representative, we capture a photograph of a single cell solution within the fixed grid dimensions of the hemocytometer.

2.5. D Spheroid Generation. We use the hanging-drop technique in order to produce spheroids from each cell type, as recommended in [16, 17, 47]. A single cell solution of 625 cells/50 ul of supplemented double-filtered DMEM is initially seeded per well in a 96-well hanging-drop plate (3D Biomatrix, USA). Two rows of wells per cell type are plated so that approximately 24 spheroids are produced. Agarose solution of 1% w/v is added to plate's reservoirs to prevent evaporation of the droplets. After 2–4 days of cells aggregating at the bottom of each droplet, we can consider that the spheroids are finally formed. The growth progress of the spheroids is monitored over time via photographs taken under set acquisition parameters to an inverted light microscope (Leica, Germany) for predecided critical time points (2-day interval).

2.6. Data Analysis. The average doubling time of each cell line is estimated using exponential linear regression on the doubling time data. The average cell size of each cell line is estimated by segmenting the area of approximately 10 randomly selected cells in brightfield images to ImageJ [48] and averaging. The tumor expansion of the 3D spheroids is again estimated based on the area shown in their brightfield images. The growth curve is estimated by the mean area value ± standard deviation over time. All the above measurements are evaluated per cell type and many experiments are performed for each cell type.

2.7. Computational Model Implementation of Tumor Spheroids. A simplistic HDC mathematical model is used to describe the observed tumor growth of the 3D *in vitro* experiments. In the context of the HDC model, each individual cell is described by a discrete cellular automaton, while the local microenvironment is approximated by partial differential equations (PDE). In the following, a concise description of the HDC model is provided, while more thorough description can be found in [49].

2.7.1. Computational Domain. To simulate a central slice of the 3D *in vitro* tumor spheroids, we set up a 2D regular lattice of size $L = 5$ mm. We assume that each $h \times h$ square lattice site fits a single cell; thus the lattice site defines the cell size as well. The same lattice is used by both the discrete and the continuous compartments.

2.7.2. Continuous Compartment. For simplicity, we assume that oxygen is the only limiting molecule required by the cells in order to proliferate. The spatiotemporal evolution of oxygen is described by the partial differential equation (PDE) shown in (1). Oxygen is assumed to diffuse through the domain with diffusion coefficient D_o, decays naturally at a rate a_o, and is consumed by the tumor cells at a rate γ_o. The

4   BioMed Research International

(a)   (b)   (c)
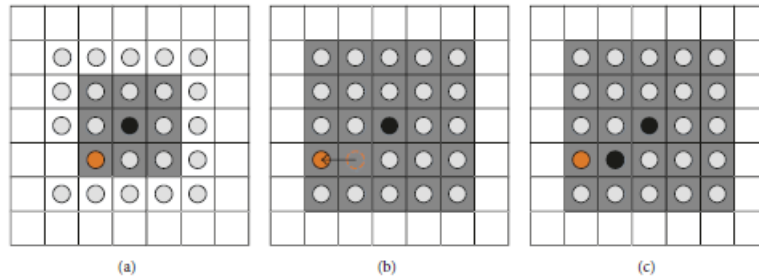
FIGURE 1: Example of a cell (shown in black) attempting to proliferate. Firstly, the cell searches the 1-Moore neighborhood highlighted by the gray squares in (a). Being unable to find an empty space, it searches the 2-Moore neighborhood indicated by the gray squares in (b) and (c). As an empty space is found, the orange cell is pushed towards the empty space as shown in (b). The latter movement frees the empty space on the 1-Moore neighborhood and allows the proliferating cell to place an identical cell (also shown in black) to the adjacent empty space (c).

term $c(i, j)$ is 1 if there is a tumor cell at the location i, j or 0 otherwise.

$$\frac{\partial o(x, y, t)}{\partial t} = D_o \nabla^2 o(x, y, t) - c_{i,j}\gamma_o - \alpha_o o(x, y, t). \quad (1)$$

2.7.3. Discrete Compartment. Each tumor cell is an individual entity with its own traits. Sets of these traits are assumed to represent a cellular phenotype. A more detailed description of the cell life cycle can be found in [49, 50].

In this work, two mechanisms of tumor cells are mainly considered: proliferation and death. Cellular movement has been neglected considering that the protocol of the *in vitro* experiments does not conditionally allow cell motility. Cells die if the local oxygen concentration drops below a defined threshold o_{deadly}. When a cell dies, its location is immediately treated as empty space. On the other hand, the live cells incrementally prepare for proliferation at every time step, until the cell age reaches their doubling time. At that moment, the cell searches for a nearby empty space at the 1-Moore neighborhood. If no empty space is available, the search is expanded to the 2-Moore neighborhood (see Figure 1) and the process is repeated up to r-Moore neighborhood, where r is defined as the proliferation depth and determines the maximum neighborhood size. Examples of Moore neighborhood can be seen in Figure 1. If more than one empty space is found in the same neighborhood, one of them is randomly chosen.

As shown in Figure 1, when an empty space is found on a neighborhood other than the 1-Moore, cells are pushed away from the location of the proliferating cell towards the empty space in order to create an empty space to the 1-Moore neighborhood. Then the cell resets its cell age and places a copy of itself at the adjacent empty space. If no empty space has been found, the cell enters a quiescent state at which it constantly searches for empty space, without further increasing its age. The extended proliferating rim describes the maximum distance over which a cell is capable of pushing other cells away in order to create space for its proliferation and reflects the mechanical growth inhibition processes observed in growing cell populations [40].

3. Results

In this work, the *in vitro* estimated doubling times and cell sizes of three in-house-established primary GB cell lines, as long as of the U87MG cells, are used to initialize the individual-cell-based mathematical model in an attempt to predict their different growth patterns. A sensitivity study is performed where the effects of important factors affecting tumor spheroid expansion such as the doubling time, the cell size, and the depth of the proliferative rim and the coexistence of multiple clones with different proliferative capacities within the tumor are computationally explored. We argue that, as expected, proliferation is one of the most defining characteristics regarding tumor expansion and that tumor predictive computational models should prioritize these remarkable variances between individuals and not just based on theoretically defined values.

3.1. In Vitro 2D Cultures

3.1.1. Cell Size Estimation. A usual answer of what a common human (cancer) cell diameter could be is about 10 to 100 microns [51, 52], and actually, most computational approaches assume cell size within 10–30 microns [29]. In 2D cultures of low confluence, the cell size and shape are in resting state and not crucially influenced by neighboring cells. As depicted in Figure 2, there is much homogeneity in U87MG culture with the cells conforming a rather prolonged typically observed shape, with a soma cell size varying between 19 and 24 microns in diameter (see also Table 1). On the contrast, all primary cells used in our study are smaller and typically round with not many cellular protrusions compared to U87MG cells, yet cells of the same cell line appear to differ within the same population. In case of U87MG cells, it is expected that after all these years in lab conditions there is not much morphological diversity within the cell population and that the cell soma size adequately represents the cell line. On the other hand, regarding primary cells, the cell size is only an average of all possible phenotypes within each cell line. More specifically as denoted in Table 1,
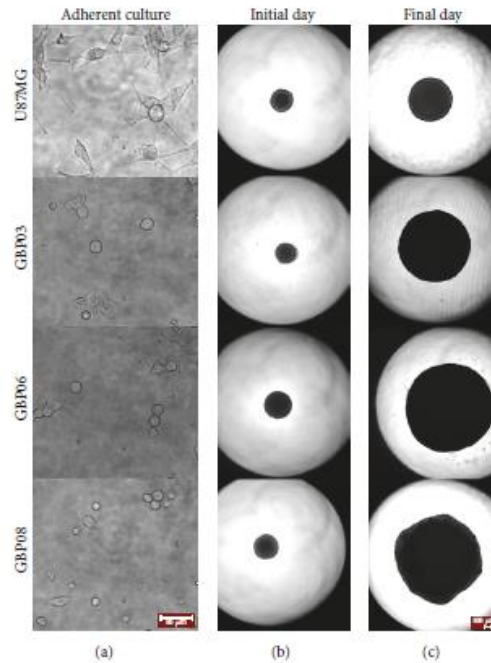
FIGURE 2: U87MG cells along with primary GB cells growing as monolayers ((a) 40x magnification) and as hanging-drop spheroids (initial day in (b) and final day in (c), 4x magnification). Scale bars are 50 and 100 microns, respectively. The initial day is set to be the first day of cell aggregation in spheroidal shape after seeding, meaning Days 2–4. Accordingly, the final day is the time point where spheroids start to deform and decompose, usually approaching well's borders. This day is Day 14 for most primary spheroids.

TABLE 1: Mean cell sizes and doubling times (±standard deviation) as estimated from the *in vitro* experiments for the respective cell lines (first column). The *in silico* values used to initialize the HDC model regarding the doubling time are also shown.

Cell type	*In vitro* estimations		*In silico* values
	Cell diameter (μm)	Doubling time (h)	Doubling time (h)
U87MG	21.5	30.8 ± 2.5	33
GBP03	19	25.4 ± 0.5	25
GBP06	16	23.5 ± 0.7	23
GBP08	15	23.0 ± 1.5	22

GBP03 cells have an average cell diameter of 19 microns, while GBP06 are approximately 16 microns and GBP08 are close to 15 microns in diameter. Also, U87MG cells, when growing in adherent cultures, intrinsically form aggregates when much confluent. On the contrary, the primary cells studied here seem to continue as monolayers no matter the level of confluence. Obviously, the average cell size of a certain cell population, no matter how well represented in 2D, it is not maintained when growing in 3D culturing since other physiological parameters that will be discussed next also affect the cell surface-to-volume ratio altering both size and shape.

3.1.2. Doubling Time Estimation. Based on literature, glioma cells usual doubling time ranges from 24 h to a couple of days [53], but more often established primary GB cell lines are recorded to vary few days [12, 54, 55]. Particularly for U87MG cells, they are supposed to have a population doubling time approximating 34 hours, according to their product sheet (ATCC HTB-14, USA). Our measurements presented in Table 1 are in line with the bibliographic records. Specifically, U87MG cells have a mean doubling time of 30.8 ± 2.5 h, which is the slowest division between the cell types we use. Among the primary cell lines, GBP03 cells divide approximately every 25.4 ± 0.5 h, while GBP06 and GBP08
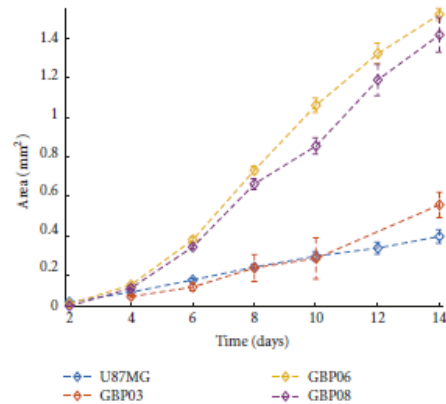
FIGURE 3: Growth of the tumor spheroid area over time for the *in vitro* experiments of each cell line.

have similar doubling times estimated at $23.5 \pm 0.7\,\mathrm{h}$ and $23.0 \pm 1.5\,\mathrm{h}$, respectively.

3.2. In Vitro GB Spheroids. The hanging-drop technique used here to generate the 3D spheroids is a method conditionally approaching the real avascular tumoral state *in vivo* [17]. The spheroid size is determined with optical microscopy and monitored over time. It should be noted that, the imaging approach used here cannot give any quantitative estimate of the compactness of the cells or any other spatial information including the number of the cells, the cell size, shape, and polarity, which are definitely different between 2D and 3D structures.

In general, we observe that both primary and U87MG cells need approximately 4 days from single cell solutions to aggregate into spheroidal structures, while during this starting period, they seem to suppress proliferation capacity. However, most often, primary cells aggregate sooner than U87MG ones after seeding.

Figure 2 illustrates the growth area of the *in vitro* spheroidal domains as imaged in 2D brightfield images at the initial and final day. The growth curves of each cell line are shown in Figure 3. An apparent difference between patients, but also between primary and conventional cell lines, can be observed. To be more specific, all primary spheroids grow larger than the U87MG cells. GBP06 and GBP08 primary spheroids follow an initial fast growing, exponential phase that slows down after approximately 6 days. U87MG spheroids have an almost linear growth pattern. It has to be clarified that the spheroids reach the well's borders before the plateau and decay phases are observed. The patients GBP06 and GBP08 adopt a high growth pattern, while the patient GBP03 follows an intermediate growth rate closer to the U87MG cell line. As already mentioned, especially for the primary cell lines, the initial distribution of the subclones, when plating the cells (Day zero), is random. This eventually

leads to a multifactorial subclonal spheroid growth integrated to average estimations.

3.3. Computational Parameter Study. Prior to parametrizing and predicting the growth pattern of the multicellular spheroids, a simple parameter study is performed to determine the extent at which the doubling time and cell size affect the 3D growth simulation, as well as explore the effect of additional parameters that could play a significant role in tumor expansion including the depth of the proliferative rim and intratumoral heterogeneity.

The discrete and the continuous part of the computational model are parametrized accordingly to meet the experimental setup as shown in Table 2. The length L of the computational domain equals $5\,\mathrm{mm}$ to resemble approximately the size of the hanging-drop plate. Both the oxygen decay rate and the cell's oxygen consumption rate were adopted from [29]. To numerically solve the PDE (1), its parameters have been nondimensionalized by using o_{max}, τ, and L, which correspond to the maximum oxygen concentration, the computational iteration time, and the domain length, respectively. Dirichlet boundary conditions are used to lock the boundaries to the maximum oxygen concentration to simulate the so-assumed adequate and stable nutrients' availability, since the culture medium during the experiment is periodically refreshed. Also, the alternating directions implicit method is used to numerically solve the PDE [56, 57].

At first, we explore the effect of doubling time on tumor expansion keeping the rest modeling parameters constant. Specifically, we assume a tumor cell of size equal to $18\,\mu\mathrm{m}$ and consider a depth of proliferative rim equal to 2 cells, while varying the doubling time from 15.5 h to 35.5 h. Figure 4(a) shows the growth curves of the tumors with different doubling times. As expected, increased proliferative capacity results in increased tumor expansion. If a reference time point is picked at 10 days, we can calculate the absolute

TABLE 2: The computational parameters used to initialize the HDC model.

Parameter	Value
Domain length, L	5 mm (methods-computational domain)
Cell (& lattice) size, h	14–20 μm (methods-computational domain)
Iteration time, τ	8 h (methods-computational domain [49])
Oxygen consumption, γ_0	$6.25 \, 10^{-17}$ M cell^{-1} s^{-1} (methods-computational domain [29])
Maximum oxygen, o_{max}	$6.7 \, 10^{-6}$ M O$_2$ cm^{-3} (methods-continuous compartment [29])
Oxygen decay rate, α_0	0.0125 (ND) (methods-continuous compartment [29, 30, 58])

(a) (b) (c)
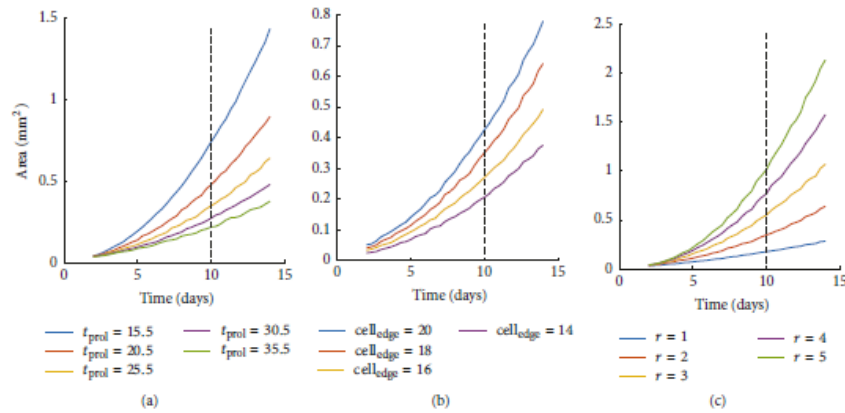
FIGURE 4: Growth of the tumor spheroid area over time as predicted from the computational model related to altering doubling time from 15.5 h to 35.5 h (a), the cell size from 14 to 20 microns (b), and the proliferation depth from 1 to 5 (c).

increase of area yielded by the decrease of the doubling time. When the doubling time is reduced from 35.5 h to 30.5 h, the area increases by approximately 24.46%; while comparing the respective areas between the doubling times 20.5 h and 15.5 h, the area is increased by 54.87%. We can thus conclude that the expansion area is affected more, when the doubling times are lower. As expected, the effect is accumulative; thus if a later/earlier time point was picked the differences would increase/decrease, respectively.

We also explore the effect of cell size on the observable tumor expansion. It should be noted that if counting of the tumor cell population was possible on the *in vitro* experiments, then this parameter would make no difference. We vary the cell size from 14 to 20 μm, while keeping the doubling time constant and equal to 25.5 h and the proliferation depth equal to 2 cells. Figure 4(b) shows that, by increasing the cell size, the tumor expansion increases as well, as expected. Indicatively, by comparing the values at simulation time 10 days, the area relatively increases by 21.5%, 29.8%, and 31.1% as the cell size increases from 14 μm, 16 μm, and 18 μm to 16 μm, 18 μm, and 20 μm, respectively.

The depth of the proliferative rim significantly affects the tumor expansion as it increases the number of proliferative cells. Figure 4(c) illustrates the effect that different

proliferation depths have on the tumor area over time. The proliferation time was set to 25.5 h and the cell size to 18 μm. At the reference point of 10 days, as the proliferation depth increases from 1 to 5 cells with a step of 1 cell, the area increases relatively to its previous value by 94.7%, 58.4%, 38.9%, and 31.3%. In other words, a considerable higher expansion of the tumor area (94.7%) is observed when the proliferation depth is increased from 1 to 2, as compared to a change from depth 4 to 5. As the proliferation depth increases, less cells enter the quiescent state and proliferate instead; this is why the growth area is increased.

To further investigate the role of heterogeneity between our cases, we proceed by performing simulations which contain multiple phenotypes identical in all traits except for their respective doubling time. All phenotypes have their cell size set to 18 μm and proliferation depth (r) equal to 2 cells. The proliferation time is randomly selected for each phenotype at the beginning of the simulation from a uniform distribution in the interval (15.5, 35.5) hours. As shown in Figure 5, to illustrate the impact of the phenotypic multitude, two scenarios are considered inspired by [29]: one at which the number of phenotypes is 100 (shown in green line) and another where 10 phenotypes are randomly selected (shown in purple line). Additionally, given the randomness
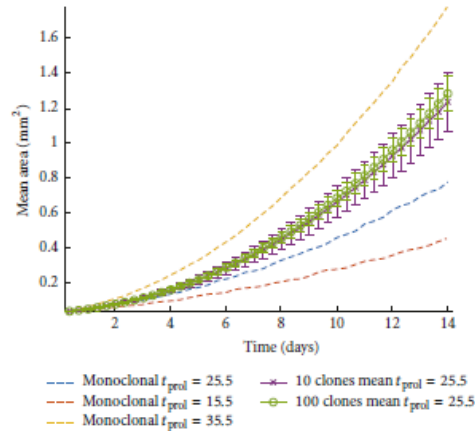
FIGURE 5: Monoclonal and polyclonal tumor area expansion. For the polyclonal case two scenarios are considered: one at which the number of phenotypes is 100 (green line) and another where 10 phenotypes are randomly selected (purple line). Each experiment is repeated 50 times and the corresponding standard deviation is also shown. The mean area of three monoclonal examples with doubling times 15.5 h (red dashed line), 25.5 h (blue dashed line), and 35.5 h (yellow dashed line) is also illustrated.
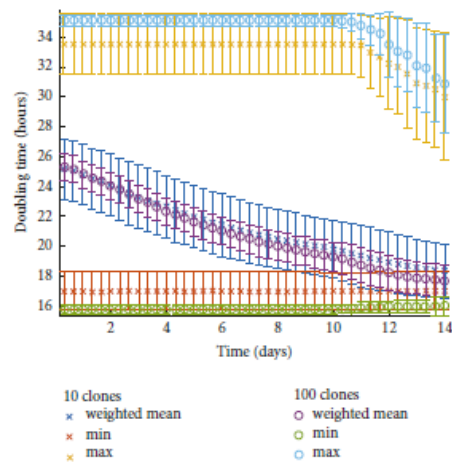

FIGURE 6: Doubling time of the populations that survive over time in a polyclonal tumor. Two scenarios are considered: one at which the number of phenotypes is 100 and another where 10 phenotypes are randomly selected. Each experiment is repeated 50 times. The minimum, maximum, and average doubling times for both scenarios are shown, as well as their corresponding standard deviations.

of the phenotypic initialization, each experimental scenario is repeated 50 times. Figure 5 also shows the area expansion over time for three monoclonal examples with doubling times 15.5 h (red dashed line), 25.5 h (blue dashed line), and 35.5 h (yellow dashed line). Figure 6 illustrates the doubling time of the populations that survive over time. As it can be seen, the mean minimum and the mean maximum values

of the doubling time are constant for a long period of time indicating the presence of both the fastest and the slowest populations within the tumor, yet the frequency of these populations becomes progressively unequal with the fastest population to actually overpopulate within the tumor. Thus, a decline to minimum values of the mean doubling time is observed.
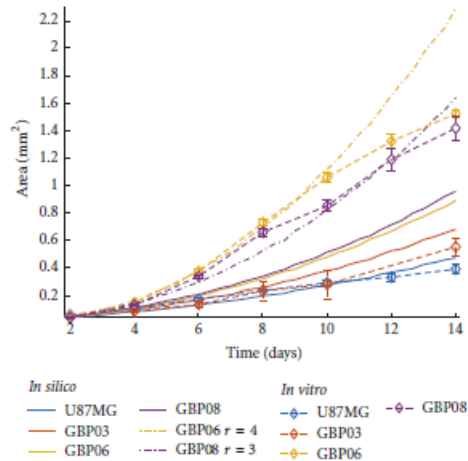
BioMed Research International 9

FIGURE 7: *In vitro* spheroidal growth as opposed to *in silico* for all four cell types with the final chosen sets of doubling times as shown in Table 1 and fixed proliferation depth equal to 2. Two additional simulated growth curves are depicted with different proliferation depth values for the GBP06 ($r = 4$, yellow dash dotted line) and the GBP08 ($r = 3$, purple dash dotted line) spheroids.

3.4. Comparison of Biological and Computational Results. In the following, we assume monoclonal populations and parametrize the mathematical model based on the estimated experimental values for the doubling time and cell size for the different GB cell lines. We also parameterize the model without taking into account the *in vitro* estimates of cell sizes and keep the cell size and all the other parameters constant in all the experiments. Parameters within the range of the experimental biological observations are chosen to achieve the best-fitting growth curves. It has to be noted that both the simulated and the biological experiments have an initial seeding population of approximately 625 cells per spheroid per cell type. The simulations show that the *in vitro* estimates of cell sizes do not improve the model predictability and that accounting only for differences in doubling time among GB lines results in very similar growth curves.

Table 1 shows the parameters used by the *in silico* model regarding the doubling time. Figure 7 shows the *in vitro* growth curves and the *in silico* predicted ones for all the GB cell lines. Based on the selected doubling time values and keeping the proliferation depth equal to 2, the growth curves of U87MG and GBP03 cell lines are closely approximated by the *in silico* model. However, the GBP06 and GBP08 cell lines diverge significantly from the *in vitro* results indicating that proliferation alone is necessary, but not sufficient to explain the tumor expansion of different GB cell lines growing under the same initial conditions. Hence, additional phenomena should be taken into account. For example, increasing the proliferative depth and/or consider the possibility that multiple phenotypes with various proliferative capacities coexist within such tumors, then the *in vitro* and *in silico* growth curves would come in line as our parameter study analysis

previously revealed. Alternatively one could advocate that GBP06 and GBP08 contain phenotypes with higher proliferation depth than U87MG (and GBP03) which are expected to thrive in compact environments such as a solid spheroid. It should be noted that the proliferative depth could also be affected by the development of extracellular matrix (ECM) substrate in 3D cultures, even in the conditional absence of a relevant substrate [17], as in our biological experiments. This, along with antagonistic and synergetic relationships of subclones within the growing spheroid, could alter the mechanical responses of dividing cells, reflected in terms of proliferation depth to our mathematical model. However, our biological approach did not take into account a priori this parameter, but it was the computational approach that indicates such possible behavior suggesting that ECM production and distribution might also be different in different cell lines.

Figure 7 also shows the simulated growth curves for the GBP06 and GBP08 after changing their proliferation depth values from 2 to 4 and 3, respectively. The *in vitro* data better correlate the relevant *in silico* data. Also notice that setting the proliferation depth of GBP06 higher than the GBP08 is important to achieve their corresponding growth patterns, where GBP06 grows faster than GBP08, given that the doubling time of the former is higher than the latter and that small differences in their cell sizes are not adequate to reverse their growth patterns. Another point that should be marked is that the subsequent decline observed after Day 8 in the *in vitro* growth curves of these two cell types cannot be predicted by the computational model. This is because the computational model we use does not account for inhibitory stimuli that are probably developed in real growing tumors, since this was beyond the scope of this study.

10

4. Discussion

This work utilizes primary tumor cells collected from GB patients and subsequently cultivated *in vitro* as 3D tumor spheroids and computational approaches to study, experimentally parametrize, and predict the growth dynamics of tumor spheroids focusing on proliferation. At first, a parameter study is performed in order to evaluate the extent to which important factors such as the doubling time, the cell size, and the depth of the proliferative rim, as well as the coexistence of multiple clones with different proliferative capacities within the tumor, affect tumor spheroid expansion when motility is inhibited. The experimentally estimated doubling times and cell sizes of three in-house-established primary GB cell lines, as long as of the U87MG cells, are then used to parametrize the computational individual-cell-based model.

Overall the parameter study verifies the significant effect of proliferation (depicted in both the cellular doubling time and the depth of the proliferative rim) on tumor expansion [40] and underlines additional factors that could play an important role on tumor growth curves including the intratumoral heterogeneity that has been widely observed in GB. We also observe that a multiclonal population with the same mean proliferation exhibits a greater tumor expansion than the corresponding monoclonal population because fitter clones survive over time driving tumor expansion at higher rates. Furthermore, the clonal heterogeneity within the tumor mass allows different clones to be selected every time an experiment is performed. Thus, a variation is observed in the growth curves. The variance is cumulative, increases over time, and can reach a difference of 100 μm in radius after 14 days of growth (Figure 5). Furthermore, the simulations also show that although the mean growth curves are quite similar, the variance highly depends on the initial number of different clones coexisting within the tumor mass such that fewer initial clones in the population produce higher variability (Figure 6).

Comparing the *in vitro* experiments with the *in silico* predictions, we observe that although the proliferation rate is necessary, yet it is not sufficient, to describe the growth curves we observe experimentally. The simulations show that additional factors including the intratumoral heterogeneity together with the overall proliferative capacity reflected in both the proliferation rate and the mechanical cell contact inhibition can predict the evolution of different GB cell lines. Nevertheless, further investigation of the underlying mechanisms is critical.

In general, compactness of the spheroids can be assigned to two factors in mesoscopic terms: (a) the cellularity, in means of cells' size and shape given the space, and (b) the levels of stress tolerance, reflecting their response against internal forces within the spheroid which vary between division and entering quiescence state, also known as "*contact inhibition.*" As smaller in size and quicker regarding divisions, GBP06 and GBP08 cells appear to grow larger in 3D over time than the other two cell types mainly because of their promoted proliferative capacity reflected by the higher proliferation depth in the respective simulated growth curves (see

Figure 7). However, this is only an assumption for our *in silico* trials since there is no indication of spheroids cell density and proliferation depth to our experimental protocol and this is a limitation of our method needed to be taken into account in future work.

The migratory capability of our cells is conditionally blocked to our experiments so that it can be assumed to play a minor role in the proliferative characteristics studied here. However, when the different cell populations grow in 3D, both ECM can be produced, and the cell shape and polarity could also be affected, such that cell-to-cell and cell-to-matrix adhesion properties could be further explain the divergence observed over time in growth patterns between the *in vitro* and *in silico* experiments.

We suggest that, instead of using bibliographic values usually referenced by common GB cell lines, cell doubling time was found to critically enhance the *in silico* predictability but is insufficient to holistically describe differences in tumor growth over time among the different GB cell lines. The mechanical cell responses to internal forces obtained during the growth of a compact tumor should be further investigated experimentally, as well as the important role of intratumoral heterogeneity. The importance of quantitative methods to provide spatial information of proliferative, quiescent, and necrotic cells as well as additional features including the remodeling of ECM and phenotypic distribution regarding intratumoral heterogeneity affecting tumor expansion becomes evident.

5. Conclusions

The massive proliferation is a defining characteristic of the tumor nature, essential for its progress. When focusing on such a greed form of cancer, such as GB, constantly growing intra-axially and aggressively disturbing brain functionality, proliferation underlying processes become incompatible in cancer progress. In GB, heterogeneity is another typical hallmark, not only among patients with differences between GB molecular subtypes, but more unexpectedly, between different regions of the same tumor with the presence of intratumoral subclonal dormancies. We claim that future research should be based on primary cells directly collected from patients and that common cell lines should only serve as landmarks to unite studies of different groups. For every primary established cell line, not only molecular but also physiological parameters should be estimated to enable a more precise future clustering of different GB cases. Estimations starting with the typical doubling time as shown here and evolving to more delicate features such as delineation of necrotic and hypoxic regions or invasive capability or others are highly important. To this front, computational models may serve as predictor tools not only for estimating cancer progress [59], but also for designing targeted biological experiments. Simulations of cancer progress, either *in vitro* or *in silico*, should not anymore be based on theoretical values, especially if clinical translation is of interest. If we target the holistic description of tumor evolution, we should follow a stepwise approach, where computational tools can definitely

help in identifying the most important parameters affecting the final outcome.

Conflicts of Interest

The authors declare that there are no conflicts of interest regarding the publication of this paper.

Acknowledgments

References

[1] D. N. Louis, A. Perry, G. Reifenberger et al., "The 2016 World Health Organization Classification of Tumors of the Central Nervous System: a summary," *Acta Neuropathologica*, vol. 131, no. 6, pp. 803–820, 2016.

[2] D. Schiffer, *Brain tumor pathology: current diagnostic hotspots and pitfalls*, Springer, Dordrecht, Netherlands, 2006.

[3] D. Sturm et al., *Hotspot Mutations in H3F3A And IDH1 Define Distinct Epigenetic And Biological Subgroups of Glioblastoma*, vol. 22, no. 4, pp. 425–437, 2012.

[4] M.-D. Inda, R. Bonavia, and J. Seoane, "Glioblastoma multiforme:A look inside its heterogeneous nature," *Cancers*, vol. 6, no. 1, pp. 226–239, 2014.

[5] M. L. Goodenberger and R. B. Jenkins, "Genetics of adult glioma," *Cancer Genetics*, vol. 205, no. 12, pp. 613–621, 2012.

[6] F. Ali-Osman, "Brain tumors," in *Contemporary Cancer Research*, p. 393, Humana Press, Totowa , NJ, USA, 2005.

[7] A. Sottoriva, I. Spiteri, S. G. M. Piccirillo et al., "Intratumor heterogeneity in human glioblastoma reflects cancer evolutionary dynamics," *Proceedings of the National Acadamy of Sciences of the United States of America*, vol. 110, no. 10, pp. 4009–4014, 2013.

[8] Y. Atlasi, L. Looijenga, and R. Fodde, "Cancer Stem Cells, Pluripotency, and Cellular Heterogeneity. A WNTer Perspective.," *Current Topics in Developmental Biology*, vol. 107, pp. 373–404, 2014.

[9] J. Chen, R. M. McKay, and L. F. Parada, "Malignant glioma: Lessons from genomics, mouse models, and stem cells," *Cell*, vol. 149, no. 1, pp. 36–47, 2012.

[10] M. J. Clark, N. Homer, B. D. O'Connor et al., "U87MG decoded: the genomic sequence of a cytogenetically aberrant human cancer cell line," *PLoS Genetics*, vol. 6, no. 1, Article ID e1000832, 2010.

[11] M. Allen, M. Bjerke, H. Edlund, S. Nelander, and B. Westermark, "Origin of the U87MG glioma cell line: Good news and bad news," *Science Translational Medicine*, vol. 8, no. 354, Article ID 354re3, 2016.

[12] C. S. Mullins, B. Schneider, F. Stockhammer, M. Krohn, C. F. Classen, and M. Linnebacher, "Establishment and Characterization of Primary Glioblastoma Cell Lines from Fresh and Frozen Material: A Detailed Comparison," *PLoS ONE*, vol. 8, no. 8, Article ID e71070, 2013.

[13] L. F. Pavon, L. C. Marti, T. T. Sibov et al., "In vitro analysis of neurospheres derived from glioblastoma primary culture: A novel methodology paradigm," *Frontiers in Neurology*, vol. 4, Article ID Article 214, 2014.

[14] B. L. Carlson, J. L. Pokorny, M. A. Schroeder, and J. N. Sarkaria, "Establishment, maintenance and in vitro and in vivo applications of primary human glioblastoma multiforme (GBM) xenograft models for translational biology studies and drug discovery," in *Curr Protoc Pharmacol*, vol. 14, Chapter 14, unit 14.16, 2011.

[15] K. M. Joo, J. Kim, J. Jin et al., "Patient-Specific Orthotopic Glioblastoma Xenograft Models Recapitulate the Histopathology and Biology of Human Glioblastomas In Situ," *Cell Reports*, vol. 3, no. 1, pp. 260–273, 2013.

[16] R. Foty, "A simple hanging drop cell culture protocol for generation of 3D spheroids," *Journal of Visualized Experiments*, no. 51, Article ID e2720, 2011.

[17] White paper, *5 Reasons Cancer Researchers Adopt 3D Cell Culture: A Review of Recent Literature*, 3D Biomatrix Inc., Michigan, USA, 2013.

[18] J. Friedrich, C. Seidel, R. Ebner, and L. A. Kunz-Schughart, "Spheroid-based drug screen: considerations and practical approach," *Nature Protocols*, vol. 4, no. 3, pp. 309–324, 2009.

[19] M. Zanoni, F. Piccinini, C. Arienti et al., "3D tumor spheroid models for in vitro therapeutic screening: A systematic approach to enhance the biological relevance of data obtained," *Scientific Reports*, vol. 6, Article ID 19103, 2016.

[20] M. Vinci, S. Gowan, F. Boxall et al., "Advances in establishment and analysis of three-dimensional tumor spheroid-based functional assays for target validation and drug evaluation," *BMC Biology*, vol. 10, article no. 29, 2012.

[21] M. A. Grotzer, A. Neve, and M. Baumgartner, "Dissecting brain tumor growth and metastasis *in vitro* and *ex vivo*," *Journal of Cancer Metastasis and Treatment*, vol. 2, no. 5, pp. 149–162, 2016.

[22] R. A. Morgan, "Human tumor xenografts: The good, the bad, and the ugly," *Molecular Therapy*, vol. 20, no. 5, pp. 882–884, 2012.

[23] T. Voskoglou-Nomikos, J. L. Pater, and L. Seymour, "Clinical predictive value of the in vitro cell line, human xenograft, and mouse allograft preclinical cancer models," *Clinical Cancer Research*, vol. 9, no. 11, pp. 4227–4239, 2003.

[24] V. Sakkalis, S. Sfakianakis, E. Tzamali et al., "Web-based workflow planning platform supporting the design and execution of complex multiscale cancer models," *IEEE Journal of Biomedical and Health Informatics*, vol. 18, no. 3, pp. 824–831, 2014.

[25] A. Roniotis, K. Marias, V. Sakkalis, G. D. Tsibidis, and M. Zervakis, "A complete mathematical study of a 3D model of heterogeneous and anisotropic glioma evolution," in *Proceedings of the 31st Annual International Conference of the IEEE Engineering in Medicine and Biology Society: Engineering the Future of Biomedicine, EMBC 2009*, pp. 2807–2810, usa, September 2009.

[26] A. Gerisch and M. A. Chaplain, "Mathematical modelling of cancer cell invasion of tissue: local and non-local models and the effect of adhesion," *Journal of Theoretical Biology*, vol. 250, no. 4, pp. 684–704, 2008.

[27] K. R. Swanson, R. C. Rockne, J. Claridge, M. A. Chaplain, E. C. Alvord Jr., and A. R. A. Anderson, "Quantifying the role of angiogenesis in malignant progression of gliomas: In Silico modeling integrates imaging and histology," *Cancer Research*, vol. 71, no. 24, pp. 7366–7375, 2011.

[28] S. M. Wise, J. S. Lowengrub, H. B. Frieboes, and V. Cristini, "Three-dimensional multispecies nonlinear tumor growth—I: Model and numerical method," *Journal of Theoretical Biology*, vol. 253, no. 3, pp. 524–543, 2008.

12

[29] A. R. A. Anderson, "A hybrid mathematical model of solid tumour invasion: the importance of cell adhesion," *Mathematical Medicine and Biology*, vol. 22, no. 2, pp. 163–186, 2005.

[30] A. R. Anderson, K. A. Rejniak, P. Gerlee, and V. Quaranta, "Modelling of cancer growth, evolution and invasion: bridging scales and models," *Mathematical Modelling of Natural Phenomena*, vol. 2, no. 3, pp. 1–29, 2007.

[31] F. Michor and K. Beal, "Improving Cancer Treatment via Mathematical Modeling: Surmounting the Challenges Is Worth the Effort," *Cell*, vol. 163, no. 5, pp. 1059–1063, 2015.

[32] J. P. O'Connor et al., "Imaging biomarker roadmap for cancer studies," *Nature Reviews Clinical Oncology*, 2016.

[33] A. L. Baldock, R. C. Rockne, A. D. Boone et al., "From patient-specific mathematical neuro-oncology to precision medicine," *Front Oncol*, vol. 3, p. 62, 2013.

[34] J. S. Lowengrub, H. B. Frieboes, F. Jin et al., "Nonlinear modelling of cancer: bridging the gap between cells and tumours," *Nonlinearity*, vol. 23, no. 1, pp. R1–R91, 2010.

[35] M. G. McNamara, S. Sahebjam, and W. P. Mason, "Emerging biomarkers in glioblastoma," *Cancers*, vol. 5, no. 3, pp. 1103–1119, 2013.

[36] J. C. Anderson, C. W. Duarte, K. Welaya et al., "Kinomic exploration of temozolomide and radiation resistance in Glioblastoma multiforme xenolines," *Radiotherapy & Oncology*, vol. 111, no. 3, pp. 468–474, 2014.

[37] C. Athale, Y. Mansury, and T. S. Deisboeck, "Simulating the impact of a molecular 'decision-process' on cellular phenotype and multicellular patterns in brain tumors," *Journal of Theoretical Biology*, vol. 233, no. 4, pp. 469–481, 2005.

[38] T. E. Yankeelov, N. Atuegwu, D. Hormuth et al., "Clinically relevant modeling of tumor growth and treatment response," *Science Translational Medicine*, vol. 5, no. 187, p. 187ps9, 2013.

[39] M. De Jong, J. Essers, and W. M. Van Weerden, "Imaging preclinical tumour models: Improving translational power," *Nature Reviews Cancer*, vol. 14, no. 7, pp. 481–493, 2014.

[40] N. Jagiella, B. Müller, M. Müller, I. E. Vignon-Clementel, and D. Drasdo, "Inferring Growth Control Mechanisms in Growing Multi-cellular Spheroids of NSCLC Cells from Spatial-Temporal Image Data," *PLoS Computational Biology*, vol. 12, no. 2, Article ID e1004412, 2016.

[41] B. Hegedüs, A. Czirók, I. Fazekas, T. Bábel, E. Madarász, and T. Vicsek, "Locomotion and proliferation of glioblastoma cells in vitro: Statistical evaluation of videomicroscopic observations," *Journal of Neurosurgery*, vol. 92, no. 3, pp. 428–434, 2000.

[42] D. Hanahan and R. A. Weinberg, "Hallmarks of cancer: the next generation," *Cell*, vol. 144, no. 5, pp. 646–674, 2011.

[43] A. Bertuzzi, A. Gandolfi, C. Sinisgalli, G. Starace, and P. Ubezio, "Cell loss and the concept of potential doubling time," *Cytometry*, vol. 29, no. 1, pp. 34–40, 1997.

[44] P. Black, "Management of malignant glioma: role of surgery in relation to multimodality therapy," *Journal of NeuroVirology*, vol. 4, no. 2, pp. 227–236, 1998.

[45] N. C. Atuegwu, L. R. Arlinghaus, X. Li et al., "Parameterizing the logistic model of tumor growth by DW-MRI and DCE-MRI data to predict treatment response and changes in breast cancer cellularity during neoadjuvant chemotherapy," *Translational Oncology*, vol. 6, no. 3, pp. 256–264, 2013.

[46] H. B. Frieboes, M. E. Edgerton, J. P. Fruehauf et al., "Prediction of drug response in breast cancer using integrative experimental/computational modeling," *Cancer Research*, vol. 69, no. 10, pp. 4484–4492, 2009.

[47] Y.-C. Tung, A. Y. Hsiao, S. G. Allen, Y.-S. Torisawa, M. Ho, and S. Takayama, "High-throughput 3D spheroid culture and drug testing using a 384 hanging drop array," *Analyst*, vol. 136, no. 3, pp. 473–478, 2011.

[48] C. A. Schneider, W. S. Rasband, and K. W. Eliceiri, "NIH Image to ImageJ: 25 years of image analysis," *Nature Methods*, vol. 9, no. 7, pp. 671–675, 2012.

[49] G. Tzedakis, E. Tzamali, K. Marias, and V. Sakkalis, "The importance of neighborhood scheme selection in agent-based tumor growth modeling," *Cancer Informatics*, vol. 14, pp. 67–81, 2015.

[50] G. Tzedakis, E. Liapis, E. Tzamali, G. Zacharakis, and V. Sakkalis, "A hybrid discrete-continuous model of in vitro spheroid tumor growth and drug response," in *Proceedings of the 38th Annual International Conference of the IEEE Engineering in Medicine and Biology Society, EMBC 2016*, pp. 6142–6145, usa, August 2016.

[51] M. M. Melicow, "The three steps to cancer: a new concept of cancerigenesis," *Journal of Theoretical Biology*, vol. 94, no. 2, pp. 471–511, 1982.

[52] D. A. Guertin and D. M. Sabatini, *Cell Size Control, in in eLS2001*, Hoboken, NJ, United States, John Wiley & Sons, in eLS2001, 2001.

[53] A. L. Stensjoen et al., "Growth dynamics of untreated glioblastomas in vivo," *Neuro-Oncology*, vol. 17, no. 10, pp. 1402–1411, 2015.

[54] E. Sandén, S. Eberstål, E. Visse, P. Siesjö, and A. Darabi, "A standardized and reproducible protocol for serum-free monolayer culturing of primary paediatric brain tumours to be utilized for therapeutic assays," *Scientific Reports*, vol. 5, Article ID 12218, 2015.

[55] C. M. L. Machado, A. Schenka, J. Vassallo et al., "Morphological characterization of a human glioma cell line," *Cancer Cell International*, vol. 5, article no. 13, 2005.

[56] J. Douglas, "Alternating direction methods for three space variables," *Numerische Mathematik*, vol. 4, pp. 41–63, 1962.

[57] E. L. Wachspress and G. J. Habetler, "An alternating-direction-implicit iteration technique," *Journal of the Society for Industrial and Applied Mathematics*, vol. 8, pp. 403–423, 1960.

[58] P. Hinow, P. Gerlee, L. J. McCawley et al., "A spatial model of tumor-host interaction: application of chemotherapy," *Mathematical Biosciences and Engineering*, vol. 6, no. 3, pp. 521–546, 2009.

[59] E. Skounakis et al., "DoctorEye: A clinically driven multifunctional platform, for accurate processing of tumors in medical images," *The Open Medical Informatics Journal*, vol. 4, no. 3, pp. 105–115, 2010.

SCIENTIFIC REP⚙RTS

Integrating *in vitro* experiments with *in silico* approaches for Glioblastoma invasion: the role of cell-to-cell adhesion heterogeneity

M.-E. Oraiopoulou [1,2], E. Tzamali [2], G. Tzedakis [2], E. Liapis [3,7], G. Zacharakis [3], A. Vakis [1,4], J. Papamatheakis [5,6] & V. Sakkalis [2]

Glioblastoma cells adopt migration strategies to invade into the brain parenchyma ranging from individual to collective mechanisms, whose role and dynamics are not yet fully understood. In this work, we explore Glioblastoma heterogeneity and recapitulate its invasive patterns both *in vitro*, by utilizing primary cells along with the U87MG cell line, and *in silico*, by adopting discrete, individual cell-based mathematics. Glioblastoma cells are cultured three-dimensionally in an ECM-like substrate. The primary Glioblastoma spheroids adopt a novel cohesive pattern, mimicking perivascular invasion in the brain, while the U87MG adopt a typical, starburst invasive pattern under the same experimental setup. Mathematically, we focus on the role of the intrinsic heterogeneity with respect to cell-to-cell adhesion. Our proposed mathematical approach mimics the invasive morphologies observed *in vitro* and predicts the dynamics of tumour expansion. The role of the proliferation and migration is also explored showing that their effect on tumour morphology is different per cell type. The proposed model suggests that allowing cell-to-cell adhesive heterogeneity within the tumour population is sufficient for variable invasive morphologies to emerge which remain originally undetectable by conventional imaging, indicating that exploration in pathological samples is needed to improve our understanding and reveal potential patient-specific therapeutic targets.

Glioblastoma (GB) is a very aggressive, highly infiltrative[1,2] cancer of the Central Nervous System classified as grade IV glioma by the World Health Organization with multiple molecular subtypes[3] and extensive intra-[4] and inter-patient heterogeneity[5,6]. GB cells migrate into the neighbouring brain parenchyma and expand, characterizing GB as a diffusive rather than a focal disease[7]. It becomes evident that it is virtually impossible from a technical point of view to totally exempt the patient from the malignancy even in the case of gross resection[8]. As a result, tumour relapse may occur[9] in the original or nearby brain regions[10] from the invasive cells that are left over. On top of that, broad heterogeneity in GBs has been identified at the genotype, phenotype and molecular evolution level even within the same tumour, whereas spatially distinct tumour samples display different subtypes[11]. Inter-and intra-tumoural heterogeneity is a major biological property of GB tumours that reflects the continuous, spontaneous, and/or drug-driven evolution of cancer cells. GB is subject to clonal and epigenetic evolution, as well as microenvironmental forces that all together result in recurrence, therapy resistance and poor prognosis in spite of recent advances. The dynamic interplay of various sub-populations that coexist within a tumour further limits progress in implementing novel, effective treatment strategies. Although current treatment usually alleviates the symptoms, GB remains a clinical challenge exhibiting very poor prognosis with less than 10% of

[1]Department of Medicine, University of Crete, Heraklion, Crete, Greece. [2]Computational Bio-Medicine Laboratory, Institute of Computer Science, Foundation for Research and Technology-Hellas, Heraklion, Crete, Greece. [3]Institute of Electronic Structure and Laser, Foundation for Research and Technology-Hellas, Heraklion, Crete, Greece. [4]Neurosurgery Clinic, University General Hospital of Heraklion, Crete, Greece. [5]Gene Expression Laboratory, Institute of Molecular Biology and Biotechnology, Foundation for Research and Technology-Hellas, Heraklion, Crete, Greece. [6]Department of Biology, University of Crete, Heraklion, Crete, Greece. [7]Present address: Helmholtz Zentrum München, German Research Center for Environmental Health (GmbH), Neuherberg, Germany. Correspondence and requests for materials should be addressed to V.S. (email: sakkalis@ics.forth.gr)
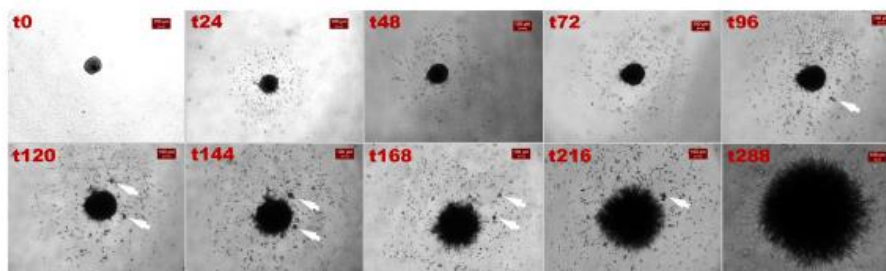
Figure 1. Invasion of the U87MG spheroids over time. Brightfield images at a 4x magnification and scalebar is set at 100 μm. White arrows indicate cell aggregates.
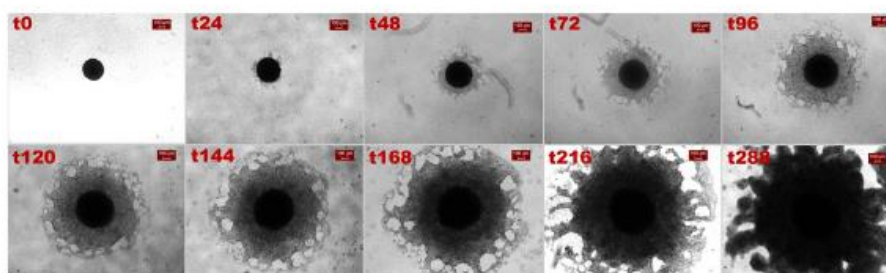

Figure 2. Invasion of the primary GB spheroids over time. Brightfield images at a 4x magnification and scalebar is set at 100 μm.

Results

***In vitro* experiments.** The invasion of primary and U87MG GB spheroids was studied in this work. Doubling time estimation experiments (as described in the Supplementary text) showed that both cell types are highly proliferative with cell population mean doubling times of 30.8 h and 25.4 h for the U87MG and the primary cell line, respectively. In the 3D invasion assay, cell migration was fully ECM-dependent, since no invasion was observed in its absence. Spheroids were monitored over a total period of 12 days and the invasive patterns formed were consistently observed in all the experiments per cell type.

Invasive pattern of U87MG cells over time. Fig. 1 presents consecutive brightfield images of a representative U87MG spheroid undergoing invasion within a 24-hour time interval (excluding the last two images, t216 and t288). As shown in Fig. 1, U87MG cells exhibited an immediate invasive phenotype within the first 24 h after seeding. They extended symmetrically from the core maternal spheroid towards the periphery, within the ECM-like substrate, following a non-cohesive migration pattern. In accordance with relevant studies[24,28,35], random prolonged cellular protrusions were also observed; yet no noticeable cell path track in the ECM was detected in the brightfield images. This type of outgrowth behaviour continues until approximately 72 h with slight variation. After 96 h, the most distant cells had reached the boundaries of the well. In line with previous reports[35], at this time, satellite cell clusters were also starting to form, and invasion adopted a more complex dynamic behaviour. Interestingly, after 288 h of allowed invasive condition with no nutritional exhaustion, the surrounding aggregates seemed to deform, whilst the maternal spheroid, that had remarkably grown, had no more defined borders, while all peripheral cells were prolonged.

Invasive pattern of primary cells over time. Primary GB spheroids adopted an apparently alternative, cohesive invasive morphology with boundary instabilities, not reported before in relevant studies[12,20,30,36,37]. Fig. 2 illustrates the evolution of the invasion pattern of a representative primary spheroid. The same invasive pattern was consistently observed in all primary GB spheroids of the same patient that we tested. Initially, few invasive cells seem to asymmetrically exit away from the maternal core spheroid towards the periphery. At intermediate time points, the invading cells appear to collectively form a cohesive, sheet-like structure (as described in[12]). Finally, in the following time points, until 288 h, the invasive pattern appears unaltered, but still enhanced.

Growth dynamics of tumour spheroids. Fig. 3 shows the temporal evolution of the average values of the core and invasive radii from all the experiments for both the U87MG and the primary spheroids, based on the segmented brightfield images. The time evolution of the negative control experiments is also depicted.
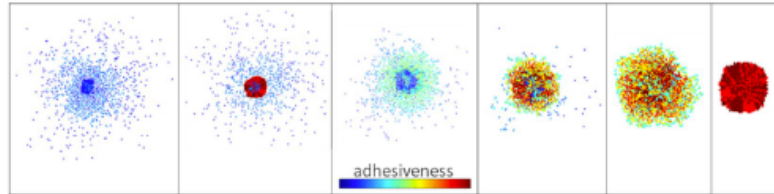
Figure 4. Snapshots of various morphologies emerging by combining phenotypes with different cell-to-cell adhesion properties. Cell-to-cell adhesiveness ranges from 0 (blue) to 7 (red) colour indicating low to strongly adhesive phenotypes, respectively. All snapshots are captured at the end of the simulation process, which corresponds to 112, 160, 144, 184, 216 and 216 h respectively, from left to right.
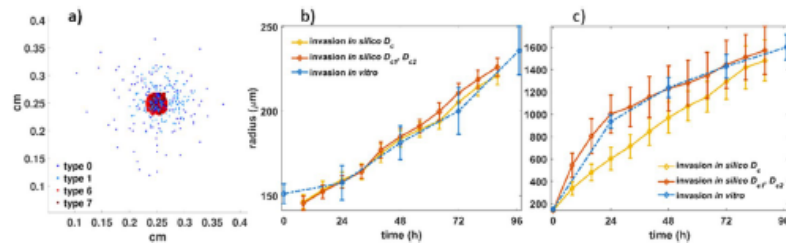

Figure 5. *In silico* predictions of the U87MG cell type: (**a**) Snapshot of the simulated U87MG spheroid at 96 h (left), (**b**) the temporal evolution of the core radius, and (**c**) the invasive radius for both the *in vitro* and *in silico* experiments over time.
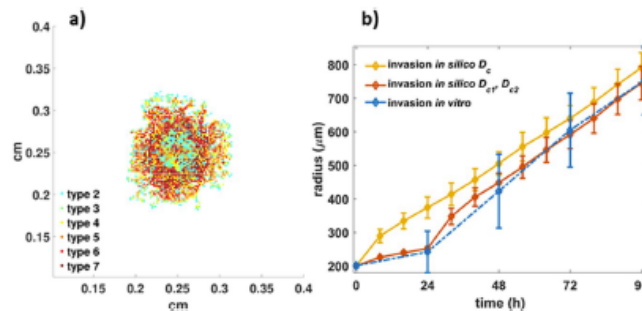
Figure 6. *In silico* predictions of the primary cell type: (**a**) snapshot of the simulated primary spheroid at 96 h (left), (**b**) the temporal evolution of the invasive radius of both the *in vitro* and *in silico* experiments.

We should note that alternative combinations of phenotypes may possibly produce similar results, as for example using only the middle adhesive phenotypes. However, as can be seen in Supplementary Text: Fig. I, in that case the tumour compactness initially decreases and only after a period of time increases forming a compact core. On the contrary, including phenotypes with high adhesion, an almost immediate increase in tumour compactness was observed, better resembling the core expansion of the *in vitro* experiments. The diffusion coefficient was set to $D_c = 2 \cdot 10^{-8} \, cm^2/s$ and the proliferation time was set to 25 h, in accordance to the doubling time estimate. A snapshot at 152 h of the tumour evolution is illustrated in Fig. 6a (see also Supplementary video SV2 and the Supplementary Text: Fig. K). As can be seen in Fig. 6b, apart from the trapped cells in the core, we can observe that relatively low adhesive phenotypes (types 2, 3, 4) tend to appear in the tips of the tumour sprouts, while phenotypes with relatively stronger cell-to-cell adhesive interactions (types 5, 6 and 7) are more likely to be found closer to the tumour core. Interestingly, all phenotypes coexist within the tumour, increasing their populations as

equal contribution of all phenotypes in the tumour composition introduces an eventual decrease of the overall cell population and tumour expansion and prompts the formation of a denser tumour (Supplementary Text: Figs BB and CC), similar to the morphology observed after 120 h in the respective biological experiment (Fig. 2). Thus, allowing random phenotype transition in both cases could possibly predict the morphologies observed at later time points, although alternative mechanisms triggered by the evolving tumour microenvironment and not necessary requiring mitosis could account for these morphologies too. Even more, a microenvironmental regulated phenotypic switch could also be a potential mechanism explaining the evolution of the invasion pattern.

Discussion

In this work, we explored the invasive potential of GB cells using a rather simple, but yet realistic, set of experimental parameters. We utilized patient-derived cancer cells of a GB patient along with the established and commonly used U87MG cell line. GB cells are cultured in 3D in an ECM-like substrate. Our biological experiments show that the two types of tumour spheroids display considerably distinct invasive patterns suggesting different mechanisms of cell migration. In an attempt to explore possible mechanisms involved, an individual cell-based mathematical approach was adopted to indicate the potential role of the intrinsic heterogeneity with respect to cell-to-cell adhesion on tumour morphology and growth dynamics.

We implemented the 3D tumour spheroid invasion assay[28,38] in order to investigate the initial steps of invasion from spheroids formed using single cell suspensions. The main advantage of this assay as compared to standard trans-well assays is that it can recapitulate the basic 3D structure of tumours and replicate features of collective cell invasion observed *in vivo*. In addition, this is a simple, quick and standardized assay that enables analysis of invasion with high reproducibility in a 96-well plate format. However, we should note that monitoring of invasion in the existing 3D spheroid invasion assays relies on brightfield imaging of the spheroid from the bottom of 96-well U-plates, which confines microscopic analysis of 3D spheroids to a 2D plane leading to exclusion of cell clusters invading in the depth dimension.

Based on the *in vitro* invasive protocol followed here, the two GB cell lines used, exhibited a markedly different invasive pattern. In consistence with other studies[24,28,36,38–41], U87MG cells appeared to colonize the ECM via a process indicating non-cohesive, starburst migration. On the other hand, the GB primary spheroids kept expanding to massively conquer the surrounding regions rather than individually migrating potentially governed by homotypic attraction[42]. A unique, collective invasive pattern with morphological instabilities of cohesive protrusions near the boundary resembling perivascular invasion in the brain[29] was observed. It is well recognized that exploring the physiological and molecular patterns of these cells might enable the design of novel therapeutics targeting the recurrence process. The ability to early detect the phenotypic composition of an evolving tumour is undoubtedly of significant prognostic value.

In order to further investigate potential intrinsic mechanisms involved in the invasion patterns observed, an individual-cell-based computational model accounting for intratumoural heterogeneity was developed. More specifically, different cell-to-cell adhesive properties adopted by the GB cells were assumed, although additional or even alternative mechanisms could also play a role in the observed tumour behaviour. Reher *et al.*[19] have extensively studied mathematically the role of cell adhesion heterogeneity specifically on cell dissemination, opening the question of whether this heterogeneity is present in gliomas and how it affects the migration mechanisms and tumour morphology. In support to our work, recent studies[14–21] have shown differential expression of cadherins, as well as observable disorganization and instability in cell-to-cell interactions within various GB cell lines. Primary cells most usually overexpress cell adhesion molecules, such as integrins or cadherins, whilst common/established cell lines do not[19,43–45]. Furthermore, complementing cell-to-cell, cell-to-ECM interactions were also shown computationally to play an important role in tumour invasion, with cell-to-cell interactions affecting predominantly the invasion pattern and cell-to-ECM influencing the invasion speed[33,46]. A variety of mathematical models have been developed to describe the emergence of invasion in cancer cells and GB specifically, as summarized in Alfonso *et al.*[32]. Yet, to the best of our knowledge, none of these studies focuses on the formation of invasive patterns, by taking into account the interplay of co-existing phenotypes with different cell-to-cell adhesion properties on tumour evolution and morphology. In this work, tumour expansion and morphology were explored and compared with the *in vitro* experimental data. Tumour expansion was quantitatively evaluated based on the temporal growth of the tumour spheroid core and the invasive radii. Furthermore, additional metrics including the locally derived sparseness and compactness were used to describe the morphologies. In general, tumour expansion is attributed to both the proliferative and migratory capacity of tumour cells. Thus, their role on tumour morphology and evolution was also investigated under the proposed framework.

Interestingly, we showed that by selecting (during model initialization) phenotypes with different cell-to-cell adhesion preference to coexist within the tumour is sufficient to resemble the distinct invasion patterns and the expansion rates we observed *in vitro* between the primary and the U87MG cells. We also observed that variation in proliferation time and diffusion coefficient affects overall the tumour compactness, sparseness, as well as the tumour expansion rates and changes the relative frequency of phenotypes according to cell type, indicating potential mechanisms that could alter tumour evolution and inhibit invasion. Forcing a strong dependence between adhesiveness and proliferation to mimic a potential "go-or-grow" mechanism (Supplementary Text: Figs M and N), we observed that although for the U87MG cells such hypothesis could possibly apply, proliferation plays a more complex and important role for the primary cells under the specific modelling assumptions. Interestingly, we also observed that by allowing cells to randomly switch phenotypes throughout tumour evolution, the self-organization of cells, reflected in the diverse frequency of each phenotype, was lost and all phenotypes involved have equal representation in the population with an impact on the evolution of the primary cell type. More specifically, in the primary tumours, we observed that by disabling the phenotypic switch, both the total tumour population and expansion increased, indicating that random phenotypic switch with respect to cell-to-cell adhesion does not favour tumour evolution.

to preserve conditional stability and support the GB cells' survival, aggregation and proliferation. Aliquots of zero stage, as well as various passages of *in vitro* cell tissue were cryopreserved, nucleic acids were extracted for further analysis and immunohistopathology was performed. The average doubling time intervals were estimated following a simple protocol in adherent cultures for both the established primary GB culture and the U87MG cell line which was used as a control (as described in[64]). All possible steps and procedures have been approved by the Institutional Ethical Committees.

Invasion assay. GB spheroids were generated using the hanging-drop technique. The 3D spheroids were formed in a Perfecta3D 96-well hanging drop plate (3D Biomatrix, USA) by seeding a single cell suspension solution of approximately 600 cells/50 μl of supplemented DMEM per well for each cell type used. An agarose solution of 1% w/v was added to the plate's reservoirs to prevent evaporation of the droplets.

After 4 days of spheroid formation, twenty spheroids per each cell type were transferred to a 96-well U-bottom plate, initially cooled on ice for 15–20 minutes. The invasion solution was made by diluting ice-cold BME Pathclear (Basement Membrane Extracts, Amsbio, Cultrex®, UK) in supplemented DMEM in a 1:1 ratio. In the U-bottom plate, 100 μl of the invasion solution was added per well containing either a primary or a U87MG spheroid. Subsequently, the U-bottom plate was centrifuged for 5 minutes at 300 rpm, at 4 °C in order to place the spheroids in the centre of each well, homogeneously distribute the invasion matrix and eliminate bubbles within it. Incubation for 1 hour at 37 °C was followed to allow solidification of the matrix. As a final step, 100 μl of warm supplemented DMEM was added per well and the plate was placed at a 37 °C humidified cell culture incubator to promote invasion to the semi-solid gel-like ECM matrix.

Negative control. As a negative control experiment, spheroids of each cell line were examined by means of growing in the absence of the ECM-like substrate (i.e. in supplemented DMEM-F12 alone). It should be noted that none of the cell lines used exhibit invasion in the absence of ECM and no exogenous ECM is required for the spheroid formation via the hanging drop technique.

Image segmentation and analysis. Spheroids were monitored using a Leica DFC310 FX inverse wide-field fluorescence microscope (Leica, Germany) over a total period of up to 12 days and photographed every 24 h, using a 4x objective lens and fixed acquisition parameters. The brightfield images were semi-automatically segmented in Matlab 6.1 (The MathWorks Inc., Natick, MA, USA).

Tumour expansion kinetics were evaluated based on: i) the time evolution of the tumour spheroid core, and ii) time evolution of the overall invasive rim[65]. The whole invasive area was measured by estimating the maximum radius taken from the core centre that encloses all the invasive cells. To estimate the invasive rim, the radius of the core maternal spheroid was subtracted from the whole invasive radius. The invasive kinetic profile was quantitatively generated by statistically analysing all results over time with regression analysis of mean values ± standard deviation.

Mathematical approach. In cellular automaton (CA) models, each tumour cell operates individually (i.e. grows, divides, moves and dies) and interacts locally with other neighbouring cells following a set of biologically-inspired rules. CA models have been also extended to hybrid discrete-continuous (HDC) models in an attempt to additionally describe the interactions between cells and the microenvironment. These models integrate data from both experimental and/or clinical sources and have been widely used to describe critical aspects of tumour evolution and invasion, including genotype to phenotype relations[66], inter- and intra-tumoral heterogeneity[19,67], the effect of autocrine/paracrine signalling on cell proliferation and motility[66,68], cell-to-cell and cell-to-matrix adhesion[33,51,67,69,70], phenotypic plasticity[71-73], the formation of invasive branches[74], evolutionary dynamics[75,76], the interplay with the brain anatomic features[77,78] and the microenvironmental factors[79], as well as treatment outcomes[80,81].

In this work, we build on the HDC model originally proposed by Anderson[33], but modify several aspects. Specifically, in order to focus on cell-to-cell adhesion, we consider the ECM to be a homogeneous passive scaffold where cells are allowed to migrate, but matrix degradation and remodelling are not considered. In our HDC approach, the phenotypic properties of the tumour cells include proliferation, motility, cell-to-cell adhesion, oxygen consumption and death. We assume that cell properties are intrinsic properties that are not regulated by the microenvironment. We account for heterogeneous cell populations, which differ only with respect to cell-to-cell adhesion properties. The rest phenotypic properties of the cells are kept the same for all cells, unless otherwise stated. The cell adhesive property is applied during cell movement and generalizes the attractive rule used in Aubert *et al.*[70]. Specifically, this property describes a cell's preference to bind with a variable number of other cells in its new position. Thus, cells select their preferred neighbourhood as they move. Cells with low cell-to-cell adhesive properties prefer empty neighbourhoods, whereas cells with high adhesive properties are attracted towards highly populated areas. Cell movement approximates a random walk in a 2D regular lattice, but it is biased towards the adhesion preference of the cell. Cell division is a fundamental process that may change cell phenotype based on genetic, epigenetic, and/or stochastic decisions. If explicitly stated, inspired by its biological counterpart, we additionally introduced an intrinsic state transition probability, where cells are allowed to stochastically switch phenotype regarding cell-to-cell adhesion only during proliferation and with probability p_{mut}. Otherwise it is assumed that the adhesive property is inherited by the daughter cells during proliferation and it is fixed throughout tumour evolution. We assumed oxygen to be the only limiting source needed by the tumor cells to grow.

Cell processes are updated asynchronously and randomly (see Supplementary Text: *In silico* methods). This ensures that in each iteration every cell arbitrarily receives a different priority in the update queue. Cell movement

Description of phenotypes. Phenotypes with different adhesion preferences were allowed to coexist and interact within the tumour. The different phenotypes are referred based on their preference adhesion value. A phenotype with low adhesion value corresponds to a cell with loose cell-to-cell adhesive interactions that prefers to be alone, while a phenotype with high adhesive value implies that a cell forms strong adhesive interactions, attracted by high populated neighbourhoods. We categorize our phenotypes as follows: we call phenotypes with adhesion preference 0 and 1, low adhesive; phenotypes with preference 6 and 7, highly adhesive; and those with adhesion preference in [2, 5], middle adhesive phenotypes.

Data Availability

All data generated and analysed during this study are included in this published article (and its Supplementary Information files).

References

1. Ellis, H. P. *et al.* Current Challenges in Glioblastoma: Intratumour Heterogeneity, Residual Disease, and Models to Predict Disease Recurrence. *Frontiers in oncology* **5**, 251, https://doi.org/10.3389/fonc.2015.00251 (2015).
2. Brat, D. J. *et al.* Pseudopalisades in glioblastoma are hypoxic, express extracellular matrix proteases, and are formed by an actively migrating cell population. *Cancer Res* **64**, 920–927 (2004).
3. Louis, D. N. *et al.* The World Health Organization Classification of Tumors of the Central Nervous System: a summary. *Acta Neuropathol* **131**, 803–820, https://doi.org/10.1007/s00401-016-1545-1 (2016).
4. Greaves, M. & Maley, C. C. Clonal evolution in cancer. *Nature* **481**, 306–313, https://doi.org/10.1038/nature10762 (2012).
5. Inda, M. M., Bonavia, R. & Seoane, J. Glioblastoma multiforme: a look inside its heterogeneous nature. *Cancers (Basel)* **6**, 226–239, https://doi.org/10.3390/cancers6010226 (2014).
6. Sturm, D. *et al.* Hotspot mutations in H3F3A and IDH1 define distinct epigenetic and biological subgroups of glioblastoma. *Cancer Cell* **22**, 425–437, https://doi.org/10.1016/j.ccr.2012.08.024 (2012).
7. Claes, A., Idema, A. J. & Wesseling, P. Diffuse glioma growth: a guerilla war. *Acta Neuropathol* **114**, 443–458, https://doi.org/10.1007/s00401-007-0293-7 (2007).
8. Lacroix, M. *et al.* A multivariate analysis of 416 patients with glioblastoma multiforme: prognosis, extent of resection, and survival. *Journal of Neurosurgery* **95**, 190–198, https://doi.org/10.3171/jns.2001.95.2.0190 (2001).
9. Ramakrishna, R. & Rostomily, R. Seed, soil, and beyond: The basic biology of brain metastasis. *Surg Neurol Int* **4**, S256–264, https://doi.org/10.4103/2152-7806.111303 (2013).
10. Hou, L. C., Veeravagu, A., Hsu, A. R. & Tse, V. C. Recurrent glioblastoma multiforme: a review of natural history and management options. *Neurosurg Focus* **20**, E5 (2006).
11. Sottoriva, A. *et al.* Intratumor heterogeneity in human glioblastoma reflects cancer evolutionary dynamics. *Proc Natl Acad Sci USA* **110**, 4009–4014, https://doi.org/10.1073/pnas.1219747110 (2013).
12. Friedl, P., Locker, J., Sahai, E. & Segall, J. E. Classifying collective cancer cell invasion. *Nat Cell Biol* **14**, 777–783, https://doi.org/10.1038/ncb2548 (2012).
13. Ilina, O. & Friedl, P. Mechanisms of collective cell migration at a glance. *J Cell Sci* **122**, 3203–3208, https://doi.org/10.1242/jcs.036525 (2009).
14. Asano, K. *et al.* Correlation of N-cadherin expression in high grade gliomas with tissue invasion. *J Neurooncol* **70**, 3–15 (2004).
15. Iwadate, Y. Epithelial-mesenchymal transition in glioblastoma progression. *Oncol Lett* **11**, 1615–1620, https://doi.org/10.3892/ol.2016.4113 (2016).
16. Lewis-Tuffin, L. J. *et al.* Misregulated E-cadherin expression associated with an aggressive brain tumor phenotype. *PLoS One* **5**, e13665, https://doi.org/10.1371/journal.pone.0013665 (2010).
17. Noh, M. G. *et al.* Prognostic significance of E-cadherin and N-cadherin expression in Gliomas. *BMC Cancer* **17**, 583, https://doi.org/10.1186/s12885-017-3591-z (2017).
18. Peglion, F. & Etienne-Manneville, S. N-cadherin expression level as a critical indicator of invasion in non-epithelial tumors. *Cell Adh Migr* **6**, 327–332, https://doi.org/10.4161/cam.20855 (2012).
19. Reher, D., Klink, B., Deutsch, A. & Voss-Bohme, A. Cell adhesion heterogeneity reinforces tumour cell dissemination: novel insights from a mathematical model. *Biol Direct* **12**, 18, https://doi.org/10.1186/s13062-017-0188-z (2017).
20. Turner, S. G., Ahmad, M. & Toms, S. A. In *Neurooncology - Newer Developments* (ed. Agrawal A.) Ch. 05 (InTech 2016).
21. Euskirchen, P. *et al.* Cellular heterogeneity contributes to subtype-specific expression of ZEB1 in human glioblastoma. *PLoS One* **12**, e0185376, https://doi.org/10.1371/journal.pone.0185376 (2017).
22. Chen, H. C. Boyden chamber assay. *Methods Mol Biol* **294**, 15–22 (2005).
23. Justus, C. R., Leffler, N., Ruiz-Echevarria, M. & Yang, L. V. In vitro cell migration and invasion assays. *J Vis Exp*, https://doi.org/10.3791/51046 (2014).
24. Cisneros Castillo, L. R., Oancea, A. D., Stullein, C. & Regnier-Vigouroux, A. Evaluation of Consistency in Spheroid Invasion Assays. *Sci Rep* **6**, 28375, https://doi.org/10.1038/srep28375 (2016).
25. Chen, J., McKay, R. M. & Parada, L. F. Malignant glioma: lessons from genomics, mouse models, and stem cells. *Cell* **149**, 36–47, https://doi.org/10.1016/j.cell.2012.03.009 (2012).
26. Carlson, B. L., Pokorny, J. L., Schroeder, M. A. & Sarkaria, J. N. Establishment, maintenance and in vitro and in vivo applications of primary human glioblastoma multiforme (GBM) xenograft models for translational biology studies and drug discovery. *Curr Protoc Pharmacol* Chapter 14, Unit 14 16, https://doi.org/10.1002/0471141755.ph1416s52 (2011).
27. White paper - 5 Reasons Cancer Researchers Adopt 3D Cell Culture: A Review of Recent Literature. *3D Biomatrix Inc* (2013).
28. Vinci, M. *et al.* Advances in establishment and analysis of three-dimensional tumor spheroid-based functional assays for target validation and drug evaluation. *BMC Biol* **10**, 29, https://doi.org/10.1186/1741-7007-10-29 (2012).
29. Gritsenko, P., Leenders, W. & Friedl, P. Recapitulating in vivo-like plasticity of glioma cell invasion along blood vessels and in astrocyte-rich stroma. *Histochem Cell Biol*. https://doi.org/10.1007/s00418-017-1604-2 (2017).
30. Grundy, T. J. *et al.* Differential response of patient-derived primary glioblastoma cells to environmental stiffness. *Sci Rep* **6**, 23353, https://doi.org/10.1038/srep23353 (2016).
31. Protopapa, M. *et al.* Clinical implications of in silico mathematical modeling for glioblastoma: a critical review. *Journal of Neuro-Oncology* **136**, 1–11, https://doi.org/10.1007/s11060-017-2650-2 (2018).
32. Alfonso, J. C. L. *et al.* The biology and mathematical modelling of glioma invasion: a review. *J R Soc Interface* **14**, https://doi.org/10.1098/rsif.2017.0490 (2017).
33. Anderson, A. R. A hybrid mathematical model of solid tumour invasion: the importance of cell adhesion. *Math Med Biol* **22**, 163–186, https://doi.org/10.1093/imammb/dqi005 (2005).
34. Domschke, P., Trucu, D., Gerisch, A. & M, A. J. C. Mathematical modelling of cancer invasion: implications of cell adhesion variability for tumour infiltrative growth patterns. *Journal of theoretical biology* **361**, 41–60, https://doi.org/10.1016/j.jtbi.2014.07.010 (2014).

74. Jiao, Y. & Torquato, S. Emergent behaviors from a cellular automaton model for invasive tumor growth in heterogeneous microenvironments. *PLoS Comput Biol* **7**, e1002314, https://doi.org/10.1371/journal.pcbi.1002314 (2011).
75. Sottoriva, A. *et al.* Cancer stem cell tumor model reveals invasive morphology and increased phenotypical heterogeneity. *Cancer research* **70**, 46–56, https://doi.org/10.1158/0008-5472.CAN-09-3663 (2010).
76. Gerlee, P. & Anderson, A. R. A hybrid cellular automaton model of clonal evolution in cancer: the emergence of the glycolytic phenotype. *Journal of theoretical biology* **250**, 705–722, https://doi.org/10.1016/j.jtbi.2007.10.038 (2008).
77. Yankeelov, T. E. Integrating Imaging Data into Predictive Biomathematical and Biophysical Models of Cancer. *ISRN Biomath* **2012**, https://doi.org/10.5402/2012/287394 (2012).
78. Swan, A., Hillen, T., Bowman, J. C. & Murtha, A. D. A Patient-Specific Anisotropic Diffusion Model for Brain Tumour Spread. *Bull Math Biol* **80**, 1259–1291, https://doi.org/10.1007/s11538-017-0271-8 (2018).
79. Kim, Y., Jeon, H. & Othmer, H. The Role of the Tumor Microenvironment in Glioblastoma: A Mathematical Model. *IEEE Trans Biomed Eng* **64**, 519–527, https://doi.org/10.1109/TBME.2016.2637828 (2017).
80. Yankeelov, T. E. *et al.* Clinically relevant modeling of tumor growth and treatment response. *Sci Transl Med* **5**, 187ps189, https://doi.org/10.1126/scitranslmed.3005686 (2013).
81. Powathil, G. G., Gordon, K. E. & Hill, L. A. & Chaplain, M. A. Modelling the effects of cell-cycle heterogeneity on the response of a solid tumour to chemotherapy: biological insights from a hybrid multiscale cellular automaton model. *Journal of theoretical biology* **308**, 1–19, https://doi.org/10.1016/j.jtbi.2012.05.015 (2012).
82. Tzedakis, G., Tzamali, E., Marias, K. & Sakkalis, V. The Importance of Neighborhood Scheme Selection in Agent-based Tumor Growth Modeling. *Cancer Inform* **14**, 67–81, https://doi.org/10.4137/CIN.S19343 (2015).

Acknowledgements

Author Contributions

M.E.O. helped with the G.B. cells collection, the primary G.B. cell line establishment. M.E.O. has analysed the *in vitro* experiments, validated the *in silico* study and co-written the paper manuscript. E.T. has conceived the study plan, the simulated experiments and co-written the paper manuscript. G.T. implemented the *in silico* experiments and contributed as a writer to the paper manuscript. E.L. created part of the experimental protocols and validated the results. G.Z. provided the equipment and consumables to conduct the *in vitro* study. A.V. conducted the G.B. cells collection and co-supervised the project. J.P. has established the primary G.B. cell line and supervised the *in vitro* experiments. V.S. has organized and major-supervised the whole study, evaluated the results and contributed as a writer to the paper manuscript. All authors reviewed the manuscript.

Additional Information

Supplementary information accompanies this paper at https://doi.org/10.1038/s41598-018-34521-5.

Competing Interests: The authors declare no competing interests.

Publisher's note: Springer Nature remains neutral with regard to jurisdictional claims in published maps and institutional affiliations.

APPENDIX

Followingly, preliminary results of interesting observations through the experiments regarding necrosis and invasion GB physiologic characteristics are briefly described.

GB cell death in 2D and 3D

Interestingly, during the observation of the MR images of the GB patients included in our study, as well as by taking into account the empirical clinical knowledge, the next remark was noted: the vast majority of the GB tumor within the brain lesion is necrotic. However, as stated before [99], this necrotic pattern is common between all GB cases and can be attributed in both hypoxia formation due to nutrient-deficiency, as well as to another critical feature of the tumor growth, the intrinsic cell death probability of the cancer cells. This spontaneous GB cell death is considered to be mainly necrosis, rather than apoptosis or autophagy [261].

The intrinsic cell death rate of the different GB cell lines was estimated as an initial step to assess the spontaneous death of the GB cells. The methods used were the trypan blue assay, the MTT assay, as well as the Fluorescence-Activated Cell Sorting (FACS) with both Annexin V (marker of apoptosis) and the propidium iodide (PI, marker of necrosis) for the quantification of cell death. The cell death rate estimates are presented in Table 7 for the different GB cell cultures and are a mean percentage from the experiments conducted with the different protocols. The data produced should be further analyzed in order to finalize the values. Bibliographic values for the spontaneous cell death in gliomas are 5-11% [262] and our preliminary results are in line to the reported ones.

Table 7. The spontaneous cell death estimates for the different GB cell lines used in our study.

Cell Type	Cell death (%)
U87MG	6
T98G	11
GBP03-P1	8
GBP06-P0	7
GBP08-P0	11

To better mimic the *in vivo* growth conditions, we used the hanging-drop technique to generate 3D cultures for the GBP03-P1 and the U87MG cell lines and evaluate the cell death in 3D untreated

spheroids. The spheroids growth was monitored for up to 14 days by bright field microscopy. As denoted before, the primary GB spheroids grow more rapidly than the U87MG spheroids. Concurrently, we measured cell death within spheroids using a combination of LSFM imaging with Draq7 and flow cytometry with PI after enzymatic dissociation of the spheroids. LSFM imaging has the major advantage of live cell imaging. Yet, since the experiment is terminal, a different representative spheroid was scanned at each time point. All images were analyzed regarding the average signal intensity and z-stacks were generated from multiple frames.

In Figure 45, dead cells are detected in the middle hypoxic region and expanding towards necrotic region through time in both cell types with U87MG showing the highest necrotic rate as evaluated in FACS. However, the procedure of the spheroid dissociation in order to produce a single cell solution is not efficient and there is a cell loss at each repetition. Therefore, the absolute values of the FACS experiments cannot be considered. The two different cell types can only morphologically be compared since LSFM signal enhancement is also not quantitative. As denoted in Figure 45, the necrotic population of the primary GB spheroids was depicted over time. In submillimeter dimensions, multiple necrotic foci were shown which subsequently expand towards the center to form a core (dead cells are marked with red). The necrotic population percentages of both spheroid types cannot be correlated to the levels of the spontaneous cell death as estimated in the 2D cultures. Additional phenomena contribute to the cell death and earlier time points should be also evaluated (e.g. the time point when the spheroids are just aggregated).

Nevertheless, as seen in Figure 45, the necrotic core is eventually configured (and not existing from the beginning) within the spheroid through time because of the restricted nutrient diffusion. In more detail, in the upper part, the merged images of the primary spheroids expressing GFP and treated with Draq7 (red) are displayed, indicating necrosis in the middle region which further expands towards center. The brightfield image of the spheroid in 5x objective LSFM lens is also shown. Note the walls of the sampling tube near the margins of the ˜800μm-diameter spheroid. In the lower part, the U87MG spheroids have necrotic cells distributed similarly to the primary spheroids, respectively.
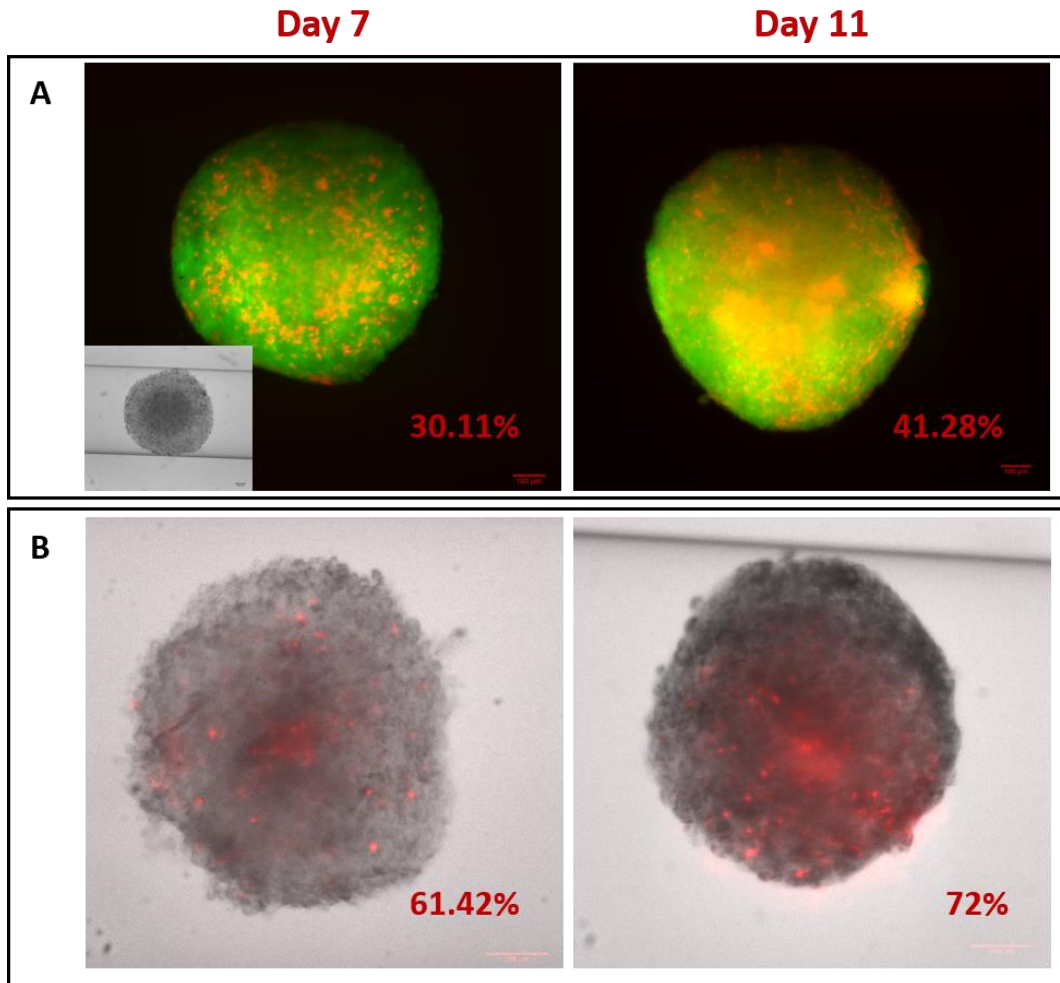
Figure 40. (A) LSFM max intensity z stack images of the GBP03-P1 primary GB spheroids in day 7 (left) and day 11 (right) after seeding. All cells express GFP and necrotic cells are labeled with Draq7 (red). The small image is the relevant brightfield image of the primary spheroid stabilized live sample within the FEP tube. (B) LSFM max intensity z stack images fused to the brightfield ones of the U87MG spheroids. Necrosis is denoted with Draq7 (red). The percentages represent the dead cells as estimated by the respective FACS scans. Scalebar is set at 100 microns.

To further evaluate our results, we permanently fixed the primary spheroids to immunohistopathologically confirm the existence of the necrotic foci. As it can be seen in, there are also necrotic regions seen as empty space that are surrounded by pseudopalisades (areas with denser cellularity) and few apoptotic cells which are positive for caspase 3 (aC3, arrow heads). In Figure 42, an image of the materials used in order to prepare the spheroid histology samples is shown. Because of the small size (<1cm³) of the spheroids, more than one fixed samples were put in flat-bottom 96-well plates and stabilized using a dense agar solution. Since the spheroids have no color, in order for the experimenter to handle the specimens, small-sized banana peels were marked with ink pigments and used as landmarks (see also [263]).
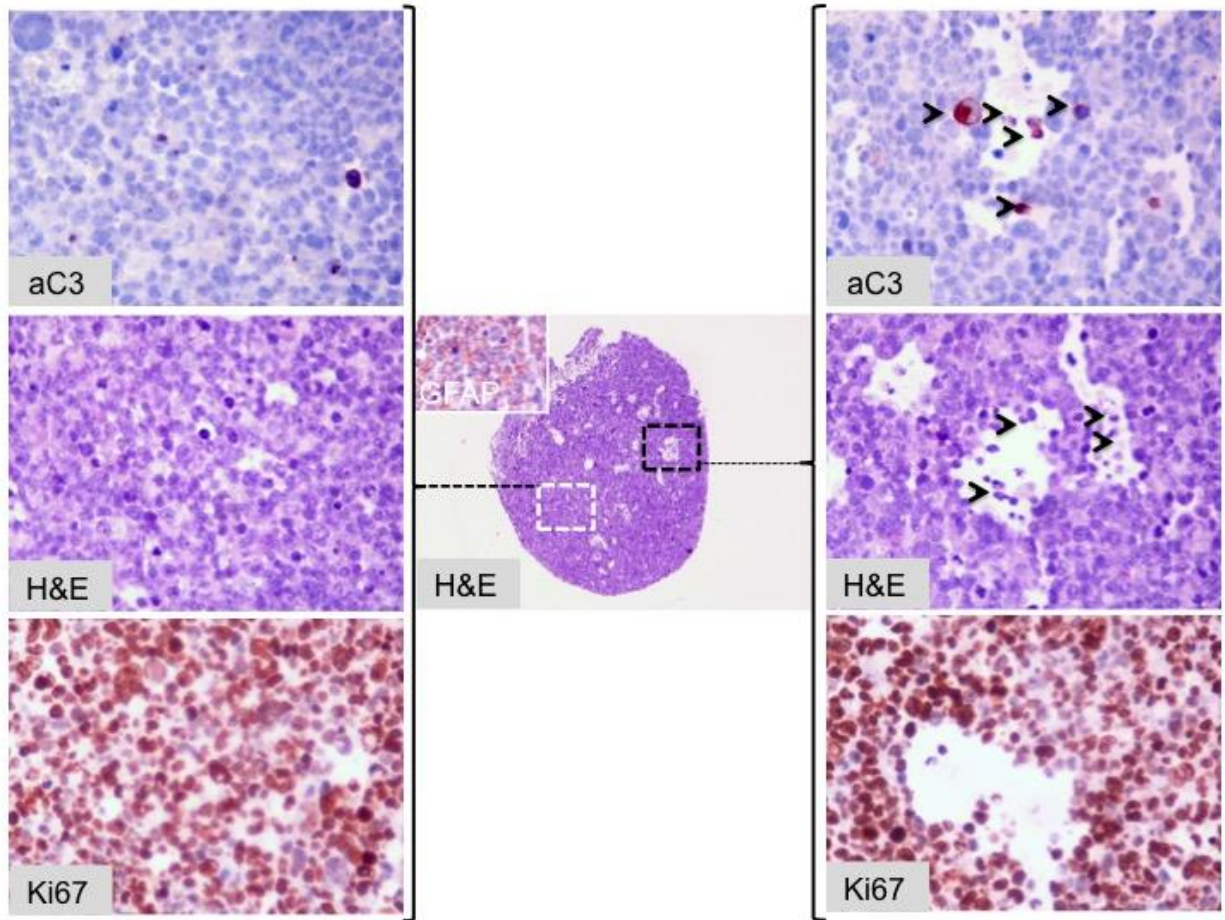
Figure 41. Immunohistopathological image of a GBP03-P1 spheroid of day 11. A non-necrotic (left) region is compared to a necrotic one (right). The non-necrotic region is homogeneous with rare apoptotic cells (aC3 positive). The necrotic area is composed by small cavities, formed because of loss of the cohesion as a result of the increased number of dead cells (arrow heads denote both necrotic-apoptotic cells). Proliferation is the same for both areas (95%). Eosin and hematoxylin stain, DAB as a chromogen, hematoxylin as counterstain. Original magnifications are 40x and 400x.
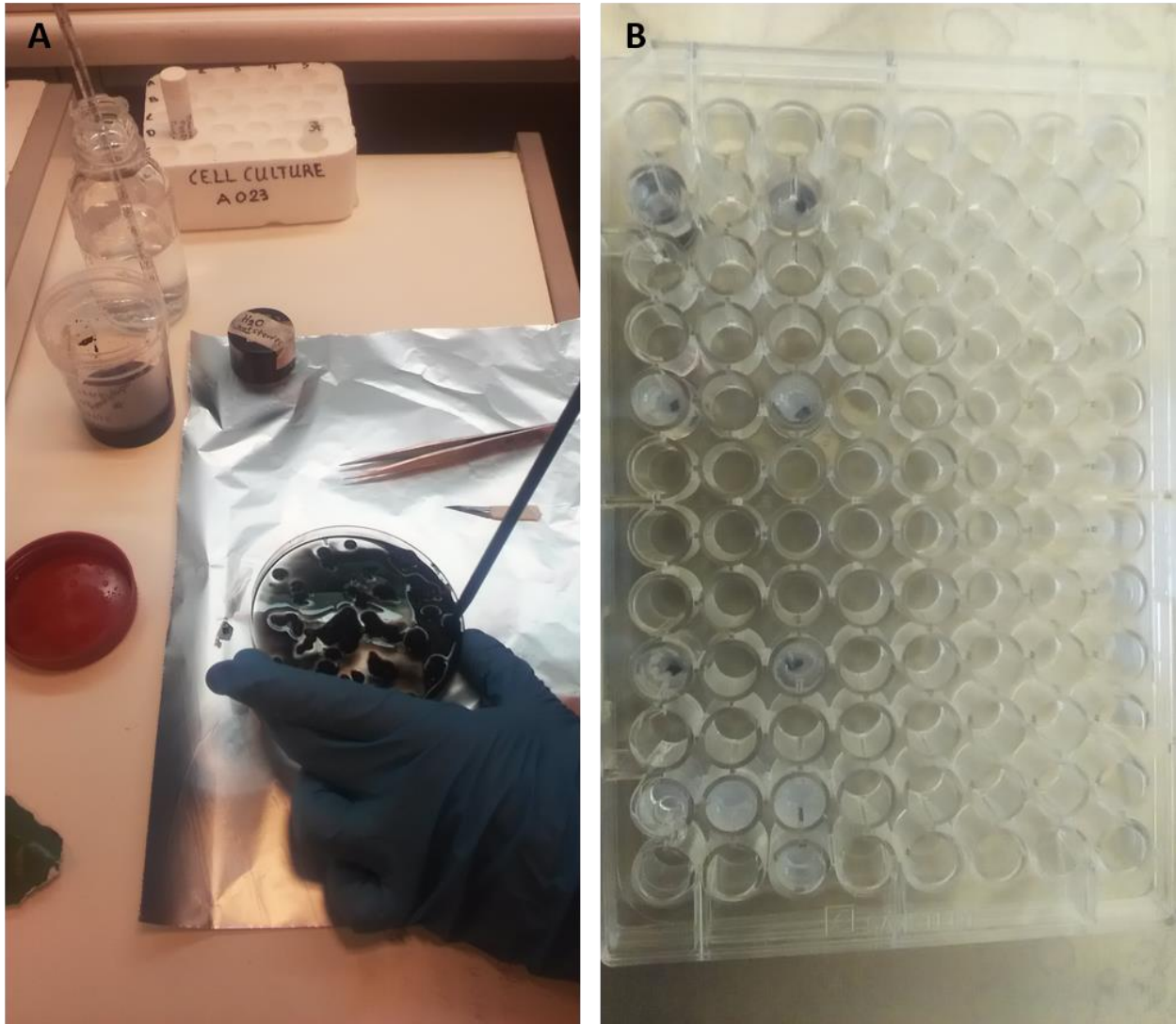
Figure 42. Histopathological sample preparation of the spheroids. (A) Small-sized banana peels were marked with ink pigments. (B) Flat-bottom 96-well plates were used to give shape to the sample. More than one permanently fixed spheroids are put at each well in a dense agar solution. A banana peel is used as a landmark of the sample.

In these set of experiments, there is evidence regarding the formation of necrotic foci and not of the necrotic core as depicted in avascular submillimeter GB tumors using LSFM imaging and immunohistopathological methods. Our results need to be further validated, yet are in line to several theories of the GB growth progress [264] and the mechanisms of the necrosis formation [17, 18].

Necrosis is an essential characteristic of GB growth that needs to be taken into consideration also in the *in silico* approaches. In Figure 43, a possible GB tumor snapshot of the simulated growth progress is shown. Notice that the dead cells initially form necrotic foci that evolve to a rather central necrotic core. The computational model used is a simple CA model that accounts for differential cell division, vessel sources formation and occlusion pressures, as well cell death and quiescence.

The idea is that using simple rule-based models like this one that was inspired by Conway's "Game of Life", the fundamental GB hallmarks can be reproduced and form the typical morphology of small GB tumors. Assessing the pathophysiology of GB necrosis formation and evolution, as well as fostering the intrinsic glioma cell death is a current treatment target to several studies [262, 265] and will further promote our GB ontogenesis understanding and the importance of necrosis as a GB diagnostic feature.
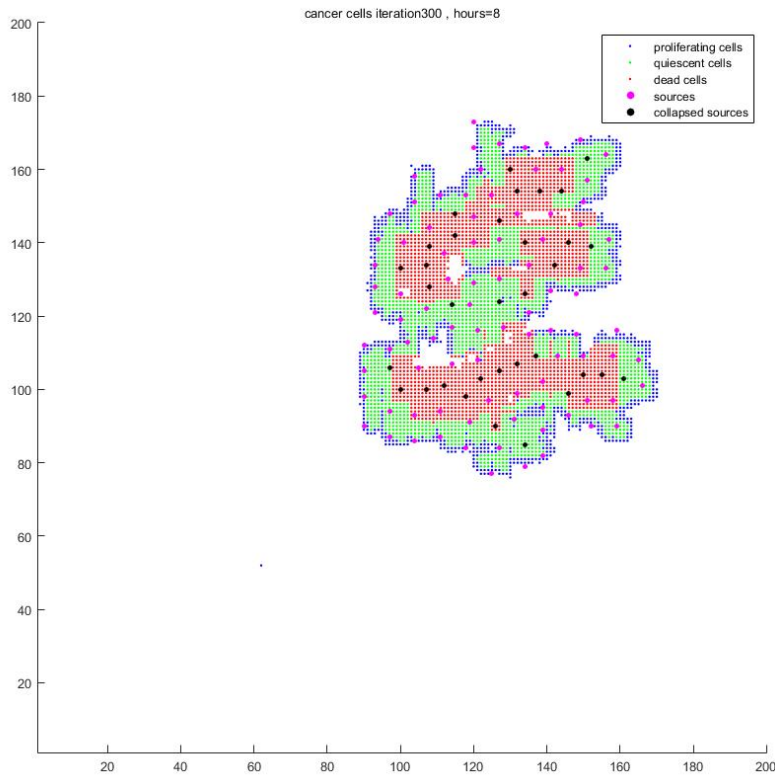

Figure 43. A simulated small-sized tumor with a CA model accounting only for proliferation, nutrients supply and cell death.

GB invasion unexpected findings

Supplementary figures on the subject of **GB** invasion (as described in chapter 4) are shown. First, in Figure 44, the spontaneous ECM production of the **U87MG** spheroids is depicted when growing as control, meaning in the absence of ECM-substrate. This observation is common among the hanging drop spheroid generation and may be experimental evidence regarding the conditional adaptation of the **U87MG** cell line.
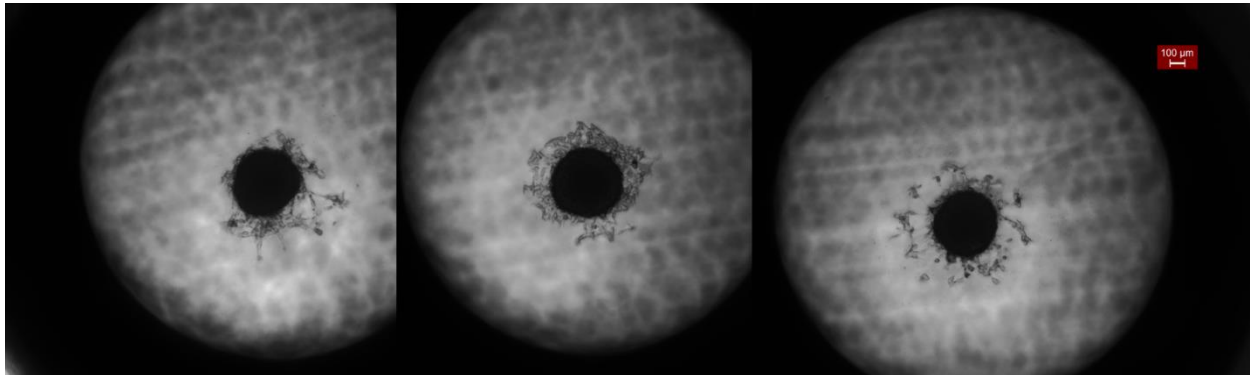

Figure 44. U87MG hanging drop spheroids 15 days after seeding. Scalebar is set at 100 microns.

Additionally to the experiments conducted regarding the invasion for the **U87MG** and the **GBP03** separately, in Figure 45, the co-culture of both cell types is shown. The GBP03-P1 were treated so as to permanently express mCherry (red). Notice that the dominant invasive phenotype is that of the **U87MG** though the **GBP03** are a growing region within the larger spheroid. The images were captured from a fluorescence optical microscope, thus the resolution is poor.
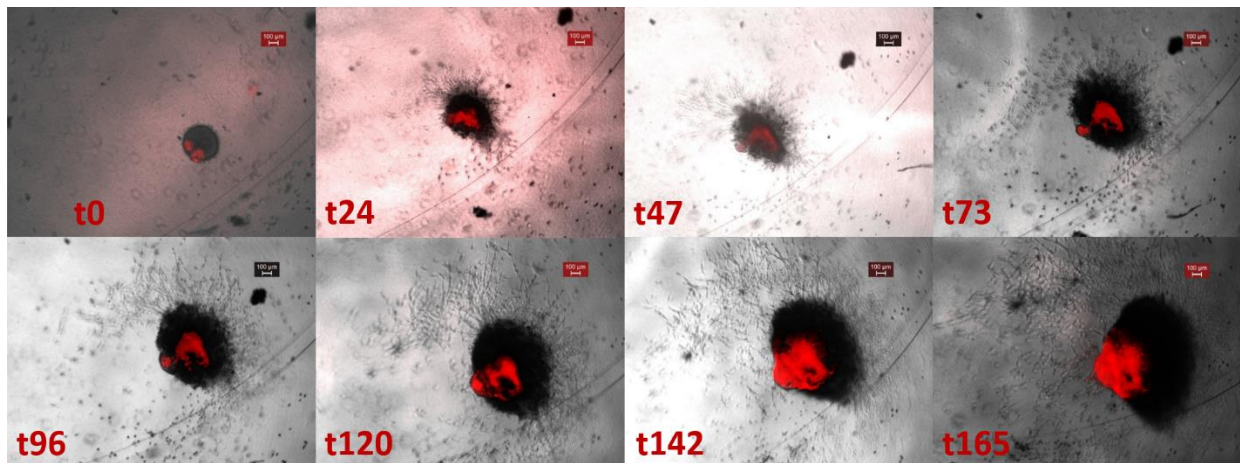

Figure 45. Co-culture of the U87MG-empty and the GBP03-P1-mCherry (red) following the invasion assay (as described in chapter 4). Scalebar is set at 100 microns.